Transient Water Table Influence upon Light Non-Aqueous Phase Liquids (LNAPLs) Redistribution: Laboratory and Modelling Studies

Simiao Sun

A thesis submitted for the degree of Doctor of Philosophy at the University of Birmingham

October 2016

Abstract

Aquifer contamination caused by persistent LNAPL (Light Non-Aqueous Phase Liquids) spills is a globally widespread problem. Fluctuating water table conditions influence capillary-held mass above and below the water table. Risks posed by such a dynamic LNAPL source zone vary over time as water tables oscillate from tidal effects, seasonality or anthropogenic interferences. Whist LNAPL dynamics are evident at the field scale, measurements of say LNAPL thickness variation in a borehole are not truly representative of the actual source zone dynamic nature and point to the necessity of laboratory quantitative visualisation and modelling studies. In this study, the first fully automated multiphase flow dynamic water table experimental system comprising both hardware and software, was developed to: i) automatically implement programmable cyclic water table fluctuations via Raspberry Pi^{TM} based inexpensive electronics; ii) dynamically monitor the real-time saturation distributions of all fluids (red-dyed-LNAPL, blue-dyed-water and air) in a 2-D sand tank, using high temporal and spatial resolution automated multi-spectral photography; and iii) accurately interpret the large detailed datasets via the advanced multi-spectral image analysis. Such automated data acquisition and processing permit the LNAPL release and its redistribution under oscillating water table conditions to be demonstrated in vivid video formats of photographic records, interpreted 2-D saturation contours and 1-D profiles of water, LNAPL, and air. A variety of eight experimental scenarios were undertaken via the system to discern the influencing mechanisms of cyclic fluctuations incorporating with other influential factors including aquifer media, the volume and timing of LNAPL release, fluctuation speed, layered heterogeneities, etc. Applicability of the standard model from US-EPA NAPL simulator was exercised with a selection of experimental data, which provided a good general match of the overall features of the release and oscillation dynamics, and examined the reliability of experimental interpretation and highlighted crucial features. Various new interesting processes were captured and quantified that may shed light on theories and practice, such as: LNAPL is dispersed through the range of water table oscillation, which may promote LNAPL entrapment at the lowermost positions and increase thickness dispersion around the uppermost positions; Saturated fine grain layers act as LNAPL barriers yet not a storage, which may also facilitate confined LNAPL below the water table that is often mistakenly characterised as DNAPL; Multiple fine grain layers may sandwich most LNAPL mass at low water table positions, which may potentially provide insights on remediation. The high-resolution and high-frequency detailed quantitative dataset harvested is expected to supplement and expand the theories of multiphase flow distribution in porous media, where owing to the realization of the automated system, unprecedented processes were captured; and serve as a robust validation source

of numerical models and conceptual models which are essential tools in contamination site characterization, prediction, and remediation formulation.

Keywords: 2D automated sand tank experimental system, LNAPL behaviour, transient water table fluctuations, multi-spectral image analysis, numerical modelling

Acknowledgement

My sincere gratitude goes to lead supervisor Michael Rivett first for granting me a life-changing opportunity to study at the University of Birmingham, and for making invaluable comments, providing tremendous support and caring, and demonstrating scientific rigour throughout this study.

Special thanks go to my unconventional co-supervisor Alan Herbert, who is a living repository of numerous inspiring ideas and unique perspectives. He demonstrated the enchantment and enjoyment of wielding scientific elements into both research and daily life.

Heartfelt thanks go to the versatile Richard Greswell, my voluntary supervisor, cultural mentor, and family in England, who not only executed the development of the 2-D tank but also has been immensely encouraging, understanding and helpful throughout my PhD.

Sincere appreciation goes to Jason Hilton and Mingmei Liang who voluntarily became my mentors and family in England with persistent support, encouragement and guidance.

Enormous admiration goes to my department head John Tellam, who has been an exemplary great scientist, a dedicated educator and a beacon to generations of hydrogeologists worldwide.

Profound gratitude goes to Cedric Kechavarzi who generously provided a copy of his PhD thesis, which inspired my monitoring methodology and allowed me to learn from and advance upon.

Thanks to the technical assistance from Steven West in Bio-workshop, and the trial experiment camera provided by Ivan Sansom. Thanks to Yan Lu and Canfa Wang for helping with the tank lifting. Thanks to the administrative and daily aid from Gretchel Coldicott and Aruna Mistry.

Thanks to the enlightening company and support from my wonderful hydro colleagues, including: Mahmoud Jaweesh, Michael Riley, Lindsay McMillan, Ben Harvey, Christopher Barry, Gary Clarke, Ban To, Mark Cuthbert and Timothy Batty. Thanks to my kindest earth science community: Rosemary Dartnall, Derren Cresswell, Murray Hogget, Kate Newton, etc.

I gratefully acknowledge my dearest and most unique friends: Sofia Vescovelli, Carlos D'Apolito, Roland Sookias, Rodrigo Neregato, Gael Lymer, Canfa Wang, Erdem Colak, Xiu Meng, Kang Guan, Blagoy Ivanov and Zdravko Milenov.

Thanks to Plamen Andreev for being my first reader, for his unconventional inspirations, creative influences and encouragements upon my endless exploration of my inner self and the outer world.

The thesis was dedicated to my grandfather Yonggui Huang, my parents Xiaobin Sun and Xiaoya Huang, who, despite having lived a difficult life, still hold enormous respect towards knowledge and have endeavoured to support my academic dream zealously.

List of contents

List of figures

List of tables

1 Background

1.1 Introduction

Light Non-Aqueous Phase Liquids (LNAPLs), notably including petroleum hydrocarbon fuels and oils (e.g. gasoline, diesel, jet fuel), are one of the most widespread pollutants of groundwater aquifer systems that may often provide essential water supplies and support hydro-ecological environments(CL:AIRE, 2014). LNAPLs are:

- long-term and persistent sources of groundwater contamination;
- complex hydrocarbon mixtures and may contain carcinogens such as benzene, toluene, that may pose a significant danger to drinking water resources, agriculture, and hydro-ecological environments;
- existent as a separate LNAPL and may undergo multiple phases (with water and air phases) which may lead to the intricacy of migration and distribution and challenging remediation (Newell *et al.*, 1995).

LNAPLs are immiscible with water, and as less dense than water, will float on or around an underlying groundwater table and may exist as LNAPL “free product” phase, aqueous, gaseous, and absorbed phases. They may volatilize or dissolve into groundwater gradually and form dissolved plume in shallow aquifers. A conceptualization of an LNAPL spills is shown in Figure 1-1.

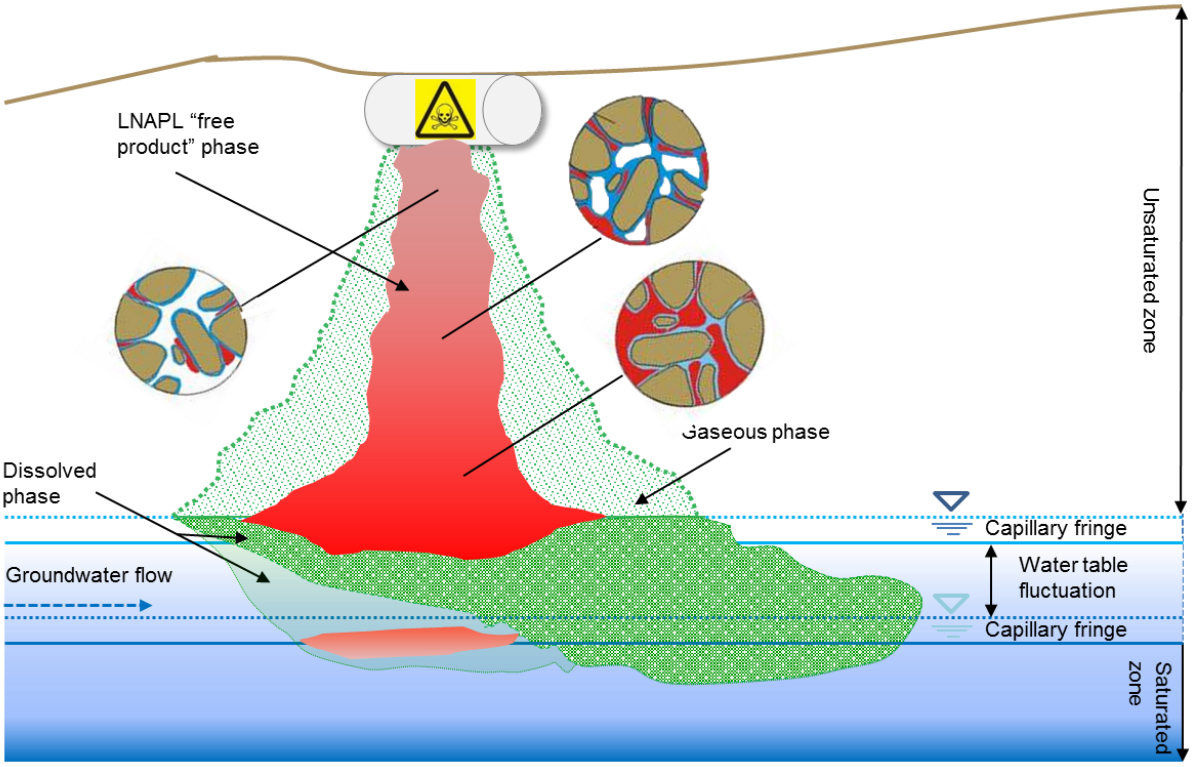

Figure 1-1 An illustrative conceptual model for one of the most common LNAPL release mechanisms: accidental leakage from above ground (such as gas stations, airports, petroleum manufacturers, etc.) or within shallow aquifer below ground. Modified from Newell *et al.* (1995); Marinelli and Durnford (1996); ITRC, (2009); Rivett *et al.* (2011); Sun *et al.* (2013); (CL:AIRE, 2014)

As a part of the dynamic subsurface hydrogeological system, groundwater tables may fall and rise over both short term and long term, according to the total aquifer storage changes caused by both natural phenomena (seasonality, tidal effect, natural recharge and discharge including precipitation and evapotranspiration, atmospheric pressure changes, etc.) and anthropogenic involvements (groundwater extraction and injection, etc.). Groundwater table fluctuations and the fact that the majority of mass in an LNAPL spill will often be present in and around the water table after spillage and potentially still decades later as many LNAPLs are not very soluble. Given the wide, near ubiquitous, use of LNAPL hydrocarbon fuels/oils (historical and current) and poor environmental awareness and management practices in the past, source (use) areas may often contain literally tonnes of LNAPL that may persist for decades. The characteristics of the water table fluctuation conditions (for instance, amplitude, frequency, fluctuation patterns, locations, etc.) may exert significant control over the quantity, distribution and timeframes of entrapped residual LNAPL by capillary forces, mobile LNAPL body and mobile lenses present in aquifer systems and also that recorded in boreholes (Marinelli and Durnford, 1996).

Therefore, it is vital to understand how transient water tables, likewise ubiquitous, may influence the migration and fate of LNAPLs, risks posed to receptors and our abilities to remediate and manage LNAPLs released to the subsurface. Although fluctuating water table conditions have been shown to enhance the distribution (entrapment and smearing) and migration of LNAPLs (Steffy *et al.*, 1997), most relevant studies have been relatively limited, and controlling factors are not clearly understood and or datasets obtained that allow adequate validation of theories.

To assess the severity and/or to predict the consequences of a NAPL spill, site characterisation (including the composition and properties of spilt NAPL, spill circumstances, aquifer geology and groundwater dynamics) must be adequately conducted, so that the LNAPL transport and fate can be simulated by validated numerical models using the theories of multiphase flow. Thereafter, contamination remediation strategies can be developed upon. However, it is mostly common that contaminations are discovered years after the spillage during pipeline /tank maintenance or by the occurrence within close-by receptors. Thus, the spill circumstances, including the spilt volume, timing, rate and sometimes the location, remains unclear, which increases the difficulty in locating and/or characterising the LNAPL body (Simpson *et al.*, 1997). Extensive field investigation can be financially and technically unattainable, depending on the features of the site-specific NAPL spill and the borehole distribution within the contaminated area, which can be made feasible by numerical models that predict the migration and distribution of the body. When borehole drilling is needed to investigate LNAPL distribution, selection of borehole locations and depths is of particular importance and should be guided with numerical model predictions, since an inadequate borehole location and depth may lead to cross-contamination, fugitive vapour release, flash fires or even explosions (Mercer and Cohen, 1990). Even with a substantial field investigation, measurements of say LNAPL thickness variation in a borehole are not very revealing of the actual source zone dynamic nature (Steffy *et al.*, 1997). All issues mentioned above regarding characterisation, prediction, and remediation implementation largely depend on the predictive capabilities of numerical models, which are built upon and rely on the validation by robust laboratory datasets. Here points out the importance of LNAPL lab visualization studies which constitute the fundaments of multiphase flow theories.

A considerable amount of numerical models have been developed to characterise and predict NAPL transport and behaviours in subsurface environment, particularly in porous medium systems, for instance: Mualem (1976); Abriola and Pinder (1985); Pinder and Abriola (1986); R. Lenhard and Parker (1987); Parker and Lenhard (1987); Parker *et al.* (1987); R. J. Lenhard *et al.* (1989); Ferrand *et al.* (1990); Guarnaccia *et al.* (1997); Oostrom and Lenhard (1998); Van Geel and Roy (2002); Johnston and Trefry

(2009). However, without robust laboratory data to accurately validate the models and tackle the gaps in theories, the models can only be used as a conceptual model or is only capable of interpreting limited processes.

1.2 Previous studies

The characterisation, prediction, and remediation of LNAPL pollution can usually be extremely challenging, expensive or infeasible, particularly at those sites where transient water table exists, which motivates the demands for an enhanced understanding on how these contaminants may re-distribute. During the past three decades, a substantial number of lab-scale experimental based investigations with some including numerical models on the theories of LNAPL migration and distribution in porous media were conducted, the topics of which can be categorized into four types:

1) the mathematical and numerical description of *K-S-P* (permeability-saturation-capillary pressure) relationships inclusive or exclusive hysteresis, such as (Abriola and Pinder, 1985; R. Lenhard and Parker, 1987; Parker and Lenhard, 1987; Parker *et al.*, 1987; R. J. Lenhard *et al.*, 1989; Ferrand *et al.*, 1990; Oostrom and Lenhard, 1998; Van Geel and Roy, 2002; Sharma and Mohamed, 2003; Johnston and Trefry, 2009);

2) LNAPL lens geometry, such as Schroth *et al.* (1995); Chevalier (1998); Miller *et al.* (2004)

3) Multi-phase flow behaviour experiments that describe the migration and distribution of LNAPL under various influential factors, including: geologically heterogeneous structure (Catalan and Dullien, 1995; Illangasekare *et al.*, 1995; Wipfler *et al.*, 2004; Fagerlund, 2006); variant water table conditions in 1-D (R. Lenhard *et al.*, 1993; Steffy *et al.*, 1995; Steffy *et al.*, 1997, 1998; S Chompusri *et al.*, 2001; S Chompusri, 2004; Kamon *et al.*, 2006; Dobson *et al.*, 2007; Flores *et al.*, 2007; Flores *et al.*, 2011; Zhou *et al.*, 2014; Flores *et al.*, 2016; Yimsiri *et al.*, 2016) and in 2-D (Van Geel and Sykes, 1997; Oostrom, Hofstee*, et al.*, 2006); particle size distribution and wettability (Francisca, 2006; Francisca and Montoro, 2014); and freezing and frozen environments (Iwakun *et al.*, 2010).

4) Literature reviews on laboratory methodology and theory advancement (Mercer and Cohen, 1990; Chevalier and Petersen, 1999; Oostrom, Dane*, et al.*, 2006; Werth *et al.*, 2010; Kamaruddin *et al.*, 2011; Alazaiza *et al.*, 2015; Alazaiza *et al.*, 2016).

Among those studies, LNAPL behaviour studies under varying water table conditions are particularly of relevance. Although fluctuating water table conditions have been shown to enhance the entrapment, redistribution, and smearing of LNAPL and significantly affect the hysteresis process (R. Lenhard *et al.*, 1993; Catalan and Dullien, 1995), studies reported in this particular area (i.e. LNAPL transport under a variable water table) have been relatively limited and controlling mechanism and factors were not thoroughly understood. Among these lab-scale investigations that have quantified the redistribution process of LNAPL under varying water table conditions were mostly conducted 1-D column experiments and only two studies in 2-D sand tanks. The first three-phase experiment with variable water table conditions (R. Lenhard *et al.*, 1993) was conducted in a 1-D flow column which focused on the LNAPL and air entrapment during water imbibition and drainage. However, the water table was implemented as an unnatural impulse, where a 5cm water table was raised or lowered in every 5 or 10-minute intervals. Cyclic patterns were not considered in this study.

A series of laboratory-scale study (1-D column setup with two cycles of water table fluctuation) associated with field investigation (Steffy *et al.*, 1995; Steffy *et al.*, 1997, 1998) were carried out to delineate three-phase *P-S* relationship during water imbibition and drainage processes, particularly vertical displacement and entrapment. The numbers of water table fluctuations in the above studies were limited, and the fluctuation pattern was either a sudden raise or an immediate decline. The gamma ray scanning was adopted as the monitoring method, and throughout the experiment, only seven scans were collected. The scanning was performed only at or near hydrostatic conditions when the water table was located at the lowermost or uppermost positions. No in-process dynamics could be recorded.

One comprehensive study discerning the influence of cyclic water table was performed in a 1-D round column as an unpublished Ph.D. study (S Chompusri *et al.*, 2001; S Chompusri, 2004).The study improved previous laboratory studies by implementing a more realistic, long-term cyclic water table oscillations to define the redistribution processes. Five influential factors including oscillation numbers and frequency, the effect of capillary fringe, different LNAPL source thicknesses, and aquifer media were investigated. However, the research applied intrusive monitoring method as the quantitative approach and imaging were only used for qualitative purposes. Conventional intrusive methods were incapable of monitoring the entire multiphase flow domain without disrupting the dynamics. Moreover, the limitation of one-dimension restrained the study from obtaining 2-D LNAPL structure

such as lateral spreading, and the round column with a larger contact area would induce a higher possibility of edge effects.

Another comprehensive series of studies looking at cyclic fluctuation influences were performed in a 1-D square column to serve as a validation of hysterisic K-S-P numerical model (Kamon *et al.*, 2006; Flores *et al.*, 2007; Flores *et al.*, 2011; Zhou *et al.*, 2014; Flores *et al.*, 2016; Yimsiri *et al.*, 2016). The monitoring method was a simplified version of the multi-spectral image analysis (Kechavarzi *et al.*, 2000), where instead of calibrating a set of samples with varied water and LNAPL saturations, only three extreme values were calibrated, which respectively are: completely dry sand (S_w=0%, S_o=0%), completely water saturated sand (S_w=100%, S_o=0%), and complete LNAPL saturated sand (S_w=0%, S_o=100%). These three values constituted a plane where the saturations in-between were interpolated with assumed linearity. The water table oscillations were operated manually and abruptly, where the water table was either quickly lowered below the column datum or promptly raised to the uppermost position. Some cyclic features during the underway drainage and imbibition were monitored, however, these recorded results not sufficient enough to describe detailed LNAPL dynamics.

In summary, there appears to be a significant dearth in the quantitative investigations that discern mechanisms of continuous cyclic water table oscillations upon LNAPL behaviour in porous media, and a lag in the development of experimental rig and monitoring methodology that flexibly executes desirable groundwater dynamics and accurately and frequently monitors full-domain multiphase fluid dynamics.

1.3 Aims and objectives

The paramount aim of this study is to observe how variations in groundwater table levels may influence the dynamic migration and redistribution of LNAPL released (spilt) into the subsurface, and thereby provide fundamental knowledge on the prediction of LNAPL distributions at sites, the risks posed to receptors and effective clean-up of polluted underground environments and including the safeguard drinking water resources of many populations worldwide. This was addressed by means of laboratory experiments with numerical model interpretations of the data arising to aid the determination of controlling processes and their sensitivities, with emphasis on both homogeneous and layered heterogeneous porous media systems.

More specifically, the objectives of this laboratory-and-modelling-based study are:

- To develop an experimental system to conduct 2-D experiments in order to observe transient migration and (re)distribution of multiphase fluids (water-LNAPL-air), where programmable and automatically controlled water table fluctuation conditions are incorporated;
- To advance new methodologies that reliably quantify real-time multiphase flow, simultaneously measuring the pore saturations of LNAPL, water, and gas phases;
- To produce original and visualized datasets of LNAPL migration and (re)distribution via a series of 2-D experiments that discern the influences of transient cyclic water table fluctuations together with other potentially influential factors, including homogeneous scenarios (medium sand aquifer scenario as a benchmark, water table fluctuation speed, release timing relative to water table high or low positions, release volume and aquifer media) and layered heterogeneous scenarios (single partial fine grain layer, single complete fine grain layer and multiple complete fine grain layers);
- To build a descriptive LNAPL distribution model to quantitatively interpret a selection of the observed experimental data, which examines the reliability of experimental interpretation and highlight the crucial features of the multi-phase flow dynamics.

1.4 Thesis approach

This thesis was organized into seven chapters:

Chapter 1, the conception of the project, including the incentives, aims, and objectives of the study.

Chapter 2, an introduction of the integrated methodology developed during the course of the study which involved two major establishments: the multiphase flow experimental system and the advanced multi-spectral image analysis. An innovative tool was developed to implement automatic programmable water table fluctuation conditions within a water-LNAPL-air three-phase flow sand-tank system. And a high-frequency, high-resolution real-time fluid mapping methodology was redeveloped with the competency of batch-processing large datasets.

Chapter 3, an overview of the eight experimental scenarios undertaken via the system, specifying the features and operational procedures along with accuracy achieved. Thereafter, a review is given on the functionality, performance, and limitations of the experimental system.

Chapter 4, an introduction to the modelling methodology including key governing equations and program improvements made for the modelling code.

Chapter 5, the results and discussions of the base case scenario performed experimentally as a benchmark for the variant scenarios in Chapter 6. The base case scenario is designed to reveal the high temporal and spatial resolution dynamics of water, LNAPL and air saturation distributions in a homogenous medium sand aquifer during an LNAPL release upon static water table condition and transient sine-wave like water table oscillation conditions. Results of the LNAPL release, a single-cycle water table oscillation and inter-cycle oscillation are analysed in detail via a selection of featured processes. The modelling results are presented alongside the experimental interpretations.

Chapter 6, the results and discussions of the variant scenarios discerning the multi-phase flow mechanisms under seven influential factors, including the aquifer media, the volume and timing of LNAPL release, water table fluctuation speed, layered heterogeneities, etc. The datasets derived from seven scenarios are inspected in detail by inter-scenario comparisons and implications towards theories and practice are given.

The two result chapters comprise sizable data presented in video and image formats, including the photographic record, fluid saturation contours, and profiles. The videos of all processes are attached in the digital appendices A.2.

Chapter 7, drawing on the conclusions, implications, and future work.

Reference

Abriola, L. M., and Pinder, G. F. (1985). A multiphase approach to the modeling of porous media contamination by organic compounds: 1. Equation development. *Water Resources Research, 21*(1), 11-18.

Alazaiza, M. Y., Ngien, S. K., Bob, M. M., Ishak, W. M. F., and Kamaruddin, S. A. (2015). An overview of Photographic Methods in Monitoring Non-Aqueous Phase Liquid Migration in Porous Medium. *Special Topics & Reviews in Porous Media: An International Journal, 6*(4), 367-381.

Alazaiza, M. Y., Ngien, S. K., Ishak, W. M. F., and Kamaruddin, S. A. (2016). A Review of Light Reflection and Transmission Methods in Monitoring Non-Aqueous Phase Liquid Migration in Porous Media. *Journal of Engineering and Applied Sciences, 11*(4), 2319-2326.

Catalan, L. J., and Dullien, F. A. (1995). Application of gravity drainage to the recovery of residual LNAPL in homogeneous and lensed sand packs. *Journal of Contaminant Hydrology, 18*(4), 279-306.

Chevalier, L. R. (1998). Experimental and numerical evaluation of LNAPL lens and polluted capillary fringe thickness. *Journal of Environmental Engineering, 124*(2), 156-161.

Chevalier, L. R., and Petersen, J. (1999). Literature review of 2-D laboratory experiments in NAPL flow, transport, and remediation. *Journal of Soil Contamination, 8*(1), 149-167.

Chompusri, S. (2004). *LNAPL redistribution under water table fluctuation condition*. Unpublished PhD thesis. University of Birmingham.

Chompusri, S., Rivett, M. O., and Mackay, R. (2001). *LNAPL redistribution on a fluctuating water table: column experiments*. Paper presented at the Groundwater quality: natural and enhanced restoration of groundwater pollution, Sheffield, UK. http://iahs.info/redbooks/a275/iahs_275_225.pdf

CL:AIRE. (2014). An illustrated handbook of LNAPL transport and fate in the subsurface. In M. O. Rivett (Ed.). London: CL:AIRE.

Council), I. I. T. R. (2009). Evaluating LNAPL Remedial Technologies for Achieving Project Goals. LNAPL-2 (L. T. Interstate Technology & Regulatory Council, Trans.). Washington, D.C.

Dobson, R., Schroth, M. H., and Zeyer, J. (2007). Effect of water-table fluctuation on dissolution and biodegradation of a multi-component, light nonaqueous-phase liquid. *Journal of Contaminant Hydrology, 94*(3), 235-248.

Fagerlund, F. (2006). *Experimental and modelling studies on the spreading of non-aqueous phase liquids in heterogeneous media.* (PhD), Uppsala University.

Ferrand, L. A., Milly, P., Pinder, G. F., and Turrin, R. P. (1990). A comparison of capillary pressure-saturation relations for drainage in two-and three-fluid porous media. *Advances in Water Resources, 13*(2), 54-63.

Flores, G., Katsumi, T., Eua-Apiwatch, S., Lautua, S., and Inui, T. (2016). Migration of different LNAPLs in subsurface under groundwater fluctuating conditions by the simplified image analysis method. *Journal of Geo-Engineering Sciences, 3*(1), 15-30.

Flores, G., Katsumi, T., Inui, T., and Kamon, M. (2011). A simplified Image analysis method to study LNAPL migration in porous media. *Soils and foundations, 51*(5), 835-847.

Flores, G., Katsumi, T., and Kamon, M. (2007). Evaluation of LNAPL migration under fluctuating groundwater by image analysis. *Disaster Prevention Research Institute Annals, Kyoto University, 50*, 399-405.

Francisca, F. M. (2006). *Effect of porosity variability on ganglia entrapment during immiscible displacement.* Paper presented at the Fifth International Congress on Environmental Geotechnics, Cardiff, Wales, UK.

Francisca, F. M., and Montoro, M. A. (2014). Influence of particle size distribution and wettability on the displacement of LNAPL in saturated sandy soils. *Journal of Environmental Engineering, 141*(6), 04014091-04014091-04014091-04014012.

Guarnaccia, J., Pinder, G., and Fishman, M. (1997). NAPL: Simulator documentation: U.S. Environmental Protection Agency.

Illangasekare, T. H., Ramsey, J. L., Jensen, K. H., and Butts, M. B. (1995). Experimental study of movement and distribution of dense organic contaminants in heterogeneous aquifers. *Journal of Contaminant Hydrology, 20*(1), 1-25.

Iwakun, O., Biggar, K., and Sego, D. (2010). Influence of cyclic freeze-thaw on the mobilization of LNAPL and soluble oil in a porous media. *Cold Regions Science and Technology, 64*(1), 9-18.

Johnston, C., and Trefry, M. (2009). Characteristics of light nonaqueous phase liquid recovery in the presence of fine-scale soil layering. *Water Resources Research, 45*(5), W05412.

Kamaruddin, S. A., Sulaiman, W. N. A., Zakaria, M. P., Othman, R., and Rahman, N. A. (2011). *Laboratory simulation of LNAPL spills and remediation in unsaturated porous media using the image analysis technique: A review.* Paper presented at the National Postgraduate Conference (NPC), 2011.

Kamon, M., Li, Y., Flores, G., Inui, T., and Katsumi, T. (2006). Experimental and numerical study on migration of LNAPL under the influence of fluctuating water table in subsurface. *Disaster Prevention Research Institute Annals, Kyoto University, 49*, 383-392.

Kechavarzi, C., Soga, K., and Wiart, P. (2000). Multispectral image analysis method to determine dynamic fluid saturation distribution in two-dimensional three-fluid phase flow laboratory experiments. *Journal of Contaminant Hydrology, 46*(3), 265-293.

Lenhard, R., Johnson, T., and Parker, J. (1993). Experimental observations of nonaqueous-phase liquid subsurface movement. *Journal of Contaminant Hydrology, 12*(1), 79-101.

Lenhard, R., and Parker, J. (1987). A model for hysteretic constitutive relations governing multiphase flow: 2. Permeability-saturation relations. *Water Resources Research, 23*(12), 2197-2206.

Lenhard, R. J., Parker, J. C., and Kaluarachchi, J. J. (1989). A model for hysteretic constitutive relations governing multiphase flow: 3. Refinements and numerical simulations. *Water Resources Research, 25*(7), 1727-1736. doi: 10.1029/WR025i007p01727

Marinelli, F., and Durnford, D. S. (1996). LNAPL thickness in monitoring wells considering hysteresis and entrapment. *Ground Water, 34*(3), 405.

Mercer, J. W., and Cohen, R. M. (1990). A review of immiscible fluids in the subsurface: properties, models, characterization and remediation. *Journal of Contaminant Hydrology, 6*(2), 107-163.

Miller, C., Durnford, D., and Fowler, A. (2004). Equilibrium nonaqueous phase liquid pool geometry in coarse soils with discrete textural interfaces. *Journal of Contaminant Hydrology, 71*(1), 239-260.

Mualem, Y. (1976). A new model for predicting the hydraulic conductivity of unsaturated porous media. *Water Resources Research, 12*(3), 513-522.

Newell, C., Acree, S., Ross, R., and Huling, S. (1995). Ground water issue: light nonaqueous phase liquids: Groundwater Services, Inc., Houston, TX (United States).

Oostrom, M., Dane, J. H., and Wietsma, T. W. (2006). A review of multidimensional, multifluid intermediate-scale experiments. *Vadose Zone Journal, 5*(2), 570-598.

Oostrom, M., Hofstee, C., and Wietsma, T. W. (2006). Behavior of a viscous LNAPL under variable water table conditions. *Soil & Sediment Contamination, 15*(6), 543-564.

Oostrom, M., and Lenhard, R. J. (1998). Comparison of relative permeability-saturation-pressure parametric models for infiltration and redistribution of a light nonaqueous-phase liquid in sandy porous media. *Advances in Water Resources, 21*(2), 145-157.

Parker, J., and Lenhard, R. (1987). A model for hysteretic constitutive relations governing multiphase flow: 1. Saturation-pressure relations. *Water Resources Research, 23*(12), 2187-2196.

Parker, J., Lenhard, R., and Kuppusamy, T. (1987). A parametric model for constitutive properties governing multiphase flow in porous media. *Water Resources Research, 23*(4), 618-624.

Pinder, G. F., and Abriola, L. M. (1986). On the simulation of nonaqueous phase organic compounds in the subsurface. *Water Resources Research, 22*(9S).

Rivett, M. O., Wealthall, G. P., Dearden, R. A., and McAlary, T. A. (2011). Review of unsaturated-zone transport and attenuation of volatile organic compound (VOC) plumes leached from shallow source zones. *Journal of Contaminant Hydrology, 123*(3), 130-156.

Schroth, M., Istok, J., Ahearn, S., and Selker, J. (1995). Geometry and position of light nonaqueous-phase liquid lenses in water-wetted porous media. *Journal of Contaminant Hydrology, 19*(4), 269-287.

Sharma, R. S., and Mohamed, M. H. (2003). An experimental investigation of LNAPL migration in an unsaturated/saturated sand. *Engineering Geology, 70*(3), 305-313.

Simpson, M. M., Weston, R. F., Willson, I. C. S., Weaver, J. W., and Charbeneau, R. J. (1997). *Experimental investigation of LNAPL transport in the vadose zone: comparison with the Hydrocarbon Spill Screening Model.* University of Texas at Austin.

Steffy, D., Johnston, C., and Barry, D. (1995). *A field study of the vertical immiscible displacement of LNAPL associated with a fluctuating water table.* Paper presented at the Groundwater Quality: Remediation and Protection.

Steffy, D., Johnston, C., and Barry, D. (1997). Monitoring residual gasoline movement associated with a fluctuating water table: American Society of Civil Engineers, Reston, VA (United States).

Steffy, D., Johnston, C., and Barry, D. (1998). Numerical simulations and long-column tests of LNAPL displacement and trapping by a fluctuating water table. *Journal of Soil Contamination, 7*(3), 325-356.

Sun, S., Rivett, M. O., and Herbert, A. W. (2013). *Research design for transient water table influence upon Light Non-Aqueous Phase Liquids (LNAPLs) redistribution: laboratory and modelling studies*. Paper presented at the "What's New in Hydrogeology 2013 ?" Research Poster Meeting, Leeds, UK.

Van Geel, P., and Roy, S. (2002). A proposed model to include a residual NAPL saturation in a hysteretic capillary pressure–saturation relationship. *Journal of Contaminant Hydrology, 58*(1), 79-110.

Van Geel, P., and Sykes, J. (1997). The importance of fluid entrapment, saturation hysteresis and residual saturations on the distribution of a lighter-than-water non-aqueous phase liquid in a variably saturated sand medium. *Journal of Contaminant Hydrology, 25*(3), 249-270.

Werth, C. J., Zhang, C., Brusseau, M. L., Oostrom, M., and Baumann, T. (2010). A review of non-invasive imaging methods and applications in contaminant hydrogeology research. *Journal of Contaminant Hydrology, 113*(1), 1-24.

Wipfler, E., Ness, M., Breedveld, G., Marsman, A., and Van Der Zee, S. (2004). Infiltration and redistribution of LNAPL into unsaturated layered porous media. *Journal of Contaminant Hydrology, 71*(1), 47-66.

Yimsiri, S., Euaapiwatch, S., Flores, G., Katsumi, T., and Likitlersuang, S. (2016). Effects of water table fluctuation on diesel fuel migration in one-dimensional laboratory study. *European Journal of Environmental and Civil Engineering*, 1-27.

Zhou, J., Li, Y., Xu, J., and Kamon, M. (2014). Testing of NAPL simulator to predict migration of a light nonaqueous phase liquid (LNAPL) under water table fluctuation in a sandy medium. *Journal of Central South University, 21*(1), 317-325.

2 Design and development of the 2-D automated multiphase flow experimental system

The overarching aim is to realise and interpret a series of 2-D LNAPL migration and redistribution experiments that allows the influence of water table fluctuations and other factors assessed. The main approach is to build a 2-D experimental system that is capable of generating programmable water table fluctuations and accurately quantifies controllable three-phase flow dynamics in real time.

A scheme of experiment scenarios was initially conceived, which were expected to inform on the mechanism of LNAPL transport and distribution under the influence of transient water table fluctuation conditions along with other key influential factors, such as the occurrence of geological heterogeneities. Based on assessing the proposed experimental scheme, attainable resources, feasible techniques and financial budget, a 2-D intermediate-scale sand tank system with automated control capacities was considered the most scientifically and financially realistic approach for this study.

The design and development of the 2-D multiphase flow experimental system were conducted during the course of this research, which was the outcome of two years' efforts. The redevelopment of the multi-spectral image analysis methodology was carried out intermittently in parallel, which took nearly one year. Specifically, the design of the multiphase flow simulation module (the sand tank) could not be improved without series of trial tests piloted in a prototype glass tank (100 x 100 x 2cm) which was inherited from a previous study (Chompusri, 2004) constructed by Dr. Richard Greswell, who also creatively executed the development of the 2-D tank in this study. The development of the automatic water table fluctuation control module and multi-spectral photography module was conducted by the thesis author with essential suggestions from supervisor Dr. Alan Herbert and inspirations from C Kechavarzi *et al.* (2000), respectively. All the scripts written including the automated control system of the three modules and the subsequent image analysis were original, examples of which have been attached in Appendices A.1.

2.1 Rationale

Core functions to be achieved that influence the subsequent system design structure are: 1) to create an easily observable and controllable artificial aquifer environment; 2) to generate repeatable and

flexible cyclic water table fluctuation conditions; 3) to observe in real time the dynamic migrations and redistributions of the three phases (LNAPL, water and air) and to interpret transient redistribution large datasets during LNAPL spills and subsequent water table oscillations.

NAPL behaviour (migration and distribution) is determined by the characteristics of its release, the physical-chemical properties, the geological setting and ambient hydro-environment amongst other factors. The experiment platform is vital as in seeks to accommodate the elements mentioned above. The primary objective is to design an intermediate-scale experimental platform that allows qualitative, quantitative and numerical model-based interpretation, the dynamic monitoring of saturations of multiphase fluids, particularly under representative cyclic water table oscillations. Compared to conducting a field-scale study, an intermediate-scale experimental setup permits significant control over the processes and conditions it simulates, thus can facilitate the comparisons that target specific parameters or processes while keeping others unchanged. Additionally, it also provides flexibility in accommodating monitoring methods whilst raising minimal environmental, health and safety concerns.

The dimension of the experimental system was selected to be two-dimensional. One-dimensional column systems are restrained by flow boundary limitations, where features and processes such as NAPL source zone geometry and lateral spreading cannot be simulated or observed. Two-dimensional apparatuses allow accurate reproductions of the capillary, viscous and buoyant forces found in the field, as well as facilitate two-dimensional flow and geology structure (Chevalier and Petersen, 1999). Three-dimensional setups, although can produce conditions and processes that are closest to observations from field studies, are difficult to be made compatible with current monitoring techniques, i.e. the proposed imaging methodology would be infeasible.

The experimental system has to possess automated control capacities. The monitoring of the complex and continuous dynamics will undoubtedly be limited and fail to discern the actual system dynamics. The water table fluctuation conditions generated manually will be oversimplified and unrealistic.

Hence, it was decided that a 2-D an intermediate-scale sand tank setup should be developed to monitor the release of LNAPLs and subsequent redistributions under transient but controllable water table fluctuation conditions. The setup was designed with significant automated control, including capabilities to:

1) Automatically mimic and flexibly program water table fluctuations (including cyclic patterns, amplitude, location, speed, etc.);

2) Dynamically and continuously monitor the saturation distributions of multiphase flow (water, NAPL and air) using non-intrusive and non-destructive monitoring techniques;

3) Automate much of the interpretation of the data produced by the system.

After investigating experimental scenarios, potential materials and current resources, core functions, and last yet most importantly, monitoring methods, the structure of the 2-D automated multiphase flow experimental system was conceived.

Figure 2-1 illustrates the design of the 2-D automated multiphase flow experimental system comprising three main modules, which is used to investigate the migration and saturation redistribution of three fluid systems (water-NAPL–air) under water table fluctuation conditions. The three main modules are: 1) the multiphase flow simulation module (i.e. the sand tank) accommodates the moisturized artificial aquifer and contains released NAPL; 2) the automatic water table fluctuation control module generates programmable water table fluctuations; and 3) the multispectral photography module that dynamically monitors fluids migration and redistribution from which fluid saturations may be subsequently estimated from the experimental data selected.

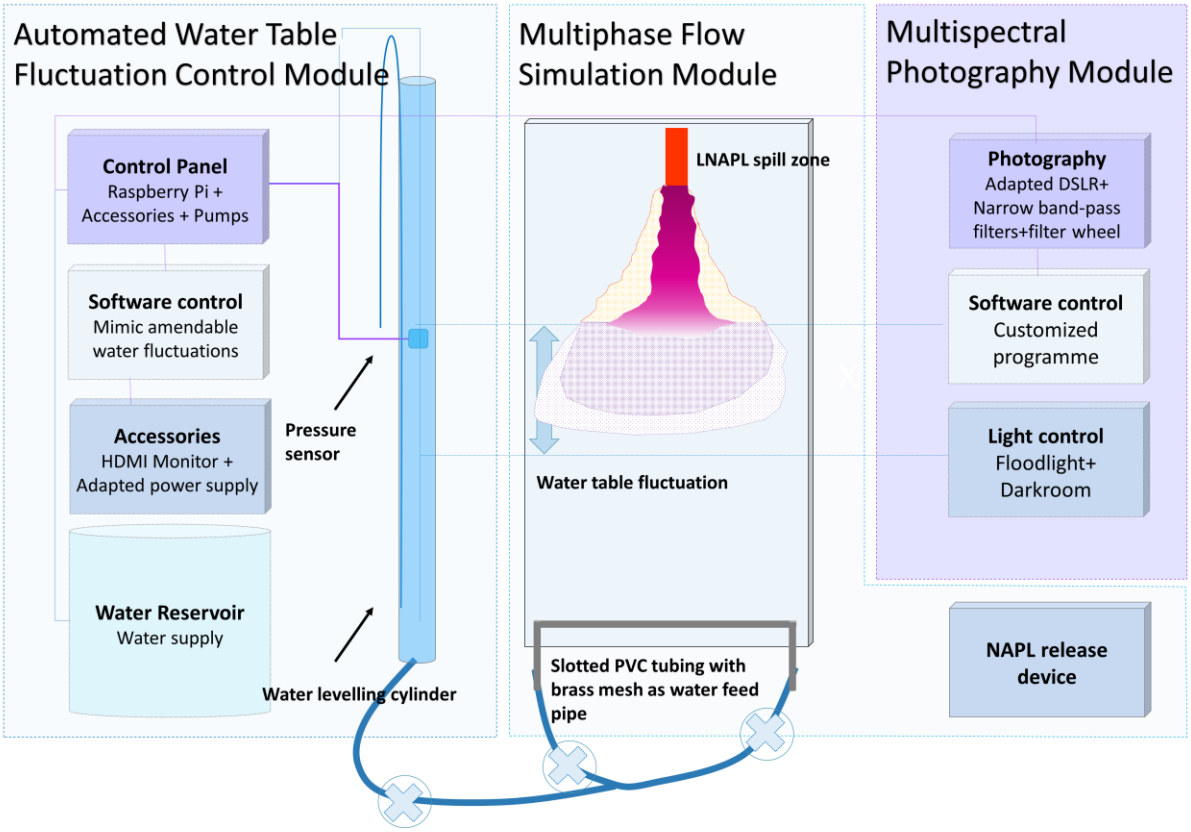

Figure 2-1 Schematic of the 2-D automated multiphase flow experimental system which consists three main modules and accessories

2.2 The multiphase flow simulation module

The aim of this section is to represent a multiphase flow system with suitable LNAPL, water and aquifer media at laboratory scale for the proposed experimental interests. The approach is to build a transparent reusable 2-D sand tank with the potentials of accommodating spilt LNAPL and controlling water table levels.

2.2.1 The sand tank

2.2.1.1 The sand tank structure

Essential features of the sand tank design should be: 1) transparency to visualize multiphase fluids and porous media; 2) modular to enable flexibility, such as to assist water table control and leakage control; 3) robust design with an appropriate size to accommodate LNAPL spillage and to be suitable for the range of proposed water table fluctuation.

The multiphase flow simulation module (i.e. the sand tank) was solely constructed with 20mm thick transparent Perspex pane. The transparency is to provide good visual observation of the fluid dynamics. The sole material being Perspex guaranteed that only one surface material is in contact with the fluids, which will eliminate unquantifiable surface effects caused by using multiple materials. The large thickness of the Perspex is expected to diminish tank bulging when fully loaded. The sand tank ($91 \times 40 \times 5.6$ cm^3 O.D. and $81 \times 30 \times 1.6$ cm^3 I.D.), fixed by a customised wooden stand, is joined by stainless steel bolts and nuts with a cut-fit rubber gasket to even tension and prevent fluid leakage in-between the panes. At the bottom of the tank, a horizontal perforated PVC tubing wrapped with metal mesh is installed over the tank width at the tank base as the water inlet and outlet, which is connected to a water levelling cylinder via two pieces of PVC tubing (Figure 2-2).

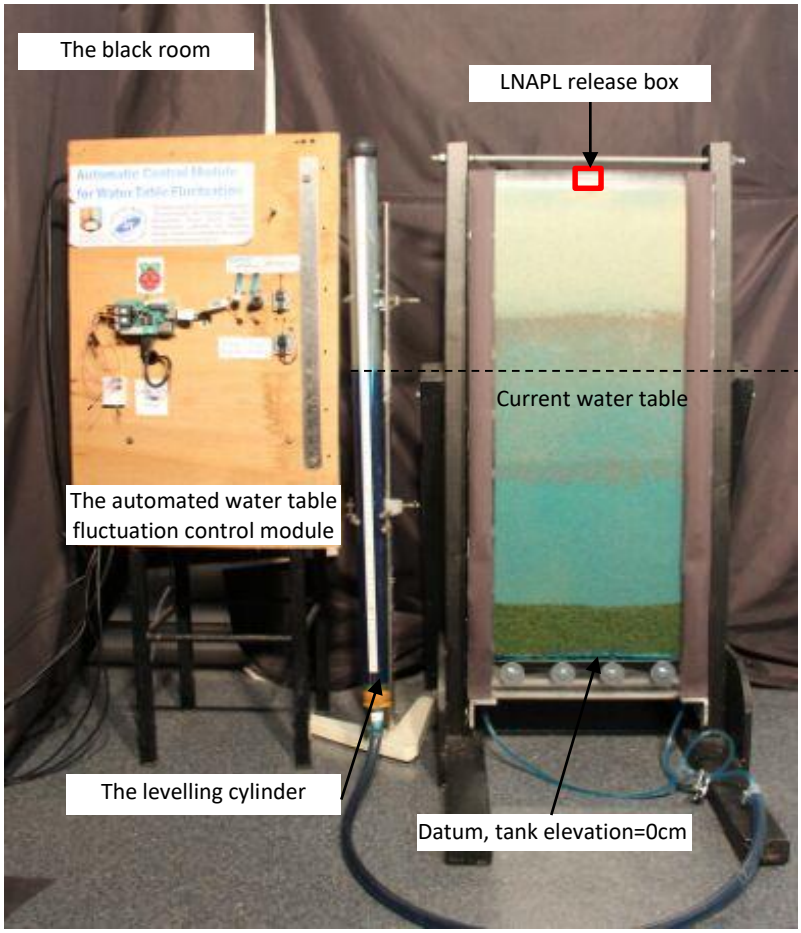

Figure 2-2 A photo of the Multiphase flow simulation module (right) with the LNAPL release source and datum marked, and the Automated water table fluctuation control module (left, Section2.3). In-between is the water levelling cylinder that connects both modules. Current water table level can be read from the water levelling cylinder. The photo was taken after an experiment, thus, LNAPL, water and sand are visible

The two pieces of PVC tubing are connected to a plastic Y-shaped tube connecter, which is connected to the base of the levelling cylinder via a PVC tubing and a tubing adapter. The levelling cylinder is made of a translucent thin wall plastic pipe (92cm tall and 4.1cm I.D.), used as a communicating vessel to control the water table in the main tank. Water table control is through both pumping and draining pumps controlled using data from a pressure sensor (details in Section 2.3.2). All tubing mentioned above have isolating valves for the purposes of maintenance, calibration and boundary condition control.

Various considerations was taken into account during the design of the tank, including the experimental aims, the compatibility with proposed methodology, health and safety issues, operational feasibility, functionality and financial feasibility, etc. The tank is reasonably thin, which is purposely designed to minimise 3-D effects. This is because the proposed image analysis methodology estimates the LNAPL saturation and LNAPL mass via the image obtained from the front pane of the tank. The shape of the tank is designed to be a rectangle rather than a square. One of the reasons is that a sizeable tank width may likely introduce a water head gradient across the width, which was not one of the proposed experimental scenarios. The other reason is that the wide tank width may introduce bulging in the centre of the panes. In that case, the width of the tank is no longer a constant, thus, will lead to calculation error in the mass balance calculation that relies on a constant tank width. Therefore, it was unnecessary and impractical to build a square shaped tank. The height of the tank is determined in the light of the intended water table dynamics, the functionality of the control module and the financial feasibility. The reasons explained above were valuable lessons from the first unsuccessful tank, which was a 100 x 100 x 2 cm^3 tank made of glass and aluminium frames, where bulging, water gradient, severe edge effects occurred.

Key features of this sand tank are as follows.

- The tank is detachable and reasonably light, the disassembling of which requires no more than two people. The cleaning, reloading and experimental operation require only one person.
- The tank size is an optimised design in consideration of the experimental scheme, functionality, safety precautions, etc. The small thickness decreases the calculation errors potentially caused by 3-D effects; the small width guarantees an even water table control over the width.
- The inner surface of the tank was made of Perspex only, where if multiple materials were used, different surface tensions between fluids and surfaces would introduce unquantifiable surface effects that change the distribution of fluids.
- The clear water levelling cylinder provides a visual reference to the water table. This is

essential for pressure sensor calibration and real-time observation of the water table in the tank.

The potential problems of this sand tank are as follows.

- Fragile surface. Compared to a glass surface, Perspex is softer which requires more care during cleaning. However, a glass tank is not easily detachable, and hence, very difficult to clean. The solution of this problem is to clean the surface very carefully with soft material to avoid scratches. The tank was made with, unfortunately, one scratch on the middle left side of the tank, and it may potentially influence the data.
- Unavoidable small inclination. Although fairly small, the inclination of the tank between front and back may remain. As a solution, for every experiment, a spirit level is used to help to adjust the tiny inclination before sand loading.

2.2.1.2 Rig clean-up and reassembly

Before each experimental run, the tank requires careful clean-up and reassembling via the following steps.

1) **Tank drainage.** After an experiment, the entire tank, filled with a mixture of LNAPL, water and sand was slowly drained of water/ LNAPL by the draining pump initially, which was controlled by the automated water table fluctuation control module (Section 2.3). In this way, the dyed water (see Section 2.2.2.1) could be safely collected in the water reservoir and securely disposed of. As the water table declined, much LNAPL was retained as residual LNAPL by capillary forces. Before the water table reached the base layer (a layer of coarse sand at the bottom) of the tank, the pumps were turned off, and the water levelling cylinder was isolated. Then, the fluid mixture was allowed to drain naturally into a bucket from the drain taps at the base of the tank. It is important to prevent air and LNAPL going into the pumps, which would cause pump contamination and damage. When the tank had only residual LNAPL and water remaining, the tank was sealed at top and bottom and removed from the wooden stand, laid horizontally onto a desk support and gradually unscrewed.

2) **Tank clean-up.** Requires removal of the front Perspex pane and very gently “shovelling” and wiping off the mixture of sand with residual LNAPL and water to a solid chemical waste container. The use of detergent should be limited since residual surfactant may very likely change the surface tension. Detergents with alcohol content should be avoided as it leaves cloudy marks on the surface of Perspex. The tank and gasket were flushed with water

rigorously and wiped gently. The perforated water feed tube was cleaned thoroughly as it could retain contaminated sand. It was necessary to avoid fine sand particles stuck within the threads of the bolts, or attached to the wet washers, nuts and the gasket surface, which could compromise the tank functionality. Therefore, these fixtures were flushed with water and wiped with a piece of dry cloth, and carefully examined before reassembling. Moreover, both the front and back panes sometimes had cloudy marks on the surface that required wiping completely to avoid errors during the image analysis.

3) **Reassembling.** The perforated tube was reinserted first and then the dry gasket fitted in between the two Perspex panes followed by gradually screwing the nuts. The nuts should be screwed in a manner that ensured even force application. The thickness of the tank needed to be checked for consistency. The tank was then mounted securely onto the wooden frame. A spirit level was placed on the top of the tank to check and avoid undue inclination that might perturb the LNAPL distribution. After adjusting the tank inclination, the tubing was attached to the levelling cylinder and leakage or blockage on both sides was checked. Although the levelling cylinder and the wooden frame are kept in place, there was still slight potential movement, and thus, a pressure sensor calibration was conducted for every experiment.

2.2.2 Fluids and porous media

2.2.2.1 LNAPL

The LNAPL used in this study is LargoGP2 mineral oil (© Morris Lubricants)(Morris-Lubricants, 2012) The colourless LargoGP2 (the relevant properties listed in Table 2.1) is a highly refined, low-odour and low-viscosity lubricating oil which is a mixture of C14~C20 hydrocarbon chains. LargoGP2 was chosen because it not only resembles the petroleum products in physical properties (viscosity, interfacial and surface tensions), i.e. common LNAPL contaminants existing in the subsurface environment, but also has negligible solubility in water, very low volatility (vapour pressure), toxicity, flash point, which makes it safe and suitable for long-term experiments that only look at LNAPL migration and distribution without dissolution, volatilization and adsorption.

Table 2-1 Physical and chemical properties of Largo GP2 (Morris-Lubricants, 2012)

Density	0.815 g/ml @15°C
Appearance	Clear colourless liquid with a mild odour
Water Solubility	<1mg/L @20°C
Flammability	Flash point at 108°C
Vapour pressure	<0.02kPa @20°C
Interfacial tension with water*	29.5 mN/m @20°C
Interfacial tension with air*	41.7 mN/m @20°C

* Inaccessible from the Largo GP2 MSDS. Data obtained from other MSDS sheet with the same CAS number 64742-46-7(Aztec-Oils-Limited, 2014)

To enhance visual observation during the experiment period and increase the light absorbance for the monitoring technique in this study, the LNAPL needs to be dyed. The dye must remain within the LNAPL phase and not partition to the aqueous phase or to the geologic solid phase. Three types of dye have widely been used in previous studies: Sudan III suggested 0.01% by weight (Van Geel and Sykes, 1994; Schroth *et al.*, 1998), Sudan IV suggested 0.06% by weight (Cohen *et al.*, 1992), and Oil Red O tested 0.01% by weight (C Kechavarzi *et al.*, 2005). Oil Red O was chosen because it mixed well with the LNAPL used and it provided distinctive contrast incorporating with the blue dyed water. After adding Oil Red O to the LNAPL, no noticeable change in the physical properties was observed. And after a one-month test of mixing dyed LNAPL and dyed water, no partitioning was found between dyed LNAPL and dyed water. Moreover, by mixing dyed LNAPL with sand for more than one month, no absorption was found.

2.2.2.2 Water phase

To ensure contrasting reflection coefficients between the spectral bands for the aqueous and LNAPL phases under the interference of yellow/white sands (Section 2.4.1), water also needs to be dyed. Two low-toxic hydrophilic dyes, both immiscible with LNAPL, have been used in previous research: Fluorescein (yellow) (Ghanem *et al.*, 2003) and Brilliant Blue FCF (blue) (Flores *et al.*, 2007; Wang *et al.*, 2008). The Acros organics Brilliant Blue FCF (Thermo-Fisher-Scientific, 2012) with 0.01% by weight was chosen over Fluorescein because the combination of blue-dyed water and red-dyed LNAPL could produce a more obvious visual contrast than yellow-dyed water and red-dyed LNAPL. Furthermore, sodium chloride (0.05M) was added as a bacterial growth inhibitor, instead of the previously frequent use of Mercuric chloride ($HgCl_2$) (0.005 mol/L) and Sodium azide (NaN_3), which are of severe toxicities. The effectiveness of the bacterial inhibitor was visually assessed by comparing two samples in clear glass vials: one sample with fresh water, LNAPL and small amount of sand and the other with same

amount of but saline water, LNAPL and sand. Slow, continuous growth of bacteria was noticed at the LNAPL-water interface from Day 4 in the fresh water sample, while after four weeks the LNAPL-water interface of the saline water sample remained visually clear. Therefore, considering the proposed longest experimental duration of a less-than-two-week period, the 0.05M sodium chloride was reckoned effective as the bacterial inhibitor in this study.

The dyed saline water is not reused in this study since the dye may be slowly absorbed by sand after a long period of time. Over a test period of 14 days, the difference in dye concentration before and after the test was tested to be negligible. However, for a much longer period, the water dye might become diluted. Hence, the dyed saline water was freshly prepared prior to each experiment out of caution.

In addition, the physical and chemical resistance against dyed LNAPL (hereafter simply referred as the LNAPL or NAPL) and dyed saline water (hereafter simply referred as water, unless specified) of all materials in contact with were tested, including Perspex, PVC tubing, vinyl tubing, silicone tubing, tubing connectors, metal mesh, plastic pipes, gaskets, rubber bung, etc.. None of them was found to be visually compromised by contact with the LNAPL or water.

2.2.2.3 Porous media

In previous NAPL laboratory scale studies, different grades of sand and glass beads have been the most frequently used porous media. Sand was chosen in this study as the study required an idealised simple, well-characterised analogue aquifer so that the main processes can be observed without over-complexities of heterogeneity. Moreover, compared to glass beads, sands are more representative of aquifer materials, easier to dispose of and cheaper at cost.

Three different types of sand were chosen particularly aiming at relatively light colours (except for the coarse sand which was only used as aquifer base), cleanness, well-sorting, and availability. Fine-grained, medium-grained and coarse-grained silica sands were purchased from Garside Sands (Aggregate-Industries, 2012). A series of characterisation tests for the porous media were conducted in this study, including Sieve analysis (Murthy, 2002), porosity measurement and hydraulic conductivity measurement (Hudak, 2004), the results of which are organised in Table 2-2 and Figure 2-3 for porous media properties. The hydraulic conductivity was measured via a customised constant head permeameter and porosity was measured by porosity. Sieve opening sizes used in the sieve analysis are listed in Table 2-3.

Table 2-2 Physical properties of the porous media*

Properties	Fine sand	Medium sand	Coarse sand
Size range (mm)	0.25-0.71	0.50-1.00	1.00-2.00
Colour	White	White	Yellow, brown
Specific gravity (g/mL)	2.650	2.650	2.650
Bulk density (g/mL)	1.674	1.654	1.551
D_{10} (mm) (Effective size)	0.357	0.612	1.104
D_{30} (mm)	0.456	0.666	1.282
D_{60} (mm)	0.785	0.785	1.495
Measured hydraulic conductivity (cm/s)	0.070	0.085	0.094
Cu (coefficient of uniformity)	1.520	1.284	1.353
Cc (Coefficient of curvature)	1.074	0.924	0.996
Porosity	36.8%	37.6%	41.5%

*Note that the size range and colour were obtained from Garside Sands (Aggregate-Industries, 2012), whereas the rest properties were obtained from analysis conducted during this study

To expend on the hydraulic conductivity and porosity measurements of the three types of sand. The hydraulic conductivities were measured via a customised permeameter that applies Darcy's Law (**Error! eference source not found.**). The flow chamber packed with sand is made of a glass cylinder with a 7cm diameter and a 10cm length, where both sides are shielded with filters to prevent the sand column from flowing or collapse. The flow chamber is connected to a constant head water reservoir on one end, and drains to a measuring cylinder that measures the discharge on the other end. The test for each sand was conducted three times and the hydraulic conductivities listed below are the average values for each type of sand. The repeatability for the coarse sand was excellent, but the hydraulic conductivities for the fine sand and medium sand tended to become larger as time lapsed. This was due to the fine particle being flushed through the filters. Therefore, the hydraulic conductivity measurement was conducted with new sand packing every time, which provided more repeatable results for the fine and medium sands. The porosity was measured by adapting the customised permeameter into a vertical flow chamber. The water reservoir provided the water from the bottom the flow chamber which was packed with dry sand to be measured. The total volume of the water residing in the flow chamber equals to the volume of void space within the sand column, which gives the value of porosity. The porosity measurement of the three sand was also conducted three times with the average values as the used porosities in this study.

Table 2-3 Sieve opening sizes used in the sieve analysis for the three types of sand (Unit: mm)

Sand type	Sieve sizes used in sieve analysis (Unit: mm)											
Coarse	2.00	1.70	1.40	1.18	1.00	0.71	0.60	-	-	-	-	-
Medium	1.18	1.00	0.71	0.60	0.50	0.43	0.36	0.30	-	-	-	-
Fine	0.71	0.60	0.50	0.43	0.36	0.30	0.25	0.21	0.18	0.15	0.11	0.08

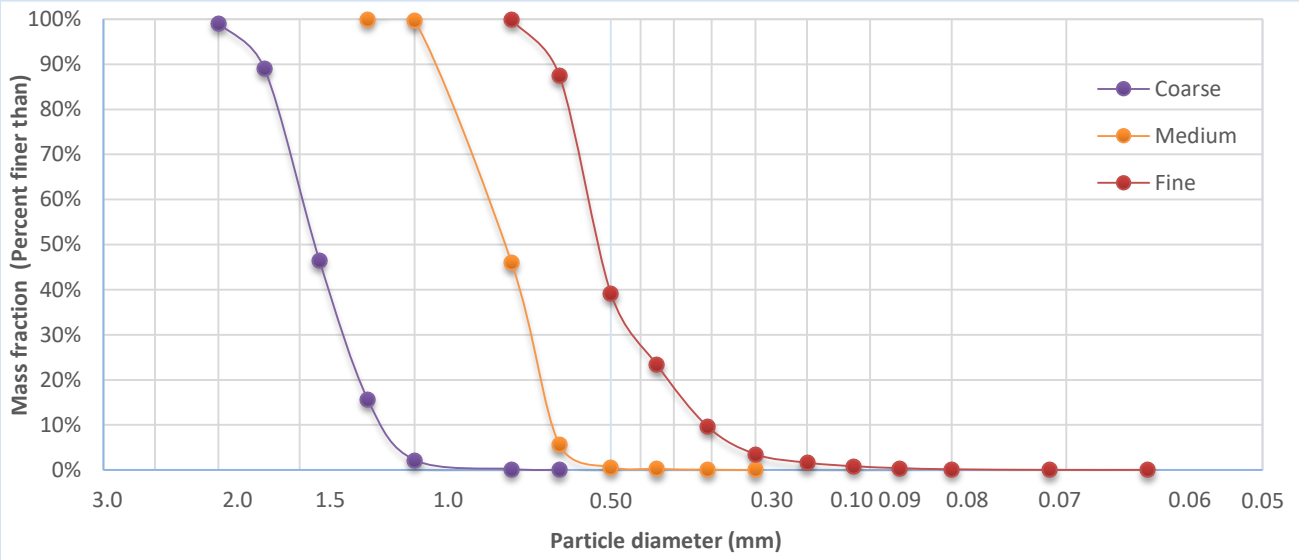

Figure 2-3 Particle diameter distributions of the porous media

The possibility of partition between the LNAPL dye, the water dye and the sand particles was taken into consideration and tested. Firstly, three clean glass vials were filled with mixtures of dyed water and sand, dyed LNAPL and sand, and dyed water, dyed LNAPL and sand respectively. After being kept static for two weeks, no obvious colour change or phase partition could be visually observed. Secondly, after one regular experimental run during the experimental stage, the used water and LNAPL were collected and tested in a UV-VIS spectrometer (introduced in Section 2.4.1.3). No obvious change in absorbance was found for both water and LNAPL. Therefore, considering that the proposed longest experimental duration was less than two week, the partition between dyes and phases in short term was considered negligible.

Sand packing of the 2-D tank aimed to emplace controlled artificial aquifer scenarios that varied from homogeneous to heterogeneous aquifers with homogeneity within sand bands. Tank loading was achieved by wet pluviation. Prior to the sand packing, the coarse sand was washed, dried and sieved, and then heated in an oven at 110 °C overnight. (The sand washing was achieved by putting the coarse sand in to a very fine sieve and flushing with running water, until the water becomes clear) Eventually,

the coarse sand was allowed to cool down before use. Whereas, the medium and fine sand was only oven-dried and cooled down with no need of cleaning.

To produce an entire homogenous aquifer or a homogenous layer within a layered heterogeneous system, the tank was first loaded with 10 cm deep water (dyed saline water) and a 10 cm lift of coarse sand was gradually deposited onto the bottom of the tank via a tremie pipe, which was repeatedly shifted across the tank width. Then, the major porous media was then introduced the same way, with an automatically controlled slow injection of water from the bottom of the tank, which allowed the sand to remain saturated throughout and avoided a long travelling distance within the water layer. If the water table is set much higher than the sand deposit, under the buoyancy force, the heavy grains will descend faster than the fine, light grains. This may lead to sand banding, where for each load of sand, the heavier grains deposited at the bottom of the layer and the smaller and finer grains deposited at the top of the layer. Therefore, the speed of water table ascending was controlled to be in accordance with the sand loading, which ensured the water table no more than 5cm above the sand layer while facilitating wet packing. It is noteworthy that the shifting speed of the tremie pipe across the tank width should maintain even. This is to ensure that the sand deposit is a gradual, even and continuous process without the occurrence of bowing, bulging or uneven sand layers.

For all experimental scenarios roughly 80 cm thickness of porous media was packed including the 10cm coarse sand base. Excluding preparation, a typical homogeneous tank loading procedure alone takes approximately 30 minutes.

2.2.3 LNAPL release device

In order to provide a simple, well-defined LNAPL release, a glass Mariotte's bottle should be customised which gives a constant head release.

To achieve a controllable and safe release of LNAPL into the tank, a release device was customised to introduce a constant head infiltration (Figure 2-4). The device consists of a gas-sealed glass Mariotte's bottle (Cedric Kechavarzi, 2001; Das and Mirzaei, 2012) and a flow-even release box (Figure 2-4) sitting on top of the aquifer surface. LNAPL infiltrates into the simulated aquifer evenly through this 3cm long line source under a small constant head (1~3cm for most experiment scenarios) provided by the 400ml Mariotte's bottle. The datum of the LNAPL head is the bottom of the release box, which also equals to the elevation of the aquifer top boundary. A flexible silicone tubing connects both the ball valve and the flow-even release box, which is an open top thin-wall aluminium box (3 cm × 3 cm × 1.6cm

O.D.) with a fine metal mesh bottom and filled with 3.5mm O.D. glass beads to ensure high K and minimal head variation over the release area. This box is painted black to avoid strong surface reflection by the flood light during photographic data acquisition, which may introduce errors during image analysis. The volumes of LNAPL releases are read from the volumetric marks on the Mariotte's bottle. The constant heads are measured prior to each release.

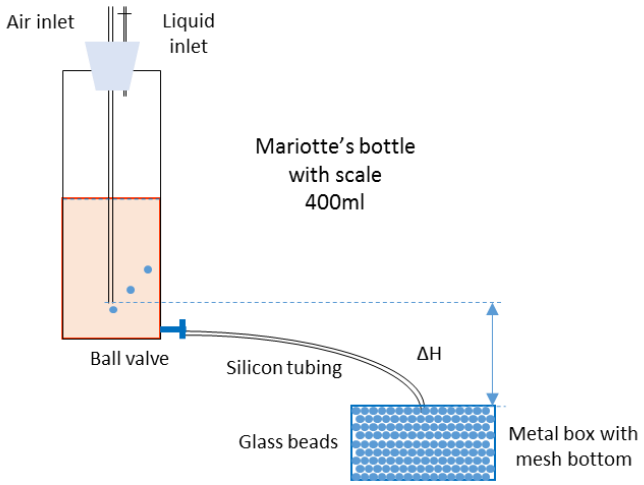

Figure 2-4 The LNAPL release device comprising the Mariotte's bottle (left) and the flow even release box (right). See Figure 2-2 for the location of the release box.

2.3 The automatic water table fluctuation control module

To date, LNAPL redistribution in a cyclic oscillating water table has not been automatically implemented at laboratory scale. The aim of the expected setup was to provide an automatic, computer controlled water table fluctuation that could be reliably cycled, altered and repeatable. For the control of water table fluctuations, and experiment monitoring, an automatic system allows more frequent and faster data acquisition, more flexibility on experimental scenarios, and is essential for this study.

The initial intent was that the water table fluctuation should at least be able to provide sine wave and linear patterns. A sine wave like fluctuation may resemble the fluctuation patterns in natural environments, for example in coastal/ estuary areas influenced by tides. The linear shape may perhaps resemble the pattern of artificial drainage or pumping and was needed during experiment preparation and maintenance. Although the time restriction of this study does not allow the experimentation of seasonal variations, they should be made achievable by the system to build.

2.3.1 Module principle

The aim of the control system is to instruct pumps to drain or pump based on the programmed features of fluctuations in response to the current water table condition measured by the sensors. A differential pressure sensor measures the difference between two pressures and outputs a voltage signal to represent that difference. A pressure sensor normally produces a linear response across the range of its operation. Therefore, by fixing the sensor and leaving one port of the sensor open to the ambient atmosphere whilst the other one submerged, the water pressure at the submerged end could be measured, and thus the water table could be obtained by converting the pressure read to water depth level. A calibration must be conducted to convert instantaneous voltage signals to actual units of water pressure, which was also proportional to water table levels.

Hence, with instantaneous detection of the water table, continuum regulation of the water table becomes possible, discernible as well as controllable water discharge and recharge to the tank system, allowing automatic and programmable water table oscillations to be achieved.

2.3.2 Hardware

There was a balance to be struck between efficacy and cost of the setup. The general aim was to assemble the module with inexpensive but reliable electronic components, which should be compatible with each other, as well as the operating system and programming languages.

This module comprised an elegant combination of inexpensive but reliable electronic components controlled by a credit-card-sized single-board computer Raspberry Pi 1 Model B (Raspberry-Pi-Foundation, 2012a) (Figure 2-5(a)) running a Linux OS -Raspbian (Raspberry-Pi-Foundation, 2012b). The components are as follows.

- The Piface digital interface (Figure 2-5(b))(Piface-Digital, 2012) which is embedded with two relays that controls two pumps.
- The ADC Pi V2.2 (Figure 2-5(c))(AB-Electronics-UK, 2012) which converts the analogue DC voltage signals output by the pressure sensor to digital signals for the Raspberry Pi to receive.
- The Phidgets differential pressure sensors (Figure 2-5(d)) are dual ported air pressure sensor that measures the pressure difference between the two ports. Two different types of sensors were used: type 1136 with ±2kPa range (PhidgetsInc., 2013a), and type 1137 with ±7kPa range (PhidgetsInc., 2013b). To adapt to an aqueous environment, the tubing connected to the sensor ports was injected with a small amount of LNAPL used in this study to prevent water or moisture

from entering the ports.

- The Potentiometer (©RS 8427, 50KΩ) and Transistor (©RS, BD 135) (Figure 2-5(f)) can provide a variable voltage range to adjust the pump flow rate manually. However since the pumping rate was a good fit for the proposed transient water table fluctuation, this component was kept idle during the experiments and reserved for potential use in the future.
- Two low flow TCS micropumps (28 x 14 x 14 mm) (TCS-Micropumps, 2015), which provided an up to 300ml/min flow rate under 3.3V, were allocated to drain or pump water from water levelling cylinder respectively. The pumps were attached with one-way valve and filters to prevent extreme fine particles being sucked into the pumps and causing pump damage.
- The tubing for the pressure sensor and pumps was selected after a series of linearity tests between voltage output and measured water depth in the cylinder. Vinyl tubing with 2mm ID was chosen for the pressure sensor and 3mm ID for the micropumps. It is because the vinyl tubing is the most gas tightened tubing attempted which provides the best linearity between pressure sensor output and water pressure.

Figure 2-5 is a schematic of the hardware composition for the control module, which reveals the circuit connections among components. The Raspberry Pi, ADC and Piface are connected and stacked up via the 26 GPIO pins where the Raspberry Pi is the base layer, and the Piface is located on the top. The HDMI monitor, keyboard and mouse re connected to Raspberry Pi directly via the HDMI and USB ports. The module is powered by an adapted ATX power supply unit which provides regulated 3.3V for the micropumps and 5V for the Raspberry Pi. One of the pressure sensors is connected to the ADC via the analogue channels, where the other one is reserved. In this study, the simultaneous control of two pressure sensors has been achieved, but not used for proposed scenarios. The micropumps are connected to the relays embedded in the Piface and the ATX power supply box. A switch is installed between the pumps and the power supply to for pump control. All the hardware mentioned above have been mounted on a control panel (Figure 2-2) and kept adjacent to the tank.

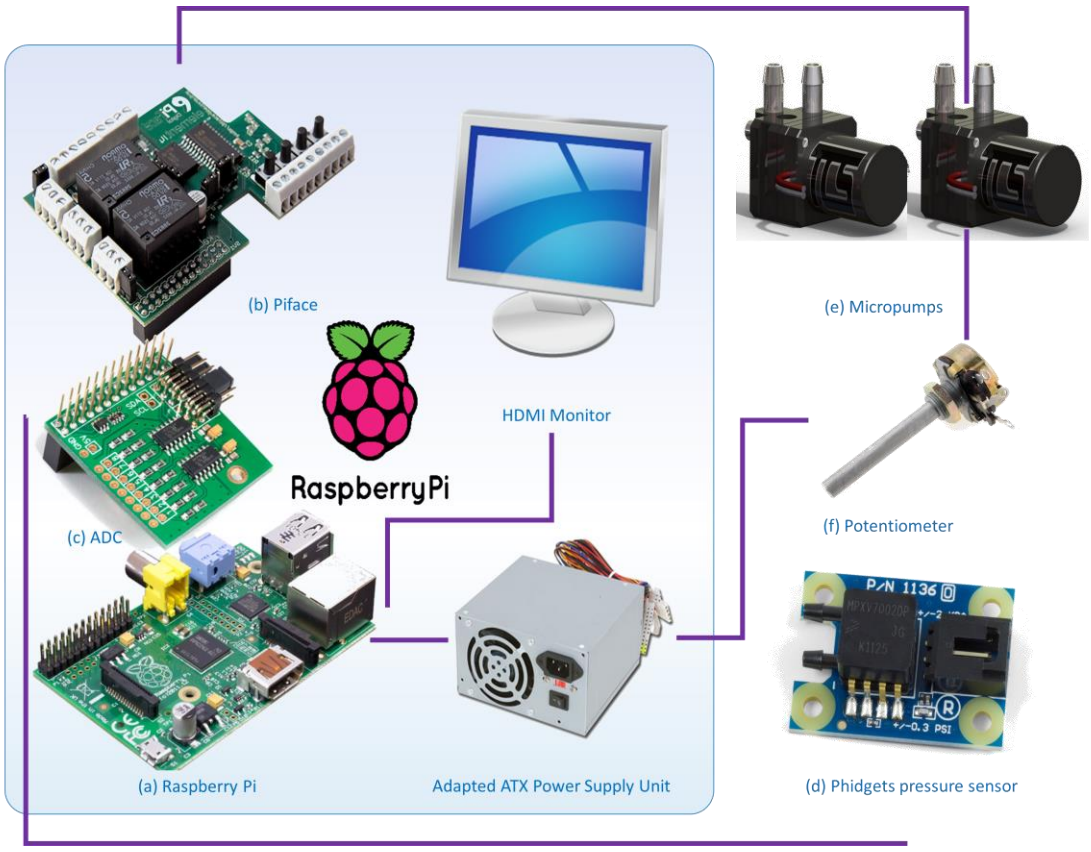

Figure 2-5 Schematic of hardware composition of the automatic water table fluctuation control module

An example of the pressure sensor calibration test is shown in Figure 2-6. For each experimental run, a pair of calibration test was performed with water table ascending and descending. Linear regression was applied to give the linear function and R^2 value for each test. The errors were calculated by evaluating the differences between the water elevations predicted by the linear functions and the directly read water elevations from the rig. The differences between the paired calibration result for most calibration tests were fairly small. The one with a slightly higher R^2 was chosen to be applied in the control script to convert pressure sensor output to water table levels.

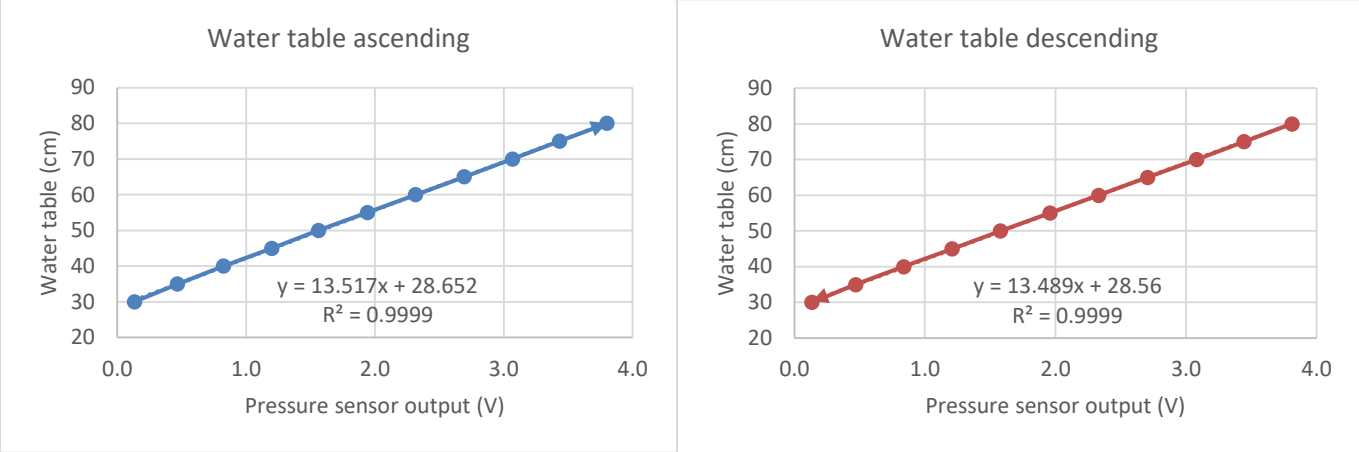

Figure 2-6 An example of pressure sensor calibration for an experimental run, where tests for both water table ascending and descending were performed. The expression with the better R^2 (correlation coefficient of the read water elevation and predicted values by the expression) was chosen in an experiment run

2.3.3 Software

The aim of this module is 1) to develop hardware interfaces to communicate with and control all the components within this module, and 2) to generate programmable water table fluctuations in the 2-D tank. A suite of scripts was developed with Python 3 (Python-Software-Foundation, 2016) to realise the following functions that are essential for the experiments:

1) Control and receive outputs from the pressure sensor(s) and convert analogue signals received by the ADC to water table via a calibration test;
2) Control the two micropumps via relays for water table cyclic variation and also for maintenance and calibration tests;
3) Generate adjustable water table fluctuations (with the controllable parameters discussed below).

The water table fluctuation control script is the core programme of the entire module, which is capable of generating a sine/cosine shape water table oscillations. The script is attached in the Appendix A.1.1. The definitions of controllable parameters are as follows.

a) The shape of oscillation; by changing the mathematical equation, the desired shape of oscillation can be altered. In this study, a negative sine wave is applied for the major experiments and a linear shape is applied during the (de)saturation and calibration processes. When the linear mode

was activated, all parameters explained below were disabled, and by specifying the initial and final water table and the duration, the script would generate the function automatically.

b) Oscillation centre (cm); the position of the centre of sine/cosine wave for water table fluctuation in tank elevation should allow adequate thickness for both capillary zone and unsaturated zone so that the NAPL may have enough travel distance to infiltrate; while still retaining sufficient thickness for the saturated zone. It was decided that 50cm elevation (tank elevation=80cm) was suitable as the oscillation centre for all scenarios.

c) Oscillation amplitude (cm); the distance between the uppermost and the lowermost position of the water table oscillation. The chosen amplitude was based on the dimension of the tank, the capillary zone thickness for different sands and the operational range of the pressure sensors. For all experimental runs, the amplitude was set to be 30 cm.

d) Oscillation frequency (cycle/day); a cycle of fluctuation is a 360-degree sine/cosine curve. It was decided that for all runs, excluding the slow oscillation run, the frequency is set at two cycles per day, and one cycle/per day for the slow oscillation run. The former is expected to represent a tidal cycle.

e) Duration (day); The duration of the water table oscillation was designed in such a way that each run contained five cycles (12 hours per cycle), and 12 hours of settling down period, during which the experiment was still monitored but with the water table fixed at the beginning position. The total cycle number of five was determined based on the data from a previous 1-D water table oscillation study (Chompusri *et al.*, 2002), in which the cyclic water table influence upon LNAPL distribution was shown to become unnoticeable after five oscillations.

An example of cyclic water table fluctuations is presented in Figure 2-7, which compares the water table generated by the module and the prescribed water table for an experimental run, including 5 cycles of oscillations and the settling down period. The error was calculated by the difference between the generated water tables and prescribed water tables divided by the prescribed values, therefore is dimensionless. The overall average error was obtained by averaging all the errors during this experimental run, the interval of which was two minutes. The agreement is fairly good with an overall average error of 0.0039. Minor differences are found during the settling down period, the reason of which is considered to be the overnight atmospheric change in the lab.

The system is capable of generating water table fluctuations more than the proposed scenarios. The stability and accuracy of the generated water table fluctuations under short/long periods (from 1 h to 240 h), with various amplitudes (5cm~50cm) at different oscillation centres, have been achieved and

tested. (Result example is shown in Figure 2-7). Consequently, the water table can be controlled to an arbitrary precision to ensure adequate control whilst minimising short cycling of the pumps.

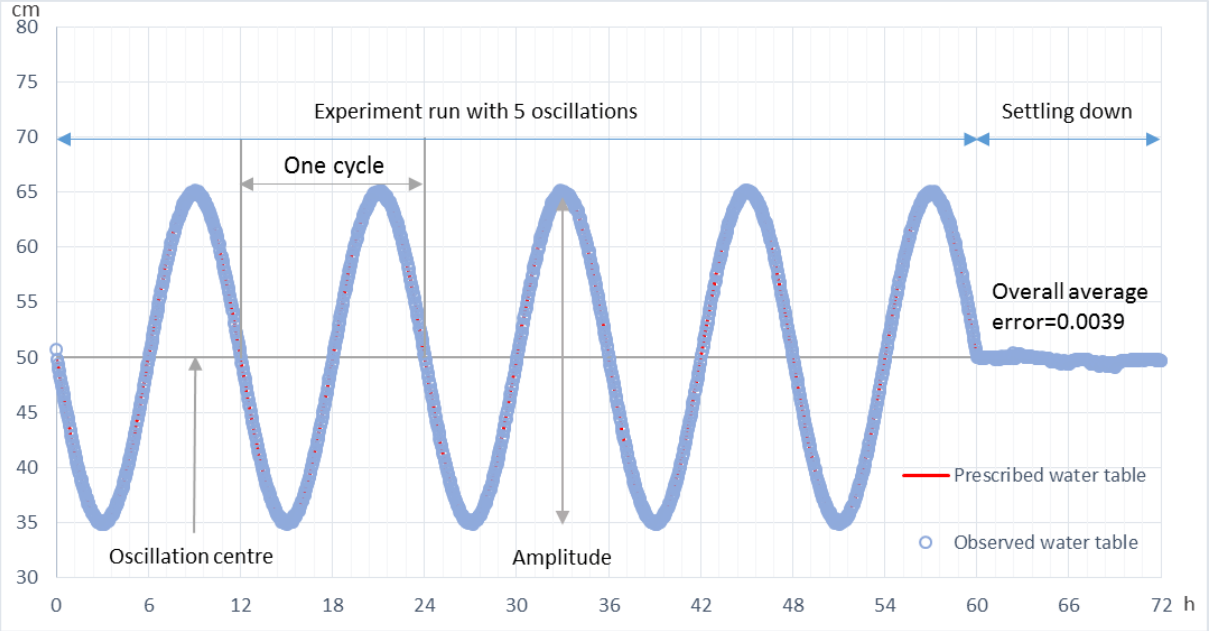

Figure 2-7 Comparison between the prescribed water table transients and the water tables generated by the control module, which illustrates the accuracy of the module with key features and stages labelled. The example is from a standard experimental run that contains 60 hr of oscillation and 12 hr of settling down period (Error unit: dimensionless)

2.4 The multi-spectral photography module

A key challenge of this module was to quantify multiphase fluid saturations in 2-D porous media that vary rapidly with time and space and efficiently process large detailed data sets produced. The solution is to achieve an automatic monitoring by the calibrated time-lapse multi-spectral imaging approach and to realise batch processing for the large data generated via image analysis.

Laboratory scale fluid dynamics in porous media, though crucial to contaminant hydrogeology research, are usually invisible and difficult to measure. In previous studies, indirect measurements including optical imaging (UV or visible light), Photon-attenuation methods (such as gamma and X-ray) and magnetic resonance imaging (MRI) were frequently applied in the measurements of the distribution of multiphase flow within artificial or natural porous media (Kamaruddin *et al.*, 2011). Among the above non-intrusive and non-destructive methods, optical imaging methods are gaining popularity in the 2-D artificial porous system due to short scanning time, low cost and extensive

monitoring domain (Werth *et al.*, 2010). Before developing the experimental system, an investigation on possible monitoring methods which could match the tank design was conducted. Preference was given to the optical imaging approach due to: its flexibility on the size of monitoring domain, controllably high resolution, accessibility of the setup, continuity in the fluid distribution of sampling points, instant imaging time, the potential of automatic control and financial feasibility. This method normally uses either light transmittance or absorbance (which is also referred as optical density) to measure fluid saturations (concentrations).

2.4.1 Module principle

The aim of this module is to achieve real-time monitoring of transient multiphase fluid saturation distributions (water, NAPL and air) of the entire flow domain under long-term cyclic water table fluctuation conditions achieved by the automatic water table fluctuation control module. The method was chosen to be the optical imaging. Therefore, the foundation was to establish a link between optical parameters that are accessible from images and fluid saturations.

2.4.1.1 The Beer-Lambert Law

In this study, the principle of the Beer-Lambert Law, which quantifies the attenuation of light intensity travelling through a specific material with an assumed linearity, was utilised to provide a possible solution from the measurable properties of spectral information to the unknown fluid concentrations. Many compounds absorb ultraviolet (UV) or visible (Vis.) light when a beam of light passes through. Within a certain range of concentration (the Law is reported not obeyed at high concentrations (Mehta, 2012), it is assumed and experimentally proved that:

1) The Absorbance A is directly proportional to the concentration c of the specific material. In a spectrometer test, it is the solution of the sample used in the experiment.
2) The Absorbance A is directly proportional to the length of the light path (l). In a spectrometer test, the light path (l) which is equal to the width of the cuvette.

Therefore (David, 2001),

$$A = \varepsilon l c \qquad \text{Equation 2-1}$$

Where:

A -- Light Absorbance.

ε -- Wavelength-dependent molar absorptivity coefficient (L M^{-1} cm^{-1});

l -- Length of the light path (cm);

c– Concentration of the measured compound in its solution (M L^{-1}).

When the surface of the material (including the container) is partially transparent, the total incident light intensity may be diverted in three different ways: the absorbed intensity, the transmitted intensity and the reflected intensity. Therefore a relationship can be assumed by:

$$A + T + R = 1 \qquad \text{Equation 2-2}$$

Where:

Absorbance A is a ratio of the absorbed intensity I_a and incident light intensity I_o at a surface at a specific wavelength. (Dimensionless);

Transmittance T is a ratio of the transmitted intensity I_t and incident light intensity I_o at a surface at a specific wavelength. (Dimensionless);

Reflectance R is a ratio of the reflected intensity I_a and incident light intensity I_o at a surface at a specific wavelength which is also called Optical Density. (Dimensionless).

In Equation 2-2, when the material (including the liquid and container) is completely transparent, the reflectance R is negligible; whereas when the material is opaque, the transmittance T is zero. Therefore, according to the Beer-Lambert Law, when the material is opaque, the reflectance R is also directly proportional to the concentration c of the specific material under a fixed length of the light path (l). Therefore, once the reflectance becomes accessible, this conclusion provides a means to quantify the LNAPL and water saturation distributions within the surface layer of the opaque sand aquifer by calibrated mathematical or numerical relationships between the reflectance R and liquid concentrations or liquid saturations.

The reflectance (aka. Optical density) of the fluid content and the sand aquifer at the tank Perspex wall can be captured photographically. By assuming the consistency of the fluid distribution along the small tank thickness, the volumes of fluids in the tank can be estimated by this method.

2.4.1.2 The Kechavarzi Multispectral Image Analysis

An innovative photographic technique that this study was initially based on and inspired by, the Multispectral Image Analysis which took advantage of the principle of Beer–Lambert law and extended

it to quantify dynamic fluid distributions of LNAPL, water and air (LNAPL and water by calibration and air by volume difference) (C Kechavarzi *et al.*, 2000; Cedric Kechavarzi, 2001). Initially, this study intended to apply this method directly. However, due to inadaptability and inaccuracy reasons discovered during a series of trail experiments, it was found that this method could be advanced significantly. Therefore, an introduction of the advanced multispectral image analysis is given below and further redevelopment will be introduced in the following sections.

This Kechavarzi method (C Kechavarzi *et al.*, 2000; Cedric Kechavarzi, 2001) was based on one study that utilized the principle of Beer-Lambert Law. Schincariol *et al.* (1993) obtained a linear relationship relating optical density (obtained via transmittance by measuring directly from scanned negatives) to the concentration of a dyed NaCl solution in a water saturated 2-D glass bead flume system. Differently, the Kechavarzi method initiated and experimentally verified the linear relationship between fluid concentrations and reflected light intensity, which was defined as via the reflectance approach, in a 2-D sand tank system.

The method required to photographically measure the reflected light intensity (defined as optical density in the series studies) of both water and LNAPL and to convert optical densities to fluid saturations using a verified linear relationship. To distinguish and further measure two fluids mixed in one system, narrow bandpass filters were introduced to ensure the spectral contrasts. To select the suitable filters, the paper firstly identified three biggest contrasts along visible light and near infra-red between LNAPL and water transmittance (same trend for the optical density). So that by applying corresponding narrow bandpass filters located within these three ranges, LNAPL and water could be distinguished to its greatest extents.

Then two calibration tests, each was conducted with a series of samples containing known saturations of LNAPL and/or water and sand mixtures in two phase (water-air or LNAPL-air) and three phase (water-LNAPL-air) situations. After experimentally verifying the correlations between optical density and the saturations of either LNAPL or water for the two-phase samples, a simple linear mathematical expression was derived, which allowed the conversion of optical density to LNAPL and water saturations for the two-phase situation. The correlation coefficient ranged from 0.95 to 0.98. However, the extreme cases of the experimented saturation range (the largely and lowly saturated samples) were not considered, resulting in an inability to resolve low saturated samples (dry sand with none or minimal LNAPL and water held within) and samples with water saturation higher than 0.69 or LNAPL saturation greater than 0.63.

Similarly, for the three-phase situations, similar calibration test was conducted in the hope of finding a similar empirical relationship. Five batches of samples were made with five fixed water saturations ranging from 0.10 to 0.58 and variable LNAPL saturations for each batch, where the maximal values of total fluid saturation (the sum of LNAPL and water saturations) of each batch were roughly 0.7. The conclusion of this test was that the relationship between optical density defined for reflected light intensity and fluid saturations was linear as well (C Kechavarzi *et al.*, 2000; Cedric Kechavarzi, 2001).

$$A_i^{wn}=\lambda_i^w S_w + \lambda_i^n S_n + \beta_i^{wn} \qquad \text{Equation 2-3}$$

Where

S_w and S_n are the water and NAPL saturations respectively;

A_i^{wn} is the average optical density for the three phase samples;

λ_i^w, λ_i^n and β_i^{wn} are the best-fit coefficients of the Multiple Linear Regression.

i stands for a specific range of wavelength.

In Equation 2-3 there were two unknown variables: S_w and S_n. Therefore, with a set of two equations which could be achieved by applying two narrow bandpass filters during the monitoring, the equations can be solved. Therefore,

$$\begin{cases} A_i^{wn}=\lambda_i^w S_w + \lambda_i^n S_n + \beta_i^{wn} \\ A_k^{wn}=\lambda_k^w S_w + \lambda_k^n S_n + \beta_k^{wn} \end{cases} \qquad \text{Equation 2-4}$$

can be rearranged as:

$$\begin{cases} S_w = \dfrac{\lambda_i^n (A_k^{wn} - \beta_k^{wn}) - \lambda_k^n (A_i^{wn} - \beta_i^{wn})}{\lambda_k^n \lambda_i^w - \lambda_i^n \lambda_k^w} \\ S_n = \dfrac{\lambda_k^w (A_i^{wn} - \beta_i^{wn}) - \lambda_i^w (A_k^{wn} - \beta_k^{wn})}{\lambda_k^n \lambda_i^w - \lambda_i^n \lambda_k^w} \end{cases} \qquad \text{Equation 2-5}$$

Note that in C Kechavarzi *et al.* (2000); Cedric Kechavarzi (2001), there were typos in the equations above. After confirming with the lead author, Equation 2-5 is the correct version with symbol changed.

2.4.1.3 The selection of narrow bandpass filters

In order to distinguish the transmittance of LNAPL and water used in this study, a minimum of two largest contrasts should be located by running a spectrometric test (technologies, 2012) within both

visible and near infrared spectrum (from 300nm to 1100nm). In Figure 2-8, the dyed saline water is shown to have a negligible impact on the spectral information compared to the dyed fresh water. Three ranges of relatively large contrasts are located: 300~500nm, 620~660nm and 960~1000nm. Specifically, within the first range, the light has been almost entirely absorbed by the dyed LNAPL, while water transmits nearly all light through. On the contrary, within the second range, dyed water absorbs most of the light, while LNAPL allows the most light to transmit through. Within the third range, the NIR spectrum, LNAPL transmits all light whereas water absorbed approximately 1/3 of the light intensity. As discussed before, these three ranges could help locate the suitable filters to achieve biggest contracts between dyed LNAPL and dyed water at a specific wavelength.

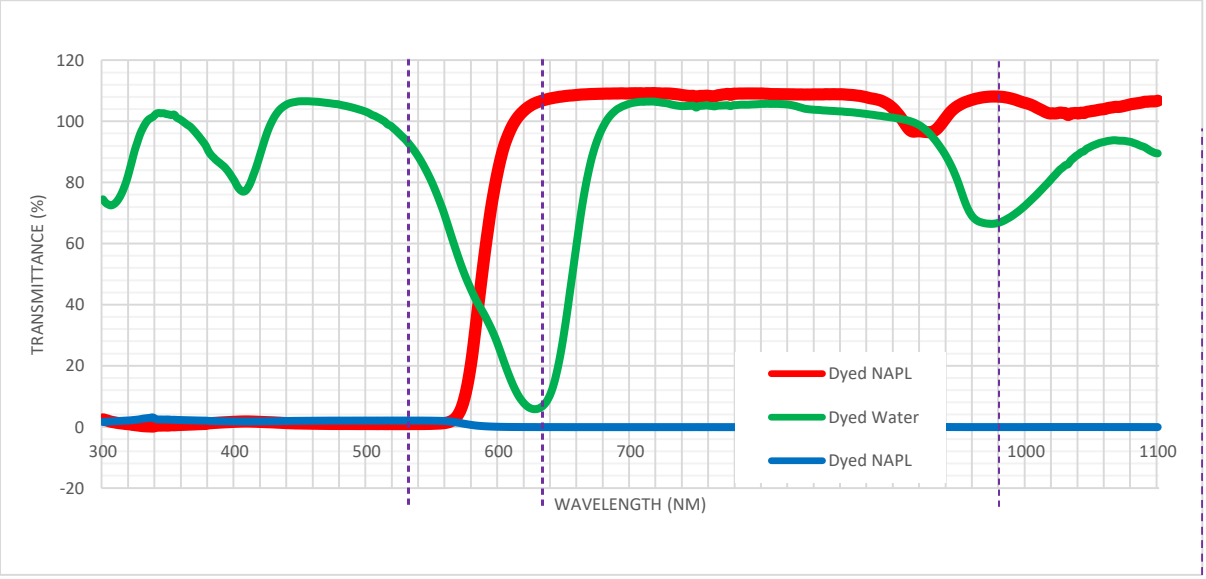

Figure 2-8 Spectrometric test result of dyed water and dyed LNAPL in the visible and NIR spectrum, where the vertical dash lines represented the wavelengths of the three chosen filters

After evaluating parameters and accessibility of narrow bandpass filters, three narrow band-pass filters, which provide the relatively large transmittance contrasts between water and LNAPL have been selected as listed in

Table 2-4.

Table 2-4 Parameters of the chosen narrow band-pass filters (CVI Laser Optics)

Product Number	Centre Wavelength (λ_c) (nm)	Full width at half maximum (FWHM) (nm)	Peak Transmittance (T_{peak}) (%)
F10-532.0-4-25.0M	532	10±2	50
F10-632.8-4-25.0M	632.8	10±2	50
F10-980.0-4-25.0M	980	10±2	45

Only two filters are required to solve the equations two unknown variables. Preference should be given to pair 532nm (a green filter), with one of the 632.8nm (red filter) and 980nm (IR filter). It is because the red and infrared filter reveal a similar pattern in the spectrometric test where LNAPL transmits all the light intensity through. This result a photo with LNAPL brighter than water. On the contrary, the green filter leads to LNAPL absorbing all the light intensity, thus, appears darker than water (Figure 2-9).

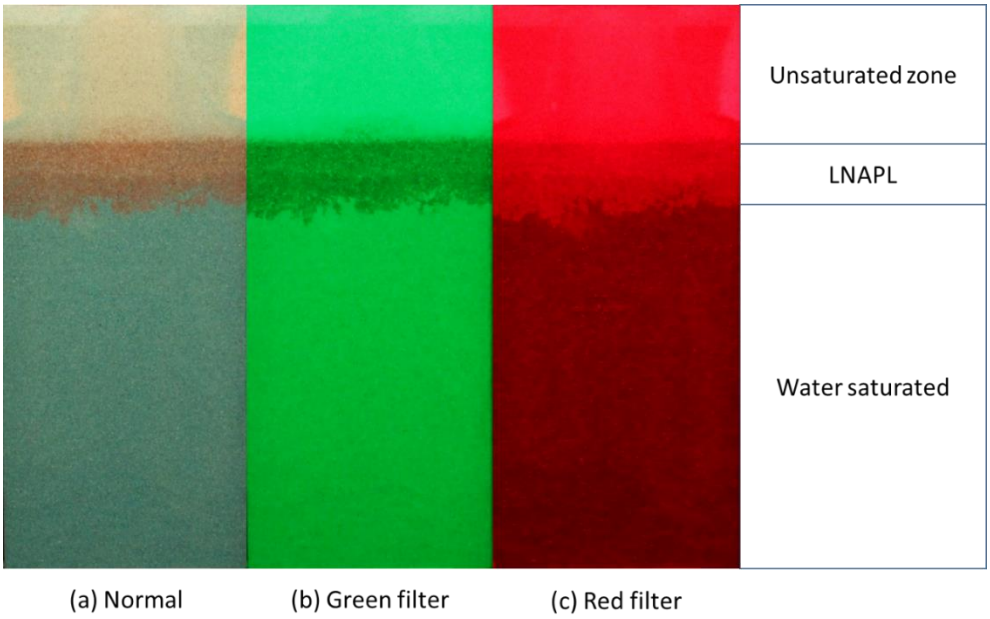

Figure 2-9 Effects of the narrow bandpass filter (images from a trial experiment, where the three photos were taken continuously under a constant light source, with no filter, with the green filter and red, respectively)

2.4.1.4 Relationship between optical density and pixel values

The challenge is to access optical density values via measurable parameters from images, i.e. making optical density readable.

Prior to adopting the reflected light intensity (optical density) approach, the colour intensity approach, which converts red, blue or green intensity values to fluid concentrations, was also considered, since colour images contain more information than grey scale images. It is theoretically feasible since the LNAPL is red dyed and water is blue dyed. For an RGB image, red, green and blue intensities can be easily calculated from the RGB pixel value, which can be directly calibrated against fluid saturations. In order to have an objective reference for all photos to minimise small differences in illumination or exposure, the colour intensities need to be calibrated against a customised colour bar that contains an array of increments in redness, which should be included in every photo. However, the result was not satisfactory mainly because no stepped colour intensity could be found on the market. With a customised colour intensity bar, he LNAPL concentrations were well calibrated and measured via red intensities. However, due to the interference of the sand colour and the light reflection on the customised colour intensity bar, the water concentration measured via either blue to green intensity had impermissible errors. Nevertheless, the reflected light intensity approach was proved feasible and accurate.

Reflected light intensity was not a directly measurable parameter from an image, although which was captured by a photograph. Therefore, some intermediate parameters which could be directly measured yet associated with optical density needed to be introduced.

In this study, RGB images were converted into 12bit grey images, so that the pixel values became the degree of greyness. Similarly, since the light condition varies slightly spatially and temporally for each photo, all photos were required to be “standardized” by an objective reference, which was a stepped grey scale bar (B.I.G. Stepped Grey Scale) (Schincariol *et al.*, 1993; C Kechavarzi *et al.*, 2000; Cedric Kechavarzi, 2001) to minimize small incidental variations in illumination and camera exposure. The grey scale bar has 20 compartments from true white to black. Each compartment represents an even increment of 0.1 in optical density. Therefore, the grey scale ranges from 0.0 to 1.9, where true white is given the value of 0.0 and the true black 1.9.

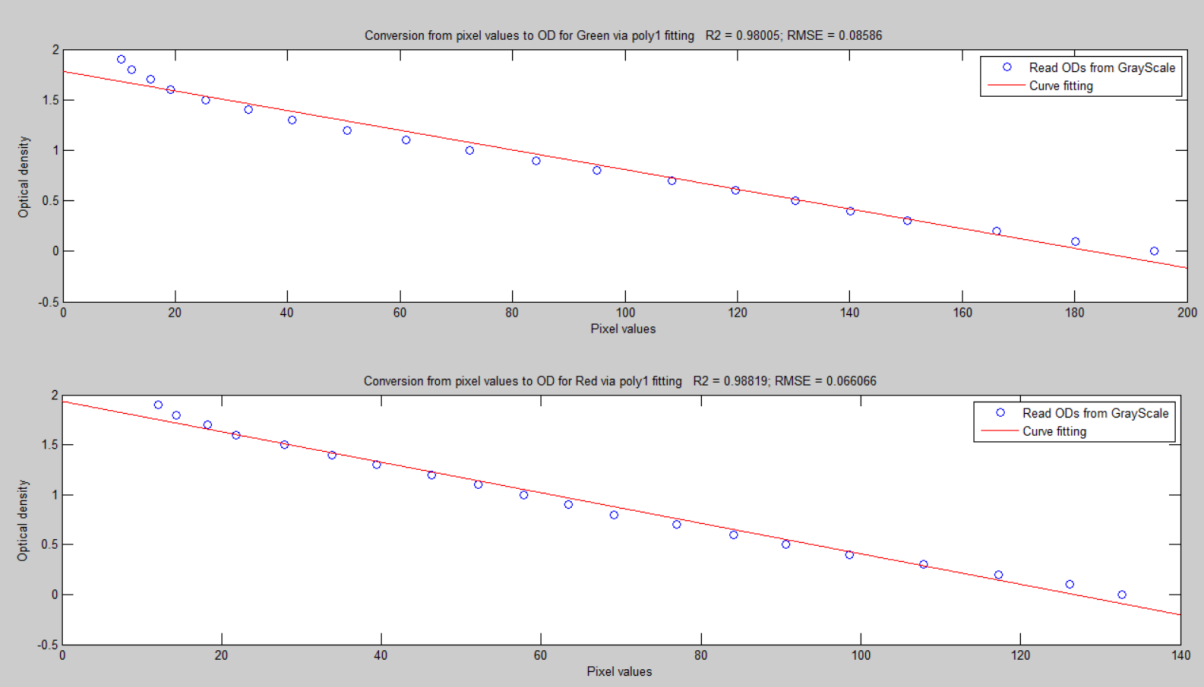

(a) Linear (Poly1)

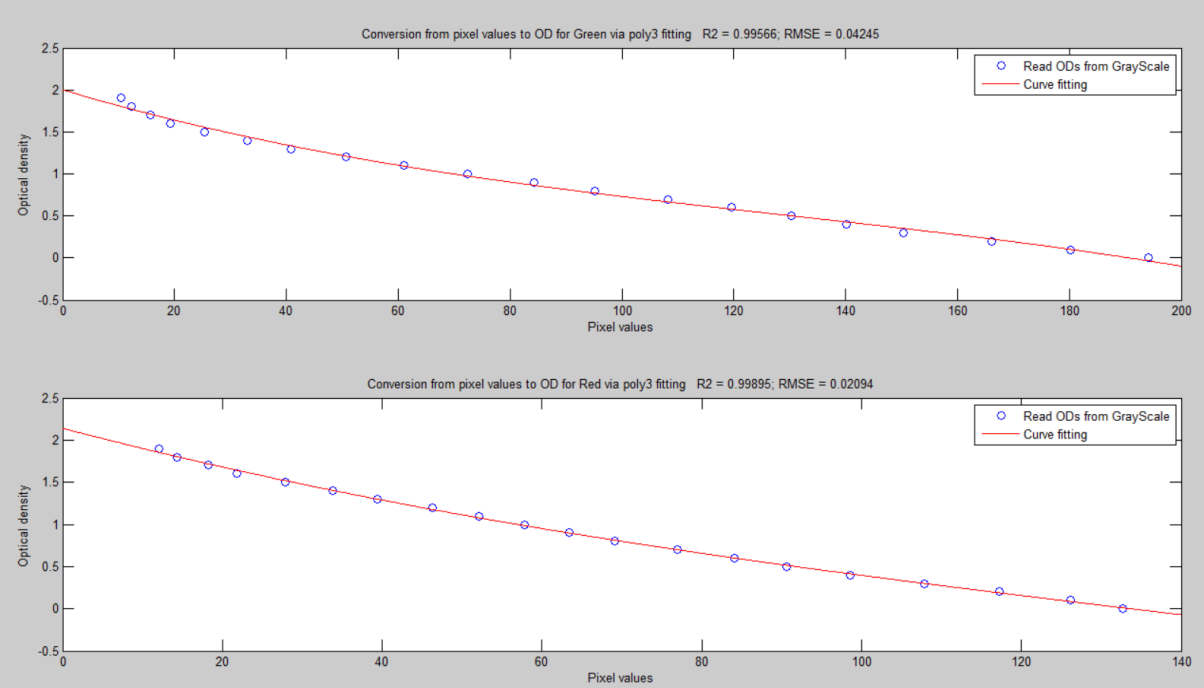

(b) Polynomial to the degree 3 (Poly3)

Figure 2-10 Examples of interpolation methods between the pixel value and optical density for the green and red filter in one calibration test. A standardised greyscale to optical density curve was calculated for each photo analysed

An interpolation method needs to be introduced to provide a full range of values within the possible boundary of optical density. From the calibration test result in Figure 2-10, it suggests that with a

linear regression, the R^2 were 98.0% and 98.8% compared to degree 3 polynomial fitting, which has improved the result to 99.6% and 99.9%. Besides, for the maximal and minimal values, the degree 3 polynomial regression allows a tighter fit. Although both methods have achieved reasonably good R^2 values, it was only found from the subsequent image analysis that the accuracy of the prediction of maximal and minimal values strongly influenced the overall accuracy of image analysis, which was evaluated by the experimental LNAPL mass balance results. Very high and very low saturations of LNAPL frequently appeared during the transient redistribution. Thus the image analysis accuracy was acutely sensitive to the interpolation result between pixel values and optical densities. Therefore, a number of curve fitting methods such high degree polynomial models, spline models, exponential models, and the Gaussian model, etc. were attempted incorporating with the surface fitting in the image analysis (Section 2.4.2.4). The degree 3 polynomial model achieved the best mass balance results in cooperation with the selected surface fitting.

Therefore, optical density has become accessible for all the photos photographed during the experiments.

2.4.2 Calibration

The aim of the calibration is that a relationship needs to be built between optical density (associated with the reflected light intensity) and fluid saturations in a three-phase flow system.

2.4.2.1 Design of the calibration test

The Kechavarzi method (C Kechavarzi *et al.*, 2000) found that for both two-phase (water-air or LNAPL-air) and three phase system (water-LNAPL-air), the relationships were linear (Multiple Linear Regression for the three phase system) based on high R^2 values and small errors, as shown in Figure 2-11 extracted from C Kechavarzi *et al.* (2000). Initially, the method was applied directly in this study. The two-phase test reported in 2.4.2.2 was the application of the Kechavarzi calibration method. And a three-phase test was also conducted, and the result of which was applied in the image analysis for a trial tank experiment. However, during the image analysis when calculated results were compared with the experimental mass balance, the errors were found unacceptable. By re-examining the calibration methodology, it was discovered that the linearity assumption was not solid. In Figure 2-11, an underestimation was observed in every plot on the relatively highly saturated values which, highly frequented in the tank experiments, would be dramatically better fitted with non-linear methods. Moreover, the lowly saturated values seemed to be overestimated by the linear fitting. Meanwhile, as analysed in Section 2.4.1.2, the distribution of the sample saturations was uneven and lacked in

highly saturated samples. These may all result in an inability to quantify low saturated and high saturation fluid distributions.

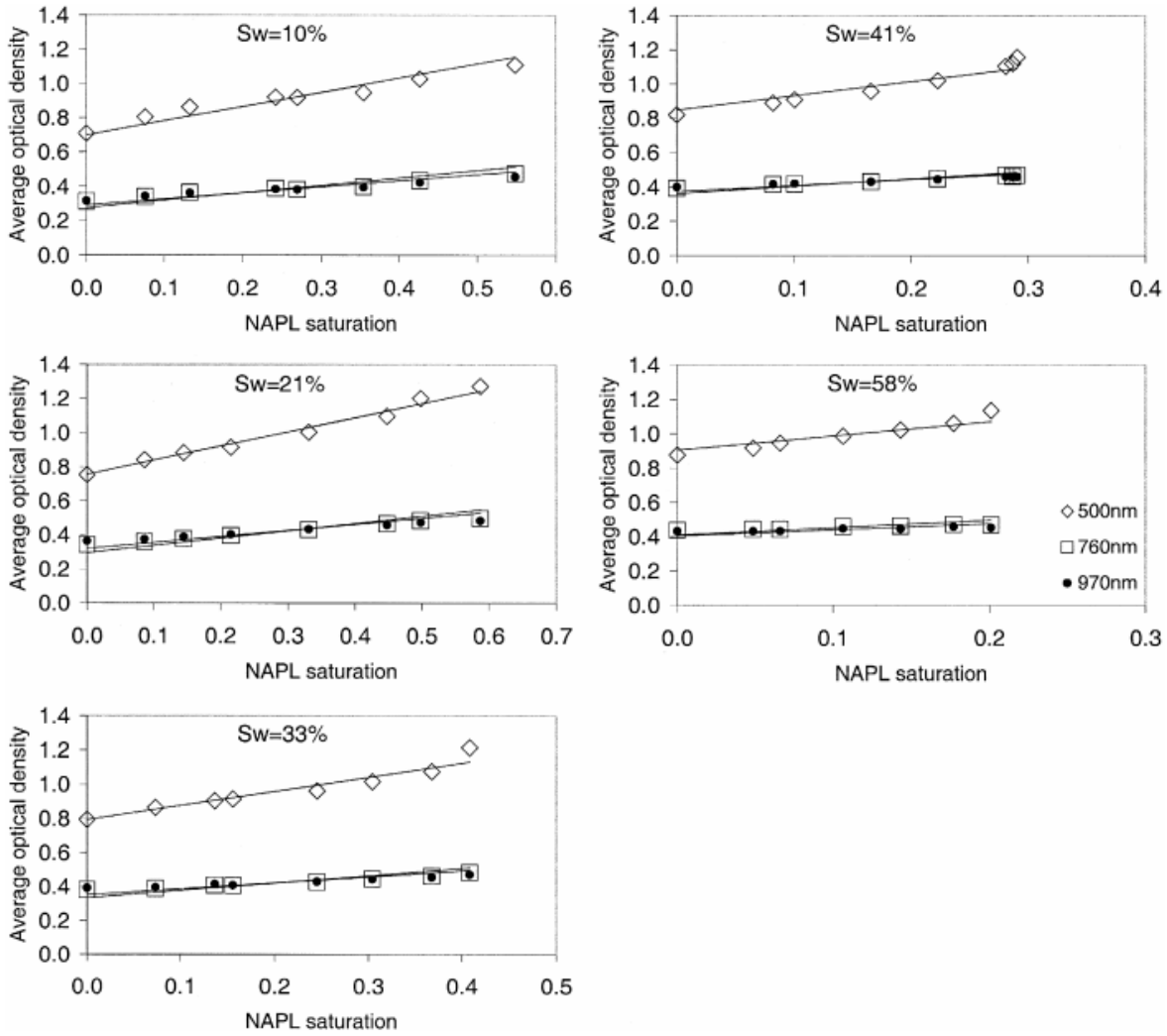

Figure 2-11 Linear relationship between average optical density and NAPL saturation for fixed water saturation for the air–NAPL–water three-fluid phase system. The solid lines are the linear relationships obtained by fitting Eq. 8 to the experimental data. The open diamonds, the open squares and the dots are the experimental data at 500, 760, and 970 nm, respectively. (C Kechavarzi *et al.*, 2000)

The reason was reckoned that in the real experiment setting which was influenced by numerous environmental factors, the reflected light intensity was somehow slightly non-linear to fluid saturations. Many factors may potentially contribute to the non-linearity: the grey scale bar has unavoidable light reflection on its surface, possibly from the light source and ambient environment; the quality of grey scale bar itself may induce errors; the distributions of fluids within a porous media

structure are different from being tested in their pure form in a spectrophotometer; the structure of the porous media was not absolutely homogeneous, etc. Therefore, a redevelopment of the method by improving both experimental design (setup) and the algorithm was conducted.

2.4.2.2 Procedure of the redeveloped calibration test

Section 2.4.1.4 has provided a method to "read" average optical density of a proposed resolution from images, therefore with a series of samples with varying known LNAPL and/or water saturations it allows to establish an empirical relationship between optical density and fluid saturations at different wavelengths.

The Kechavarzi method (C Kechavarzi *et al.*, 2000) put one sample at one time on an inclined wooden surface and fixed the camera to face the samples directly. For each sample, it took roughly one minute to swap the three narrow bandpass filters and to conduct photography. By photographing samples individually, this may induce errors due to the inconsistent light condition. By placing samples onto an inclined surface, no matter how rapidly the photography was conducted, the fluids within the porous media may flow downwards due to gravity, and it would facilitate fluid drainage at the lower part of the sample, thus, resulting unevenness in optical density and saturation. The inclined surface may also induce a difference in lightening condition. For the tank experiment, the tank was vertical, and the floodlight illumination was horizontal. On the contrary, in the calibration test, the samples were not vertical, and the light direction and intensity were significantly different from the tank experiment.

Consequently, in this study, samples were arranged in a vertical array immediately in front of the tank and camera was fixed at the same place for the tank experiments, so that

- One set of photos can contain all calibration samples to avoid lightening or photography variation between samples and images, which took less than 30 seconds of photography time in total;
- Fluid drainage caused by gravity or sample exceeding residual saturation of have been reduced by significantly decreasing the photography duration;
- Optimal similar lightening conditions have been achieved, where the illumination setup is identical to that in the tank experiments.

As shown in Figure 2-12, samples were mixed in a separate disposable container and relocated promptly to the cubic Perspex boxes for photography. The front side of the customised box (I.D. 2.5cm x 2.5cm x 2.5cm), made of 2cm thick Perspex, identical as the tank surface, served as the photographic

window for each sample. Other sides were made of 0.5cm Perspex sheet including a lid on top, which was expected to minimise potential evaporation loss and prevent sample spillage. The optical density of the samples was measured by the camera via the photographic window of the boxes. The measurement was the average optical density of the photographic window. This specific arrangement was designed to minimise the influence of unavoidable fluid drainage. Even with the occurrence of fluid drainage, it would be recorded in the photos and reduced in the averaging process of the image analysis.

Figure 2-12 Setup of the improved three-phase calibration test, where samples were placed in front of the tank with black cloth as background to reduce tank surface reflection and a grey scale bar at the bottom of the tank used for tank experiments

Once the samples were aligned, one group of four photographs were recorded: 1) clear view, 2) with the green filter, 3) the red filter, and 4) the infrared filter, respectively, which was introduced in Section

2.4.1.3. The photography was automatically controlled by the Multi-spectral photography module, the hardware and software of which will be introduced in Section 2.4.4.

During the calibration test analysis, the green and red filters were proven useable, while the infrared filter exhibited incompatibility with the method and setup. Therefore, for further analysis and experiments, the infrared filter will be abandoned.

For different sand, separate calibration tests were carried out. The following illustrations are results of the medium sand, which is most frequently used major aquifer media in the experiments.

2.4.2.3 Two phase calibration test

For both LNAPL-air and water-air tests, 11 samples were prepared, with LNAPL or water saturation ranging from 0.08 to 0.97. The sand was pre-dried overnight in an oven at 110 °C. The methodology referred to the introduction of Kechavarzi calibration method in the early part of Section 2.4.2.2.

Figure 2-13 gives the linear regression equations and R^2 values for each spectral band in both LNAPL-air and water-air systems. The relationships of average optical density and fluid saturations exhibit linear behaviour in two phase systems.

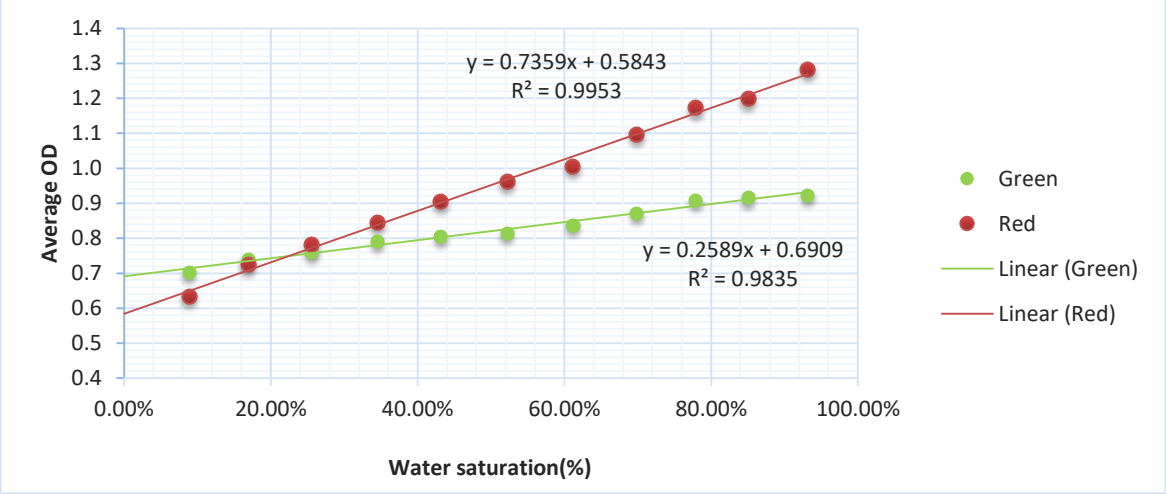

(a) Water-air

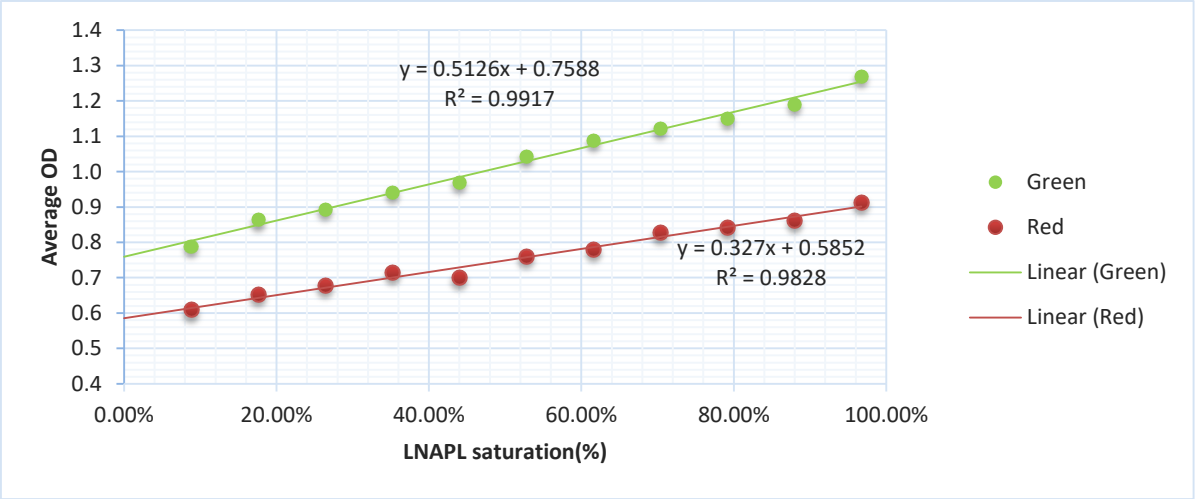

(b) LNAPL-air

Figure 2-13 Average optical densities vs fluid saturations for the two-phase systems (water-air and LNAPL-air) with best-fit coefficients and coefficient of determination from linear regression

2.4.2.4 Three phase calibration test

For the water-LNAPL-air three-phase calibration test, 32 samples were prepared, with LNAPL, water and total fluid saturation ranging from 0.00 to 1.00. The distribution of sample saturations was shown in Figure 2-14. The sand was pre-dried overnight in an oven and cooled down to room temperature before sample preparation. Water was firstly mixed with sand since water acted as the most wetting fluid in this system and then prescribed LNAPL saturations were mixed. After the mixing, the samples were then packed in the Perspex boxes immediately. The sample making should be conducted as fast as possible to reduce fluid drainage, in particular for the samples with saturations that exceed the residual saturation, which have a higher tendency to drain.

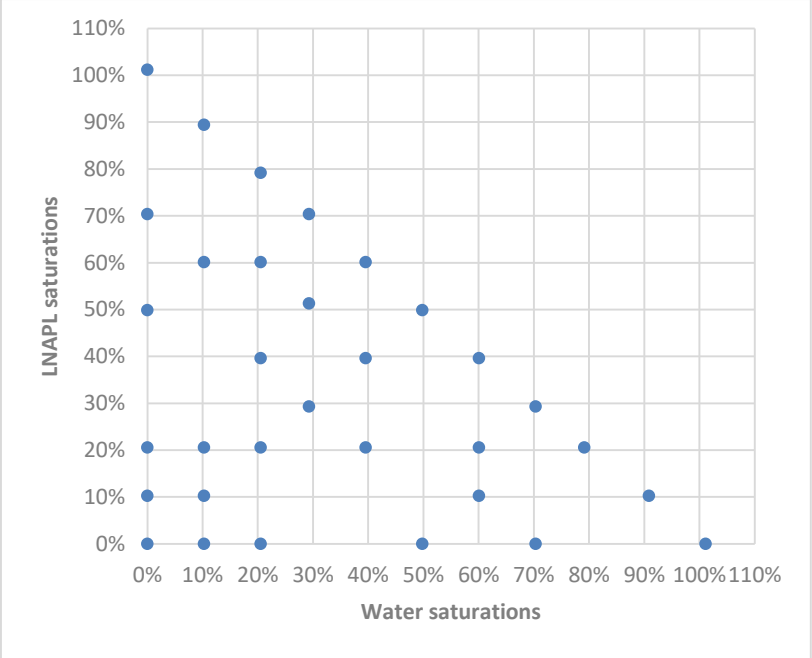

Figure 2-14 Fluid saturation distribution of samples for the water-LNAPL-air three-phase calibration test

It is clear that a multiple linear regression cannot reach the desirable accuracy of the image analysis. Thus, a better fitting method to correlate optical densities and fluid saturations should be introduced. The following surface fitting and spline fitting methods have been attempted, including Polynomial surface fitting, Linear interpolation, Nearest neighbour interpolation, Cubic spline interpolation, Thin-plate spline interpolation and Lowess Model (Matworks, 2015). A thorough investigation of the best fitting method was conducted as follows. Firstly the tightness of fit for each method was evaluated with the R^2 values, average errors and observing the tightness of individual samples. Then, by applying each method, the testing calibration result was applied to interpret tank experiment, which was compared against the mass balance result. This this case, the distribution of individual errors and an overall error for each method were validated against the result of mass balance recovery. The thin-plate spline interpolation was chosen due to its highest R^2 values, the tight fit of individual points across the entire surface, and a small overall error. The reason was reckoned as that the thin-plate spline interpolation directly applied the measured values of calibration samples, which meant that the interpolation was "loyal" to the individual measured values. Therefore, the interpolated values between samples relied on the surrounding measured sample values rather than the overall trend of all samples (Figure 2-15 (b)). On the contrary, other surface fitting methods such as Polynomial surface fitting to the degree 3 and 3 (Figure 2-15 (a)), which although achieved good R^2 values, normally generated bigger disagreements between measured values and predicted values of the calibration

samples. It reveals an overall trend of the data than paying attention to local irregularities. Therefore, it produces larger errors at the boundary values, i.e. the low and high saturated samples.

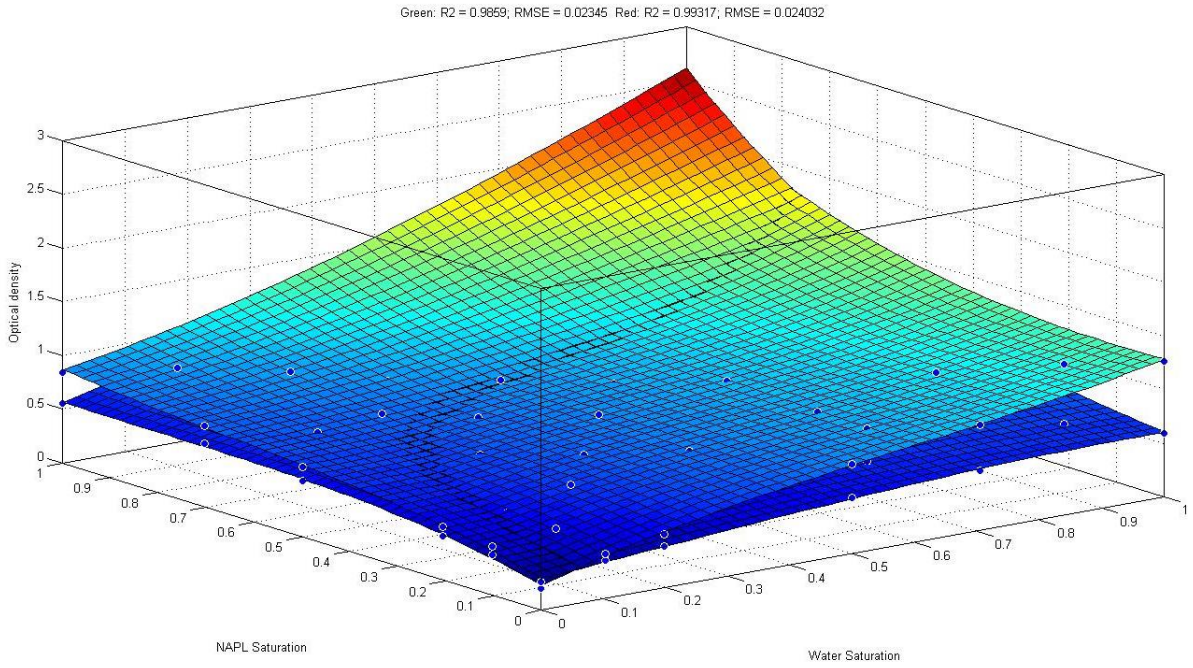

(a) Polynomial surface fitting to the degree 3 and 3 (Poly33)

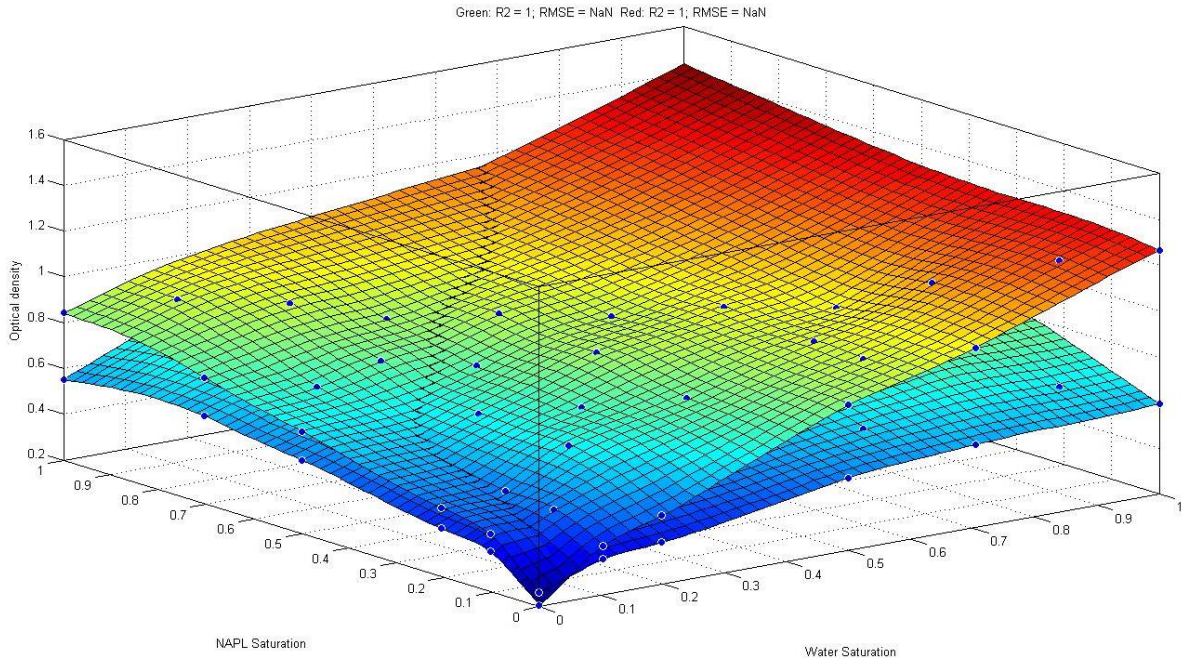

(b) Thin-plate spline interpolation

Figure 2-15 Examples of comparison between different fitting methods for the three-phase calibration test

A new challenge emerged that spline fitting does not provide mathematically expression as normal interpolation methods. As a consequence, in this case, the LNAPL and water saturations cannot be mathematically expressed by a set of optical density values directly. Therefore, a numerical approach was developed to convert the two optical density values (by both the green and red filter), to fluid saturations.

The approach is as follows. For a given pair of optical density values (green and red), the intersections of horizontal planes representing these two values in 3-D with the calibrated 3-D surfaces were calculated (Figure 2-15 (b)). The interceptions should be two 3-D curves. Then by projecting the two 3-D curves down onto the x-y plane, the interception of two curves should give a simple intersection point, the X,Y coordinates of which should be the desired LNAPL and water saturations. This method was programmed with MATLAB (Mathworks, 2014) to achieve batch processing.

However, this approach was computationally intensive and to apply this to each pixel in the interpretation of every image captured during the tank experiment would take weeks to finish the analysis of one experimental run. Therefore, an alternative indexing method was developed to shorten the calculation time. The approach was that an evenly segmented array of flat plains within the boundary of possible optical density for the green and red filter were given to intercept the two 3-D surfaces obtained from the calibration test. Therefore, a list of values containing the optical densities of the green and red filters, together with LNAPL saturation and water saturation were calculated. By indexing the known optical densities, given an admissible resolution, the approximate yet very accurate pair of LNAPL saturation and water saturation could be quickly determined. This method was implemented in MATLAB and the running time for generating the calibration indexing range from 2 hours to 2 days depending on the precision and resolution intended to achieve. An arbitrary precision can be accomplished by selecting a larger number of indexed values. In this study the precision used was about 0.005 x 0.005 fluid saturations.

Thus, transient fluid saturations can now finally be accurately quantified by indexing a pair of optical density values.

2.4.3 Image analysis

The remaining challenges for the image analysis are: 1) the cancellation method of the uneven light intensity distribution over the tank height; 2) an efficient method for batch processing the large detailed image analysis data.

2.4.3.1 Mathematical cancellation of unwanted surface glare

Although efforts have been made to decrease the unevenness of light intensity distribution over the tank height from the hardware perspective (the installation of light diffuser, floodlight setup, etc.), the image analysis errors brought by directly applying Equation 2-5 were still unsatisfactory due to the glare on the tank surface which leads to uneven light intensity over the tank height. Thus, a glare cancellation method must be introduced, which is presented as Equation 2-6. Specifically, a pair of images were captured during the completely water saturated condition (${D'}_g$ and ${D'}_r$), which contain the glare, 100% water saturation and sand (Hereafter referred as the "water saturation images") in the form of optical densities. Whereas a pair of images to be analysed (${D^o}_g$ and ${D^o}_r$) contain the same glare, the unknown water and LNAPL saturations, and sand in optical densities. By subtracting the water saturation images from the image to be analysed, the glare and sand are cancelled mathematically, leaving LNAPL saturation unchanged, water saturated changed by 100%, and sand deleted completely. However, the multiphase system contains sand and the correct water saturation, hence, they both should be added back to the optical density matrices. The optical densities of a small cube of completely saturated sand without glare have been recorded in the one of the samples in the calibration test (D_{gw0}, D_{rw0}). Therefore, by extending the scale of the dry sand sample to the size of the tank, the optical densities of the completely saturated sand without glare can be added back to the system, which finalises the glare cancellation process.

$$\begin{cases} D_g = {D^o}_g - {D'}_g + D_{gw0} \\ D_r = {D^o}_r - {D'}_r + D_{rw0} \end{cases} \qquad \text{Equation 2-6}$$

where D_g and D_r are the corrected optical density matrices of the green filtered image and the red filtered to be solved in the image analysis;

${D^o}_g$ and ${D^o}_r$ are the optical density matrices of the green filtered image and the red filtered image obtained from the images via the standardized greyscale to optical density curves;

${D'}_g$ and ${D'}_g$ are the reference optical density matrices of the green filtered image and the red filtered image obtained from the images via the standardized greyscale to optical density curves; Preferably the pair of photos should be captured when the aquifer is fully water saturated.

D_{gw0} and D_{gw0} are the optical density matrices of the green filtered image and the red filtered image of one of the calibration sample with 100% water saturation and without glare. Due to the size difference between the small calibration sample and the tank, the size of the matrices should be expanded accordingly to fit the tank size.

2.4.3.2 Procedure of the batch processing of image analysis

Putting together the developments described above, the final procedure for the image analysis was achieved with MATLAB in a single script. The crucial procedures are as follows:

1) **Image preparation.** Approximately 500 photos were recorded for one experimental run by the multi-spectral photography module. All original photos (example in Figure 2-16(a)) within one run were cropped uniformly to preserve just the flow domain with a grey scale bar captured (Figure 2-16 (b)~(d)).

2) **Grey conversion.** The cropped photos were converted from RGB24 to 12-bit grey images.

3) **Grey scale to optical density conversion.** The grey scale to optical density conversion was conducted for every pixel on every image via a unique curve calibrated for each image.

4) **Resizing.** After obtaining the optical density from the grey scale bar, the grey scale bars were cut out from all images. Failing to do so would result in the grey scale bar being involved in the saturation calculation. Thus, being allocated with fluid saturation values and included in the mass balance calculation.

5) **Resolution of calculation** (Coarsening the AOI). The resolution of an AOI (Area of Interest) in calculation could be arbitrary, which ranged from 1 x 1 pixel up to the size of one image. However, the result from using extremely fine AOI division appeared fairly noisy, due to that 1 pixel (approx. 0.035cm) was finer than a sand particle; whereas on the contrary, a coarse AOI division might produce inaccuracy. Therefore, after evaluating a variety of AOI sizes, AOI was set to be 20x20 pixels (roughly 0.7cm x0.7cm). In this step, the AOIs were divided with the prescribed AOI size and the optical density of each AOI was assigned by averaging the optical density values of the AOI being calculated. In this way, the optical density information of the entire flow domain was stored in a rearranged matrix, which could represent the area feature fairly while significantly reduce running time and noise interference.

6) **Mathematical cancellation.** The mathematical cancellation was conducted for each pair of photos by subtracting the biased photos with the reference photos, examples of which were illustrated in Figure 2-16 (e)(f).

7) **Fluid saturation calculation.** For each AOI, the average LNAPL and water saturations were obtained by indexing their paired optical densities from the three-phase calibration result (Section 2.4.2.4). The air saturation was obtained by volume balance.

8) **Plotting results.** Three contours were plotted to illustrate results in 2-D: the saturation distribution of LNAPL, water and air (Figure 2-16 (g)). Profiles were also plotted by averaging the saturation of each row of AOIs over the tank length.

9) **Mass balance.** Mass balance recovery is conducted at each photographic event during the experimental run. The result is recorded in one excel file.

$$V_N = \sum_{i=1}^{m} S_{n_m} \times A_m \times T \times \rho \qquad \text{Equation 2-7}$$

Where:

V_N is the total LNAPL volume for one photographic event, which was used in the mass balance recovery to calculate relative errors;

S_{n_m} is the average LNAPL saturation of the m^{th} AOI;

A_m is the area of the m^{th} AOI;

T is the tank thickness;

ρ is the porosity of the aquifer medium.

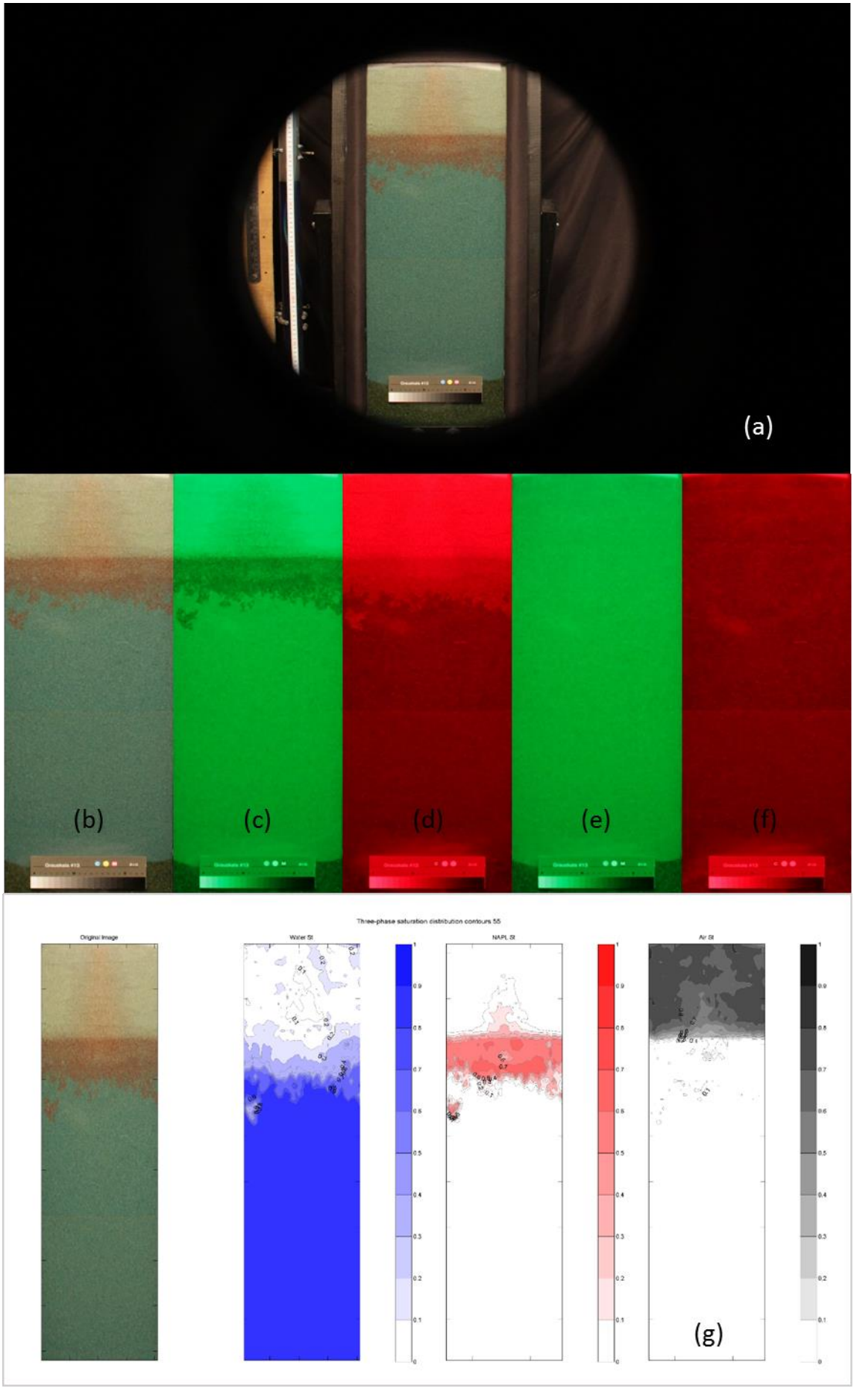
(a)
(b)
(c)
(d)
(e)
(f)
Three-phase saturation distribution contours 55
Original Image
Water St
NAPL St
Air St
(g)

Figure 2-16 Illustration of the original images before the image analysis and the output result after the image analysis. (a) was the original photo without filter which was taken together with two other photos under the green and red filters; (b)~(d) were the cropped photos; (e) and (f) were the reference photos captured during fully water saturation; and (g) was a set of contours of saturation distribution as the output of image analysis, which respectively were: photo record, water saturation contour (blue), LNAPL saturation contour (red) and gas saturation contour (grey).

In summary, with the assistance of multispectral photography, this redeveloped image analysis method accurately associates the pixel values directly accessed from photographed images, with the saturations of water, LNAPL and air (air by volume balance). The resolution is high and controllable, yet the processing time is short due to the realisation of batch processing. However, it is worth mentioning that this method only provides the saturation values for the fluid adjacent to the Perspex face of the front of the tank. Therefore assuming this is representative of the saturations across the tank thickness, however intentionally small, may still lead to mass balance errors, especially when the fluid is mobile and edge effects may influence behaviour.

2.4.4 Hardware and software

To achieve automatic mechanical control over the time-lapse photography procedure, the automatic control over photography and filter swapping should be achieved. The approach is to realise the automation of the multi-spectral time-lapse photography by controlling a camera and a USB-controlled filter wheel.

2.4.4.1 Hardware

The hardware composition of the Multi-spectral photography module is as follows (Figure 2-17):

Camera: A converted to allow near infrared camera (Canon EOS 350D,Canon (2005)) was initially used for testing and determining appropriate filters. After the infrared filter was considered the least attractive filter and thus abandoned, a normal DSLR camera (Canon EOS 700D, Canon (2013)) was used, which provides a better resolution. The camera (Figure 2-17(b)) is fixed with a metal tripod and focused on the centre of the tank. The camera is also controlled by the Raspberry Pi (Section 2.4.4.2).

Filters: Two narrow band-pass interference filters are used for every pair of photos (Figure 2-17(a)). Filters are cleaned regularly to ensure no interference were with the experimental recording.

USB controlled filter wheel: A Starlight-Xpress USB filter wheel (Starlight-Xpress-Ltd., 2009) is responsible for accommodating the two chosen filters and swapping among them regularly to take photos in two specific spectrum bands. A photo without any filter is also recorded for visual reference. A series of step-down connectors are attached the filter wheel to fit the camera lens (Figure 2-17(b)). The filter wheel is also controlled by the Raspberry Pi (Section 2.4.4.2).

The darkroom: Required by the image analysis, the light condition should carefully maintained to achieve constant light intensity for all experimental runs. Therefore, a semi-permanent darkroom was built due to financial and laboratory resource constraints. The three core modules were located within the dark room except for the monitor and keyboards, which enabled experimental monitoring from outside the dark room.

Illumination: A floodlight with two 400w eco tungsten halogen lamps (equal to 500w lamps with lumen of 9000 lux) was fixed onto a slotted frame to provide a broad spectrum light source (Figure 2-17(b)). Ideally, the light intensity across the entire tank should be consistent. However, significant variation of reflected light intensities was found over the length of the tank, whereas no noticeable variation was found over the tank width. Therefore, a light diffuser was introduced in front of the floodlight in parallel to even the light intensity. With a diffuser blocking the air circulation within the dark room, the heat generated by the floodlight would quickly and dramatically increase the temperature which would very likely influence the interfacial tensions of the fluids and cause safety concerns. Therefore, a socket plug timer was attached to the system to turn on/off the floodlight regularly. The floodlight needs roughly a minute to reach the full lumen. Therefore, the floodlight is normally set to activate 3~4 mins before the photographic event, so that floodlight is allowed to lighten up and remain consistent.

The floodlight is perhaps the most fragile component of the hardware system. Due to low budget of the project, the floodlight bought was not of high-end quality. Combined with large amount of heat generated during the light on, light bulbs tend to burn and die unexpectedly, which had actually wasted various groups of results. It is recommended that replication of this method should utilise a quality floodlight, or use a spacious darkroom with ventilation if permitted.

(a) Composition of the module

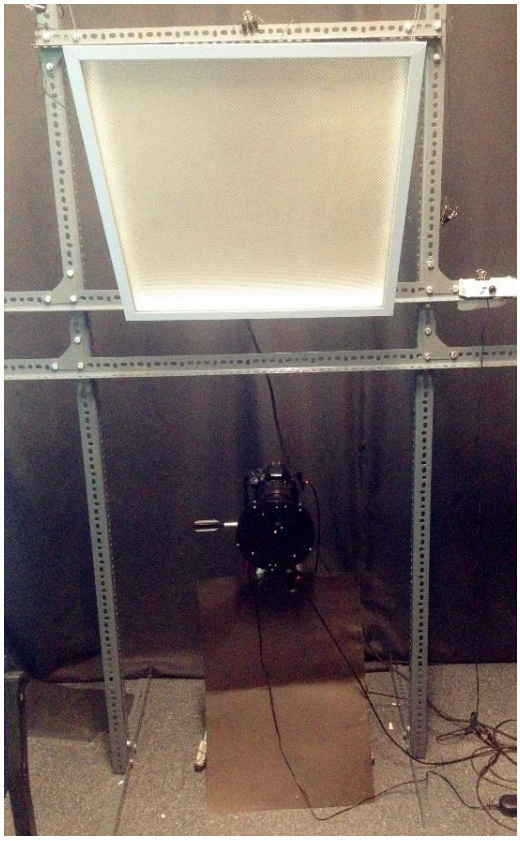

(b) Setup of camera, wheel, diffused light source and dark room

Figure 2-17 Hardware composition of the Multi-spectral photography module

2.4.4.2 Software

The purpose of this module is to realise automatic time-lapse photography for multiple spectral bands. Specifically, three photos are taken as one set: the clear vision, with the green filter and the red filter. Each photo requires a different exposure time. The script also includes the control of photography timing, i.e. the frequency of photography and the total number of sets to be recorded. When a photographic event is scheduled to occur, the filter wheel is designed to swap to the corresponding filter slot and a photo taken with a specific exposure time. The script then will send the photo taken back to the Raspberry Pi. Therefore, the core functions are threefold:

1) Communication between Raspberry Pi and the filter wheel;
2) Communication between Raspberry Pi and the camera;
3) The automatic time-lapse photography with both the camera and filter wheel.

2.4.4.2.1 The filter wheel control

A UI program for Windows OS written with C was available, which was incompatible with the OS used in this study. Therefore, the communication towards filter wheel was achieved by adapting the script provided into Python 3 (Python-Software-Foundation, 2013), which was used for all control scripts in this study. The adapted script can mechanically turn the carousel with five filter slots to a prescribed position.

2.4.4.2.2 The camera control

The gPhoto2 (Waugh *et al.*, 2015) is applied to remote control camera. The gPhoto2 is a free, redistributable, ready-to-use set of digital camera software applications for Unix-based systems including Linux, and supports a broad range of commercial cameras. The gPhoto2 has time-lapse photography options embedded. However, after testing, it was considered not suitable for the specific need of this study. Therefore, the gPhoto2 is mainly used to capture images and to retrieve images back to be stored in Raspberry Pi. The gPhoto2 is also used to overwrite camera settings (exposure time, etc.) to match up with different filters.

Table 2-5 Photography settings during major experiments for Canon EOS DSLR 700D, realised by gPhoto2

Parameters	Clear filter	Green filter	Red filter
White balance		Custom	
Flash		Off	
Focal length		F16	
ISO		1600	
Shutter speed	1/30s	0.5s	1.3s

2.4.4.2.3 Time-lapse photography

Compared to the time-interval-based time-lapse auto-photography which, say, records a photo in a prescribed time interval which is of the order of minutes, it would be more convenient to sync photography according to water table fluctuation control. In this way, crucial moments of LNAPL redistribution can be captured selectively. Therefore, the camera control delivered by gPhoto2 was successfully combined with the programme for water table fluctuation control, where every cycle of fluctuation is divided into 360 steps represented by 360 degrees in a sine wave. The photography frequency, which is defined as how many degrees a set of photos should be taken, hence becomes an extra input in the combined program. In this way, crucial moments such as the beginning (at 0°), the

peak and low of sine/cosine waves (at either 90° or 270°), the end (at 360°) and other key timings can be accurately recorded.

During the trial shooting, it was found that renaming filenames manually was time-consuming. Therefore, a renaming function was further added into the programme, where all images are automatically renamed in the following format "phototype-degree-datetime.jpg" for the convenience of further analysis (The photo types are presented as c(lear), g(reen) and r(ed)).

Table 2-6 Parameter configuration of the automatic time-lapse multispectral photography

Sine or Cosine	--	Negative sine wave
Water table fluctuation centre	cm	50
Amplitude	Cm above the datum	30
Frequency	Cycle/day	2 (except for low speed case)
Duration	day	2.5+0.5
Starting degree	degree	0, 90, 180, 270
Photography frequency	Degree/photo	15 (equivalent to 30 mins /photo)

2.5 Summary

To produce robust datasets of LNAPL distribution and migration under transient water table conditions, particularly cyclic oscillations, an intermediate scale 2-D sand tank multiphase flow experimental system was successfully designed and developed to conduct and monitor the release of LNAPLs and subsequent redistribution under dynamic, but controlled water table conditions. Subsequent batch analysis for real-time data was also developed and tested. This chapter presented the details in the design and development of this fairly complicated and capable system, the deduction and redevelopment of the monitoring method—multi-spectral image analysis was presented, and an original batch processing image analysis applying this method was successfully developed. In summary, the setup had significant automated control systems, including capabilities to:

1) Automatically mimic and flexibly program cyclic water table fluctuations;
2) Dynamically real-time image the saturation distributions of all fluids (red-dyed-LNAPL, blue-dyed-water and air phases) using high temporal and spatial resolution time-lapse multispectral photography;

3) Combining a combination of physical, mathematical and numerical methods in a MATLAB script to efficiently and accurately interpret the mass data produced by the system to better understand the mechanism of multiphase flow transport.

Significant advancement and novelty of methodologies of potential value to other research in this and related field has hence been achieved.

Reference

AB-Electronics-UK. (2012). ADC Pi v2 datasheet.

Aggregate-Industries. (2012). Sand type at Leighton Buzzard silica sand quarry. from http://www.aggregate.com/products-and-services/aggregates-and-specialist-sands/specialist-sand/specialist-sand-quarries/leighton-buzzard/

Aztec-Oils-Limited. (2014). Aztec oils MSDS.

Canon. (2005). Canon EOS 350D product specifications.

Canon. (2013). Canon EOS 700D product specifications.

Chevalier, L. R., and Petersen, J. (1999). Literature review of 2-D laboratory experiments in NAPL flow, transport, and remediation. *Journal of Soil Contamination, 8*(1), 149-167.

Chompusri, S. (2004). *LNAPL redistribution under water table fluctuation condition*. Unpublished PhD thesis. University of Birmingham.

Chompusri, S., Rivett, M. O., and Mackay, R. (2002). LNAPL redistribution on a fluctuating water table: column experiments. *IAHS PUBLICATION*, 225-234.

Cohen, R. M., Bryda, A. P., Shaw, S. T., and Spalding, C. P. (1992). Evaluation of visual methods to detect NAPL in soil and water. *Groundwater Monitoring & Remediation, 12*(4), 132-141.

Das, D. B., and Mirzaei, M. (2012). Dynamic effects in capillary pressure relationships for two-phase flow in porous media: Experiments and numerical analyses. *AIChE Journal, 58*(12), 3891-3903.

David, G. L. (2001). *Analytical Chemistry*: University Press.

Flores, G., Katsumi, T., and Kamon, M. (2007). Evaluation of LNAPL migration under fluctuating groundwater by image analysis. *Disaster Prevention Research Institute Annals, Kyoto University, 50*, 399-405.

Ghanem, A., Soerens, T. S., Adel, M., and Thoma, G. (2003). Investigation of fluorescent dyes as partitioning tracers for subsurface nonaqueous phase liquid (NAPL) characterization. *Journal of Environmental Engineering, 129*(8), 740-744.

Hudak, P. F. (2004). *Principles of hydrogeology*: CRC Press.

Kamaruddin, S. A., Sulaiman, W. N. A., Zakaria, M. P., Othman, R., and Rahman, N. A. (2011). *Laboratory simulation of LNAPL spills and remediation in unsaturated porous media using the image analysis technique: A review.* Paper presented at the National Postgraduate Conference (NPC), 2011.

Kechavarzi, C. (2001). *Physical modelling of immiscible multiphase flow in porous media.* University of Cambridge.

Kechavarzi, C., Soga, K., and Illangasekare, T. (2005). Two-dimensional laboratory simulation of LNAPL infiltration and redistribution in the vadose zone. *Journal of Contaminant Hydrology, 76*(3), 211-233.

Kechavarzi, C., Soga, K., and Wiart, P. (2000). Multispectral image analysis method to determine dynamic fluid saturation distribution in two-dimensional three-fluid phase flow laboratory experiments. *Journal of Contaminant Hydrology, 46*(3), 265-293.

Mathworks. (2014). *MATLAB documentations* Retrieved from http://uk.mathworks.com/help/matlab/

Matworks. (2015). List of Library Models for Curve and Surface Fitting. from http://uk.mathworks.com/help/curvefit/list-of-library-models-for-curve-and-surface-fitting.html

Mehta, A. (2012). Ultraviolet-Visible (UV-Vis) Spectroscopy – Limitations and Deviations of Beer-Lambert Law. *Analytical Chemistry, Notes.* from http://pharmaxchange.info/press/2012/05/ultraviolet-visible-uv-vis-spectroscopy-%E2%80%93-limitations-and-deviations-of-beer-lambert-law/

Morris-Lubricants. (2012). Largo GP2 MSDS: Morris Lubricants.

Murthy, V. (2002). *Geotechnical engineering: principles and practices of soil mechanics and foundation engineering*: CRC Press.

PhidgetsInc. (2013a). 1136 User Guide. http://www.phidgets.com/docs/1136_User_Guide

PhidgetsInc. (2013b). 1137 User Guide. http://www.phidgets.com/docs/1137_User_Guide

Piface-Digital. (2012). Piface digital documentation.

Python-Software-Foundation. (2013). *Python v3.2.5 documentation* Retrieved from https://docs.python.org/release/3.2.5/

Python-Software-Foundation. (2016). Python 3.X documentation.

Raspberry-Pi-Foundation. (2012a). Raspberry Pi documentation. from https://github.com/raspberrypi/documentation

Raspberry-Pi-Foundation. (2012b). Raspbian Documentation. from https://www.raspbian.org/RaspbianDocumentation

Schincariol, R. A., Herderick, E. E., and Schwartz, F. W. (1993). On the application of image analysis to determine concentration distributions in laboratory experiments. *Journal of Contaminant Hydrology, 12*(3), 197-215.

Schroth, M., Istok, J. D., Selker, J. S., Oostrom, M., and White, M. D. (1998). Multifluid flow in bedded porous media: laboratory experiments and numerical simulations. *Advances in Water Resources, 22*(2), 169-183.

Starlight-Xpress-Ltd. (2009). SX USB filter wheel. from https://www.sxccd.com/sx-usb-filter-wheel

TCS-Micropumps. (2015). M100-series data sheet.

technologies, A. (2012). Agilent Cary 60 UV-Vis specifications.

Thermo-Fisher-Scientific. (2012). MSDS of Erioglaucine disodium salt.

Van Geel, P., and Sykes, J. (1994). Laboratory and model simulations of a LNAPL spill in a variably-saturated sand, 1. Laboratory experiment and image analysis techniques. *Journal of Contaminant Hydrology, 17*(1), 1-25.

Wang, H., Chen, X., and Jawitz, J. W. (2008). Locally-calibrated light transmission visualization methods to quantify nonaqueous phase liquid mass in porous media. *Journal of Contaminant Hydrology, 102*(1), 29-38.

Waugh, T., Niedermann, H. U., Rensing, M. J., and Meissner, M. (2015). The gPhoto2 manual. from http://gphoto.org/doc/manual/

Werth, C. J., Zhang, C., Brusseau, M. L., Oostrom, M., and Baumann, T. (2010). A review of non-invasive imaging methods and applications in contaminant hydrogeology research. *Journal of Contaminant Hydrology, 113*(1), 1-24.

3 Overview on the experimental datasets and evaluation of the experimental system

This chapter provides an overview of all experimental datasets, which includes:

1) An introduction of the detailed setup, procedure and boundary conditions for all experimental scenarios;

2) Brief commentary on the features of each successful scenario, alongside presentation of selective obsolete runs with the rationale for their discarding;

3) Data quality examination of each successful run.

An evaluation of the functionality, performance, as well as limitations of the overall experimental system, are reviewed. Detailed interpretations of experimental datasets are made in the subsequent chapters.

3.1 Summary of experimental run scenarios

After the completion of the experimental system, the scheme of experimental LNAPL release – water table cycle scenarios proposed prior to the design was adjusted based on the actual functionality of the experimental system achieved, the results of various test runs and the accessibility of materials. It was decided that for all the experimental runs, cyclic water table fluctuations were implemented as the key hydrogeological condition and the number of water cycles should be five. The reason was derived from the observation of the results from Chompusri (2004), where the cycle number of water table fluctuation was set at 10. No evident change was discovered during the last five cycles. The frequency of water table fluctuation was two cycles per day in accordance with tidal effects. The pattern of water table fluctuation was a sine-wave shape instead of simple linear shape, which bore the most resemblance to the pattern of a natural fluctuation. A fluctuation centre of 50cm and an amplitude of 30cm were considered the best fit for the tank size and experimental requirements. The datum of all experiments was set at the bottom of the tank. In addition to the preparation and clean-up, each experimental run contained two major stages: the LNAPL release period, including a settling down period post release, and the transient water table fluctuation period with another settling down period monitored. With the exclusion of one scenario, which required a small volume of release, the LNAPL release volume was set at approximately 100ml, which permitted a significant body of LNAPL.

Eight experimental scenarios were successfully conducted eventually, investigating key influential factors including cyclic water table fluctuations, aquifer media, the water table fluctuation speed, the volumes and timing of LNAPL release, and layered heterogeneities. The completed scenarios were tabulated below in Table 3-1.

Table 3-1 Completed experimental run scenarios with key features

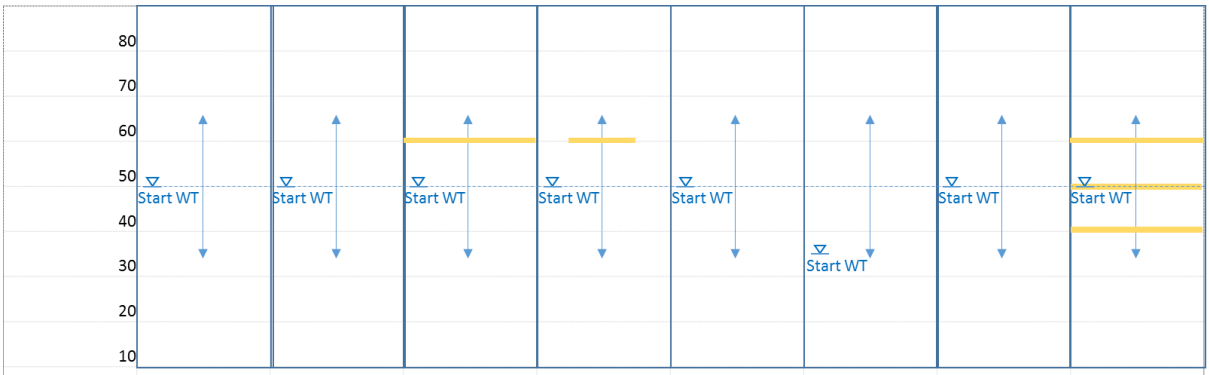

Run number	Run4T3	Run5T1	Run6T2	Run7T1	Run8T1	Run9T1	Run10T3	Run12T1
Run name	Base case	Low oscillation rate	Single complete fine grain layer	Single partial fine grain layer	Small release	Release timing at lowest WT	Fine sand	Multiple complete fine grain layers
Aquifer media	Medium	Medium	Medium+Fine	Medium+Fine	Medium	Medium	Fine	Medium+Fine
Oscillation centre	50cm	50cm	50cm	50cm	50cm	50cm	50cm	50cm
Amplitude	30cm	30cm	30cm	30cm	30cm	30cm	30cm	30cm
Oscillation starting location	50cm	50cm	50cm	50cm	50cm	35cm	50cm	50cm
Frequency	2 cycles/day	1 cycles/day	2 cycles/day	2 cycles/day	2 cycles/day	2 cycles/day	2 cycles/day	2 cycles/day
Duration*	2.5d+0.3d	5d+1d	2.5d+0.5d	2.5d+0d	2.5d+0.5d	2.5d+0.5d	2.5d+0.5d	2.5d+0.5d
Release volume	99ml	110ml	98ml	100ml	14ml	104ml	105ml	103ml
Release duration	70min	32min	56min	34min	6min	17min	72min	32min
Relevant run 1	Run3T2 100ml 3.0cm 53min		Run6T1 140ml 2.1cm 52min				Run10T1 131ml 0.8cm 34min	
Relevant run 2	Run4T2 100ml 3.0cm 26min						Run10T2 110ml 2.5cm 40min	

* The duration includes the length of oscillation and settling-down period, excluding the preparation, LNAPL release, clean-up and post-experimental analysis. After LNAPL had been released, approximately one day was left for LNAPL to come to rest prior to starting the water table oscillation. The total experimental duration for each run excluding image analysis (except for Run5T1) was roughly seven consecutive working days.

3.1.1 Experiment scenario 1 (The base case scenario)

The aim of scenario Run4T3 is to establish a benchmark that may be compared with other scenarios. The run also provides an opportunity to examine the influences on the three fluid phase (re)distribution under cyclic water table oscillations. This scenario used medium sand as its sole

aquifer medium, which was designed to be homogeneous (Table 3-1). A total amount of 99ml of LNAPL was released into the system gradually over 70 minutes. The LNAPL body was expected to reach the lateral tank sides and would be representable of LNAPL in the central main body of an LNAPL spill. The oscillation centre of the water table fluctuation, i.e. the static water table during the release period, was set at 50cm (51cm actually in this case). The water table started to oscillate from the previous post-release condition where the water table had risen by 3cm from the initial position. The water table oscillated between 35cm to 65cm elevations. The fluctuation period lasted two and half days, and the settling down period set to be half a day further, whereas only lasted four hours since no obvious change was observed.

3.1.2 Experiment scenario 2 (Low water table fluctuation speed)

The aim of scenario Run5T1 is to examine a decrease in water table fluctuation rate: the water table fluctuation was set at one oscillation cycle per day (compared to the base case scenario of two cycles per day). Other run condition remained the same as the base case. Accordingly, the fluctuation period lasted five days, and the settling down period one further day. The release of this run was relatively a fast one with 110ml of LNAPL spilt within 32 minutes. The release rates were set different among cases to find out the influences upon the LNAPL distribution.

3.1.3 Experiment scenario 3 (Release timing at the lowermost water table)

The aim of scenario Run9T1 is to identify whether the starting point of water table oscillation after the release could influence the fluid (re)distribution. An accidental NAPL spill may occur at any stage of a water table fluctuation cycle. In order to identify the possible differences, the LNAPL was released at the lowermost water table of 35cm with the oscillation centre remained at 50cm. All other run conditions remained as the same as the base case. The fluctuation period lasted two and half days, and the settling down period one further day. The release rate was a fairly fast, where 104ml of LNAPL was introduced within 17 minutes.

3.1.4 Experiment scenario 4 (Small LNAPL release)

The aim of Run8T1 is to investigate the behaviour of a smaller amount of LNAPL release. In particular, to reduce the potential for LNAPL to reach the tank lateral boundaries. Thus, only 14 ml of LNAPL was released within 6 minutes. Unusually, the mass balance error for this run was the largest among all runs, since the release volume was significantly small, and any small variation may induce a sizable error.

3.1.5 Experiment scenario 5 (Fine sand homogeneous aquifer)

The aim of scenario Run10T3 is to study the influence of different aquifer media upon LNAPL behaviour. Therefore, the aquifer medium in this scenario was replaced by a homogeneous fine sand. To prevent the fine sand leaking into the coarse sand base, which was an experimental water entry/exit design feature of the system, a 5cm layer of medium sand was placed between the coarse sand base and the major fine sand aquifer as a buffer. This scenario run was attempted three times, due to pump breakdown failures (beyond repair). Pumps were jammed by extremely fine particles within the fine sand, despite that pump filters were installed specifically to prevent pump clogging. The relatively successful attempt was due to the installation of pump filters on both the pumping and the draining pumps and an attentive monitoring in person. The pumps were immediately cleaned and fixed once the clogging was noticed. A total volume of 105ml of LNAPL was released within 72 minutes.

3.1.6 Experiment scenario 6 (Single partial fine grain layer)

It should be mentioned that the permeability difference between the medium sand and fine sand is not great. The name of fine grain layer and which is also referred as the low- or low-permeability layer/ scenario is merely a convenient phrase as the fine sand is still quite permeable.

The aim of scenario Run7T1 is to examine influence upon the three-phase flow (especially the LNAPL) of an embedded partial fine grain layer during both the release and fluctuation periods. A fine sand layer (2.5cm in depth x 15 cm in length, about half width of the tank) was embedded at around 56~58cm in elevation in the medium sand main aquifer, leaving 7cm space on both sides towards the lateral tank sides. A total volume of 100ml of LNAPL was released within 34minutes. Unfortunately, there was no photographic record of the settling down period of this run due to the malfunction of the floodlight.

3.1.7 Experiment scenario 7 (Single complete fine grain layer)

The aim of scenario Run6T2 is to observe the influence of a complete fine grain layer that completely extended across the tank laterally. An approximately 2cm thick fine sand layer was inserted horizontally at around 58~60cm of tank elevation within the medium sand principal aquifer. The upper boundary of the fine layer was slightly uneven due to the uneven weight spreading of the medium sand layer above whilst packing. A total volume of 98ml of LNAPL was released within 56 minutes.

3.1.8 Experiment scenario 8 (Multiple complete fine grain layers)

The aim of scenario Run12T1 is to evaluate the influence of a complex heterogeneous system involving multiple complete fine grain layers. Three 2.5cm thick fine sand layers, laterally extending fully across the tank width, were carefully packed horizontally at 40, 50 and 60cm in elevation within the medium-sand principal aquifer. These heights were specifically designed to investigate the potential for LNAPL to penetrate the lowest layer when the water table was brought lower than that layer, and whether LNAPL could migrate past the uppermost layer when the water table was brought above that layer. A total volume of 103ml of LNAPL was released within 32 minutes.

3.1.9 Obsolete runs with useable data

There were five more runs conducted with some compromised results due to either hardware failure or human errors. Most of the data collected were still usable and representative. For the base case scenario, both the release and the fluctuation periods for Run3T2 and the fluctuation of Run4T2 were useable. Run3T2 was abandoned because the volume of LNAPL released was around 75ml, which was significantly lower than standard releases. Run4T2 was abandoned due to floodlight malfunctions which compromised the records of some photographic events. For the complete fine grain layer scenario, Run6T1 gave an excellent illustration of LNAPL release and good fluctuation. However, too much LNAPL was accidentally released (140ml) into the system which could not be correlated with other scenarios. For the fine sand aquifer scenario, both Run10T1 and Run10T2 provided good release data. Nevertheless, few photographic events during both fluctuation periods were compromised by clogging pumps.

3.1.10 Data format

The data obtained from each experiment is as follows:

1) Each photographic event comprises three photos: one photo with clear vision, one with the green narrow band-pass filter and then the red filter respectively. Each experimental run contains over 500 photos, which started from the records of complete water saturation of the tank until the end of settling down period after the water table oscillation period.

2) A water table level (in cm) history log in the form of .txt printed by the automatic water table fluctuation control module.

3) A hardcopy of experimental log recording the status of every step of the procedure.

Results interpreted from each experiment are as follows:

1) A set of 2-D contours (.png) generated by the image analysis for each photographic event, which consists of four sub-images: the original photo record, the 2-D contours of water saturation distribution in blue, LNAPL saturation distribution in red, and air saturation distribution in grey, respectively.

2) A set of 1-D saturation distribution profiles (.png) generated by the image analysis for each photographic event, which consists of three sub-images: the profiles for water, LNAPL, and air saturations respectively. The 1-D saturation profiles are derived from averaging the saturations of a row of AOIs (Areas of interests) over the tank width.

3) A set of spreadsheets (.xlsx) outputting the 1-D profile data and mass balance recovery calculation.

4) A set of short videos (.mp4) illustrating the dynamics of (re)distribution of water saturation, LNAPL saturation and air saturation along with the photographic record of both LNAPL release period and water table fluctuation period. The videos contain the results of all photographic events.

3.2 Experimental setup

The preparation and post-experiment procedures have been introduced in Section 2.2. This section focuses on the configuration details during the pre-release period, LNAPL release period and transient water table fluctuation period.

3.2.1 Pre-release period

Given that the artificial aquifer was wet packed, the tank was fully saturated when packing was completed. The tank was then covered loosely to inhibit water evaporation as well as vacuum, and left for 24 hours to ensure a thoroughly water-saturated aquifer condition, during which time a few sets of photo records were obtained. These photos were important since the image analysis method used them as a background value in every calculation step. An insignificant variation in light intensity in these background photos may lead to a significant overall error of the image analysis for an entire experimental run. Afterwards, the water table was lowered gradually by the slow desaturation script to the prescribed water table oscillation centre and kept static for hours. The LNAPL release device was then set up, and the LNAPL head in the release device was measured.

3.2.2 LNAPL release period

1) Initial and boundary conditions

Throughout the LNAPL release period, the water table is kept static by turning off the tank valves. The lateral sides of the tank are both no flow boundaries. The top of the tank is a constant LNAPL head boundary, and the bottom of the tank a constant water head boundary. No water inflow or outflow occurs during this period. With LNAPL invading the capillary zone and possibly the saturated zone, the water table is temporarily pushed up. After the completion of the LNAPL release, the LNAPL settling-down period starts when the only change in boundary conditions is that the top boundary becomes a constant air head boundary.

2) Monitoring

The multi-spectral photography was conducted automatically by the multi-spectral photography module with every set of photos captured in every 2 minutes during the release period. For some runs, an interval of 10 minutes was applied during the post-release settling down period.

3.2.3 Water table fluctuation period

1) Initial and boundary conditions

During the water table fluctuation period, the water table is of a transient-state, which is implemented by the water table fluctuation control module (Figure 3-1). The lateral sides of the tank are no flow boundaries. The top of the tank remains a constant air head boundary. Water inflow and outflow take place only at the bottom of the tank and each moment is considered as a specified water head boundary. No LNAPL inflow or outflow occurs during this period.

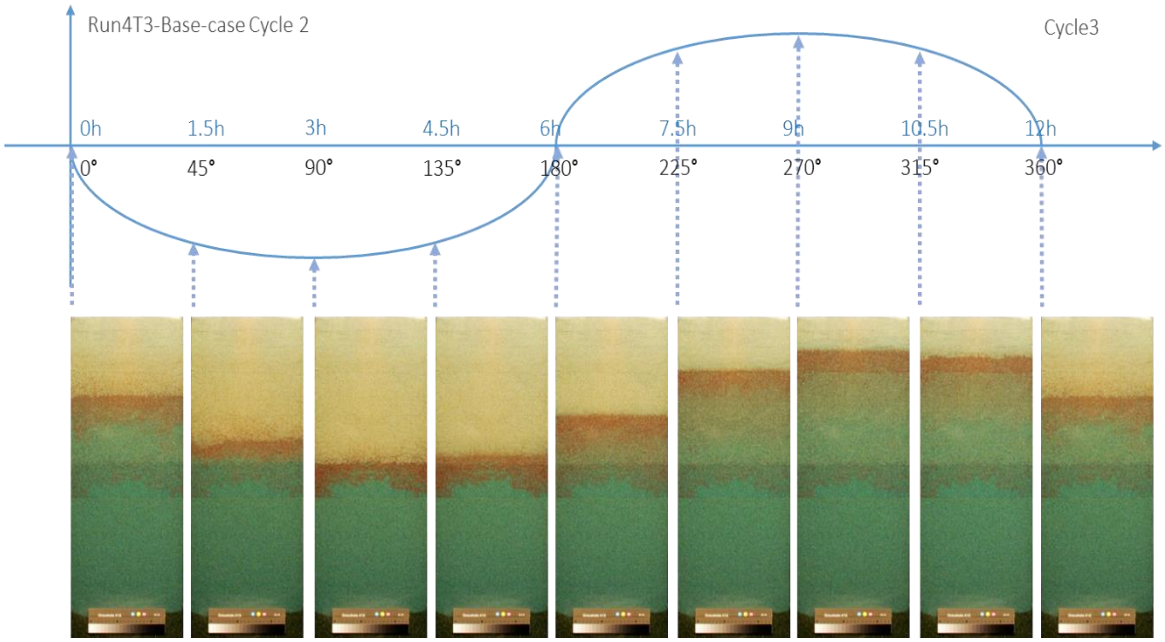

Figure 3-1 An illustration of one cycle of the water table fluctuation (a negative sine wave pattern)

2) Monitoring

The multi-spectral photography is controlled automatically by the multi-spectral photography module with a photography event captured every 30 minutes, except for the low fluctuation frequency run, which was a 60 minutes interval. Photos are renamed and arranged automatically to be exported.

3.3 Mass balance calculation

3.3.1 Calculation method

In order to examine the accuracy of the image analysis, the mass (actually fluid volume) balance recovery calculation was conducted for every photographic event of all experimental scenarios. This was achieved by the batch processing of image analysis coupled with the image analysis script. The calculated LNAPL volume for each photographic event is conducted by Equation 3-1. Note that the flow domain to be analysed is divided by a grid system into small squared areas, the size of which is to an arbitrary resolution. These small areas are called areas of interests (AOIs). The saturation of each AOI has been calculated by the image analysis so that the LNAPL volume of each AOI can be obtained. By summing up the volumes for each AOI, the total LNAPL volume of one photographic event can be obtained.

$$V_n = \sum_{m=1}^{m} S_{nc_m} \rho A_m d \qquad \text{Equation 3-1}$$

Where V_n is the volume of LNAPL for a specific photographic event calculated by the image analysis script;

m is the total number of AOIs divided by the gridding system defined in the image analysis script, which means the entire calculation area of the tank is divided into m AOIs;

S_{nc_m} is the calculated average saturation of the m^{th} AOI at the current photographic event;

ρ is the porosity of the aquifer media;

A_m is the area of the m^{th} AOI, equals to the width of AOI multiplied by the length;

d is the thickness of the tank, which was measured for each experimental run and assumed homogeneous across the tank.

For water table fluctuation periods, the LNAPL volume remains a constant, since the volatilization and dissolution of the LNAPL used are negligible. However, for the LNAPL release periods, the LNAPL volumes introduced into the system are transitory. Consequently, the errors have to be validated against the transient LNAPL volumes at each photographic event.

Table 3-2 is a summary of mass balance calculation for all experimental scenarios with the overall average relative errors for both the release period and the fluctuation period presented. One overall average relative error was obtained by calculating the relative errors of all photographic events of one scenario between calculated LNAPL volumes by the image analysis and the measured LNAPL volumes released into the system. Specifically, the relative error equals to the quotient between the difference between the measured value and observed value and the measured value. For the fluctuation periods, each run contained roughly 160 photographic events; whereas, for the release period, the photographic event numbers varied due to the differences in monitoring durations among different runs, which normally comprised dozens of photographic events. On average, the global error for all experimental runs during the release period was 4.21% whereas 8.38% for the fluctuation period.

To further validate the accuracy of the image analysis, besides the mass balance for LNAPL, the fluid distributions of water, LNAPL and air estimated by the image analysis for every photographic event were examined against the photographic records.

In previous NAPL behaviour studies, the Coefficients of determination (R2) and Mean square errors (MSEs) were most frequently used as data quality estimators. However, the MSRs which equal to the quadratic values of the relative errors were preferably used due to the “better look” (smaller values) it gives than the relative errors, which represented the same quality of data with bigger values. This

study adopted the "more honest" relative errors and R^2 to evaluate data quality. Moreover, in previous studies, the errors were the estimations of a small selection of calculating events, which were considerably less representative of the entire process compared to this project. For instance, the (Kechavarzi, 2001) study listed the overall average errors for four experimental scenarios conducted, which were 8.9%, 10.5%, 2.8% and 11.3 % respectively. Each of the errors was derived from only 4~7 calculating events, with the maximal momentary error of 36.5%. This study dramatically improved the data accuracy by the significant decrease in error values, albeit having a remarkable increase in the monitoring and calculating frequencies. Therefore, it could be concluded that the accuracy of the image analysis was satisfactory. The reasoning over the cause of errors will be analysed in the following section.

Table 3-2 The overall average relative errors for all experimental scenario runs

	Run4T3	Run5T1	Run6T2	Run7T1	Run8T1	Run9T1	Run10T3	Run12T1
Release period	2.45%	3.35%	5.30%	2.93%	6.40%	5.91%	4.61%	2.76%
Fluctuation period	7.29%	7.38%	7.04%	8.56%	18.40%	7.44%	5.19%	5.74%

3.3.2 Mass balance error analysis

As analysed before, the overall accuracy achieved by the advanced multi-spectral image analysis in this study was high with the exception of Run8T1, the small LNAPL volume scenario, where insignificant variations may lead to sizable relative errors owing to the fairly small dominators (the LNAPL release volume). After reviewing the contoured saturation distribution results, the fluid distributions of this scenario were still considered representative and reasonable. Various possible reasons for the mass balance errors were outlined below.

Figure 3-2 illustrates an example of the mass balance calculation for the LNAPL release period. The average error of 2.45% suggests the high accuracy of the image analysis. The figure indicates that the image analysis tends to marginally underestimate LNAPL volume, particularly when the LNAPL release is nearing or at completion. The calibration appears slightly less accurate on its extremes, where the smallest fluid saturations and the biggest fluid saturations occurs. It is not only because that samples with significantly low or high saturations are harder to make, but also the nature of polynomial fitting during the grey scale calibration may slightly underestimate the extreme values (Figure 2-10). When the LNAPL body moves downwards, the saturation of the LNAPL main lens spikes which may trigger the underestimation in the mass balance calculation.

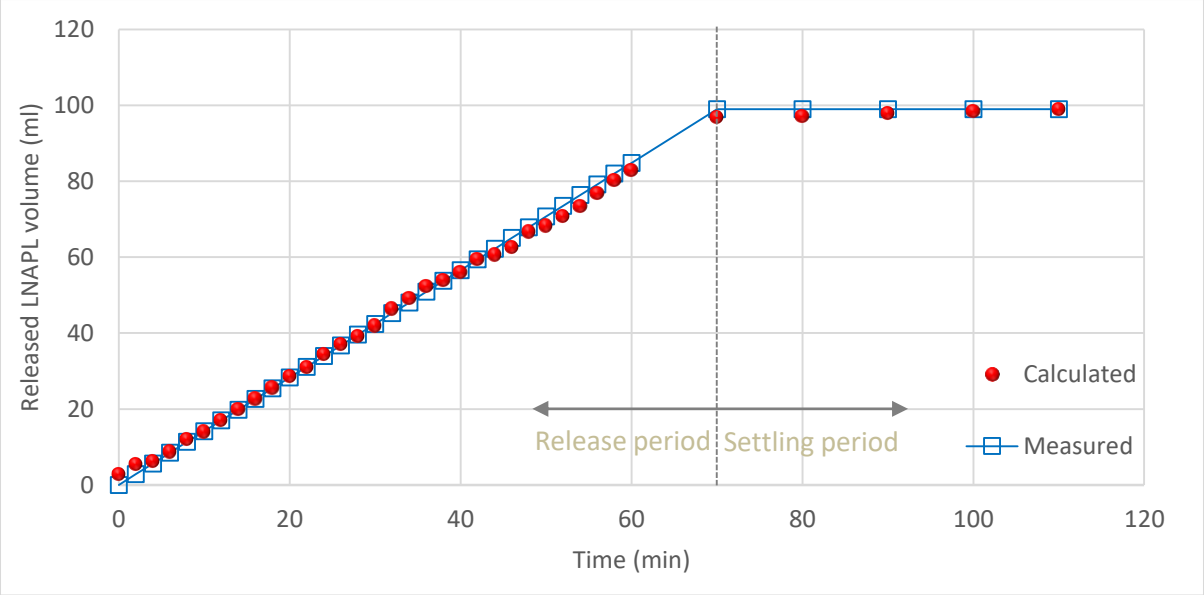

Figure 3-2 Mass balance calculation of LNAPL volume for the LNAPL release period (Run4T3-the base case scenario), where an overall average relative error of 2.45% was found (excluding the first point where the dominator was 0)

Figure 3-3 provides an example of the mass balance calculation for the water table fluctuation period. The average error of 7.29% of suggests of image analysis. The superimposing of the water table curve reveals some periodicity of errors.

1) Largest cyclical errors, where LNAPL volumes are overestimated, occur when the water table returns to around the oscillation centre with the water table ascending. The feature of this period is that the three-banded LNAPL body gradually formed, leading by the most LNAPL dense band (the LNAPL lens) and following by an intermediately and a lowly LNAPL saturated band respectively. The lowly LNAPL saturated band is mixed with a significant amount of water and air which increases the difficulty for the image analysis to calculate the LNAPL content accurately. This highly mixed three-phase system is considered the cause of the LNAPL overestimation. Another possible cause for this cyclical error may be inconsistent local porosity or edge effect. The sand packing may result in local porosity heterogeneity. Since the mass balance calculation is based on the assumption of uniform of material and fluid distribution over the tank thickness based on only the image obtained from the tank front pane, errors may also arise due to local porosity variation and edge effects.

2) Second largest cyclical errors appear around the lowermost water table positions, where LNAPL saturations are underestimated. The feature of this period is that the longest trail of residual LNAPL left in the unsaturated zone formed. The calibration of low saturations is the main challenge.

3) The errors occurring at the beginning of the fluctuation period is a one-off error that likely results from the malfunction of the floodlight, which did not provide enough illumination at the beginning of this run. After fixing the problem, the beginnings of other cycles appeared normal.

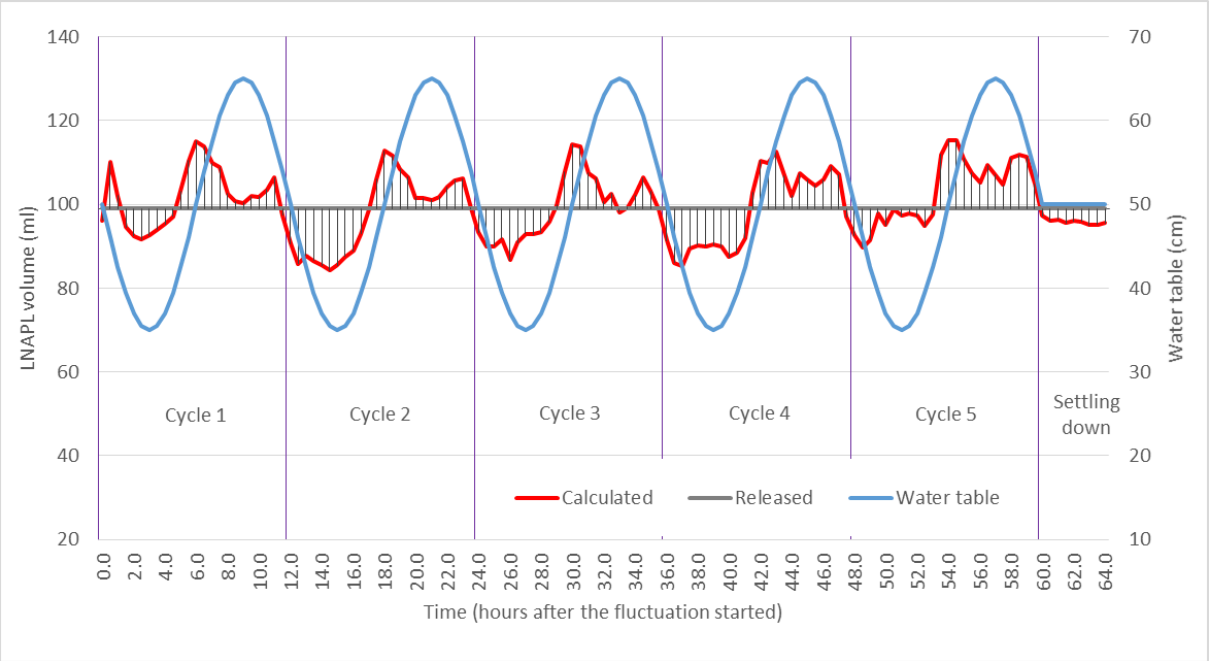

Figure 3-3 Mass balance calculation of the LNAPL volume for the water table fluctuation period (Run4T3-the base case scenario), where an overall average relative error of 7.29% was found

Overall, the types of errors were summarised as follows.

1) Errors caused by hardware

- Floodlight. The floodlight is considered the most unreliable hardware component within the system. Due to the heat generated from illumination in the darkroom without ventilation, the light bulbs become more fragile and have a tendency to burn out within a few days. Furthermore, for every photographic event, the small instantaneous variation of illumination is inevitable, uncontrollable and undetectable. Darker photos result in greater absorbance values, which during the image analysis are recognised as the existence of LNAPL and/or water.

Malfunction of floodlight was the most frequent cause of errors that several experimental scenarios had to be re-conducted. The errors had been decreased by intensive manual maintenance. However, it may be minimised or avoided by substituting to a high-end floodlight and setting up the experiment in a spacious dark room.

- The inconsistency between the front and back panes of the 2D tank. Some errors may be produced by the variation in fluid migration between the front and back panes of the tank. These may be caused by local surface effect, the inclination between front and back panes and local aquifer heterogeneity. This occurrence is more apparent during the release period as LNAPL preferentially follows the lowest entry pressure route that may locally vary over the 1.6cm tank thickness of the 2-D plane. The initial release migration is the dynamic aspect of a run and may produce some local contrast. Visual observations of the front and back pane indicate that there have been some variations between the front and back pane which did not appear to be significant, and the 3-D migration was insignificant. The results essentially report a front pane realisation of a 2-D tank experiment that may exhibit some local variation for say the central tank 2-D plan as the back pane.

- The darkroom. Restrained from laboratory environment, the dark room used in this study had to be a semi-temporary setup made of blackout materials and heavy duty Velcro tapes, which sometimes may leak light through seams. It could be avoided by setting up the experiment in a dark room.

2) Errors induced by calibration test

The calibrated image analysis may induce marginal imprecision at extremely low and high LNAPL saturations. This type of error may be and have been reduced by improving the quality of calibration samples, finding the best-fit numerical recipe, etc., but unavoidable.

3) Inconsistent local porosity.

Errors may also arise not only through the calibration procedure but also through variations and differences in porosity within the tank, as this was immeasurable directly in the tank, and through the assumption that the imaged surface was typical of the whole tank thickness.

4) Errors caused by human errors.

There have been minor and infrequent missing steps during the experimental operation that may have compromised the data to a certain degree, such as, failing to modify camera resolution, the inadequate manual setting of the white balance, unexpected change of LNAPL release head, scratching the tank during clean-up, etc.

3.4 An evaluation on 2-D automated multiphase flow experimental system

3.4.1 Functionality and performance

The 2-D automated multiphase flow experimental system developed in this study can produce more generic scenarios than the few scenarios generated in this study with no or little modification.

1) Materials

The system is not restrained by fluid density. Any two-phase or three-phase multiphase flow system with a non-wetting (or intermediate-wetting) fluid that possessed negligible solubility and volatility is suitable for the system. The aquifer media can be replaced by general porous media including a whole range of different sand, soil, glass beads. Homogeneity and heterogeneity are allowed in the system.

2) Water table fluctuation

The system can generate programmable water table fluctuations automatically. The shape of the water table fluctuation can be arbitrary by altering the mathematical expression. The fluctuation centre, location, and amplitude can be set arbitrary within the flow domain. The fluctuation frequency can be adjusted from every second to days, and the duration of the test can last months.

3) Multispectral photography

By realising Time-lapse Multispectral Photography, the system can monitor and quantify the migration and distribution of multiphase flow with high temporal frequency and spatial resolution. The duration and frequency of photography can be set arbitrary in accordance with the length of the experiment. The monitoring can include multiple stages when photography settings can be configured differently. Different fluids will simply require different narrow band-pass filters and camera settings to adapt.

4) Image analysis and result output

The resolution of the image analysis is changeable via altering the size of AOIs in the script. The numerical algorisms, the configuration of the graphic outputs including the saturation contours and

profiles and data outputs (original dataset, the mean values, sums, volume ratio below or above the water table and other calculations) may alter as well.

3.4.2 Limitations

The system is restrained by dimensions, which can only accomplish 2-D experiments. At the moment, the system cannot comprehend complicated NAPL fate that includes dissolution and volatilization. The water table fluctuation, although changeable in many parameters, is kept level across the tank width. The inclination of the water table can be achieved by adding a symmetrical system on the other side of the tank, which is simply a duplication of the control module.

3.4.3 Cost performance evaluation

Although the system has achieved very complicated functionality and is proved of excellent performance, the manufacturing cost remains low due to the application of inexpensive electronic components (Table 3-3). The two most expensive items are the tank Perspex and the camera, which account for 60% of the total cost. The automatic control module costs less than £300, which is significantly low cost. The entire module is even cheaper than a conventional water pressure sensor used in similar setups alone. The system is portable and easy to replicate.

Table 3-3 Approximate cost of the core modules of the 2-D automated multiphase flow experimental system

Multiphase flow simulation module		**Automatic water table fluctuation control module**		**Multi-spectral photography module**	
Core components	Approx. cost (GBP)	Core components	Approx. cost (GBP)	Core components	Approx. cost (GBP)
The tank	£800.00	Raspberry Pi	£28.00	Narrow bandpass filters x3	£201.00
Mariotte's bottle	£50.00	Pressure sensor	£35.00	Filter wheel	£296.00
Accessories	£20.00	Other electronic components	£70.00	Camera	£550.00
		Pumps and accessories x2	£140.00	Floodlight	£37.00
Subtotal	£870.00	Subtotal	£273.00	Subtotal	£1,084.00
				Total	£2,227.00

3.4.4 Suggestions on system improvement

1) Illumination and surrounding environment

For anyone who attempts to adopt this method or conduct similar experiments, improvements on light source should be the priority. A high-end floodlight may avoid unexpected interruption. Other types of light source may provide desirable illumination, such as a matrix of LED lights, which provides constant visible light with minimal heat generated, is perhaps a better option. Moreover, if LEDs are applied, no ventilation will be required.

2) Sloping water table

By duplicating the water table fluctuation control module, where two modules are set up to control the water table from both sides separately, transient sloping water table conditions combined with water table oscillations could be achieved, so that the influences of water table gradient upon LNAPL distribution can be studied.

3) Shape and size of the tank

To obtain a more comprehensive view of the flow domain, or to conduct a water table gradient experiment, a square tank may be more suitable. Changing the size/ shape of the tank will require a review of the sand packing techniques, the size of the dark room as well as the photography setting.

4) Monitoring

A wide angle lens may shorten the photography distance and save space and perhaps material for the dark room.

5) Pressure transducer matrix

In previous 2-D tank studies(Van Geel and Sykes, 1994a, 1994b), capillary pressure data was obtained from a matrix of pressure transducers implanted on the rear wall of the tank. Such setup can be introduced to modify the system so that precious K-S-P lab-scale dataset can be collected. As to the feasibility of modification, the Perspex tank surface allows drillings for the probes. The Raspberry Pi can control over the pressure transducers can be easily achieved.

6) A different image analysis approach ---Colour intensity

Currently, the interpretation method is not using the full potential of the images taken, which are colour photos. The NAPL and water are dyed in different colours, which possess different colour intensities (red, green or blue). By measuring colour intensities of different fluids, theoretically, fluid

saturations can be obtained accurately (Kashuk *et al.*, 2014). This approach was tested, developed but abandoned eventually, not because it was not feasible or inaccurate, but because there were no accurate colour bars on the market to be used for calibration.

3.5 Summary

A tabulated overview of the characteristics and datasets of all experiment scenarios was presented. To comprehensively evaluate the functionality and performance of the 2-D automated multiphase flow experimental system (including corresponding interpretation method), the mass balance calculations for all experimental scenarios were conducted. The global error for all experimental runs during the release period was 4.21% and 8.38% for the fluctuation period, which significantly improved the data accuracy, resolution and frequency compared to similar research and certainly gave credibility to the system. Possible reasons were recognised for the mass balance errors, and countermeasures were given to avoid or minimise the interference. More general functions of the system were explained while limitations of the system were summarised. Lastly, from the further cost performance evaluation, the system was considered as low-cost, low-power-consumption, portable and replicable while having achieved fairly complicated automated functionality and good performance. Proposals on how to further improve and upgrade the system were also expounded.

References

Chompusri, S. (2004). *LNAPL redistribution under water table fluctuation condition*. Unpublished PhD thesis. University of Birmingham.

Kashuk, S., Mercurio, S. R., and Iskander, M. (2014). Visualization of dyed NAPL concentration in transparent porous media using color space components. *Journal of Contaminant Hydrology, 162*, 1-16.

Kechavarzi, C. (2001). *Physical modelling of immiscible multiphase flow in porous media.* University of Cambridge.

Van Geel, P., and Sykes, J. (1994a). Laboratory and model simulations of a LNAPL spill in a variably-saturated sand, 1. Laboratory experiment and image analysis techniques. *Journal of Contaminant Hydrology, 17*(1), 1-25.

Van Geel, P., and Sykes, J. (1994b). Laboratory and model simulations of a LNAPL spill in a variably-saturated sand, 2. Comparison of laboratory and model results. *Journal of Contaminant Hydrology, 17*(1), 27-53.

4 The modelling methodology

The aim of this chapter is to build a descriptive model that quantitatively interprets a selection of the observed experimental data, in order to confirm the reliability of experimental datasets and to highlight crucial features of the multi-phase flow dynamics.

The chapter introduces the choice of modelling code --- the NAPL simulator, followed by the identification of the major assumptions along with the governing equations of the model to build which consists of the mass balance equations, constitutive relation equations and hysteretic K-S-P model. During the modelling setup, some external improvements of NAPL simulator had to be carried out to complement current functions, including the development of a practical graphic user interface (GUI), the batch processing for the visualization of modelling results and the implementation of the transient initial and boundary conditions which is essential to the simulation of the water table fluctuation period. Lastly, the numerical model is built to theoretically substantiate and interpret the processes and results harvested from selective well-controlled laboratory experiments on LNAPL migration and (re)distribution, specifically, the release and fluctuation periods of the base case scenario (Run4T3). The model is constructed and calibrated based on segments of data from the base case scenario (Run4T3). On account of the thesis readability, the modelling setup, results and discussions will be presented in Chapter 4 in comparison with the experimental results.

4.1 Problems and objectives

In order to improve current understanding of LNAPL migration and (re)distribution, the overall aim of this chapter is to develop numerical models to describe the migration and (re)distribution of water-LNAPL-air three-phase flow in porous media systems with the emphasis on the transient water table conditions. Specifically, to simulate the fluid dynamics under an LNAPL release upon a static water table condition and the following cyclic water table fluctuation conditions. The aim is addressed by the following objectives.

1) Choose a modelling code that can be applied to simulate three-phase multi-phase flow redistribution including hysteresis effects within porous media.
2) Summarise the governing equations controlling the LNAPL migration and (re)distribution with no mass transfer, chemical or biological reactions, absorption or volatilization involved.

3) Improve the NAPL simulator by developing a graphic user interface (GUI), batch processing visual outputs of modelling results, and achieve the modelling of transient initial and boundary conditions, which is not supported in NAPL simulator.
4) Based on a fraction of experimental data from the base case scenario (Overviewed in Section 3.1.1 and results presented in Chapter 4), build a model to confirm the equations describing the physical process of LNAPL distribution in the NAPL simulator. Calibrate the model with laboratory data so that essential features and dynamics can be accurately simulated.

4.2 Choice of software

The suitable modelling code should be equipped with standard equations that allow the simulation of three-phase non-volatile fluid in porous media and consider hysteresis effects in its constitutive relation equations. Many NAPL modelling codes were successfully applied in relevant studies with desirable functionality and reliability that could serve this study, such as NAPL simulator (e.g.(Kamon *et al.*, 2006; Zhou *et al.*, 2014)), STOMP simulator (e.g. (Schroth *et al.*, 1998; Oostrom *et al.*, 2006)), and MOFAT (e.g. (Steffy *et al.*, 1998; Cedric Kechavarzi, 2001)).

The modelling software selected for this study was the NAPL Simulator V2.0 developed by the National Risk Management Research Laboratory of US Environmental Protection Agency (J Guarnaccia *et al.*, 1997a). NAPL simulator consists a set of standard mathematical and numerical models for subsurface multi-phase flow and transport modelling. NAPL simulator was a finite element model that could simulate both physical and chemical process of flow and solute transport of up to three-dimensional, three-phase flow system in near-surface heterogeneous porous media. The detailed documentation can be found in J Guarnaccia *et al.* (1997a).

The NAPL simulator gives special focuses among quantifying the complicated NAPL migration process, where two of these emphases are of particular relevance to this study, which are: 1) Fluid entrapment and release; and 2) Hysteresis in the relative permeability-saturation-capillary pressure (K-S-P) constitutive relations. It is because the water table fluctuation condition would result in sequential imbibition and drainage processes and cyclic fluctuations would lead to a more remarkable hysteresis phenomenon. Thus, to accurately quantify the LNAPL transport and distribution under water table fluctuation conditions, the residual saturation of all fluids, which are the main cause for hysteresis phenomenon and specifically the LNAPL residual saturation acts as persistent source of pollution,

deserve more attention (C Kechavarzi *et al.*, 2005; Zhou *et al.*, 2014) and would be essential to the assembly of the model.

The NAPL simulator was chosen also owing to its successful track records of applications in the simulation of LNAPL migration and distribution with variant water table conditions, such as 1-D lab-scale studies concerning the K-S-P relationship under simple water table variations (Josegh Guarnaccia *et al.*, 1997b; Kamon *et al.*, 2006; Pasha *et al.*, 2014; Zhou *et al.*, 2014) were successfully simulated with NAPL simulator. Moreover, the NAPL simulator was an open-source, free modelling code which possessed the potential for redevelopments according to specific requirements.

4.3 Governing equations

This study does not intend to build new models, but to utilise the embedded mathematical and numerical models in the NAPL simulator. Therefore the introduction of the governing equations follows the logics in (J Guarnaccia *et al.*, 1997a).

As mentioned in Chapter 1, this study focused on the migration and (re)distribution of LNAPL with no mass transfer between phases and solute transport, chemical or biological reactions, absorption or volatilization involved. Considering that, the LNAPL chosen was a single chemical species that possesses negligible solubility and volatilization. During the laboratory experiments, the temperature and pressure variations involved were minimal. Therefore, the density, viscosity and interfacial tensions of all fluid phases were assumed constant. Furthermore, the artificial aquifer only consisted of well-graded clean sands with relatively high hydraulic conductivities. Thus, the aquifer was assumed incompressible, which implied that the porosity remained constant. The NAPL simulator could only be applied in incompressible systems. In accordance with the experiments, the wettability constraint of the fluid phases towards the aquifer followed the sequence that water > LNAPL > air.

4.3.1 Mass balance equations

The general mass balance equations (continuum balance equations) for the water-LNAPL-air three-phase flow system with constant fluid properties and without mass exchange between phases are as follows (Pinder and Abriola, 1986; Josegh Guarnaccia *et al.*, 1997b).

$$\varepsilon \frac{\partial S_W}{\partial t} = -\nabla \cdot q^W$$
$$\varepsilon \frac{\partial S_N}{\partial t} = -\nabla \cdot q^N \qquad \text{Equation 4-1}$$
$$\varepsilon \frac{\partial S_G}{\partial t} = -\nabla \cdot q^G$$

Where:

ε denotes the porosity of the porous medium, which, due to constant temperature and the incompressibility assumption, is constant and not dependent on the phase saturations or pressures;

S_W, S_N and S_G are the saturations of the water, LNAPL and gaseous phases respectively;

q^W, q^N and q^G are the flow per unit area (also called Darcy velocity vector) of the water, LNAPL and gaseous phase respectively [1/T], which are solved in the Darcy's law below.

Hereafter, the following superscripts and subscripts, N denotes the NAPL phase, W the water phase, and G the gaseous phase.

Another volume balance equation should be introduced that the sum of the saturations of all phases should equal to 1 (Bear and Cheng, 2010):

$$\mathrm{S}_W + \mathrm{S}_N + \mathrm{S}_G = 1 \qquad \text{Equation 4-2}$$

In porous media, the flow of a fluid is determined by the interaction between gravity, pressure, viscosity and inertial force, where the inertial force is usually considered negligible, gravity and pressure are considered the driving forces and viscosity as resistance. Darcy's law is the mathematical expression of the balance between gravity, pressure, and viscosity. For a 1-D flow system in a homogeneous porous medium, Darcy's law is expressed as (Muskat and Meres, 1936) which was cited in (Mayer and Hassanizadeh, 2005) :

$$q = -\frac{k}{\mu}(\nabla p - \rho g \nabla z) \qquad \text{Equation 4-3}$$

Where:

q is the flow per unit area of the fluid as above;

μ is the dynamic viscosity of the fluid;

p is the pressure of the fluid;

ρ is the density of the fluid;

k is the effective permeability of the medium towards the fluid, which is defined by relative permeability k_r and intrinsic permeability κ:

$$k_r = \frac{k}{\kappa} \qquad \text{Equation 4-4}$$

The relative permeability for phase α is a scaling factor that ranges between 0 and 1 ($0 \leq k_r^{\alpha} \leq 1$), which is a function of the fluid saturation (S_α) of the phase α. As presumed earlier that the wettability order obeys water>LNAPL> air in this study, the following functional relationship is assumed:

$$\begin{gathered} k_r^W = k_r^W(S_W) \\ k_r^N = k_r^N\left(S_{W,} S_T\right) \\ k_r^G = k_r^G(S_T) \end{gathered} \qquad \text{Equation 4-5}$$

Where S_T is the total saturation of liquid phases, which is defined as (Mayer and Hassanizadeh, 2005):

$$\mathrm{S}_T = \mathrm{S}_W + \mathrm{S}_N \qquad \text{Equation 4-6}$$

By substituting Equation 4-4 into Equation 4-3 yields the Darcy's law for a specific fluid α in the multiphase flow system (Mayer and Hassanizadeh, 2005):

$$q^{\alpha} = -\frac{\kappa^{\alpha} k_r^{\alpha}}{\mu^{\alpha}}(\nabla p^{\alpha} - \rho^{\alpha} g \nabla z) \qquad \text{Equation 4-7}$$

Therefore, for a three-phase flow system consists of water, LNAPL, and air, Darcy's law can be extended to the following form, assuming that the driving force for each phase is determined by its gradient in the phase pressure and gravity (Aziz and Settari, 1979; Mayer and Hassanizadeh, 2005).

$$\begin{gathered} q^W = -\frac{\kappa^W k_r^W}{\mu^W}(\nabla p^W - \rho^W g \nabla z) \\ q^N = -\frac{\kappa^N k_r^N}{\mu^N}(\nabla p^N - \rho^N g \nabla z) \\ q^G = -\frac{\kappa^G k_r^G}{\mu^G}(\nabla p^G - \rho^G g \nabla z) \end{gathered} \qquad \text{Equation 4-8}$$

Therein, the parameters known are the properties of the porous medium and the multiphase flow, which include: the density and viscosity of each fluid phase and the porosity, intrinsic permeability and relative permeability of the porous medium. The relative permeability is a function of fluid saturation). The saturation and pressure of each fluid phase are unknown, whereas the pressure is a

function of fluid saturation. To numerically solve this set of non-linear partial differential equations, constitutive relationships between fluid saturation, pressure and relative permeability (*K-S-P* relationships), which are mostly empirical, should be given.

4.3.2 Constitutive relations

To ensure the global mass conservation throughout the modelling, a number of quantitative constraints need to be specified, including: the total volume balance equation (Equation 4-2) capillary pressure- saturation relationships (S-P relationships) and relative permeability- saturation relationships (K-S relationships). By linking the constitutive relation equations and the mass balance equations (including the three-phase Darcy's Law), the governing equations of the numerical model will be finalized (Bear and Cheng, 2010).

4.3.2.1 Capillary pressure-saturation relationships (S-P relationships)

$$p_{cNW}(\mathrm{S}_W) = p_N - p_W$$
$$p_{cGN}(\mathrm{S}_T) = p_G - p_N \qquad \text{Equation 4-9}$$

Where:

$p_{c\alpha\beta} = p_\alpha - p_\beta$ represents the capillary pressure between a non-wetting phase α and a wetting phase β.

The capillary pressure between immiscible fluids is defined as a function of fluid saturation, which should remain continuous in time and space and simutaneously satisfy the following relationship from Leverett (1941) which was cited in Mayer and Hassanizadeh (2005):

$$\frac{p_{cNW}}{\sigma_{NW}} = \frac{p_{cGN}}{\sigma_{GN}} = \frac{p_{cGW}}{\sigma_{GW}} \qquad \text{Equation 4-10}$$

Where $\sigma_{\alpha\beta}$ represents the interfacial tension between phase α and phase β, and the air-water capillary pressure can be derived from the following relation:

$$p_{cGW} = p_{cNW} + p_{cGN} \qquad \text{Equation 4-11}$$

By measuring the S-P relationship of one phase pair and applying both Equation 4-10 and Equation 4-11, the relations of the other two phase pair can be obtained.

When the phase pair cannot be measured directly, the Van Genuchten model (Van Genuchten, 1980) is most often used to predict or fit the two-phase capillary pressure-saturation relationship (S-P relationship), which is defined as:

$$S_e = [1 + (\alpha h_c)^n]^{\frac{1}{n}-1} \quad \text{Equation 4-12}$$

Where S_e is the effective saturation which will be defined below, α and n are empirical fitting parameters for the model that describe the curve shape, and h_c is the capillary pressure head in terms of an equivalent height of a water column under the same pressure p_c (Mayer and Hassanizadeh, 2005).

$$h_c = \frac{p_c}{\rho_w g} \quad \text{Equation 4-13}$$

Where ρ_w is the density of water, and p_c is the capillary pressure.

The effective saturation S_e of water in an water-air two-phase system is defined as (Van Genuchten, 1980):

$$S_{ew} = \frac{S_w - S_{wr}}{1 - S_{wr}}, \quad 0 \leq S_{ew} \leq 1 \quad \text{Equation 4-14}$$

Where S_{ew} stands for the effective saturation of the wetting phase in the system, which, in this case, is water;

S_w is the saturation of the wetting phase, in this case, water;

S_{wr} is the irreducible saturation of the wetting phase., in this case, the irreducible saturation of water.

In this study, the phase pair selected is the water-air, which was firstly fitted using the Van Genuchten model (Equation 4-12) based on part of the experimental data. Then, by applying both Equation 4-10 and Equation 4-11, the relations of the other two phase pair (water-LNAPL and LNAPL-air) were be obtained.

However, the Van Genuchten model only characterizes a two-phase capillary pressure-saturation relationship (S-P relationship) that is monotonic without considering hysteresis and pore entrapment.

Therefore, to apply the Van Genuchten model in the study upon a three-phase flow system under cyclic water table fluctuation conditions, where the hysteresis effect is essential, the Van Genuchten model should be extended to a three-phase system and be adapted to accommodate hysteresis.

4.3.2.2 Relative permeability- saturation relationships (K-S relationships)

Besides the experimental measurement which is often unavailable, the relative permeability-saturation relationship (K-S relationship) is usually described by Mualem (1976). In the NAPL simulator, the K-S-P model adopts the combined model of both S-P (Van Genuchten, 1980) and K-S (Mualem, 1976), which was recorded in (Parker *et al.*, 1987).

$$k_r^W(S_W) = (S_{eW})^{\zeta}[1-(1-S_{eW}^{1/m})^m]^2$$
$$k_r^G(S_G) = (S_{eG})^{\xi}[1-(1-S_{eG}^{1/m})^m]^2 \qquad \text{Equation 4-15}$$

where $m = 1 - 1/n$ defined in Equation 4-12; S_{eW} is the effective saturation of water defined in Equation 4-14; and ζ and ξ are the pore connectivity parameters for the water phase and gaseous phase respectively that are utilised in NAPL simulator (J Guarnaccia *et al.*, 1997a).

The pore connectivity parameter was defined in Mualem (1976) which is an empirical pore tortuosity/connectivity parameter that is normally assumed to be 0.5 for most soils in the same literature. This value has only been determined for liquid phases, yet for the gaseous phase, the value of 0.5 was simply applied in Parker and Lenhard (1987) without discussion. The value of approximately 0.3 for the gaseous phase was suggested by Luckner *et al.* (1989). It was also suggested that the value for the wetting phase(s) should be larger than the non-wetting phase(s) in the NAPL simulator documentation (Josegh Guarnaccia *et al.*, 1997b), where the illustration Figure 4-1 was included. The values of choice have taken the statements above into account and will be shown in Table 5-1.

Aziz, K., and Settari, A. (1979). *Petroleum reservoir simulation*: Chapman & Hall.

Bear, J., and Cheng, A. H.-D. (2010). *Modeling groundwater flow and contaminant transport* (Vol. 23): Springer Science & Business Media.

Guarnaccia, J., Pinder, G., and Fishman, M. (1997a). *NAPL: Simulator documentation*: National Risk Management Research Laboratory, United States Environmental Protection Agency, Research and Development.

Guarnaccia, J., Pinder, G., and Fishman, M. (1997b). NAPL: Simulator documentation: U.S. Environmental Protection Agency.

Kamon, M., Li, Y., Flores, G., Inui, T., and Katsumi, T. (2006). Experimental and numerical study on migration of LNAPL under the influence of fluctuating water table in subsurface. *Disaster Prevention Research Institute Annals, Kyoto University, 49*, 383-392.

Kechavarzi, C. (2001). *Physical modelling of immiscible multiphase flow in porous media.* University of Cambridge.

Kechavarzi, C., Soga, K., and Illangasekare, T. (2005). Two-dimensional laboratory simulation of LNAPL infiltration and redistribution in the vadose zone. *Journal of Contaminant Hydrology, 76*(3), 211-233.

Leverett, M. (1941). Capillary behavior in porous solids. *Transactions of the AIME, 142*(01), 152-169.

Luckner, L., Van Genuchten, M. T., and Nielsen, D. (1989). A consistent set of parametric models for the two-phase flow of immiscible fluids in the subsurface. *Water Resources Research, 25*(10), 2187-2193.

Mayer, A., and Hassanizadeh, S. M. (2005). *Soil and Groundwater Contamination: Nonaqueous Phase Liquids, Principles and Observations* (Vol. 17): American Geophysical Union.

Mualem, Y. (1976). A new model for predicting the hydraulic conductivity of unsaturated porous media. *Water Resources Research, 12*(3), 513-522.

Muskat, M., and Meres, M. W. (1936). The flow of heterogeneous fluids through porous media. *Journal of Applied Physics, 7*(9), 346-363.

Oostrom, M., Hofstee, C., and Wietsma, T. W. (2006). Behavior of a viscous LNAPL under variable water table conditions. *Soil & Sediment Contamination, 15*(6), 543-564.

Parker, J., and Lenhard, R. (1987). A model for hysteretic constitutive relations governing multiphase flow: 1. Saturation-pressure relations. *Water Resources Research, 23*(12), 2187-2196.

Parker, J., Lenhard, R., and Kuppusamy, T. (1987). A parametric model for constitutive properties governing multiphase flow in porous media. *Water Resources Research, 23*(4), 618-624.

Pasha, A. Y., Hu, L., and Meegoda, J. N. (2014). Numerical simulations of a light nonaqueous phase liquid (LNAPL) movement in variably saturated soils with capillary hysteresis. *Canadian Geotechnical Journal, 51*(9), 1046-1062.

Pinder, G. F., and Abriola, L. M. (1986). On the simulation of nonaqueous phase organic compounds in the subsurface. *Water Resources Research, 22*(9S).

Schroth, M., Istok, J. D., Selker, J. S., Oostrom, M., and White, M. D. (1998). Multifluid flow in bedded porous media: laboratory experiments and numerical simulations. *Advances in Water Resources, 22*(2), 169-183.

Steffy, D., Johnston, C., and Barry, D. (1998). Numerical simulations and long-column tests of LNAPL displacement and trapping by a fluctuating water table. *Journal of Soil Contamination, 7*(3), 325-356.

Van Genuchten, M. T. (1980). A closed-form equation for predicting the hydraulic conductivity of unsaturated soils. *Soil Science Society of America Journal, 44*(5), 892-898.

Zhou, J., Li, Y., Xu, J., and Kamon, M. (2014). Testing of NAPL simulator to predict migration of a light nonaqueous phase liquid (LNAPL) under water table fluctuation in a sandy medium. *Journal of Central South University, 21*(1), 317-325.

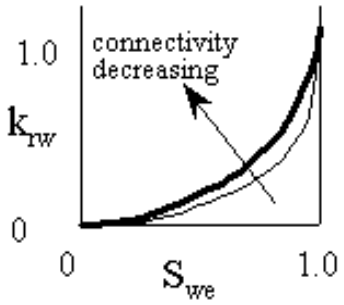

Figure 4-1 The illustration of pore connectivity parameter extracted from Josegh Guarnaccia *et al.* (1997a)

4.3.2.3 The augmentation from a two-phase system to a three-phase system

Direct measurements of the K-S relationship of the full three-phase systems is beyond challenging. However, the K-S relationships can be extended from a known two-phase relation to an unknown three-phase system based on the wettability sequence assumption, which again is water > LNAPL > air in this study. Hence, the relative permeability of water k_r^W is entirely decided by the water saturation S_W, and the relative permeability of air k_r^G is completely determined by the air saturation S_G. Whereas, the relative permeability of LNAPL as an intermediate wetting fluid k_r^N is dependent on both water and air saturations (S_W and S_G). By applying the capillary pressure scaling described in Equation 4-10, the three phase K-S-P relationship can finally be augmented.

4.3.3 Hysteresis

4.3.3.1 Sub-model for phase entrapment and release

During the imbibition process and the drainage process within a multiphase flow system, the capillary pressure curves do not coincide at same saturations. Specifically, the wetting fluid is “reluctant” to drain during its drainage process and is “reluctant” to imbibe during its imbibition process. This

phenomenon that the capillary pressure curve depends on both the direction and the history of drainage and imbibition process, is called hysteresis (Bear and Cheng, 2010).

Two reasons are considered responsible for the hysteresis phenomenon in *K-S-P* relationships, the effects of capillary and contact angle (Type 1 hysteresis), and fluid entrapment due to saturation path reversals (Type 2 hysteresis) (R. J. Lenhard *et al.*, 1989). For the Type 1 hysteresis, the drainage process relies on the narrow pore throats, whereas the imbibition process is dominated by the maximal diameters of pore bodies. For the Type 2 hysteresis, during the drainage process, a portion of fluid becomes immobile by either capillary segregation in the case of a non-wetting fluid, or capillary and adhesive forces in the case of a wetting fluid. A fraction of these immobile fluids can be re-mobilised by fluid displacement during imbibition (Josegh Guarnaccia *et al.*, 1997a). On the contrary, the fluid saturation that becomes irreversibly entrapped is defined as the residual saturation $S_{\alpha r}$ for phase α. Similarly, the entrapped volume of phase α is defined as the corresponding volume of residual saturation $S_{\alpha r}$, which is the volume of phase α that is permanently entrapped during the drainage or imbibition process. Given that Darcy's law merely applies to the volume that is hydraulically associated, this entrapped volume should be viewed as part of the porous structure. Consequently, the relative permeability ($k_{\alpha r}$) of phase α is no longer a function of its saturation (S_α), but a function of the fraction of S_α that is hydraulically connected (J Guarnaccia *et al.*, 1997b). Herein, $S_{\alpha f}$ and $S_{\alpha t}$ are defined for further discussion, where $S_{\alpha f}$ denotes the saturation of the free volume which still responds to gradient (hydraulically connected) and $S_{\alpha t}$ represents the saturation of the entrapped volume. It is obvious that $S_\alpha = S_{\alpha t} + S_{\alpha f}$ and measurement towards $S_{\alpha t}$ and $S_{\alpha f}$ is impossible. Therefore, an empirical relationship must be established in to estimate these parameters (J Guarnaccia *et al.*, 1997b).

$$S_{\alpha t} = S_{\alpha t}^{min} + (S_{\alpha r}^{*} - S_{\alpha t}^{min}) \left[\frac{S_\alpha^{max} - S_\alpha}{S_\alpha^{max} - S_{\alpha r}^{*}}\right]^e, e > 0 \qquad \text{Equation 4-16}$$

Where:

$S_{\alpha t}$ is the saturation of the entrapped fluid of phase α, which is influenced by the flow direction as to wither imbibition or drainage, and the flow history which may differ depending on the number of imbibition and drainage processes. $S_{\alpha t}$ should lie between: $S_{\alpha t}^{min} \leq S_{\alpha t} \leq S_{\alpha r}^{*}$;

$S_{\alpha t}^{min}$ is the minimal limit of the saturation of entrapped fluid of phase α, where a linear relationship is assumed between $S_{\alpha t}^{min}$ and S_α in NAPL simulator.

S_α^{max} is the maximal limit of the saturation of entrapped fluid of phase α that has occurred since it was last at immobile residual conditions;

$S^*_{\alpha r}$ is the magnitude of the residual saturation of phase α, which satisfies $0 \leq S^*_{\alpha r} \leq S_\alpha$ at the terminus of the drainage process of phase α. $S^*_{\alpha r}$ is computed using the Land model (Land, 1968); e is defined as a blending parameter which represents the speed for how fast the phase α becomes immobile during drainage, or becomes re-mobilised during imbibition. In NAPL simulator, e can be set as 1 or 0 as illustrated in Figure 4-3.

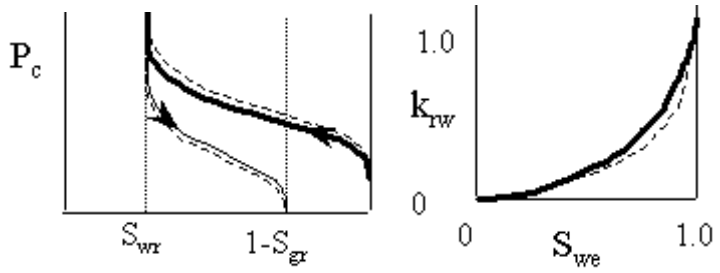

Solid curve: e=1; dashed curve: e=0

Figure 4-2 The illustration of the blending parameter extracted from Josegh Guarnaccia *et al.* (1997a)

In summary, the two-phase (i.e. the water –gas system) flow hysteresis model considering fluid entrapment and release is established. Three inputs are required by this model: S_{Wr}, S_{Gr} and e, and the remaining parameters $S^*_{\alpha r}$, $S^{min}_{\alpha t}$ and S^{max}_{α} are functions of the flow-path history (J Guarnaccia *et al.*, 1997b).

To augment this model to a three-phase system, the mechanism of entrapment and release for the intermediate wetting fluid needs to be reviewed. In a water- LNAPL- air system, water is the most wetting fluid, LNAPL is the intermediate wetting fluid, and air is the most non-wetting fluid. The entrapment mechanism of water S_W can be regarded as being displaced by non-wetting fluids S_{Tn}, where S_{Tn} stands for the sum of both S_N and S_G. It can be assumed that the magnitude of S_{Wt} will remain the same regardless of the number of non-wetting fluids. The same argument stands for S_G.and S_{Gt}. for the gaseous phase as it is the most non-wetting phase. Therefore, for the three-phase system, Equation 4-16 holds for both water and gas phase, where $\alpha = W \; and \; G$.

The mechanism for LNAPL is different thus S_{Nt} is different. It is because depending on the process and the location, LNAPL can act as a wetting phase and/or non-wetting phase. Therefore, two residual saturations for LNAPL should be introduced for LNAPL as a wetting phase S_{Nwr} or a non-wetting phase S_{Nnr} respectively. Correspondingly, the last equation for the three-phase sub-model is Equation 4-16 when $\alpha = N$, and the definition of S_{Nr} is (Fayers and Matthews, 1984):

$$S_{Nr} = S_{Nwr}\left(\frac{S_G}{S_W + S_G}\right) + S_{Nnr}\left(\frac{S_W}{S_W + S_G}\right) \qquad \text{Equation 4-17}$$

In summary, the three-phase hysteresis sub-model for entrapment and release consists of Equation 4-16 ($\alpha = W, N\ and\ G$) and Equation 4-17. Five inputs are required: S_{Wr}, S_{Gr}, S_{Nwr}, S_{Nnr} and e. The remaining nine parameters $S^*_{\alpha r}$, $S^{min}_{\alpha t}$ and S^{max}_{α} are functions of the flow-path history (J Guarnaccia *et al.*, 1997b).

4.3.3.2 Sub-model for the Saturation- Capillary pressure (P-S relationship)

Equation 4-10 has presented the interfacial tension scaling, which provides a method to augment the two-phase model into a three phase model by fitting one phase pair against the Van Genuchten model parameters α and n. By distinguishing the α during the imbibition and drainage process, which respectively are α_i, and α_d , the hysteresis can be accommodated in the P-S relationship.

In summary, in the NAPL simulator, the three-phase hysteretic P-S model requires the following input (J Guarnaccia *et al.*, 1997b):

1) The fitting parameters for hysteretic Van Genuchten model which distinguish the drainage and imbibition process: α_i, α_d and m;
2) The four fluid residual saturations including water, air, LNAPL as wetting fluid and non-wetting fluid S_{Wr}, S_{Gr}, S_{Nwr}, S_{Nnr}, and the blending parameter e for entrapment as explained above;
3) Two of the three interfacial tension parameters: σ_{NW}, σ_{GN} or σ_{GW} with the unknown calculated by $\sigma_{GW} = \sigma_{NW} + \sigma_{GN}$.

4.3.3.3 Sub-model for the Relative permeability –Saturation (K-S relationship)

Regarding the three-phase hysteretic K-S model, one assumption related to the wettability sequence needs to be confirmed that most wetting phase, the intermediate wetting phase and the most non-wetting phase preferentially fill the smallest, middle and the largest pores respectively. This assumption implies that the wetting fluid and non-wetting fluid become spatially segregated to the extent that their relative permeabilities are functions of their saturations only. Therefore, for the effective saturation of the water and air phases in the three-phase system, the definitions should be altered from Equation 4-14 to account for the presence of entrapped NAPL.

Definition 1:
$$S_{eW} \text{ or } S_{eG} = \frac{Reduced\ saturation}{Total\ \%\ pore\ volume\ available\ for\ flow} \qquad \text{Equation 4-18}$$

$$S_{eW} = \frac{S_W - S_{Wt}}{(1 - S_{Wt} - S_{Nt} - S_{Gt})}$$

$$S_{eG} = \frac{S_G - S_{Gt}}{(1 - S_{Wt} - S_{Nt} - S_{Gt})}$$

Definition 2:

$$S_{eW} \text{ or } S_{eG} = \frac{Reduced\ saturation}{Total\ \%\ pore\ volume\ available\ for \text{ phase } flow} \qquad \text{Equation 4-19}$$

$$S_{eW} = \frac{S_W - S_{Wt}}{(1 - S_{Wt})}$$

$$S_{eG} = \frac{S_G - S_{Gt}}{(1 - S_{Wt})}$$

In addition, by giving the K-S equation for the intermediate phase, which is LNAPL in this case, the three-phase hysteretic K-S model is completed (R. Lenhard and Parker, 1987).

$$k_r^N(S_W, S_G) = (S_{eN})^{\varphi}\left\{[1 - (1 - S_{eTn}^{1/m})^m]^2 - [1 - (1 - S_{eTw}^{1/m})^m]^2\right\} \qquad \text{Equation 4-20}$$

Where

$m = 1 - 1/n$, the fitting parameter for the Van Genuchten model.

S_{eN} is the effective saturation of LNAPL defined by amending Equation 4-14, which is introduced below;

φ is the pore connectivity parameter;

S_{eTn} is the effective total non-wetting phase saturation, and S_{eTw} is the effective total wetting phase saturation. Each has three admissible definitions depending on the process which are defined as follows. The trapped quantities in the following equations are computed from Equation 4-16.

Definitions of S_{eN}:

Definition 1:

$$S_{eN} = \frac{Reduced\ saturation}{Total\ \%\ pore\ volume\ available\ for\ flow} \qquad \text{Equation 4-21}$$

$$S_{eN} = \frac{S_N - S_{Nt}}{(1 - S_{Wt} - S_{Nt} - S_{Gt})}$$

Definition 2:

$$S_{eN} = \frac{Reduced\ saturation}{Total\ \%\ pore\ volume\ available\ for \text{ NAPL } flow} \qquad \text{Equation 4-22}$$

$$S_{eN} = \frac{S_N - S_{Nt}}{(1 - S_{Nt})}$$

Definitions of S_{eTn}:

Definition 1:

$$S_{eTn} = \frac{Reduced\ saturation}{Total\ \%\ pore\ volume\ available\ for\ flow}$$

$$S_{eTn} = \frac{S_N + S_G - S_{Nt} - S_{Gt}}{(1 - S_{Wt} - S_{Nt} - S_{Gt})} \quad \text{Equation 4-23}$$

Definition 2:

$$S_{eTn} = \frac{Reduced\ saturation}{Total\ \%\ pore\ volume\ available\ for\ LNAPL\ and\ gas\ flow}$$

$$S_{eTn} = \frac{S_N + S_G - S_{Nt} - S_{Gt}}{(1 - S_{Nt} - S_{Gt})} \quad \text{Equation 4-24}$$

Definition 3

$$S_{eTn} = \frac{Reduced\ saturation}{Total\ \%\ pore\ volume\ available\ for\ LNAPL\ flow}$$

$$S_{eTn} = \frac{S_N + S_G - S_{Nt} - S_{Gt}}{(1 - S_{Nt})} \quad \text{Equation 4-25}$$

Definitions of S_{eTw}:

Definition 1:

$$S_{eTw} = \frac{Reduced\ saturation}{Total\ \%\ pore\ volume\ available\ for\ flow}$$

$$S_{eTw} = \frac{S_W + S_N - S_{Wt} - S_{Nt}}{(1 - S_{Wt} - S_{Nt} - S_{Gt})} \quad \text{Equation 4-26}$$

Definition 2:

$$S_{eTw} = \frac{Reduced\ saturation}{Total\ \%\ pore\ volume\ available\ for\ \text{LNAPL and water}}$$

$$S_{eTw} = \frac{S_W + S_N - S_{Wt} - S_{Nt}}{(1 - S_{Wt} - S_{Nt})} \quad \text{Equation 4-27}$$

Definition 3

$$S_{eTw} = \frac{Reduced\ saturation}{Total\ \%\ pore\ volume\ available\ for\ LNAPL\ flow}$$

$$S_{eTw} = \frac{S_W + S_N - S_{Nt}}{(1 - S_{Nt})} \quad \text{Equation 4-28}$$

In NAPL simulator, the definitions of these effective saturations and total effective saturations can be manually chosen via setting flags. The flags and corresponding equations used are tabulated in

. For each flag, the value can be set once during one modelling.

Table 4-1 The effective saturation flags and corresponding equations

Phase	Flag name	Flag value	Equation used
Water phase	nsew1	1	$S_{eW} = \frac{S_W - S_{Wt}}{(1 - S_{Wt} - S_{Nt} - S_{Gt})}$
	nsew1	2	$S_{eW} = \frac{S_W - S_{Wt}}{(1 - S_{Wt})}$
Gaseous phase	nseg1	1	$S_{eG} = \frac{S_G - S_{Gt}}{(1 - S_{Wt} - S_{Nt} - S_{Gt})}$
	nseg1	2	$S_{eG} = \frac{S_G - S_{Gt}}{(1 - S_{Wt})}$
NAPL phase	nsen1	1	$S_{eN} = \frac{S_N - S_{Nt}}{(1 - S_{Wt} - S_{Nt} - S_{Gt})}$
	nsen1	2	$S_{eN} = \frac{S_N - S_{Nt}}{(1 - S_{Nt})}$
	nsen2	1	$S_{eTn} = \frac{S_N + S_G - S_{Nt} - S_{Gt}}{(1 - S_{Wt} - S_{Nt} - S_{Gt})}$
	nsen2	2	$S_{eTn} = \frac{S_N + S_G - S_{Nt} - S_{Gt}}{(1 - S_{Nt} - S_{Gt})}$
	nsen2	3	$S_{eTn} = \frac{S_N + S_G - S_{Nt} - S_{Gt}}{(1 - S_{Nt})}$
	nsen3	1	$S_{eTw} = \frac{S_W + S_N - S_{Wt} - S_{Nt}}{(1 - S_{Wt} - S_{Nt} - S_{Gt})}$
	nsen3	2	$S_{eTw} = \frac{S_W + S_N - S_{Wt} - S_{Nt}}{(1 - S_{Wt} - S_{Nt})}$
	nsen3	3	$S_{eTw} = \frac{S_W + S_N - S_{Nt}}{(1 - S_{Nt})}$

In summary, the P-S model is made accountable for the hysteresis phenomenon and augmented to adapt a three-phase flow system. The input parameters include the model fitting parameter m and pore connectivity parameters ζ, φ and ξ for water, LNAPL and air respectively (J Guarnaccia *et al.*, 1997b).

Therefore, a hysteretic three-phase *K-S-P* model that applies Van Genuchten model as fitting method is finalised.

4.4 Improvements of the modelling code

The NAPL simulator consists of a set of modelling programs written in FORTRAN, which can be compiled into a Windows executable program, and an Excel pre-processor (the 2-D version is named 2D.xls) to organize model inputs and outputs, which include modelling physics and parameters, initial

and boundary conditions, and some outputs. The modelling input are stored in a set of files with the extension name of .in. The modelling outputs are gathered in two groups of files: the restart files (.rs) and the output files (.out), which reserve the solutions of every calculated time-step. The pre-processor is also embedded with a screen output function which can generate the water and NAPL saturation profiles of the last calculated event.

The procedure of using the NAPL simulator is explained as follows.

1) Compile the executable program when model physics is altered.
2) Input initial and boundary conditions as well as modelling parameters via the Excel pre-processors (several spreadsheets in 2D.xls) and generate a batch of input files (.in) via embedded vba micro.
3) Start the modelling by running the executable program compiled in Step 1. The modelling runs in DOS window.
4) Simulation finishes with a set of output files generated.
5) Extract and generate the saturation profiles of the last calculated event via the Excel pre-processor.

Limitations were found during the trial modelling. Firstly, it was inconvenient and time-consuming to operate NAPL simulator without a user friendly button-based UI, which can be easily programmed with Visual Basic Application (VBA) at the backstage of Microsoft Excel. Secondly, the visual output of NAPL simulator only contained the saturation profile of the last calculated event, where, in this study, illustrated outputs for up to hundreds of crucial moments were expected to be generated. Thirdly and most importantly, the modelling parameters and initial and boundary conditions became fixed once the modelling started to run. However, to simulate transient water table fluctuation, the initial and boundary conditions along with some parameters had to be altered for every time slice. Therefore, modifications and improvements for the NAPL simulator should be achieved to realize the modelling of transient water table conditions over time and to improve the user experience and output functionality.

4.4.1 Model illustrated output

A MATLAB program was developed to improve the model output functions, which is capable of batch processing the visualization of the results of all modelling moments. The extended model output include:

1) Reorganize the date format of the saturation output file that records the results for all

calculation moments into a batch of readable files to for MATLAB to import.

2) Based on the model dimension and gridding system, generate contours of the saturations of water, LNAPL and air automatically from the model saturation output file.
3) By calculating the average saturation of each row, generate profiles of the average saturations of water, LNAPL and air.
4) Read the corresponding experimental datasets and superimpose the experimental saturation profiles onto the modelling profiles.

The result examples will be presented in comparison with the experimental results in Chapter 4.

4.4.2 Implementing transient initial and boundary conditions

A VBA program was developed to enable transient initial and boundary conditions and corresponding parameters. The principle is to create an external time step, which uses one entire modelling process introduced earlier as one stress period during the fluctuation modelling, which is equivalent to the photography interval in laboratory experiments. Specifically, for each stress period of the water table fluctuation modelling, the program automatically changes the conditions and parameters needed to be altered, which in this case are the water tables and corresponding time parameters, followed by generating new input files for the current stress period. Afterwards, the program runs the executable program to start the modelling via Windows Shell Service until the modelling finishes with output and restart files generated, which are immediately prepared and saved in the format for the MATLAB result visualization. In this way, the program repeats the condition updating and calculation of the next stress period until reaching the modelling destination.

4.4.3 Model UI

A command-button-based UI was developed to control a set of customized VBA scripts and Windows DOS commands (.bat) to improve operational efficiency of the NAPL simulator (Figure 4-3). The UI integrates commonly used functions during modelling, which include: to calculate node system for boundary condition inputs, to generate input files for the modelling, to initiate the modelling by running the executable, to reorganize data format for result visualization, to copy, delete and transfer specific type of modelling files and results, etc.

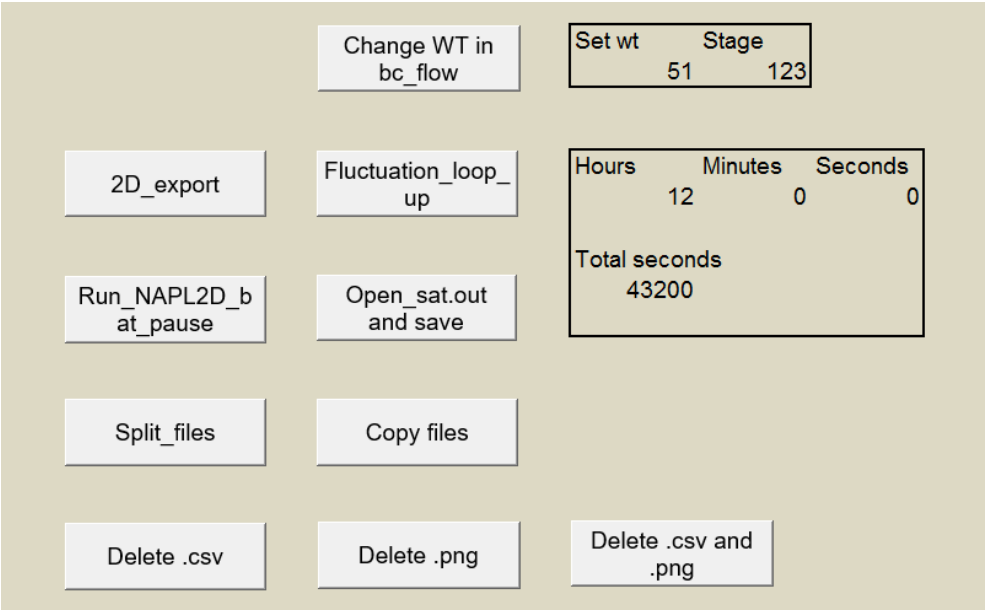

Figure 4-3 The customized UI for the NAPL simulator

The setup of the numerical model and the modelling results will be introduced in Chapter 5.

4.5 Summary

This chapter presented the modelling approach used based on the use of the US-EPA NAPL Simulator software. Primary governing equations, including the mass balance equations and constitutive relations along with assumptions used in the NAPL simulator were summarised. The three-phase hysteretic K-S-P model was constituted upon an augmentation of the two-phase non-hysteretic sub-models. Secondly, the modelling code was enhanced by the development of a GUI, the visualization of modelling outcomes including the generation of contours and comparative averaging profiles, and the realization of the transient boundary/initial condition specifically for the simulation of the water table fluctuation period. Lastly, a numerical model was constructed which was expected to accommodate the modelling for both the LNAPL release period and the water table fluctuation period. However, the physical dimension, initial and boundary conditions and model parameters will be demonstrated in Chapter 5 along with the modelling results.

References

Bear, J., and Cheng, A. H.-D. (2010). *Modeling groundwater flow and contaminant transport* (Vol. 23): Springer Science & Business Media.

Fayers, F., and Matthews, J. (1984). Evaluation of normalized Stone's methods for estimating three-phase relative permeabilities. *Society of Petroleum Engineers Journal, 24*(02), 224-232.

Guarnaccia, J., Pinder, G., and Fishman, M. (1997a). NAPL: Simulator documentation: U.S. Environmental Protection Agency.

Guarnaccia, J., Pinder, G., and Fishman, M. (1997b). *NAPL: Simulator documentation*: National Risk Management Research Laboratory, United States Environmental Protection Agency, Research and Development.

Land, C. S. (1968). Calculation of imbibition relative permeability for two-and three-phase flow from rock properties. *Society of Petroleum Engineers Journal, 8*(02), 149-156.

Lenhard, R., and Parker, J. (1987). A model for hysteretic constitutive relations governing multiphase flow: 2. Permeability-saturation relations. *Water Resources Research, 23*(12), 2197-2206.

Lenhard, R. J., Parker, J. C., and Kaluarachchi, J. J. (1989). A model for hysteretic constitutive relations governing multiphase flow: 3. Refinements and numerical simulations. *Water Resources Research, 25*(7), 1727-1736. doi: 10.1029/WR025i007p01727

5 Results and discussions 1: the base case scenario

This chapter presents the experimental and modelling result of the base case scenario (Run4T3), which is designed to reveal the behaviours of water, LNAPL and air in a homogenous medium sand aquifer under transient water table oscillations.

This chapter includes the experimental results showing the dynamics of multiphase flow (water, LNAPL and air) saturation distributions during the LNAPL release upon a static water table, and during five cycles of water table oscillations, where the single cycle pattern and inter-cycle evolution re observed and analysed. The results of numerical simulations of both the LNAPL release period and the first cycle of water table fluctuation period are also presented in comparison with the experimental results. Therefore, this chapter has to start with the setup and calibration of the numerical model.

The experiment provides a baseline set of data that the later, more complex scenarios (Chapter 4) may be benchmarked or compared with. To visually and quantitatively demonstrate water-LNAPL-air dynamics, the experimental results are presented using via a selection of figure sequences with commentaries, which includes snapshots, contoured fluid saturation distributions, and profiled fluid saturation distributions as the experimental interpretation (profile data refer to Appendices A.2.1.1). Moreover, the experimental results for every photographic event were compiled in short videos which captured full dynamics of fluid migration and distribution (Appendices A.2.1.2).

It is noteworthy that these are the first NAPL laboratory-scale experiments with automated water level control, automated photography and image analysis realised. As such they allow significant advance in: the complexity of experimental scenarios; duration and frequency of monitoring; and the accuracy and efficiency in data collection and interpretation. This may enable new insights in the detailed, quantitative dynamics of the LNAPL-water-air distributions.

Main observations were constructed to show the division of flow domain into three characteristic zones: the unsaturated zone (often referred as the vadose zone), the capillary zone, and the saturated zone. Some ambiguity is evident in the definition of zones in shallow aquifer, where the unsaturated zone is defined as the area between groundwater table and ground surface, thus capillary zone is sometimes considered as the lower section within the unsaturated zone (USGS, 2016). However, in LNAPL migration studies, significant differences in the hydrogeological characteristics are often

observed between the capillary zone and the under-saturated area above. Therefore, to accurately characterize the features and the subsequent processes above the water table, in this study, the unsaturated zone refers to the under-saturated area between the top of capillary fringe and the ground surface (i.e. the upper boundary of the sand tank aquifer) (Freeze and Cherry, 1979).

5.1 Setup and calibration of the numerical model

The aim of this section is to numerically describe the transport and distribution of water-LNAPL-air three-phase flow in porous media during a constant LNAPL release under the static water table condition and the corresponding water table fluctuation condition. The model to build is also expected to theoretically verify the experimental data.

The model was built by applying the modelling theory explained in Section 4.3. The modelling for the LNAPL release period was performed with the NAPL simulator 2-D mode, while the modelling for the water table fluctuation period was performed in the 1-D mode, which was restrained by the computational resources that was insufficient to support the realization of 2-D numerical modelling within a reasonable timeframe. It was intended that the modelling setup should be as similar as the experimental setup (including the physical dimension, time dimension, initial and boundary conditions, and model parameters), however small adjustments had to be made to comply with the modelling code.

5.1.1 Physical dimension

5.1.1.1 Model domain for the LNAPL release period

The dimension of the flow domain was 80cm x 30cm x 1.6cm, which was divided into 80 x 30 x 1 elements in the x, y and z dimensions (one cubic element was 1cm x 1cm x 1.6cm) and a total of 2511 nodes. Node 1 to Node 81 represented the top boundary and Node 2481 to Node 2511 represented the bottom boundary. Since LNAPL was released via a 3cm long release box located in the middle of the top boundary, the source zone should be represented by the nodes in the top row, which was also imposed with a boundary condition. However, the NAPL simulator did not allow the confusion caused by using the same nodes to define both boundary condition and source zone. Therefore, node 45~48 within the second row from the top boundary was allocated to represent the LNAPL source.

It should be mentioned that two other different grid sizes have been attempted during the trial modelling, which respectively are: 160 x 60 x 1 and 40 x 15 x 1. Both grid sizes were able to provide

reasonable modelling result that were similar to the grid size selected (80 x 30 x1). However the coarse grid size, despite providing a shorter modelling timeframe, gave a slightly lower resolution in the 2-D contours. And the modelling timeframe was not desirable for the fine grid size. The dimension of the model has always been conducted as 2-D.

5.1.1.2 Model domain for the water table fluctuation period

The flow domain was also 80cm x 30cm x 1.6cm, which was divided into 80 x 1 x 1 elements in the x, y and z dimensions (one cubic element was 1cm x 30cm x 1.6cm) and a total of 156 nodes. Node 1 to Node 2 represented the top boundary and Node 161 to Node 162 represented the bottom boundary.

5.1.2 Initial and boundary conditions

5.1.2.1 Initial condition

The simulation for the LNAPL release period consists of three stages: Stage 1 reproduces the water drainage starting from 100% water saturated aquifer; Stage 2 represents the LNAPL release period; and Stage 3 is the settling down period of after LNAPL being released.

The simulation for the water table fluctuation period consists of only one stage, which is set to start from the end of the settling down period of the LNAPL release (T=19800s) and to finish after five cycles of water table oscillations of 60 hours (T=235800s).

5.1.2.2 Boundary condition

The left and right sides of the flow domain are both set to be no-flow boundaries throughout the simulation. The top boundary remains a constant air head boundary, where h_g=0 remains constant throughout the entire simulation. During the LNAPL release period, the bottom boundary is set as a constant water head boundary with a head value that equals to corresponding to the oscillation centre. During the water table fluctuation period, the water table is oscillated by changing the bottom boundary condition at each calculated stress period, the length of which is set to be equal to the experimental photographic interval of 1800s. This automatic setup and iteration of the transient boundary conditions is realized by the customized VBA code introduced in Section 4.4.2, which creates an external time control that uses one original modelling as a time segment in the modelling so that the conditions and parameters are amendable for each stress period. At the beginning of each calculated stress period, a new boundary condition is imposed and the initial condition for this stress period is imported from the result of the previous stress period. It should be mentioned that during the simulation, the water table cannot be changed within on stress period, while during the laboratory

experiment the water table was gradually changed. Therefore, the shape of the simulated water table remains a zigzag sine curve, while the shape of the experimental water table appears as a smooth sine curve

5.1.3 Model calibration and parameters

Parameters applied in the model simulation are listed in Table 5-1, which have been applied for the modelling of both release and fluctuation stages. The parameters include the model spatial and temporal dimensions, the properties of the simulated aquifer, the physical and chemical properties of the fluids, and fitting parameters for the three-phase hysteretic K-S-P model. The parameters can be categorised into five types based on sources: directly measured from physical experiments (MP), indirectly measured from experimental results (IM), obtained from manufacture specifications (SPEC), standard values (STD), and model calibrated best-fit values (CAL). The standard values are obtained from Wikipedia.

Table 5-1 List of model parameters

Parameters	**Symbols**	**Value and unit (as used in NAPL simulator input)**
Number of elements in the X,Y,Z dimensions	*nex, ney, nez*	80 x 30 x 1
Size of element	-	1cm x 1cm x 1.6 cm
Simulation time (NAPL release)	*T*	Stage 1: 12000s Stage 2: 16200s Stage 3: 19800s
Simulation time (fluctuation)	*T*	Stage 1: 235800s
Gravity magnitude	*g*	980.616 $cm \cdot s^{-2}$ (STD)
Intrinsic permeability	κ	9.21 E-07 cm^{-2} (MP)
Soil bulk density	*bulkb*	1.6536 $g \cdot cm^{-3}$(SPEC) (Aggregate-Industries, 2012)
Soil porosity	ε	0.376 (MP)
Kinematic viscosity of water	μ_W	0.01 $cm^2 \cdot s^{-1}$ (STD)(Wikipedia, 2016c)
Kinematic viscosity of LNAPL	μ_N	0.0253 $cm^2 \cdot s^{-1}$(SPEC)(Morris-Lubricants, 2012)
Kinematic viscosity of air	μ_G	0.0002 $cm^2 \cdot s^{-1}$ (STD)(Wikipedia, 2016c)
Density of water	ρ_W	0.9982 $g \cdot cm^{-3}$ (STD)(Wikipedia, 2016a)

Parameters	Symbols	Value and unit (as used in NAPL simulator input)
Density of LNAPL	ρ_W	0.815 g·cm^{-3} (SPEC)(Morris-Lubricants, 2012)
Density of air	ρ_G	0.0015 g·cm^{-3} (STD)(Wikipedia, 2016a)
Interfacial tension air-water	σ_{GW}	72.75 mN·m^{-1} (STD)(Wikipedia, 2016b)
Interfacial tension LNAPL-water	σ_{NW}	29.5 mN·m^{-1} (SPEC) (Aztec-Oils-Limited, 2014)
Interfacial tension air-LNAPL	σ_{GN}	41.7 mN·m^{-1} (SPEC)(Aztec-Oils-Limited, 2014)
Residual water saturation	S_{Wr}	0.16 (IM)
Residual LNAPL saturation as a non-wetting phase	S_{Nwr}	0.08 (IM)
Residual LNAPL saturation as wetting phase	S_{Nnr}	0.06 (IM)
Residual air saturation	S_{Gr}	0.09 (IM)
van Genuchten imbibition α	α_i	0.13 cm^{-1} (CAL)
van Genuchten drainage α	α_d	0.11 cm^{-1} (CAL)
van Genuchten *n*	*n*	10.0 (CAL)
Connectivity parameters for water, NAPL and air respectively	ζ, φ, ξ	0.5, 0.4, 0.3 (CAL)
Flag that determines S_{eW}	nsew1	1 (CAL)
Flag that determines S_{eN}	nsen1	1 (CAL)
Flag that determines S_{eTn}	nsen2	3 (CAL)
Flag that determines S_{eTw}	nsen3	3 (CAL)
Flag that determines S_{eG}	nsew1	1 (CAL)
Blending parameter	*e*	1 (linear) (CAL)

Explanations of the parameters and model calibrations are as follows.

As mentioned before, the model element size (grid size) was decided based on the reasonability and resolution of the trial modelling result and computational capacity of computers used after 3 different attempts. The simulation time for the fluctuation period was set to start from the end of the LNAPL release settling down period and was set to finish after 60 hours of fluctuation experiments. However, the model stoped to converge around 65000s which was the beginning of the second oscillation.

The following values are derived from standard values: Gravity magnitude, Kinematic viscosity of water and air, density of water and air, interfacial tension of air and water. The following values are obtained from manufacture specifications, where units may have been converted: Soil bulk density, kinematic viscosity of LNAPL, density of LNAPL, interfacial tension between LNAPL and water and air and LNAPL. The intrinsic permeability is derived from the hydraulic conductivity measurement conducted in Section 2.2.2.3 (Hudak, 2004), where porosity was also measured.

The following four residual saturation values are indirectly measured from the experimental results of the base case scenario including a selection of 2-D contours and 1-D profiles: residual water saturation, residual LNAPL saturation as a wetting-phase, residual LNAPL saturation as a non-wetting-phase and residual air saturation. Specifically, the residual water saturation was estimated from the water drainage; LNAPL residual saturation as a wetting-phase was estimated from the LNAPL release period and confirmed with the water table lowering down during the fluctuation period; LNAPL residual saturation as a wetting-phase and residual air saturation were estimated from the water table rising up during the fluctuation period. A calibration was undertaken for these four residual saturations, where the current values were moderately adjusted accordlingly. Once calibrated, these parameters are used in all following simulations that do not need recalibration.

The van Genuchten parameters were carefully calibrated to fit the 1-D profiles harvested from the LNAPL release period. Once calibrated, these parameters are used in all following simulations that do not need recalibration.

Connectivity parameters for water, LNAPL and air were initially decided upon values recommended in previous literature, which have been explained in Section 4.3.2.2. The values were kept after the calibration. A sensitivity analysis was conducted which indicated that the connectivity parameters are among the insensitive parameters in the overall LNAPL distribution. Whereas, the permeability, the residual saturations of different phases and the van Genuchten parameters are the most effective parameters that affect the LNAPL distribution.

The flags that determine different effective saturation equations and the blending parameter were chosen based on the recommendation by the NAPL simulator documentation.

5.2 Results and discussions of the pre LNAPL release period

As introduced in 3.2.1, prior to the LNAPL release, the water table was gradually brought down to the prescribed water table oscillation centre from the fully water saturated condition. Therefore, a water drainage curve in a water-air two-phase system was observed experimentally and simulated by the numerical model introduced in Chapter 4, which uses a three-phase hysteretic model and applies the Van Genuchten relationship. The input parameters of the model have been shown in Table 5-1, where the Van Genuchten parameters are determined by fitting the base case experimental profile data of the pre-release and release periods. These parameters are used in all following simulations with no recalibration.

The modelling result of the pre LNAPL release period is illustrated in Figure 5-1(a), where the modelling profiles are compared with experimental profiles. Noticeably, the first node from the top of the experimental water profile appears abnormal, which is associated with an incidental light reflection on the top right corner of the tank. Accordingly, the experimental air profile, obtained from the volume balance, appears abnormal as well. The photographic records (e.g. Figure 5-2 (a,b,d)) have confirmed the assumption that the light reflection on the top right corner was recognized as water content by the image analysis, thus, resulting the water and air profile abnormality at the first node.

In general, the modelling profiles are in good agreement with the experimental profiles which indicates that the Van Genuchten fitting is appropriate (Figure 5-1(a)). The Van Genuchten fitted curves have provided good representations of the key features of the experimental result, especially the residual water saturation, fluid distribution in the upper unsaturated zone, capillary zone and saturated zone. In the upper unsaturated zone, the experimental water and air curves appear slightly dispersed due to local heterogeneity, whereas the modelling curves, although seemingly smoother, indeed capture the main feature of this process.

Small discrepancies are found in the capillary zone and the lower unsaturated zone (Figure 5-1(a)). The difference in the capillary zone (Z=53~60cm), where an LNAPL saturation of less than 0.005 is observed in the modelling curve that should be zero and a water saturation of 0.96 is observed that should be 1.00, is owing to the artifact in the image analysis. The difference in the lower unsaturated zone, where the experimental curve appears sharper than the modelling curve, is due to the limitation of the Van Genuchten relationship in the NAPL simulator. To achieve a shaper front via Van Genuchten fitting, the current grid size is not fine enough to facilitate model convergence, whereas the realisation of a finer grid is restrained by computational resource.

Figure 5-1 (b) presents the simulated contours of the saturation distributions of water, LNAPL and air at the end of the water drainage, which is compared with the experimental result of the moment prior to the LNAPL release illustrated in Figure 5-2 (b,c,d). As it is impossible to achieve an idealized homogeneous sand packing, the 2-D water distribution in the experimental result appeared to be dispersed. Accordingly, the air distribution appears uneven as well. However, the simulated residual saturation of water presents good match with the experimental water residual saturation, which confirms that the model parameters are reasonable.

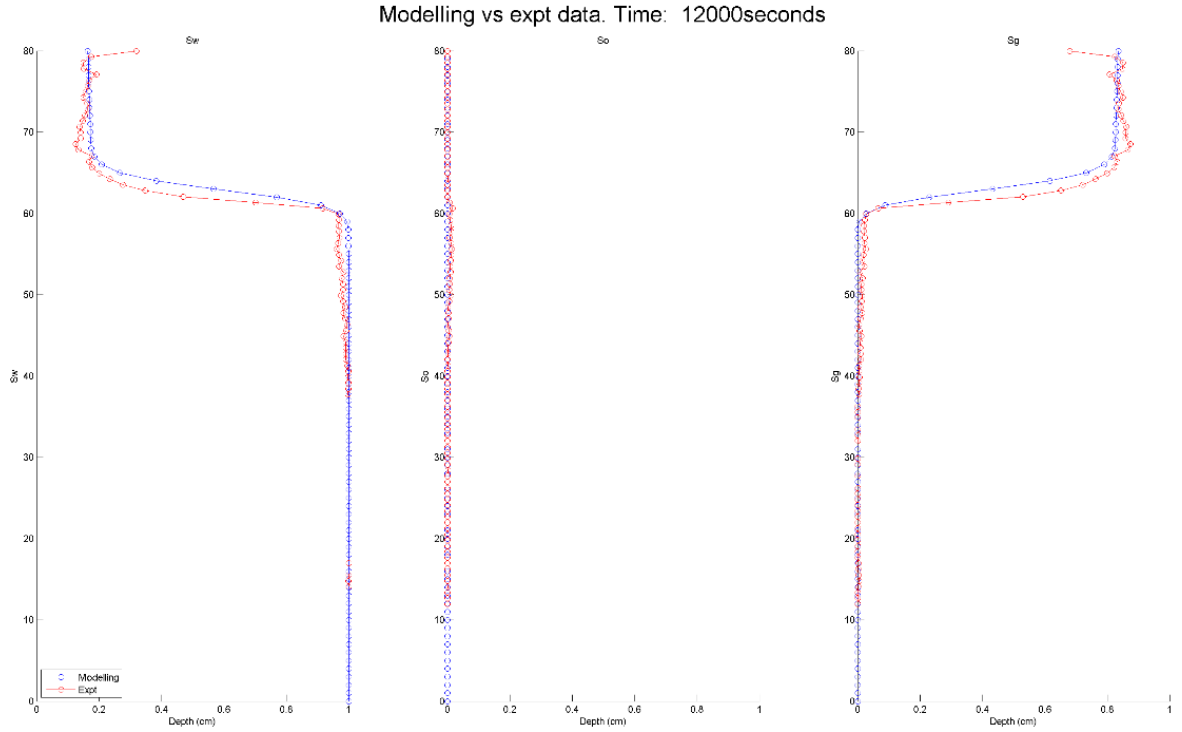

(a) Comparison of the fluid distributions during the water drainage process between experimental result (in red) and modelling result (in blue), where the water saturation curve is located on the left, LNAPL in the middle and air on the right

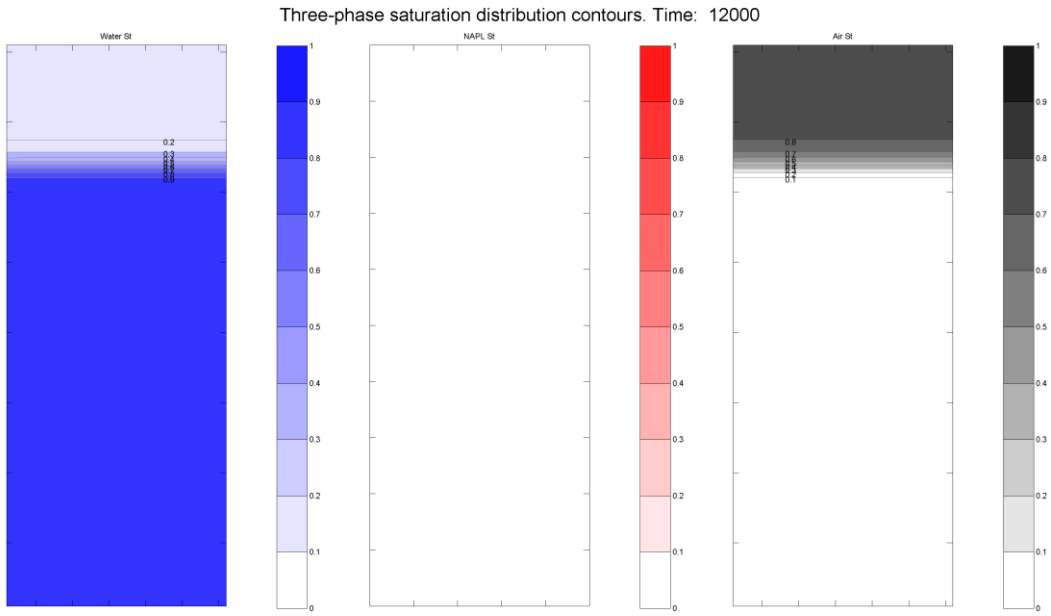

(b) Simulated contours of the fluid saturation distributions at the end of the water drainage process (In comparison with Figure 5-2)

Figure 5-1 Modelling result of the water drainage process prior to the LNAPL release period

The next section presents the result of the LNAPL release period, where the modelling results are introduced in the end (Section 5.3.4). The Van Genuchten parameters and the residual water saturation value determined at the pre-release period will be used predictively to model LNAPL release period and water table oscillation experiments without recalibration.

5.3 Results and discussions of the LNAPL release period

Following the water-air two-phase equilibrium state achieved prior to the LNAPL release, the LNAPL release commenced at time T=0 min and was terminated at T=70 min. LNAPL was then left to redistribute until reaching its equilibrium state. The monitoring of this settling down period post-release terminated at T=110 min. Different perspectives of the same process are presented in the following group of figures: Figure 5-2 to Figure 5-13 are a group of compilations illustrating the full process of the LNAPL release period. Each group contains five figures. From left to right, Figure (a)s present the photographic records of the LNAPL release at different photographic event. Figure (b)s, (c)s and (d)s, illustrate the behaviour of each fluid phase (water, LNAPL and air respectively) of the same process in the form of contours otherwise unnoticeable on photographs. The contours are interpretations of the experimental result via the image processing developed in Section 2.4 Figure (e)s are the combined fluid profiles (water-LNAPL-air) shaded with fluid saturations (occupancy in pore

space). The contours, computed from the image analysis, not only depict the process advancing in time, in both separate phases and integrated view, but also characterise and quantify the process, which include parameters such as: the residual saturations of multiphase flow (water-LNAPL- air), the velocity of the LNAPL front, the maximum and minimum LNAPL saturations and volumes in different characteristic zones, the air entrapment volumes, the height of the capillary zone, etc. Figure 5-14, Figure 5-15 and Figure 5-16 present the time-dependent dynamics of each fluid phase in the form of 1-D vertical saturation profiles, which are generated to visualise, characterise and quantify vertical distributions and interactions among fluids. In addition, for the visualisation of the complete process of LNAPL release in video format, refer to the Appendices A.2.1.2 (1), and for the raw dataset of profiles refer to the Appendices A.2.1.1 (1).

Key observations are summarised below and expanded upon in the following discussion with reference to the figures.

- During the LNAPL release upon a static water table, the body, radiating from the source zone, predominantly extended vertically, following by a significant horizontal spreading after reaching the capillary zone, and accumulating thickness upon. The shape of the developed body resembled a Mexican sombrero.
- The migration of LNAPL body became progressively sensitive to the ambient heterogeneity as the LNAPL release proceeded, where fingering and discrete blobs tended to form and grow dramatically during the late stage of LNAPL release or shortly after the LNAPL release.
- LNAPL may intrude the capillary zone and occasionally penetrate the water table, depending on the release history and the ambient aquifer geology.
- Residual water saturation in the unsaturated zone remained steady with a small decrease observed after the original water-air two-phase system being replaced by the water-LNAPL-air three-phase system. The rate of water displacement by LNAPL mainly depended on the LNAPL pressure head after LNAPL invaded the capillary fringe.
- Air could be entrapped within the capillary zone and/or the saturated zone during the LNAPL release. A recovery process of air saturation in the unsaturated zone was observed due to the LNAPL pressure change and displacement between LNAPL and air.

Taking Figure 5-2 as an example of all follow-up compilations in Chapter 4, to note that the scale of the photographic record (a), the scale of contours(b,c,d), and the scale of the profile (e) are slightly different. The scale among the three contours is consistent. The scale bars locate on the right-hand

side of each contour are the scale of fluid saturations from 0.0~1.0. Due to that during the LNAPL release period, the water table within the sand tank was raised up by LNAPL intrusion, the water tables are immeasurable and thus not showing in the figures. The tank elevation is plotted on the left y-axis in the profile (e), where the water table saturation axis is located at the bottom x-axis and the LNAPL uses the top x-axis.

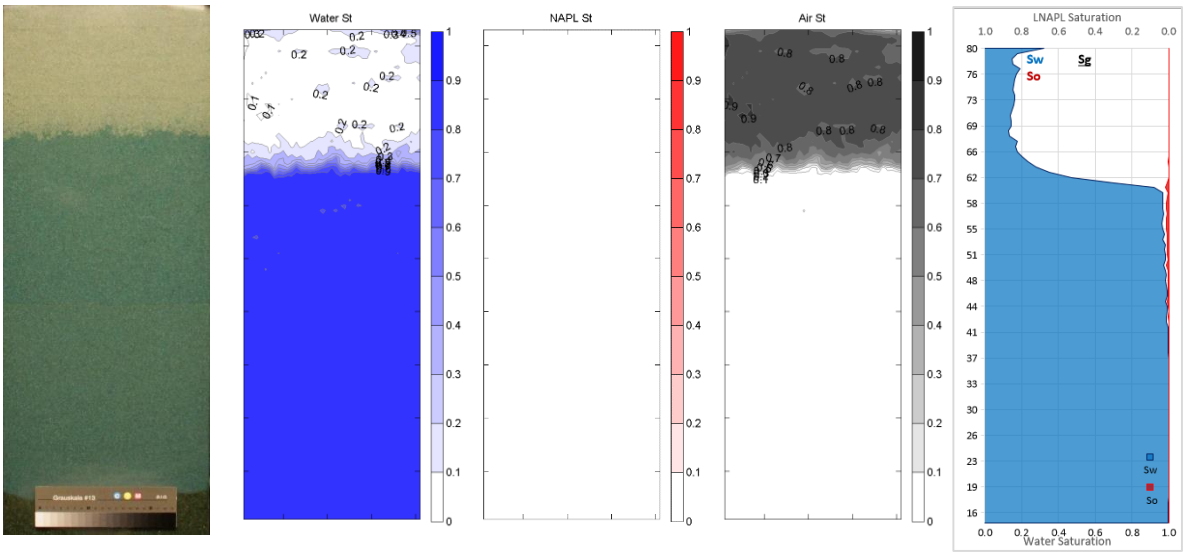

(a) (b) (c) (d) (e)

Figure 5-2 Compilation of photographic record, fluid saturation contours (water in blue, LNAPL in red, and air in grey respectively) and combined vertical saturation profiles of the LNAPL release period at T=0 min

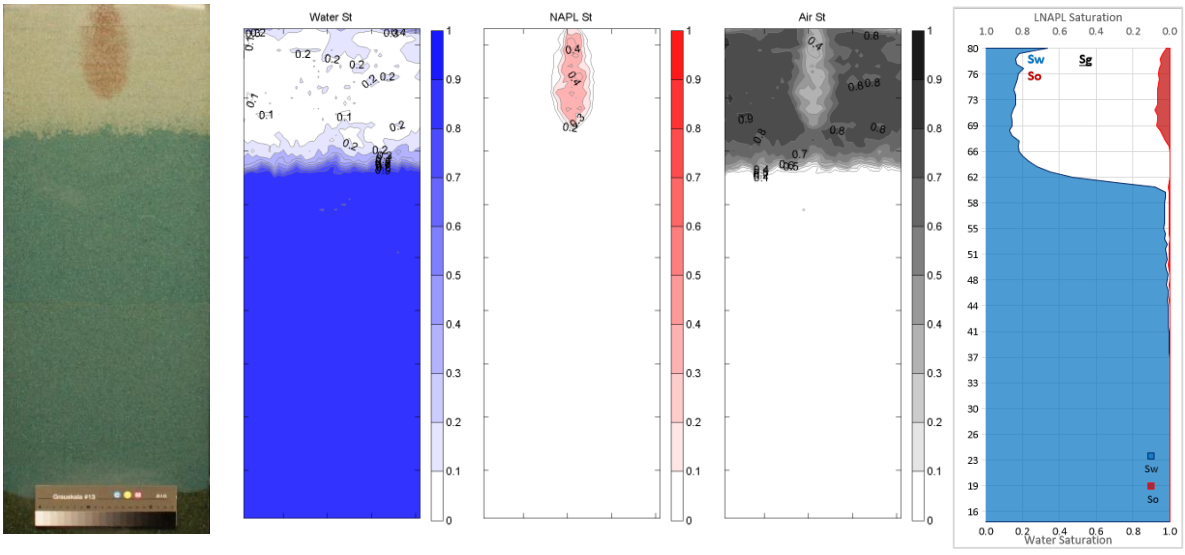

Figure 5-3 Compilation of photographic record, fluid saturation contours and combined vertical saturation profiles of the LNAPL release period at T=10 min

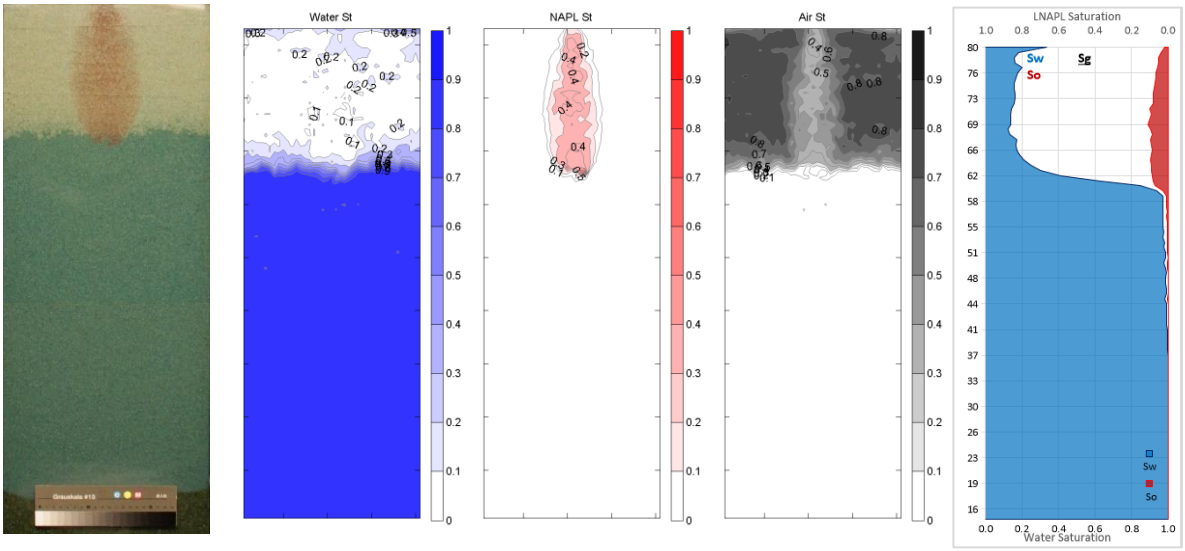

Figure 5-4 Compilation of photographic record, fluid saturation contours and combined vertical saturation profiles of the LNAPL release period at T=20 min

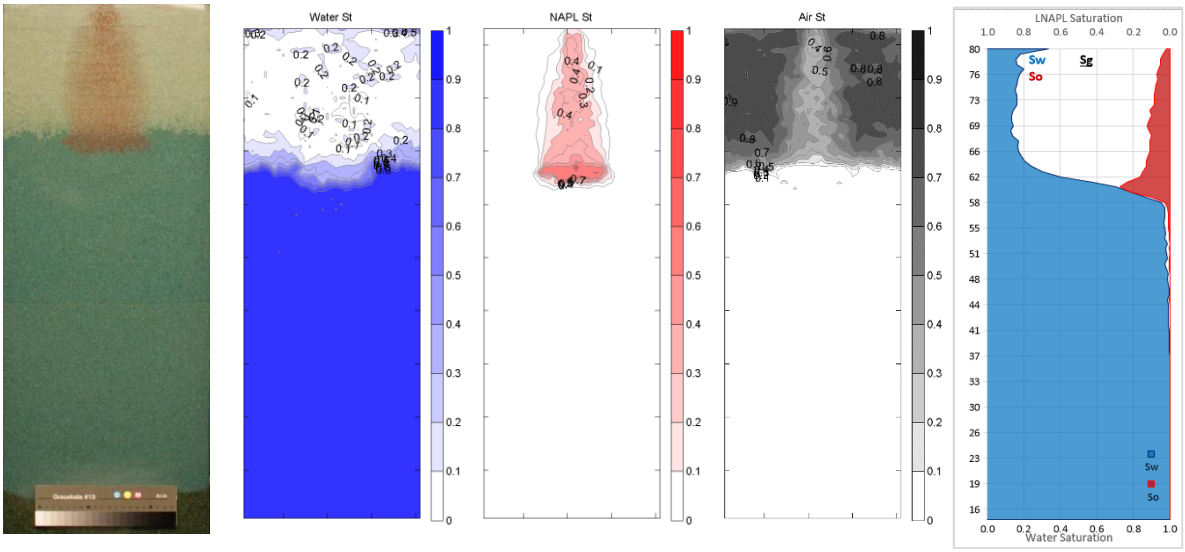

Figure 5-5 Compilation of photographic record, fluid saturation contours and combined vertical saturation profiles of the LNAPL release period at T=30 min

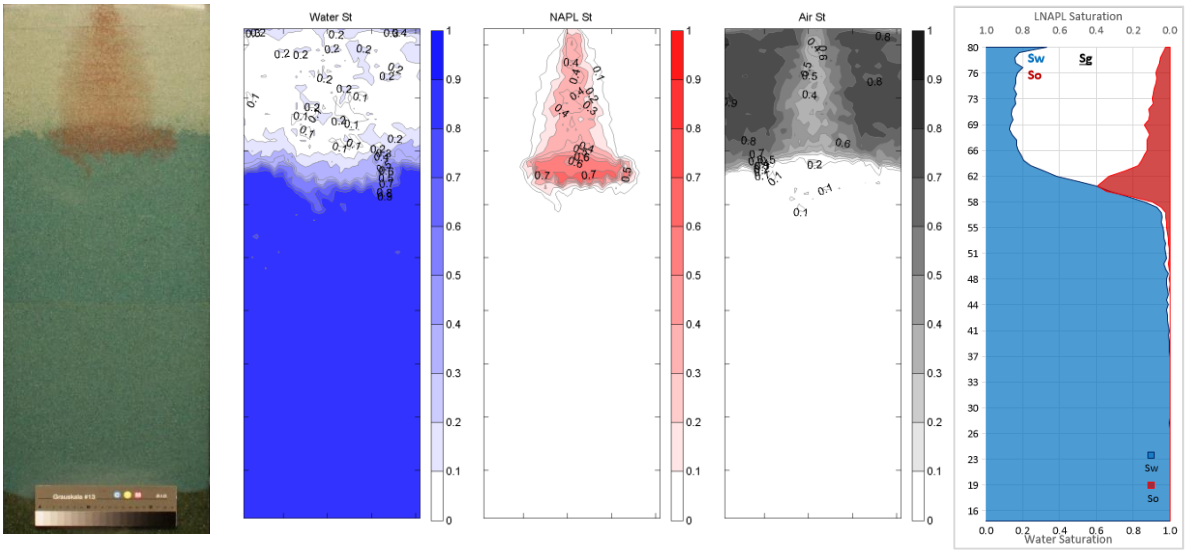

Figure 5-6 Compilation of photographic record, fluid saturation contours and combined vertical saturation profiles of the LNAPL release period at T=40 min

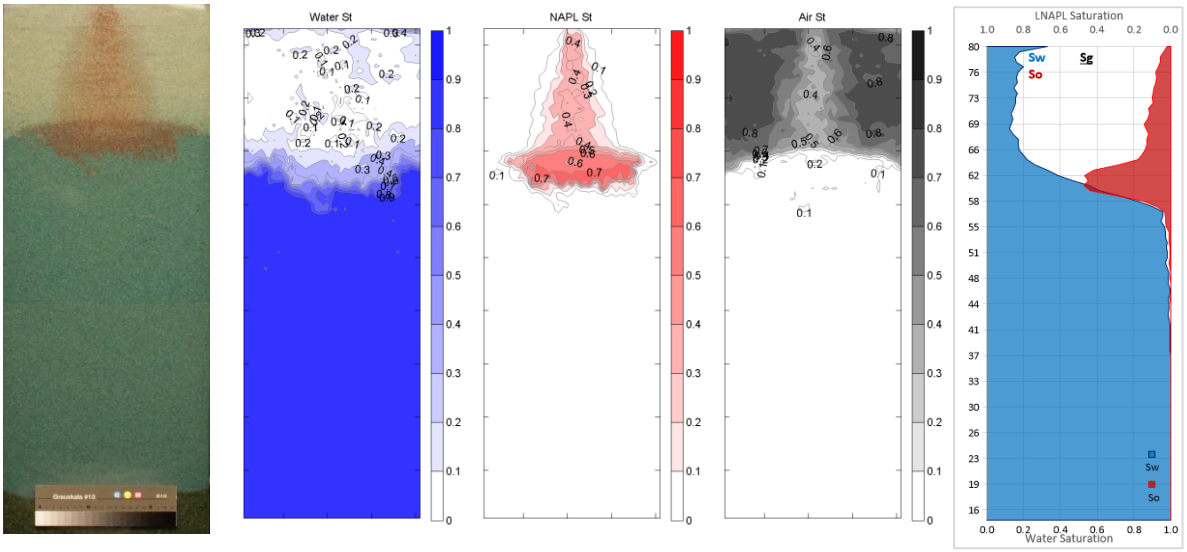

Figure 5-7 Compilation of photographic record, fluid saturation contours and combined vertical saturation profiles of the LNAPL release period at T=50 min

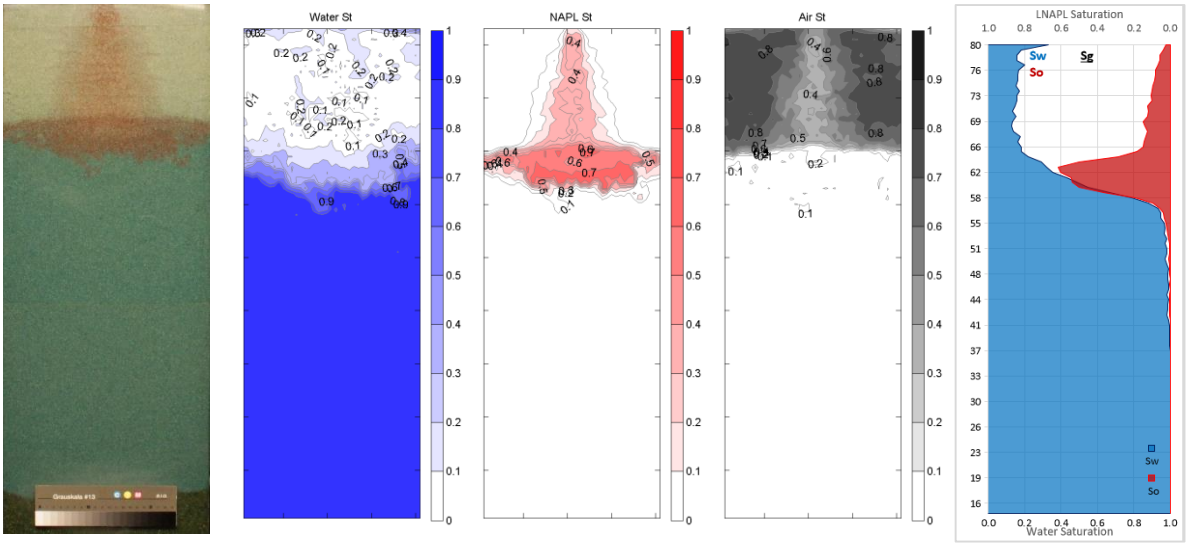

Figure 5-8 Compilation of photographic record, fluid saturation contours and combined vertical saturation profiles of the LNAPL release period at T=60 min

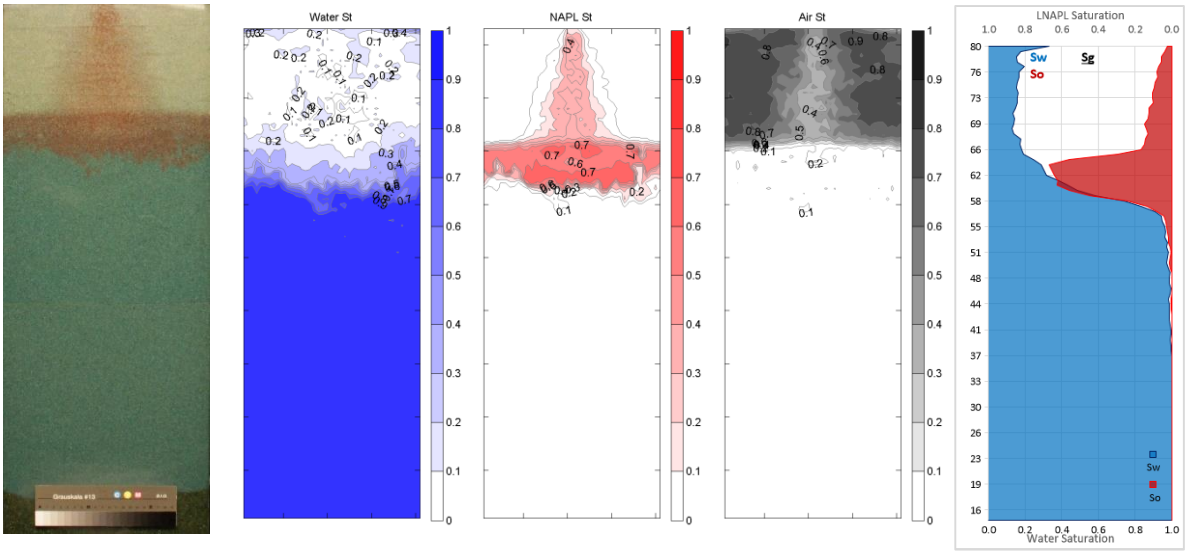

Figure 5-9 Compilation of photographic record, fluid saturation contours and combined vertical saturation profiles of the LNAPL release period at T=70 min

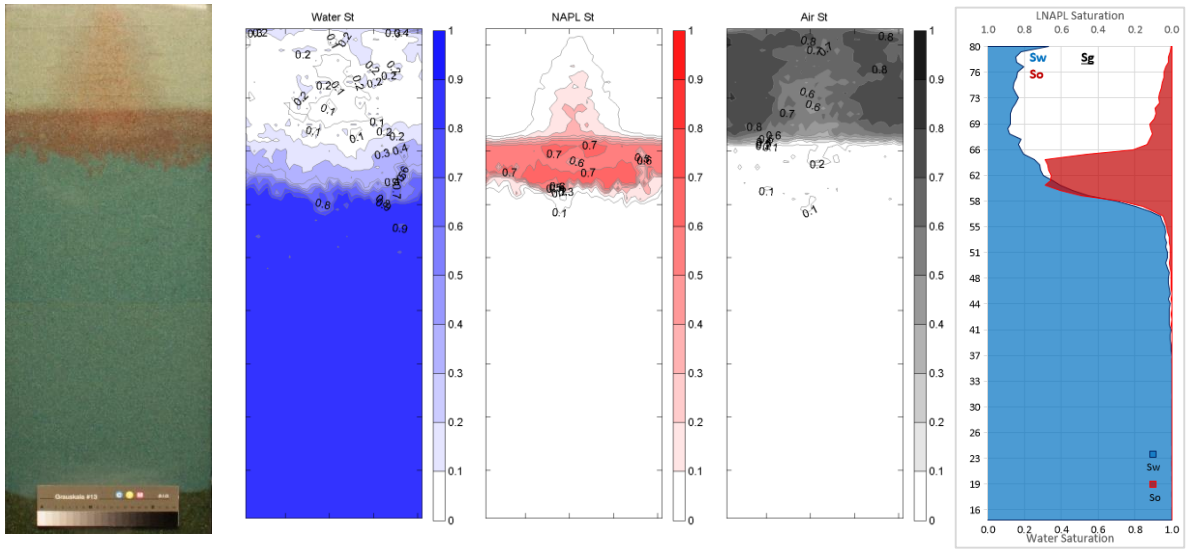

Figure 5-10 Compilation of photographic record, fluid saturation contours and combined vertical saturation profiles of the LNAPL release period at T=80 min

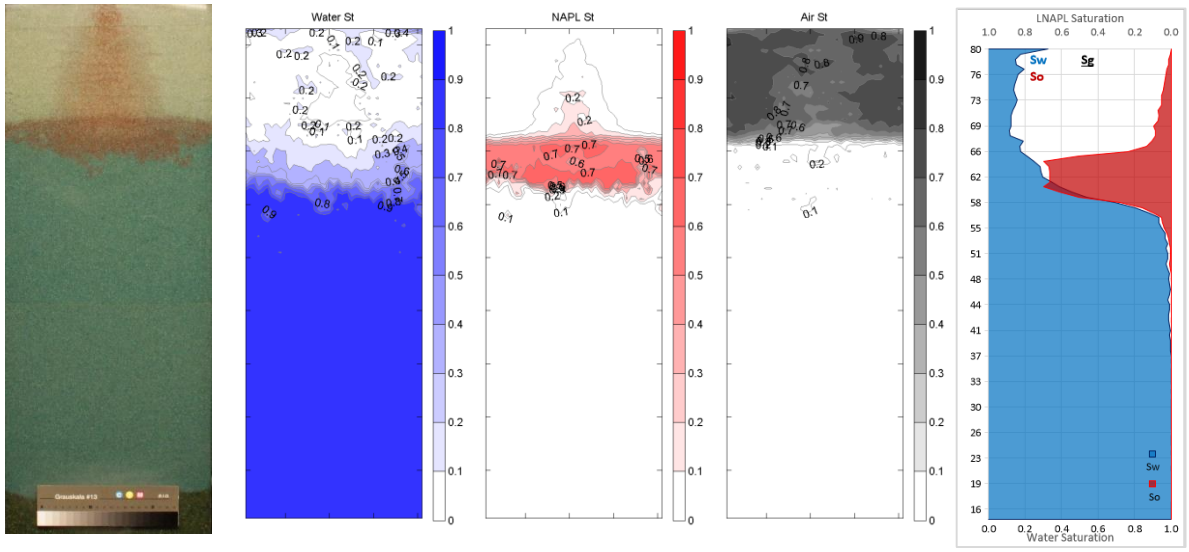

Figure 5-11 Compilation of photographic record, fluid saturation contours and combined vertical saturation profiles of the LNAPL release period at T=90 min

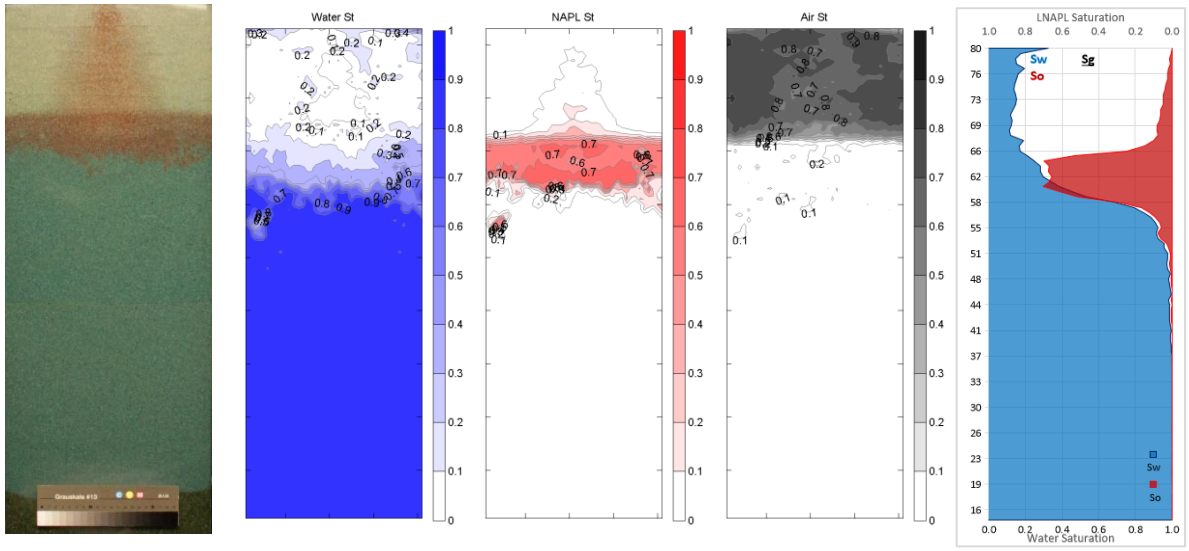

Figure 5-12 Compilation of photographic record, fluid saturation contours and combined vertical saturation profiles of the LNAPL release period at T=100 min

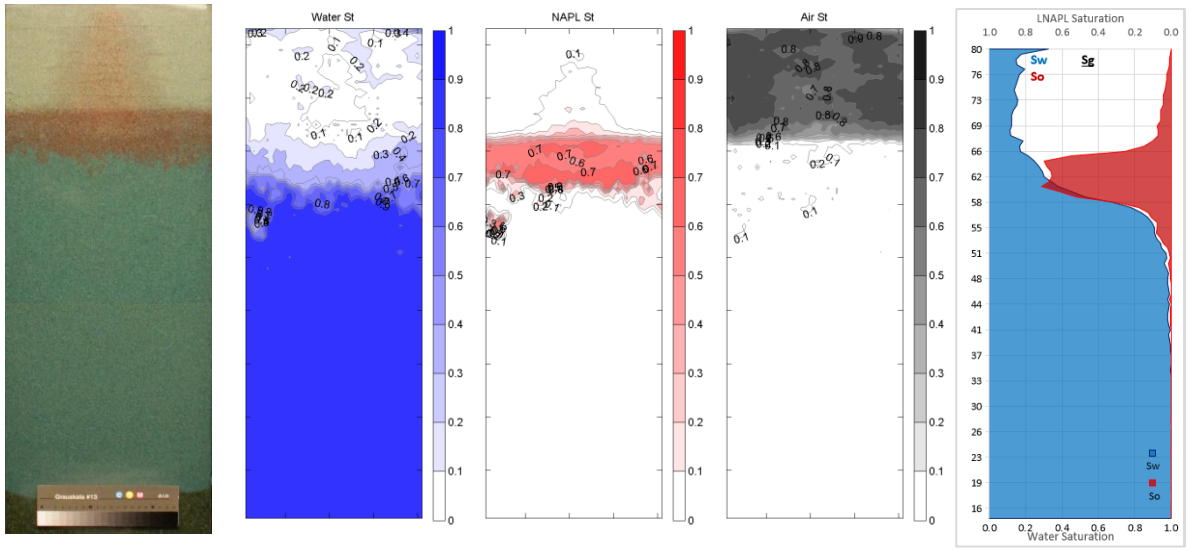

Figure 5-13 Compilation of photographic record, fluid saturation contours and combined vertical saturation profiles of the LNAPL release period at T=110 min

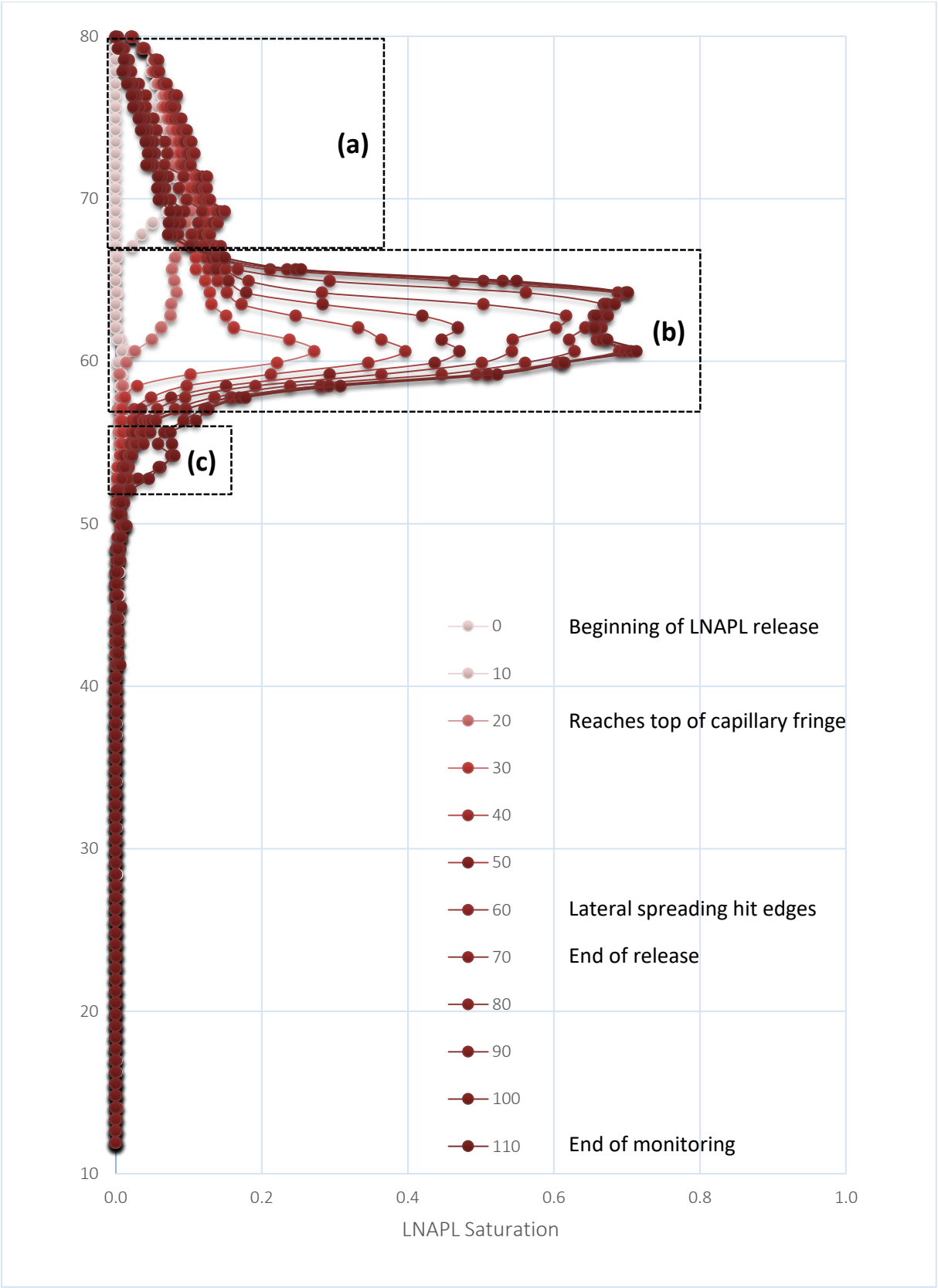

Figure 5-14 LNAPL vertical saturation distribution profiles advancing with time during the LNAPL release period of the base case scenario (Unit: minutes)

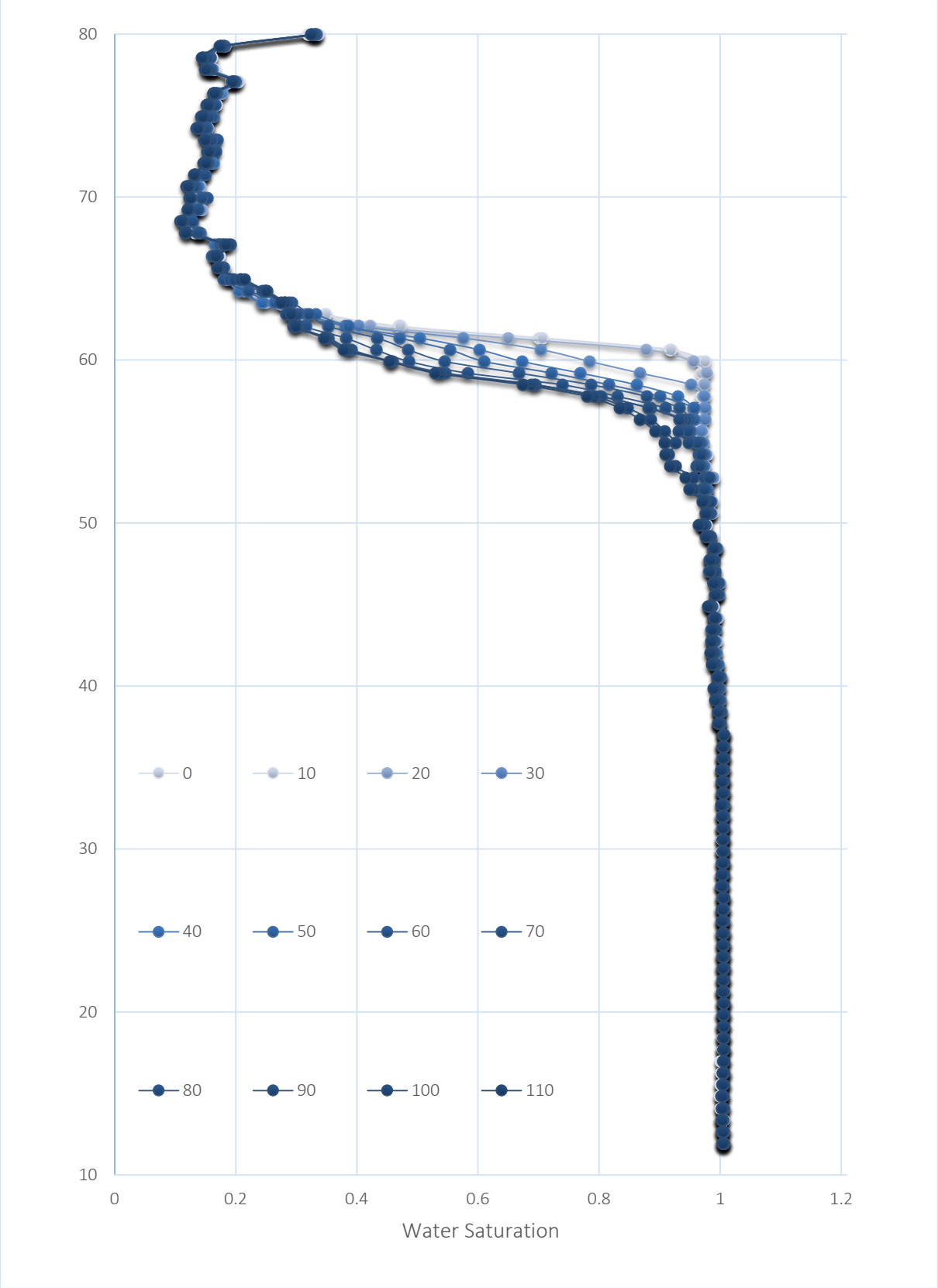

Figure 5-15 Water vertical saturation distribution profiles advancing with time during the LNAPL release period of the base case scenario (Unit: minutes)

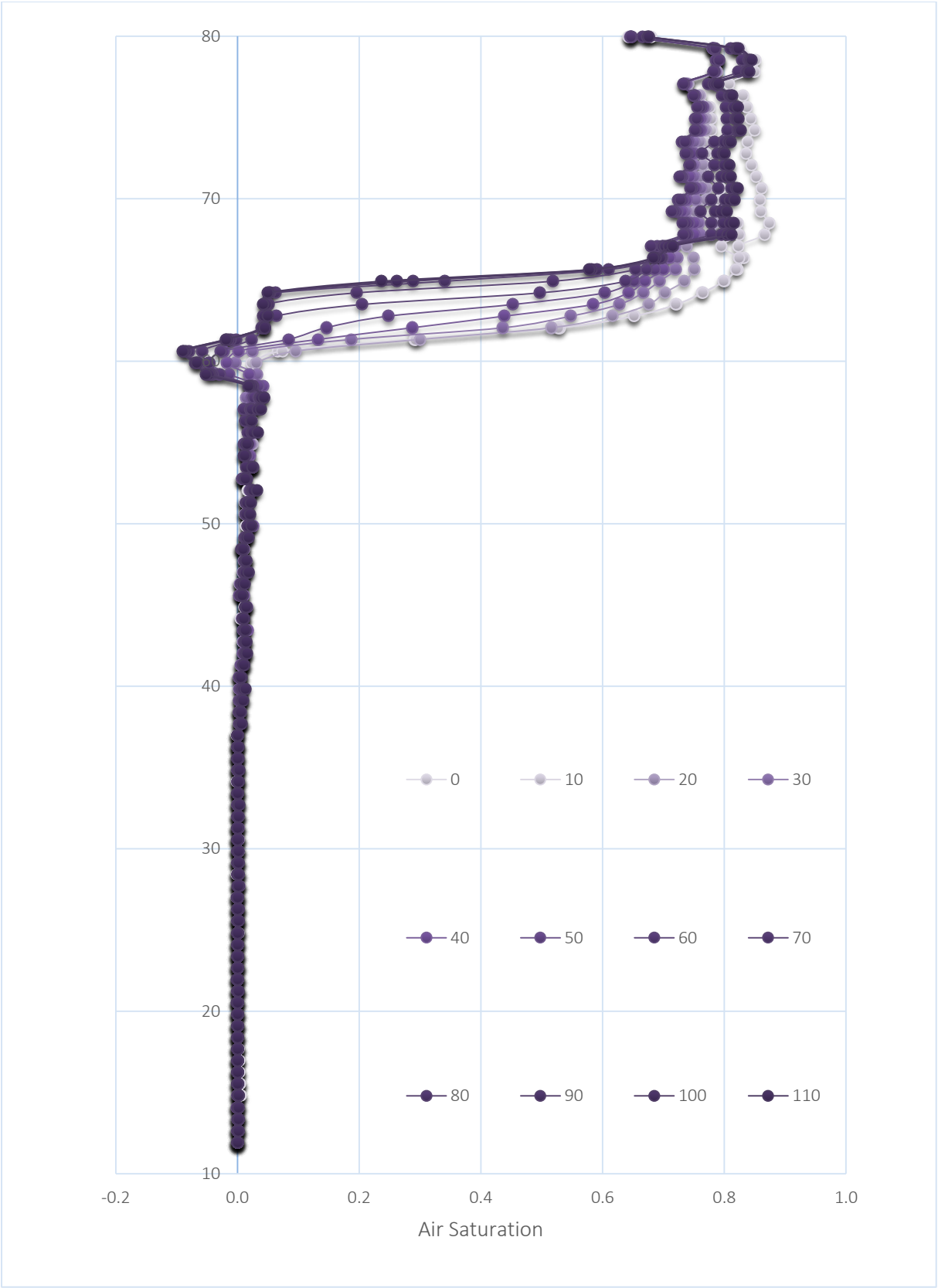

Figure 5-16 Air vertical saturation distribution profiles advancing with time during the LNAPL release period of the base case scenario (Unit: minutes)

5.3.1 LNAPL behaviour during the LNAPL release upon a static water table

5.3.1.1 LNAPL mass migration and distribution during the early stage of release (from T=0 till T=30)

From T=0, LNAPL was released at the centre of the upper boundary in the plot (Figure 5-2). During the early stage, the LNAPL migration was predominantly vertical as the result of gravity. Both short axis and the long axis of the thin elliptical LNAPL body expanded with time, as the body was radiating from the source (Figure 5-3). At T=20, the LNAPL front reached the upper margin of the capillary zone and started to spread laterally (Figure 5-4). The shape of the LNAPL body then began to assume the shape of a bell at T=30 (Figure 5-5). The body developed symmetrically and uniformly across the tank width, which indicated that the movement of the LNAPL body in the unsaturated zone was uninfluenced by local aquifer heterogeneity. This was because that in a less saturated water surrounding, the relative permeability of LNAPL was much higher compared to a water saturated zone. This enabled LNAPL to be driven downwards easily and quickly developed a vertical infiltration within the unsaturated zone. Furthermore, comparing the speed of vertical LNAPL movement (the infiltration rate) to the speed of horizontal movement (the spreading rate) during this stage, the infiltration rate was more predominant before the LNAPL front penetrated into the capillary zone. On the contrary, the spreading rate became bigger after LNAPL thrust into the capillary zone. At the end of this stage, the depression of capillary zone was observed.

5.3.1.2 LNAPL mass migration and distribution during the middle and late stage of release (from T=30 till T=70)

From T=30, the LNAPL body began to manifest as two different segments: the bell-shaped upper unsaturated zone body and the pancake shape lens upon the capillary fringe. Thereafter, the expansion within the upper unsaturated zone (approximately ≥65cm) body ceased, whereas peripheral and inner capillary-zone lens continued to swell (Figure 5-5 to Figure 5-7). At T=60, the LNAPL spreading reached the tank edges, which further increased the saturation of the LNAPL lens (Figure 5-8). At the end of the release at T=70, the entire LNAPL polluted area formed a Mexican sombrero shape (Figure 5-9) with a highly LNAPL saturated lens in the capillary zone, and a medium LNAPL saturated bell-shaped body in the unsaturated zone.

During this stage, the infiltration rate dramatically declined as a consequence of the water saturation in the lower unsaturated zone and the capillary zone becoming considerably and increasingly high. Accordingly, the relative permeability of LNAPL diminished expeditiously. As the LNAPL thrusting into the capillary fringe, the interfacial tension shifted from the previous air-water to primarily LNAPL-water, which was significantly smaller. Since the LNAPL source was still providing a constant LNAPL

head, the pressure at LNAPL front was sufficient enough to overcome the entry pressure of pore throats as a non-wetting fluid and to displace water within pore space. Consequently, LNAPL began to accumulate upon and within the capillary zone and formed an LNAPL lens. Compared to the air displacement by LNAPL at the beginning of the release, water was harder to be displaced due to its larger density and viscosity. Many pores within the capillary fringe had already been occupied by LNAPL. Therefore, LNAPL started to find preferential paths to invade and/or occupy local heterogeneities. Accordingly, LNAPL fingering and asymmetrical distribution developed (e.g. lower boundary of the LNAPL lens in Figure 5-8). At this stage, LNAPL mass movement became increasingly sensitive to ambient aquifer heterogeneity.

5.3.1.3 LNAPL mass migration and distribution during the settling-down period post release (from T=70 till T=110)

From T=70 to T=110 the LNAPL body in the upper unsaturated gradually subsided as the LNAPL source exhausted, with gravitational flow continuing to drive the LNAPL content that exceeded the residual saturation to move downwards until an equilibrium state was achieved (Figure 5-9(c) and Figure 5-13(c)).

The thickness of the LNAPL main lens in the capillary zone and the upper saturated zone peaked at 9cm (Figure 5-13). Alongside the exhaustion of LNAPL pressure head, the LNAPL movement became highly sensitive to local heterogeneity, manifested by the formation of pronounced, visually disconnected blobs (Figure 5-12 and Figure 5-13, below the LNAPL main lens on the left) and ganglia (e.g. Figure 5-10, the asymmetrical lower boundary of the LNAPL main body). Within the LNAPL main body, non-uniformity of LNAPL distribution was apparent due to local heterogeneity. The LNAPL ganglia (fingering) and blobs were preferentially formed in areas with high hydraulic conductivities (loose structure). This was caused by LNAPL acting as a non-wetting fluid compared to water as a wetting fluid, which exhibited a stronger affinity for sand particles. Therefore, the wetting phase would strive to remain coating on the sand surface or to reside in the small pores. In addition, a smaller pore throat would result in a higher entry pressure for LNAPL to overcome, which accounted for the reason that the non-wetting fluid, LNAPL in this case, favoured bigger pores.

A significant feature was observed during this stage was that LNAPL penetrated the capillary zone and became retained in the margin of the capillary zone and saturated zone during the LNAPL release. This mainly depended on the release history and the structure of the aquifer. In this release, partial LNAPL ganglia and blobs were found near the water table (such as Figure 5-13 (a,c) for its appearance and

Figure 5-13 (e) for its quantity). Because before the release was finished, LNAPL pressure exceeded the local entry pressure of some loose structure, thus being pushed into and retained afterwards. The formation of saturated zone LNAPL body required a continuous LNAPL release with sufficient release volume and a relatively low release rate, and heterogeneities within the aquifer. The intrusion of LNAPL body within the upper saturated zone was indeed observed in another base case experiment where a larger volume of LNAPL was released at a similar rate. A large rapid LNAPL release, i.e. a significant release volume under a high release rate, was also monitored. The thickness of the LNAPL lens formed as a result of a large rapid release was smaller, and the penetrating depth was shallower. After LNAPL was promptly released, pore space under the source zone was quickly occupied by the downward LNAPL, which significantly reduced the LNAPL effective permeability vertically. Thus, the continuous LNAPL release was forced to spread horizontally where the effective permeability was high.

The layered structure has been shown to increase LNAPL retention within the original water saturated area, which will be illustrated in the three-layered heterogeneous scenarios in Chapter 4.

5.3.1.4 Dynamics of the 1-D LNAPL saturation profiles

Figure 5-14 presents the temporal and spatial dynamics of the 1-D LNAPL saturation distribution profiles, which are calculated by averaging the saturations of every row of cells within the tank dimension. The profile confirms the features of the three crucial stages analysed in the previous sub-sections, where LNAPL initiated vertical expansion, followed by predominant horizontal spreading and finally assuming a sombrero shape with fingerings and blobs. During the early stage (from T=0 until T=30), the infiltration rate (vertical movement) was approximately 1.05 cm/min, whilst the spreading rate (horizontal movement) was slightly less than 0.5cm/min.

By looking at the dynamics in the unsaturated zone in Figure 5-14(a), the bell-shaped body continued to spread laterally until the release terminated at T=70 with a maximal average saturation of 0.15. There appeared a retrieving trend for the profiles in the unsaturated zone from T=70 to T=110, which illustrated the decline of LNAPL saturation in the unsaturated zone. The maximal average saturation was found 0.10 at T=110. Under the gravitational force, the LNAPL volume that exceeded the residual saturation would travel downwards to replenish the LNAPL main lens, which led to a small increase in the thickness after the release.

Figure 5-14(b) focuses on the formation of the LNAPL lens, which started to form at T=30 and developed at T=70 with its maximal value of 0.68. At this moment, the “shark fin” (CL:AIRE, 2014)

shape of the profiles manifested. Nevertheless, the profiles did not appear to be a strictly idealised shark fin (the maximal LNAPL values) due to local heterogeneity. Furthermore, the thickness of the LNAPL main lens grew considerably during this stage with a maximal value of 9cm.

Throughout the terminal stage (from T=70 to T=110), both LNAPL infiltration and spreading rates gradually decayed until an equilibrium state was established, whereas the thickness of the LNAPL main lens, the maximal LNAPL saturation and the depth of LNAPL penetration all peaked. The maximal thickness of the LNAPL main body was 10 cm, and the greatest LNAPL saturation peaked at 0.71 at the end of the monitoring (T=110). Approximate 26.8 % of the total LNAPL volume was retained in the originally water saturated capillary zone, and the maximal average LNAPL saturation in the capillary zone was 0.17, which was found at T=110 (Figure 5-17).

Figure 5-17 illustrates the time-dependent variation of the mean saturations of water, LNAPL and air within the estimated original unsaturated zone and capillary zone. Due to water drainage, LNAPL imbibition started to take place. Therefore a gradual increase of average LNAPL saturation was observed in the unsaturated zone from 0.0 to the peak of 0.22 at T=70. As mobile LNAPL kept migrating downwards after the release ceased, the average LNAPL saturation and decreased to 0.21 at the end of the monitoring. Whereas the LNAPL saturation in the capillary zone gradually rose from 0.0 at the beginning to 0.17 in the end. Further discussion on saturations of air and water will be introduced in the following sections.

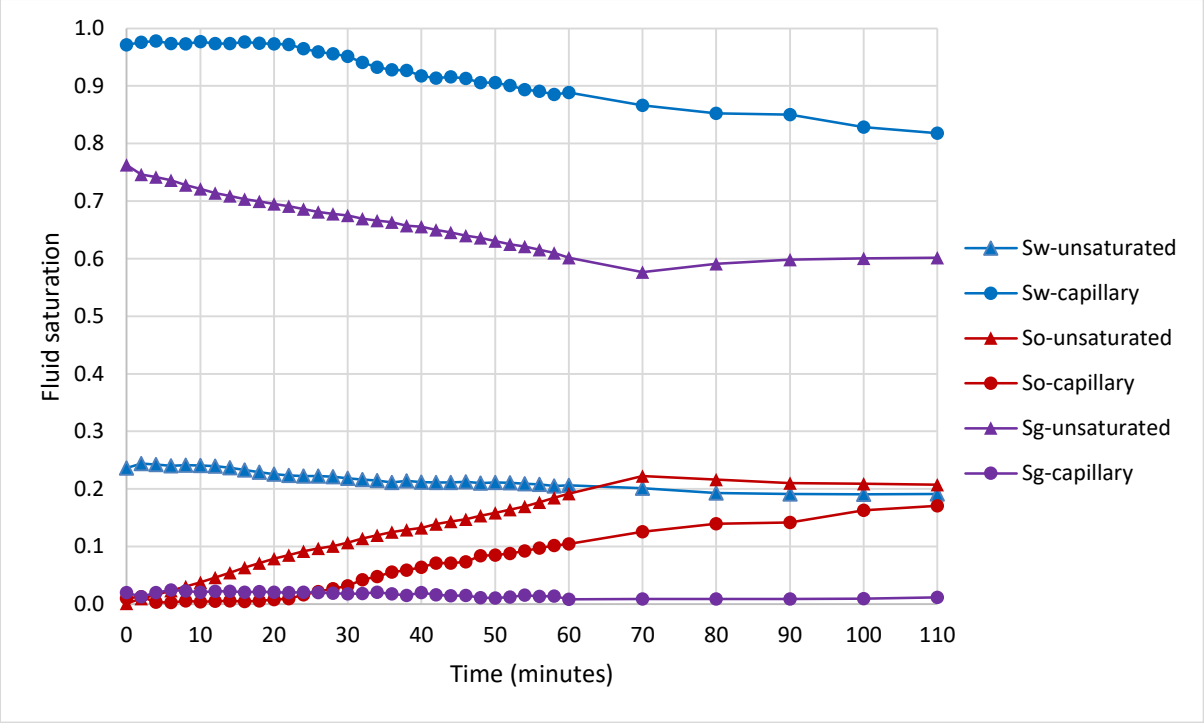

Figure 5-17 Average fluid saturation distributions within the unsaturated zone and the capillary zone throughout the LNAPL release period

5.3.2 Water behaviour during the LNAPL release upon a static water table

Figure 5-2 to Figure 5-13(e)s display the combined profiles of the water-LNAPL-air three-phase system of the same time interval, where fluid saturations are shaded particularly to illustrate the occupancy of pore space at each presented moment. No evident changes in water profiles can be observed during the early stage of LNAPL release (Figure 5-2 and Figure 5-4), when LNAPL front had not arrived at the capillary zone yet. At T=30, when a small magnitude of LNAPL neared the edge of the capillary zone, the capillary height began to be depressed by the LNAPL intrusion and water displacement began to occur with an accelerating speed. As the LNAPL front displacing the water content, by the end of the release (T=70), the water saturation in the capillary zone reduced from almost fully saturated originally to 0.87. After the termination of the release, water displacement by LNAPL still continued which eventually dwindled to 0.82. In the saturated zone, it was evident that water saturation remained at 100% at first before LNAPL intrusion.

Figure 5-15 illustrates the dynamics of 1-D water saturation profiles, throughout the release process, the residual saturation remains relatively stable at around 0.16, with only a small decrease of 0.01 observed when the predominantly water-air system became a water-LNAPL-air three-phase system.

Moreover, there appears some local non-uniformity for the water saturation distribution due to local aquifer heterogeneity, although the overall regional distribution seems relatively symmetrical.

5.3.3 Air behaviour during the LNAPL release upon a static water table

In the unsaturated zone, during the early stage, displacement of air by LNAPL was fairly smooth as the result of the considerably low density and viscosity of air compared to LNAPL and water. It can be observed from both Figure 5-16 and Figure 5-17 that there was evidently a recovery process: The average air saturation in the unsaturated zone went down from 0.76 (T=0) to 0.58 (T=70) and recovered back to 0.60 eventually. This was due to that LNAPL infiltration initially displaced the air in the system, and after the shrinkage of LNAPL pressure head after the release seized, air quickly recovered, yet not a full recovery. The opposite trends of the air saturation distributions were due to the fluid phase system change from water-air two-phase system to water-LNAPL-air three phase system, where residual LNAPL saturation as intermediate wetting phase forced the decrease in both air saturation and residual water saturation in the unsaturated zone. This phenomenon was also featured in Figure 5-16. The water table was raised by the invading LNAPL, whereas the thickness of the unsaturated zone was lessened consequently.

One image analysis error is featured between Z= 58cm and 62cm in the air profiles in Figure 5-16, where the last few photographic events were showing negative air saturations from approximately 0.00 to -0.09. The LNAPL volume estimations at those moments (roughly between 96~99ml) were adequately close to the real release volume (99ml) with slight underestimation. And by examining the LNAPL distribution against the photographic records, the accuracy of LNAPL estimation by the image analysis was found good. Therefore, the overestimation in water saturation within this range was considered responsible for the error which led to the air profile error. The error may be decreased by conducting three-phase calibration test rather than obtaining the air saturation from volume balance.

In the capillary zone, no air trapping was found during the early stage of LNAPL release, since the capillary zone was fully water saturated (e.g. Figure 5-3). Only after the LNAPL front arrived at the capillary fringe, a small amount of air entrapment started to take place beneath the LNAPL front (e.g. Figure 5-8). Despite the fact that the low viscosity and high buoyancy forces would encourage air to escape, the trapped air, with a saturation of 0.024 (Figure 5-17), mainly located around the centre, within the LNAPL lens or beneath the LNAPL front. This was because the largest LNAPL pressure was found around the central vertical line. Air was driven by the LNAPL front to puncture the capillary zone, and some even reached the saturated zone. The interfaces between air and the top margin of capillary

fringe shifted along the process. The initial interface was a flat water-air interface (Figure 5-2 and Figure 5-3), which was shifting into a curvy water-LNAPL interface gradually (Figure 5-4, Figure 5-5 and Figure 5-6). From T=60 till the end, the interface grew into a flattened LNAPL-air interface.

In the saturated zone, prior to the LNAPL release, it was fully water-saturated with no presence of air. Although it could not rule out the possibility that there might be an insignificant amount of air trapped in dead-end pore space during the tank saturation, it was not significant enough to be noticed in any figure. The reason for air entrapment in the original water saturated area was more complicated. It may be led by the local aquifer heterogeneity, where air inclined to be trapped beneath low-permeable barriers despite its tendency to float up (e.g. from Figure 5-10 to Figure 5-13 (d) and (e)). Low permeable layers tended to be occupied by the wetting fluid in the system, which, in this case, was water. The LNAPL and air once trapped underneath a fine layer, with decreasing pressure, they could not escape. Moreover, when a high concentration of LNAPL found its preferential path and accumulated in a relatively loose structure thus becoming an LNAPL blob, water saturation in those areas was mostly displaced by invading LNAPL. LNAPL started to coat onto the grain surface under a large LNAPL pressure head, becoming the wetting fluid, whereas the air that followed LNAPL downwards acted as the non-wetting fluid in the primarily LNAPL-air system. Most of the entrapped air could not overcome coated LNAPL or water blobs to escape. The maximal air saturation entrapped in these LNAPL blobs was found 0.1 on the left side of near the water table in Figure 5-12 (d) and Figure 5-13 (d).

5.3.4 Modelling perspective on the LNAPL release period

The input parameters of the model have been shown in Table 5-1. These parameters are used in all following simulations that do not need recalibration.

Figure 5-18 to Figure 5-20 demonstrate the modelling result of the LNAPL release period, comprising both saturation profiles and 2-D contours of three crucial photographic events, which respectively are: the early stage and the terminal moment of the LNAPL release, and the end of the monitoring of the settling down period. By comparing the modelling contours with their corresponding experimental contours, key features of this process, including the shape of the LNAPL body, the distribution of water and air, the residual saturation of water and LNAPL, the invading speed of LNAPL front, the penetrating depth of LNAPL, etc., were considered reasonably simulated. By reviewing the overall time-dependent dynamics of LNAPL release, the modelling result and the experimental result were fairly agreeable and consistent. Although small differences occurred, such as that the experimental contours generally

appeared noisy, which was mainly resulted from the unavoidable local heterogeneity. And the shape of LNAPL body in the lower unsaturated zone appeared slightly narrower in the experimental result than the modelling result.

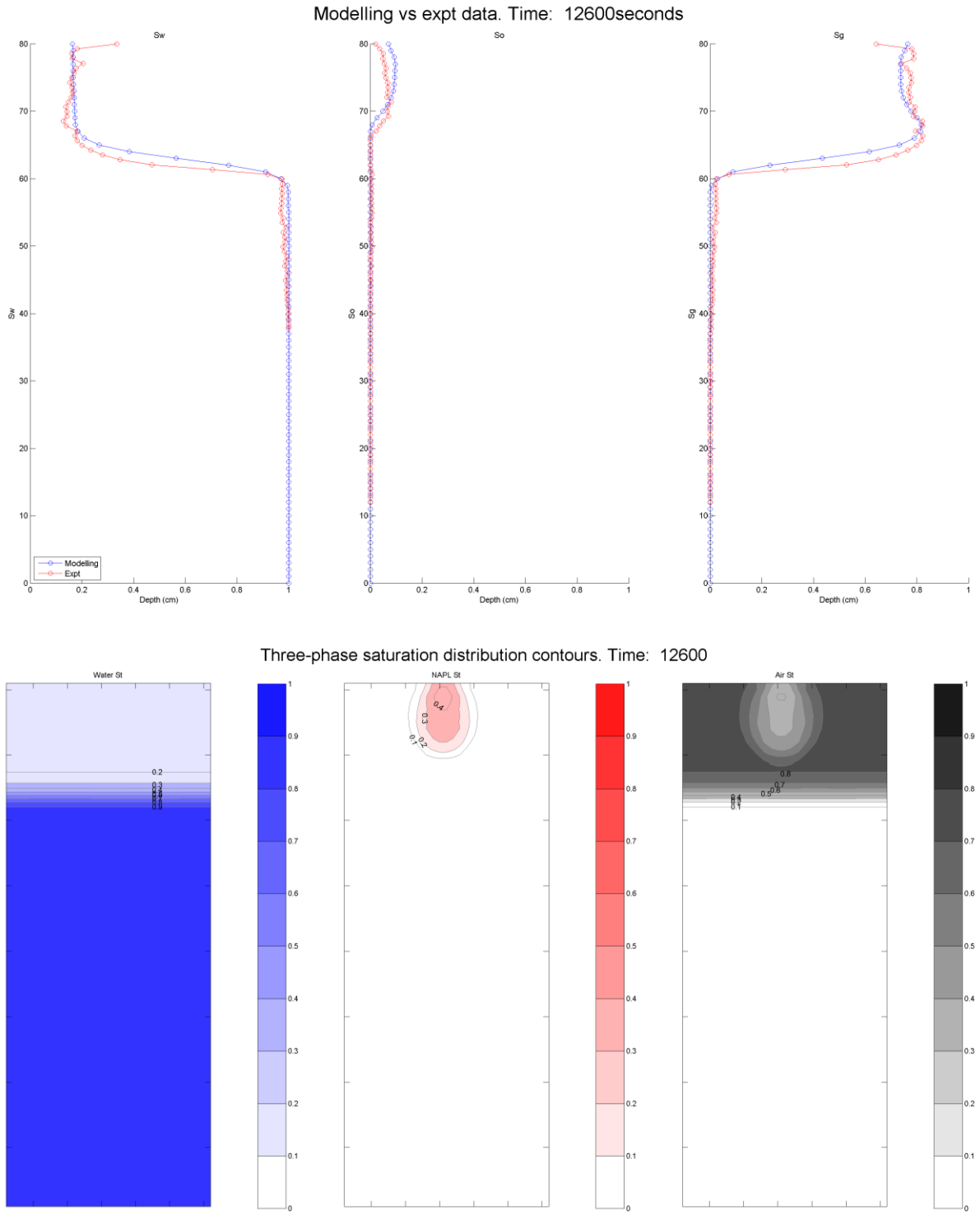

Figure 5-18 Modelling result of the LNAPL release period T=10 min, profiles above and contours below (In comparison with Figure 5-3)

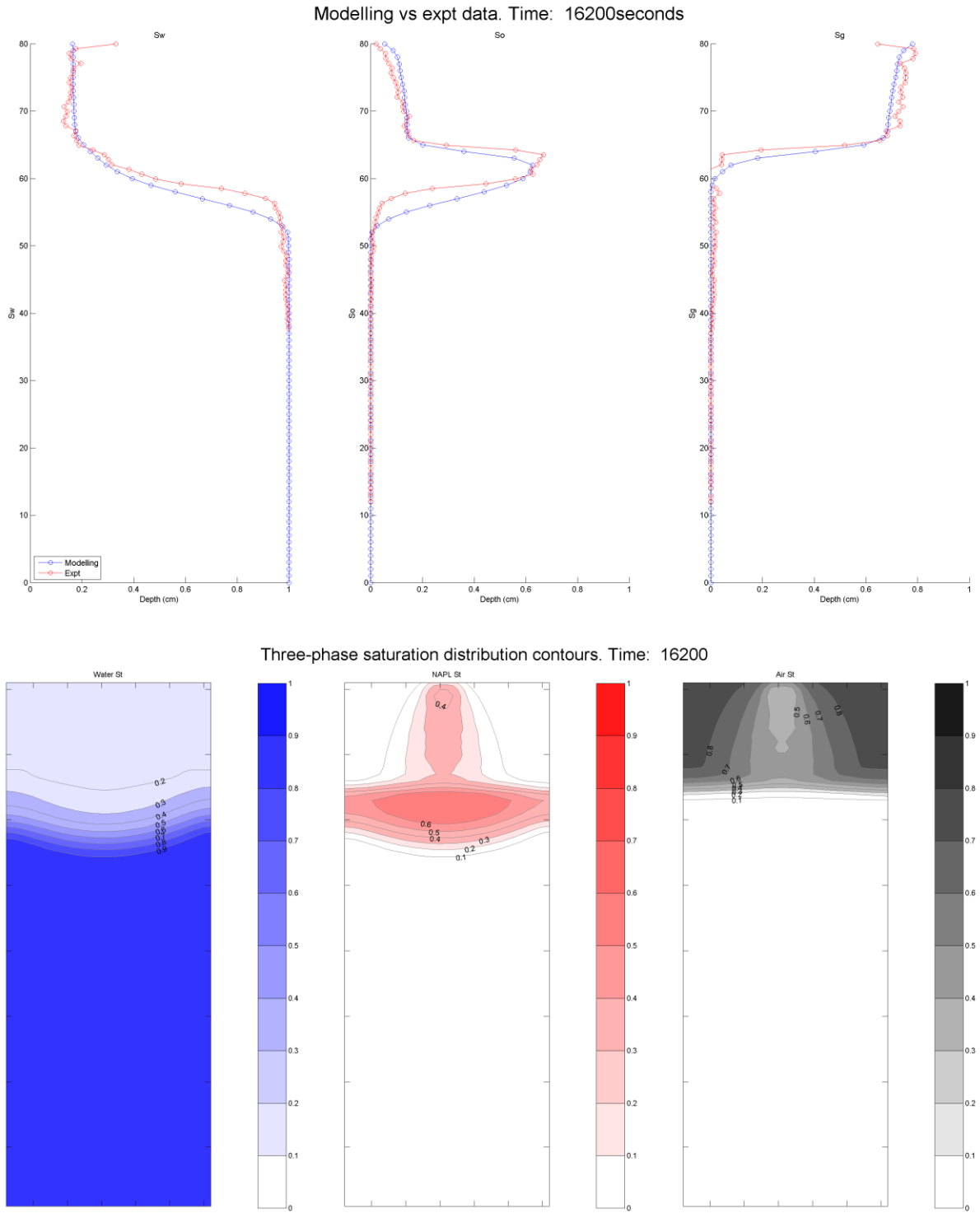

Figure 5-19 Modelling result of the LNAPL release period T=70 min, profiles above and contours below (In comparison with Figure 5-9)

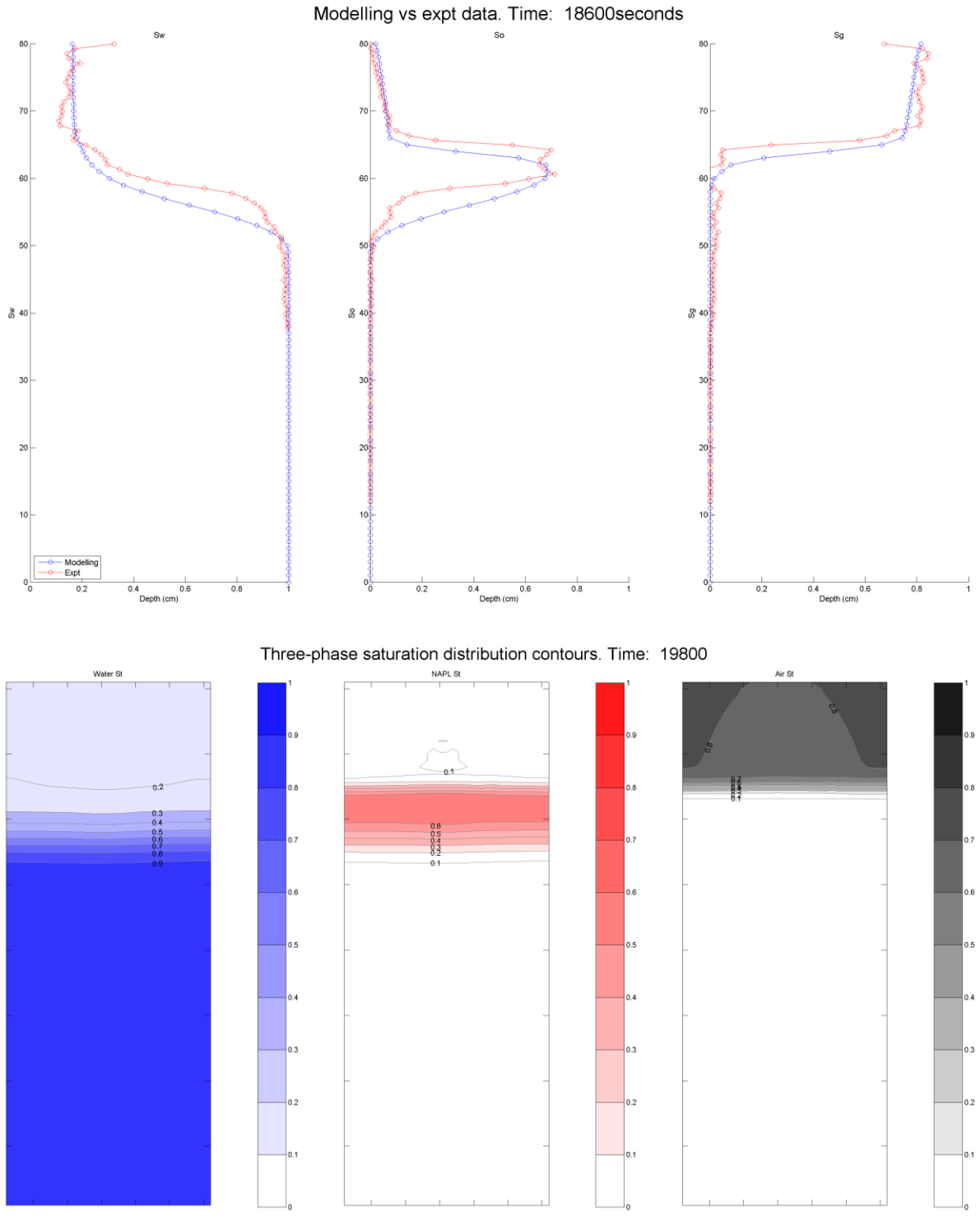

Figure 5-20 Modelling result of the LNAPL release period T=110 min, profiles above and contours below (In comparison with Figure 5-13)

By comparing the superimposed profiles, although minimal differences can be observed from the water and air profiles, the overall agreement is good. These differences are primarily induced by different boundary condition retrained by NAPL simulator, the modelling fitting method, local heterogeneity in the aquifer and the small inherent inaccuracy induced by the image analysis.

The disagreement found in the water profiles, where the modelling water tables are generally lower than the experimental water tables (Figure 5-19 and Figure 5-20). It is because, in the experiment, the bottom valves were kept shut during the LNAPL release and the LNAPL invasion increased the original water table in the tank. Whereas, the water table had to be set fixed in the NAPL simulator throughout the LNAPL release in the model simulation, which meant as LNAPL invading, water may drain from the modelling tank to maintain the fixed boundary conditions.

Variable boundary condition setting for the LNAPL release modelling was only achieved at the latest stage of this study, where the water table was drained from the tank first to the prescribed water table, and then a second modelling was started with the bottom boundary as a no flow boundary, while using the water drainage modelling as the initial condition of this new modelling stage. The results for the beginning of the LNAPL release were almost identical, whereas the new modelling was capable of simulating the raised water table by LNAPL intrusion at the end of the LNAPL release. However, the new result did not show dramatic improvement with the original parameters. For further modelling study, recalibration and detailed modelling are recommended for the new modelling with the impermeable tank base.

Additionally, the differences arise from the possible errors induced when associating the tank size and position to pixel prior to the image analysis. Specifically, the top of the LNAPL modelling profiles in Figure 5-18 and Figure 5-19 appeared to be larger than the experimental values. It was because that in the model, LNAPL release source had to be set as an even number to prevent asymmetrical release, which was set to be 4cm wide, whereas the real release width was 3cm in the experiment.

Considering the variations in the input parameters and/or the mathematical and numerical simplifications of the adequately complicated three-phase system during the modelling of the LNAPL release, the quality of the simulation is overall satisfactory. And by examining the modelling result of all photographic events, it can be concluded that the descriptive model is capable of capturing key features of the LNAPL release process in a three-phase system and has yielded reasonable and consistent simulation results.

In summary, for a slow, continuous and sufficient LNAPL release into a porous unsaturated zone, LNAPL accumulates upon and/or within the capillary zone. LNAPL fingerings and blobs may eventually penetrate the depressed capillary zone and become entrapped around or below the water table,

depending on the release history and aquifer geology. During this period, the water table and its capillary fringe above act as a hydraulic barrier that prevents LNAPL from moving downwards.

5.4 Results and discussions of single cycle patterns during the water table fluctuation period

After the LNAPL release, the prescribed water table fluctuation condition was imposed as presented in Chapter 3. Specifically, this section narrates the features and implications of the fluid migration and distribution during the initial cycle of the five-cycled water table fluctuation period, which commenced at time T=0h and ended at T=12h. The experiment was carried on without intermission. Different perspectives of the same process are exhibited in the following group of figure compilations from Figure 5-21 to Figure 5-33. Similarly as before, Figure (a)s to (e)s present the photographic record, 2-D contours of water, LNAPL and air, and the shaded 1-D vertical fluid saturation profiles respectively. Furthermore, for the visualisation of the complete process of water table fluctuation in the video format, refer to Appendices A.2.1.2 (2), and for the raw dataset of the profiles refer to the Appendices A.2.1.1 (2).

Key observations are summarised below and elaborated upon in the underlying discussion with reference to the figures.

- As water table descending, LNAPL quickly drained from the main lens accumulated during the LNAPL release period, which is regarded as the new source zone, and accumulated onto and/or within the depressed capillary fringe at the lowermost water table position.
- As the water table ascending, a considerable amount of LNAPL became the entrapped saturation that persisted as a horizontal band around the lowermost water table position with pronounced fingering.
- Evident air entrapment occurred when the water table being raised after the first water drainage.
- From the thickness and maximal average saturation perspective, the lowermost position presented the thinnest LNAPL lens with the highest maximal average saturation, and after the uppermost position, the thickest LNAPL lens formed with slightly smaller average LNAPL saturation.

5.4.1 LNAPL behaviour during a single-cycle of water table fluctuation period

The main observations are discussed by following the division in time:

- Stage 1: Water table descent from mid-position to the lowermost position: T=0h to 3h;
- Stage 2: Water table ascent from lowermost position to mid-position: T=3h to 6h;
- Stage 3: Water table ascent from mid-position to the uppermost position: T=6h to 9h;
- Stage 4: Water table descent from the uppermost position to mid-position: T=9h to 12h.

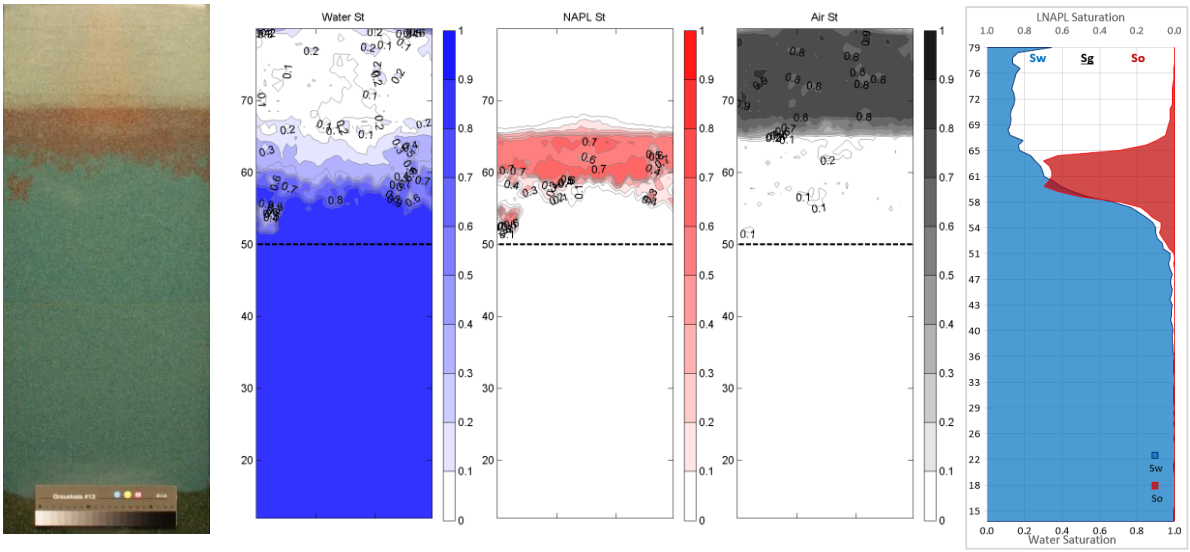

Figure 5-21 Compilation of photographic record, fluid saturation contours and combined vertical saturation profiles of the water table fluctuation period at T=0h. The water table levels are plotted as dash lines in every follow-up contours

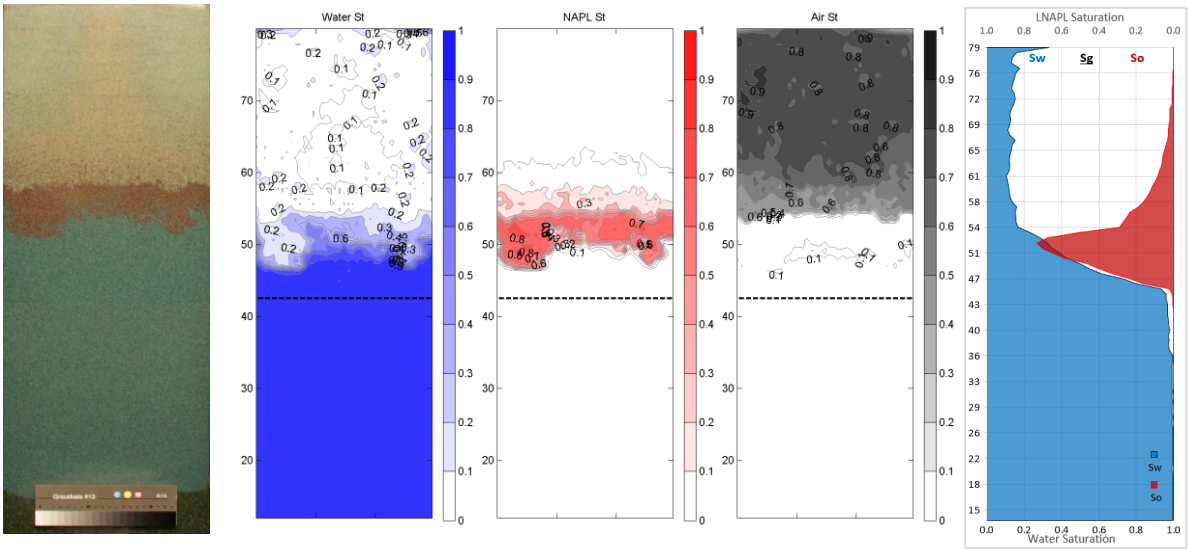

Figure 5-22 Compilation of photographic record, fluid saturation contours and combined vertical saturation profiles of the water table fluctuation period at T=1h

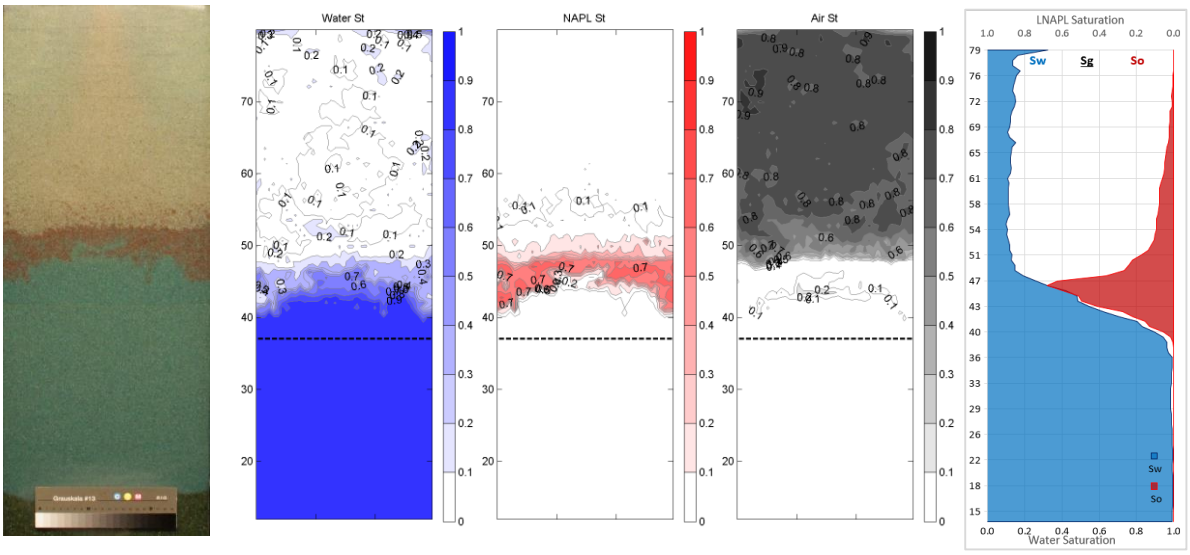

Figure 5-23 Compilation of photographic record, fluid saturation contours and combined vertical saturation profiles of the water table fluctuation period at T=2h

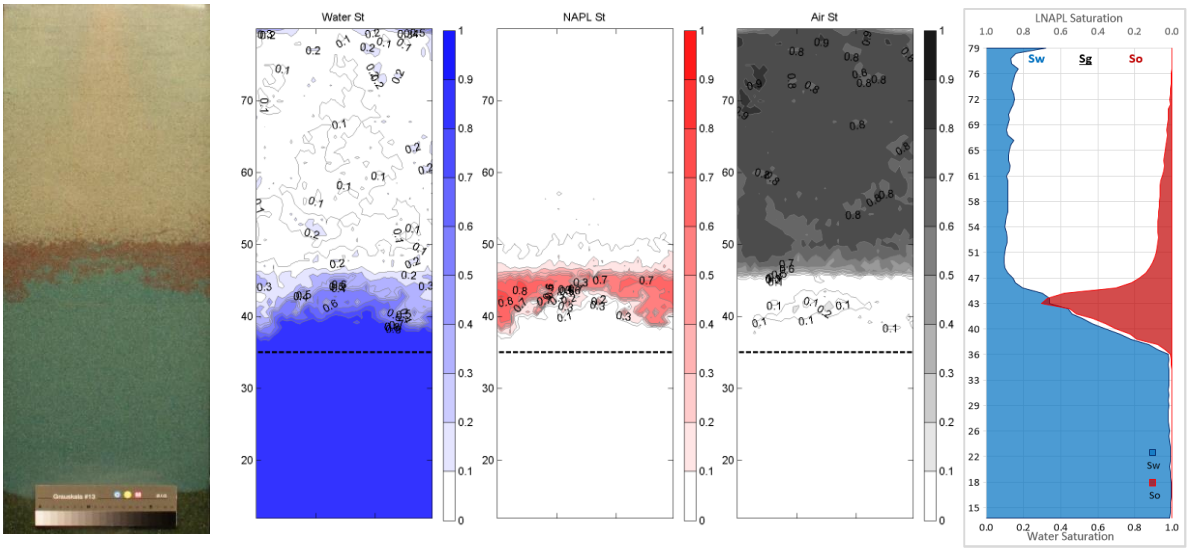

Figure 5-24 Compilation of photographic record, fluid saturation contours and combined vertical saturation profiles of the water table fluctuation period at T=3h

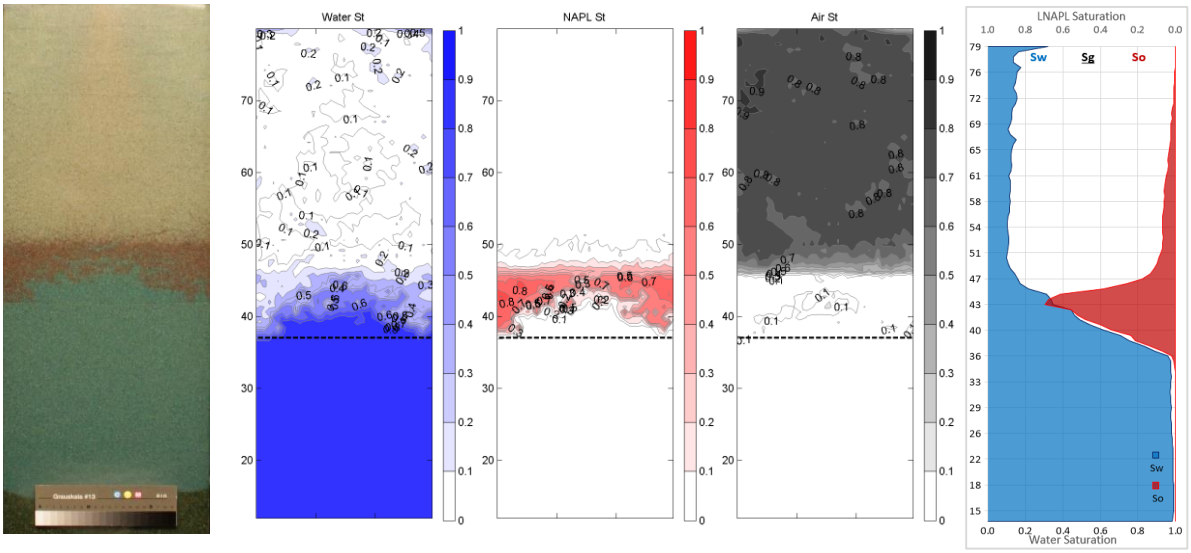

Figure 5-25 Compilation of photographic record, fluid saturation contours and combined vertical saturation profiles of the water table fluctuation period at T=4h

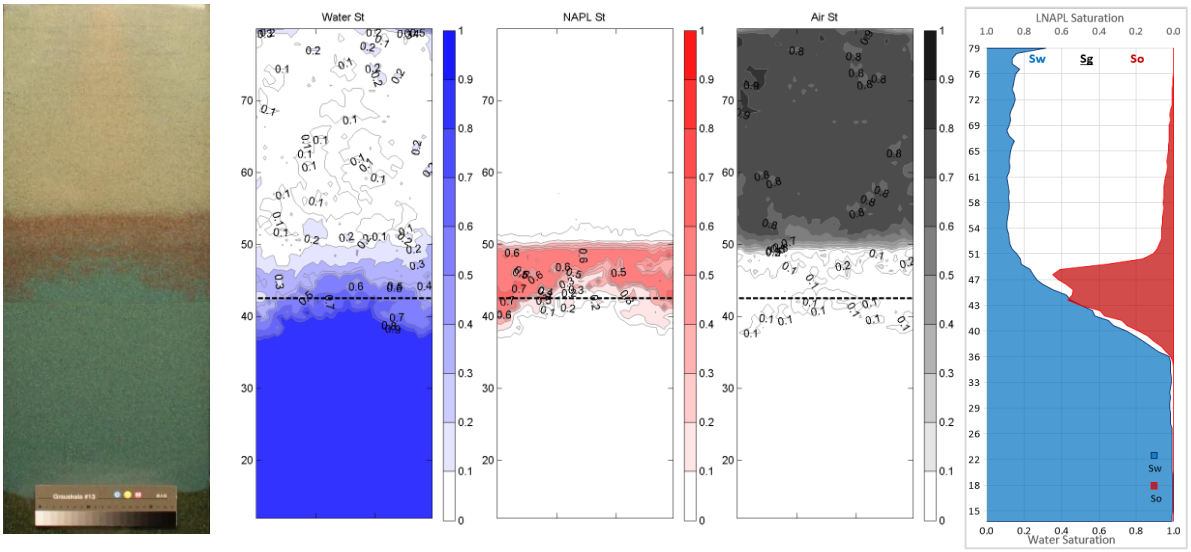

Figure 5-26 Compilation of photographic record, fluid saturation contours and combined vertical saturation profiles of the water table fluctuation period at T=5h

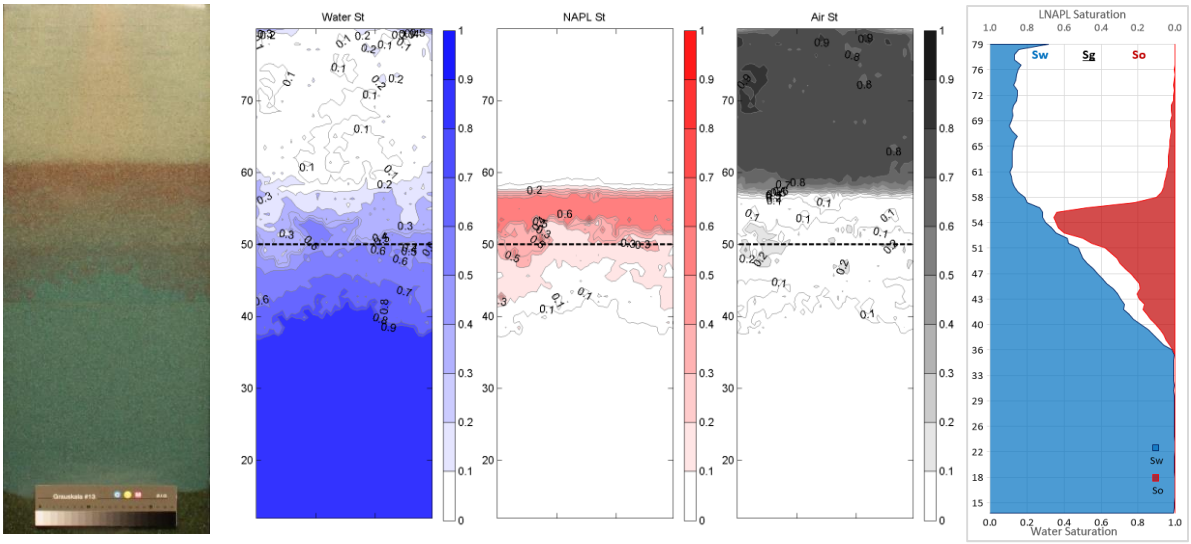

Figure 5-27 Compilation of photographic record, fluid saturation contours and combined vertical saturation profiles of the water table fluctuation period at T=6h

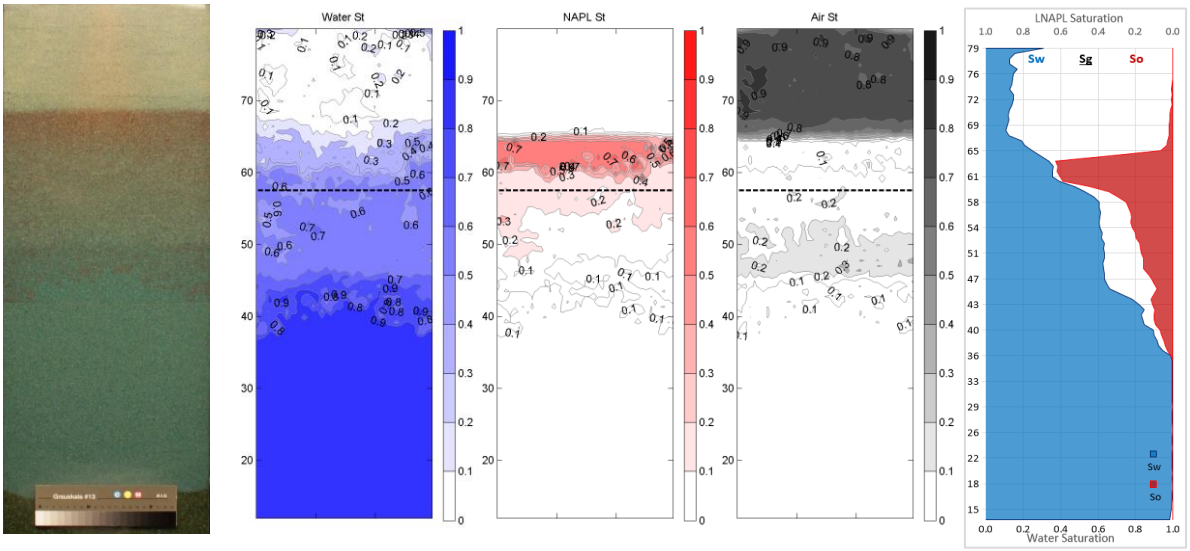

Figure 5-28 Compilation of photographic record, fluid saturation contours and combined vertical saturation profiles of the water table fluctuation period at T=7h

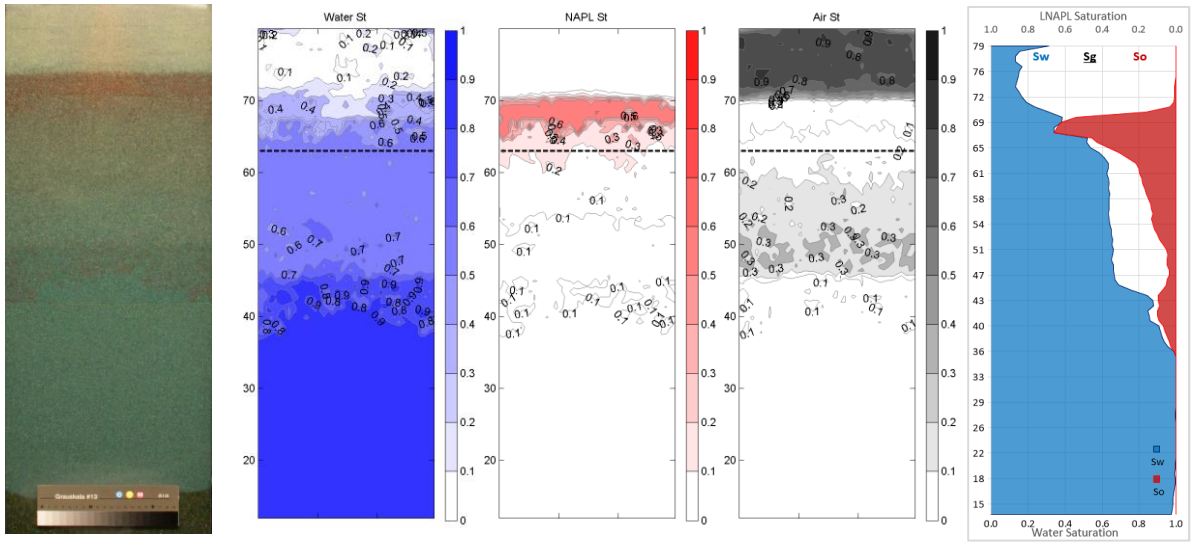

Figure 5-29 Compilation of photographic record, fluid saturation contours and combined vertical saturation profiles of the water table fluctuation period at T=8h

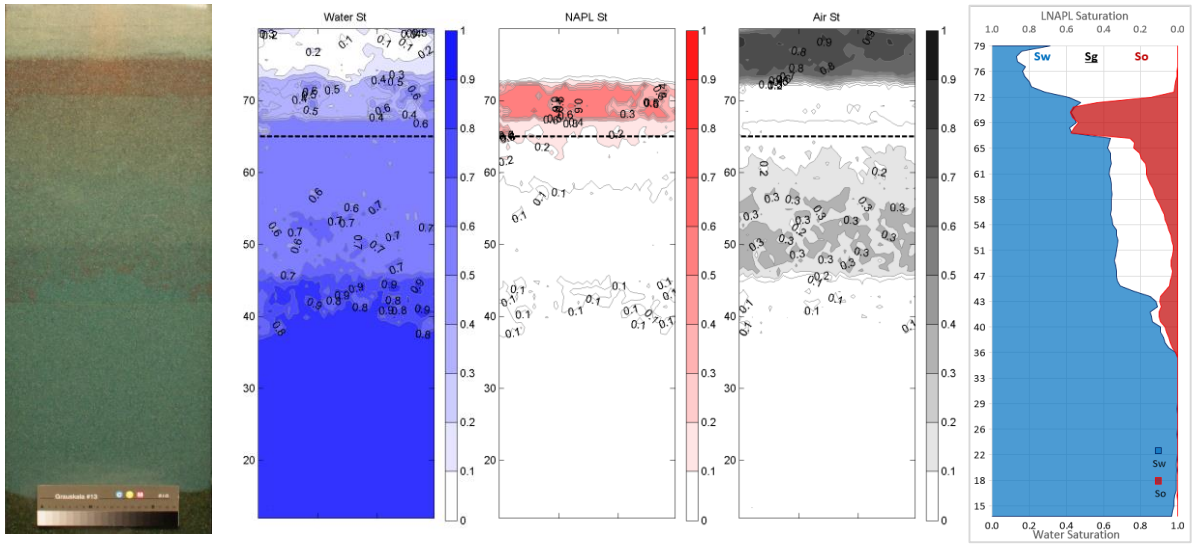

Figure 5-30 Compilation of photographic record, fluid saturation contours and combined vertical saturation profiles of the water table fluctuation period at T=9h

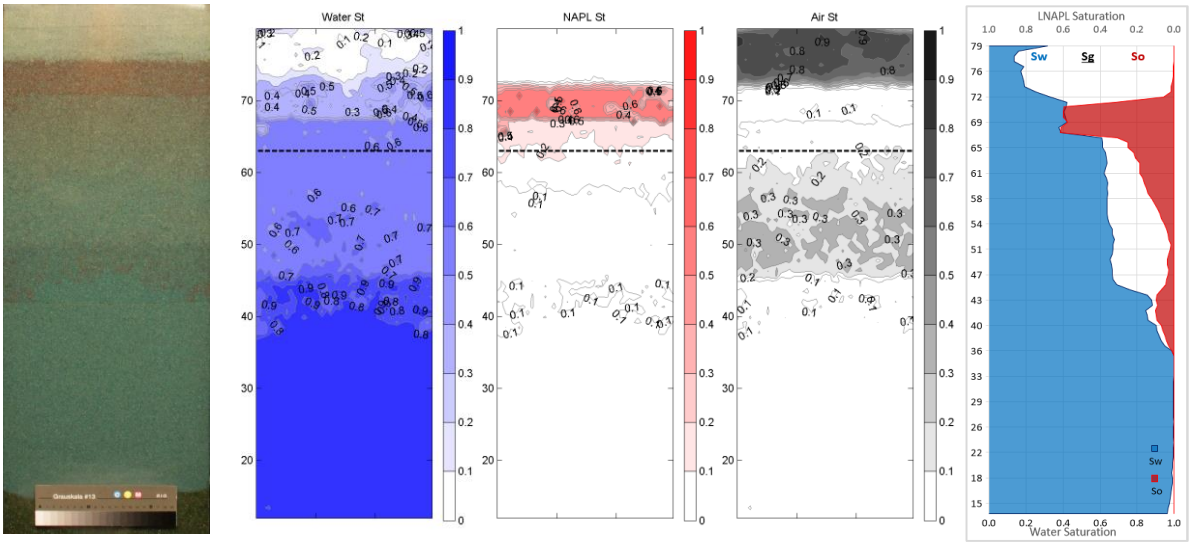

Figure 5-31 Compilation of photographic record, fluid saturation contours and combined vertical saturation profiles of the water table fluctuation period at T=10h

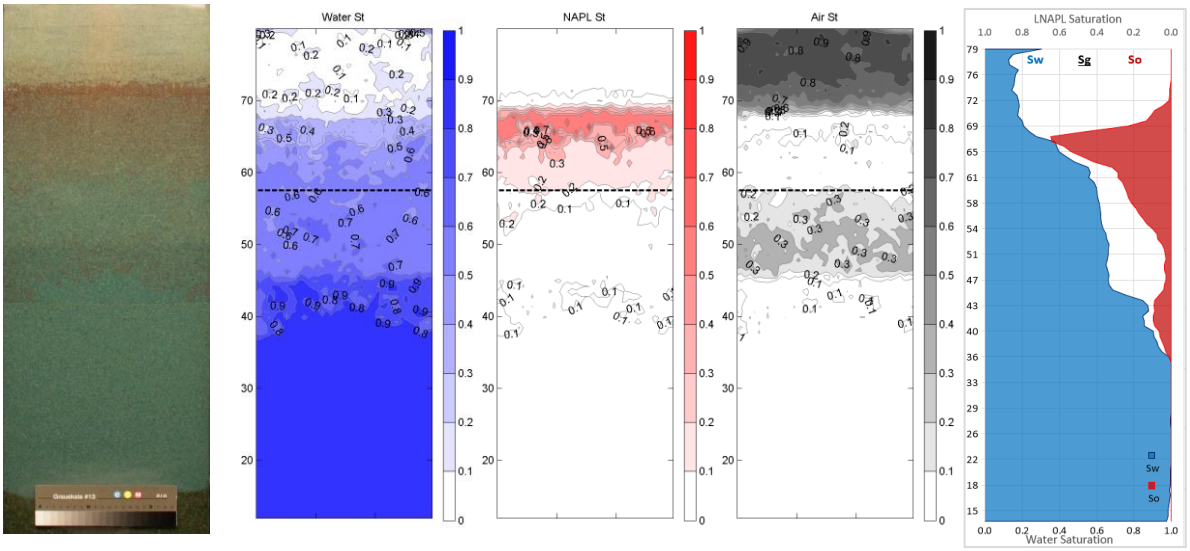

Figure 5-32 Compilation of photographic record, fluid saturation contours and combined vertical saturation profiles of the water table fluctuation period at T=11h

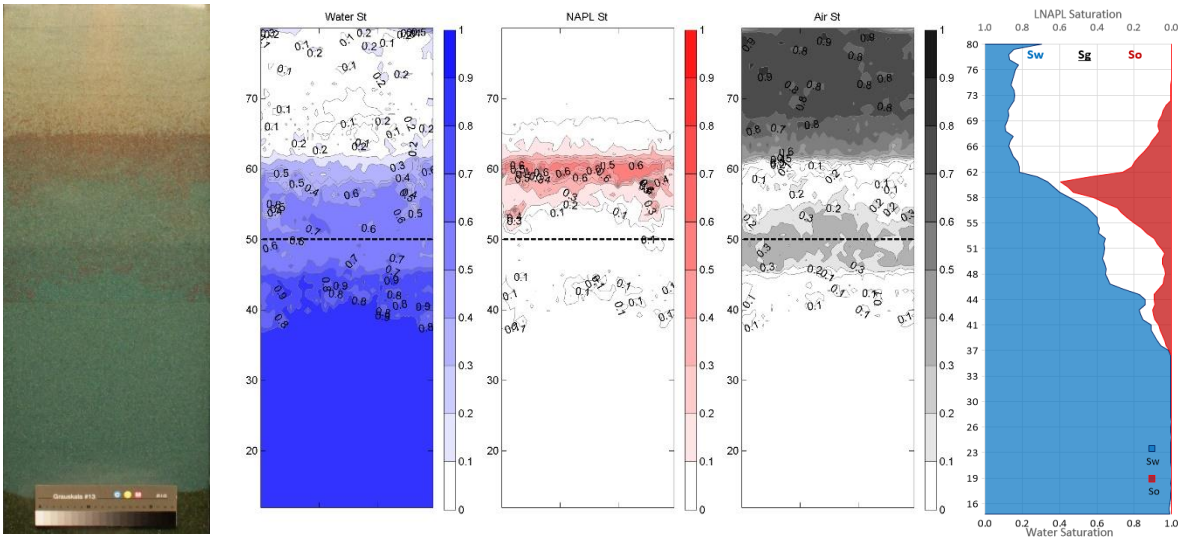

Figure 5-33 Compilation of photographic record, fluid saturation contours and combined vertical saturation profiles of the water table fluctuation period at T=12h

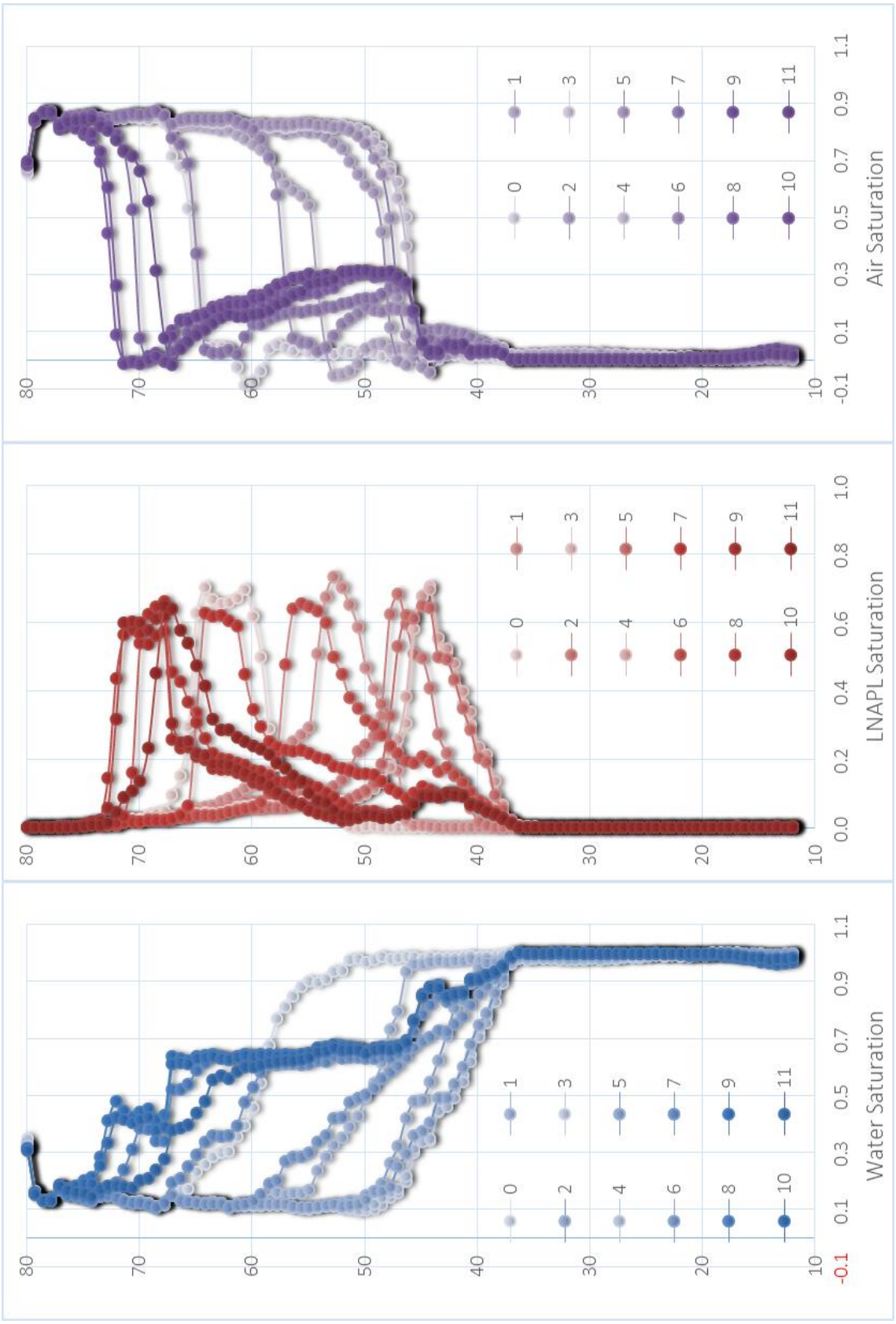

Figure 5-34 Water, LNAPL and air saturation distribution profiles advancing with time during the first cycle of water table fluctuation (Unit: hour). The numbers 0~11 marked in the legends represent hour, which are in accordance with the moments in Figure 5-21 to Figure 5-32.

5.4.1.1 LNAPL mass movement during stage 1

At the beginning of the water table fluctuation, the LNAPL main body was an oval-shaped band with an average LNAPL saturation of greater than 0.6 and a thickness of 7.0cm (Figure 5-21 (a,c)). The water table at this moment was at 53cm since the LNAPL intrusion had raised the water table up. As the water table being lowered down, the discrete LNAPL blobs entrapped below the water table during the LNAPL release were quickly connected with the downward LNAPL main lens, merged as part of the LNAPL front. The thickness of the LNAPL main lens was reduced to 5.0cm with an increased average saturation of more than 0.7 (Figure 5-22(a,c)). Following the main lens, there formed two tail-like continuous less-saturated bands with average saturations of 0.3 and 0.1, and thicknesses of 3.5cm and 4cm respectively. With the further descending of the water table, the thickness of LNAPL main lens shrank to a minimum of 4.5cm with the less saturated bands dramatically diminished in depth (Figure 5-24(a,c)). The length of the aquifer occupied by residual LNAPL saturation maximised, which almost took up the length between the original LNAPL source to the upper boundary of the LNAPL main lens. To note that the LNAPL lens at the lowermost water table position was a thin band which was highly LNAPL saturated (maximal average saturation 0.72).

Figure 5-34 presents the corresponding saturation distribution profiles advancing in time during the first cycle of water table fluctuation, where in the upper unsaturated zone close to the LNAPL release source, the LNAPL saturation is found only marginally above zero, which is remarkably less the LNAPL residual saturation value. It is because this saturation is an average value of the LNAPL saturations of a row of cells over the entire tank width, where the LNAPL body is centred with no occupancy beyond the LNAPL body boundary.

Figure 5-44 and Figure 5-45 present the variations of fluid saturations and fluid volume percentages below and above the water table, where stage 1 is between 0 to 3 hours. Below the water table there was barely any LNAPL found (roughly 1%) whereas 99% of LNAPL volume resided above the water table, with a saturation ranging from 0.18 at the beginning to 0.12 at the end of Stage 1 (Figure 5-44).

5.4.1.2 LNAPL mass movement during stage 2

During the stage 2, the water table recovered from the lowermost position to the oscillation centre, where the LNAPL tail switched to the LNAPL front. Consequently, the upper boundary of LNAPL lens changed from a fingering shape to an evenly horizontal boundary due to the resistance of water content within the pores that prevented LNAPL from entering. The LNAPL smearing length progressively increased as the LNAPL being raised up by the advancing water table. Meanwhile, the

average LNAPL saturation of the main LNAPL lens diminished from greater than 0.7 at T=4h (Figure 5-25 (a,c)) to 0.65 at T=5h (Figure 5-26 (a,c)). The three-banded LNAPL body gradually formed where the LNAPL front was the most LNAPL dense band (with an average saturation larger than 0.5), following by two less saturated bands with average saturations of 0.3 and 0.1 respectively (Figure 5-27(a,c)). Up till this moment, the three bands were still connected to each other. It could be found in Figure 5-44 and Figure 5-45 that the quantity of LNAPL resided above the water table decreased significantly from 98% to 70% with LNAPL saturation increased from 0.12 to 0.14, while the LNAPL quantity below the water table surged from less than 2% to 30%.

5.4.1.3 LNAPL mass movement during stage 3

During the stage 3, the water table continued to elevate from the oscillation centre to the uppermost position. The most remarkable feature emerged during this stage was that a significant amount of LNAPL was still entrapped around the lowermost position of the oscillation (35~45cm), forming a fourth discrete and uneven LNAPL band (Figure 5-28(a,c)). It seemed as if the lowly saturated LNAPL band was torn off from the LNAPL main body and left behind as entrapped saturation in a predominantly water-LNAPL system, whereas the LNAPL front continued to be pushed up by the rising water table, with an intermediately saturated band as its tail. The thickness of the highly saturated LNAPL band further reduced to 3cm with an additionally diluted saturation of 0.6. It was evident in Figure 5-29 (a,c) and Figure 5-30 (a,c) that the lowly saturated tail of LNAPL body redeveloped behind the intermediately saturated band, whilst the residual LNAPL entrapped at the bottom co-existed. Once formed, the residual LNAPL band at the bottom was mainly made up of immobile LNAPL, which stayed fairly settled unless the LNAPL-water two-phase system was repeatedly disturbed by significant pressure changes and/or fluid phase system changes. In-between the immobile LNAPL band at the bottom and the tail of the LNAPL front, there existed a lowly saturated three-phase body with fingering, which will be introduced the air entrapment Section 5.4.2.

The overall thickness of LNAPL lens recovered to approximately 9cm at T=9h including the intermediate saturated tail with a lower average saturation compared to T=3h (the lowermost water table position). The LNAPL tail and the LNAPL smearing length appeared to be the longest of all time, which resulted from the advancing LNAPL front being gradually trapped behind and the ascending water table gradually picked up residual LNAPL entrapped during the first water drainage. This indicated that an increasing amount of LNAPL body was not provided with enough pressure to exceed the entry pressure of upper pores and thus left behind, which further exhausted the LNAPL total pressure and left more LNAPL entrapped.

From Figure 5-44 and Figure 5-45 that the average saturation of LNAPL above the water table went up rapidly from 0.15 to 0.22, whilst a steady decrease in the saturation below the water table could be monitored. From the volume perspective, a reduction in the volume above the water table was observed from 70% to 61%, whilst the volume left below the water table appeared otherwise. The biggest LNAPL volume below the water table occurred during this stage with 40% at T=7h.

5.4.1.4 LNAPL mass movement during stage 4

During the stage 4, three distinguished zones were still noticeable (e.g. Figure 5-30), which respectively were: 1) the LNAPL polluted zone with the LNAPL front, intermediately saturated tail and lowly saturated tail; 2) the three-phase zone with residual LNAPL saturation in a three-phase system, coexisting with residual water saturation and air contents; and 3) the entrapped LNAPL zone at the lowermost position, which remained the same throughout the period. The LNAPL tail was forced to switch to the LNAPL front again at the beginning of this stage due to the direction change of water table. As the water table descending, a lag formed between the water table front and LNAPL front. Along the moving path, the LNAPL front gradually picked up the entrapped LNAPL to expand, while leaving a trace of residual immobile LNAPL behind. Accordingly, during stage 4, the thickness of LNAPL lens including the intermediately saturated tail further increased from 9cm at T=9h, to the maximum thickness of 12cm at T=11h, and then shrank to 8cm at T=12.

A small increment in the average LNAPL saturation above the water table could be observed from T=9h at 0.22 to T=10h at 0.23 (Figure 5-30 and Figure 5-31), which was the highest average saturation above the water table observed during the entire process. Whereas the volume of LNAPL above the water table went up acceleratedly and spiked at the end of Stage 4 at 84.7% (Figure 5-33 and Figure 5-45).

In summary, some implications could be inferred from the process analysed above. Firstly, it might be difficult to observe and quantify pollutant source terms at the low water table positions, such as late summer, low tide, or under a high groundwater abstraction rate. The LNAPL body might be completely dispersed along the water table pathway, leaving no LNAPL lens presented. It also indicated that by lowering the water table down, the original LNAPL source zone could further contaminate the deeper aquifer. LNAPL free phase re-accumulated at the water table when the water table was around maximal elevation, which could potentially be used to locate, evaluate or evacuate the LNAPL lens (e.g. spring, high tide, artificial recharge).

5.4.2 Water and air behaviours during a single-cycle of water table fluctuation period

Figure 5-34 illustrates the time-dependent vertical saturation distribution profiles of water, LNAPL and air. Figure 5-21 (e) to Figure 5-33 (e) presented the shaded profiles of fluids with pore space occupancy. During stage 1, the water profile appeared as a standard drainage curve since below the water table it was fully water saturated. No fluid phase system change occurred, until the water table started to recover at the beginning of stage 2. However, above the water table, the predominantly water-LNAPL two-phase system was gradually replaced by a primarily LNAPL-air system with residual water saturation. At this moment, LNAPL and air were competing for the pore space vacated by water drainage, and since LNAPL was the wetting fluid compared to the air, LNAPL would be the preferential fluid to be retained by most pore space, while there was still a considerate amount of air occupying the big pores. No air was entrapped below the water table by this moment. Above the water table in the LNAPL body zone, air entrapment was found with a maximal saturation of 0.1, which was previously pushed into the capillary zone by the LNAPL front.

During stage 2, the rising water table started to displace the LNAPL and air. Despite the considerably lower densities of air and LNAPL where they had the tendency to float, a significant amount of LNAPL and air entrapment formed. The entrapped air volume below the water table increased to 3.6% at the end of this stage with an average saturation of 0.025. Meanwhile, the average water saturation below the water table decreased from 0.99 to 0.92 due to air entrapment and residual LNAPL. The residual air and LNAPL were not entirely immobile, part of which still followed the ascending water table.

A similar trend for the distributions and dynamics of water and air could be observed during Stage 3. The average water saturation below the water table continued to decrease gradually (from 0.91 to 0.86) due to the occupancy by residual LNAPL and entrapped air along the dynamic range of the water table. And the increasing average air saturation below the water table tripled at 0.10 at the end of Stage 3 compared to the end of Stage 2. The total volume of air increased expeditiously from 7.0% at the beginning to 43.9% due to fast water ascending. A more densely air-saturated band formed around 42cm to 50cm at T=7h (Figure 5-28). This was caused by ascending air originally accumulated at the bottom of the tank when the water table was at the lowest position.

During Stage 4, as the water table descending, the average saturation of the newly formed densely air-saturated band increased. It was due to the compression of the residual air by the quickly descending water table. The average air saturation below the water table gradually decreased from 0.10 to 0.07, whereas the total volume of air below the water table responded to the water table

descending much slower, which remained around the maximum value of 0.47for 1.5 hours (Figure 5-30(d) and Figure 5-31(d)), then started to decline rapidly at 0.18.

5.4.3 Modelling perspective during a single-cycle of water table fluctuation period

One disagreement was observed in the LNAPL and air distributions in the unsaturated zone throughout the fluctuation period. The fluctuation modelling was performed in 1-D due to computational limitations. Therefore, the previous LNAPL release imported as the pre-condition of the fluctuation period modelling had to be additionally simulated in 1-D due to compatibility requirement of the code. Hence, the beginning of the fluctuation modelling in 1-D was slightly different the 2-D simulation, the comparison of which is illustrated in Figure 5-35. The 1-D boundary condition, where only 2 nodes were allowed horizontally instead of 31 nodes in the 2-D simulation, mandates the LNAPL being released through these 2 nodes, which is the entire width of the tank. Not allowing 2-D structure (release LNAPL in a much longer 1-D source) resulted in a larger average LNAPL saturation being retained in the upper unsaturated zone, and consequently, a smaller air saturation.

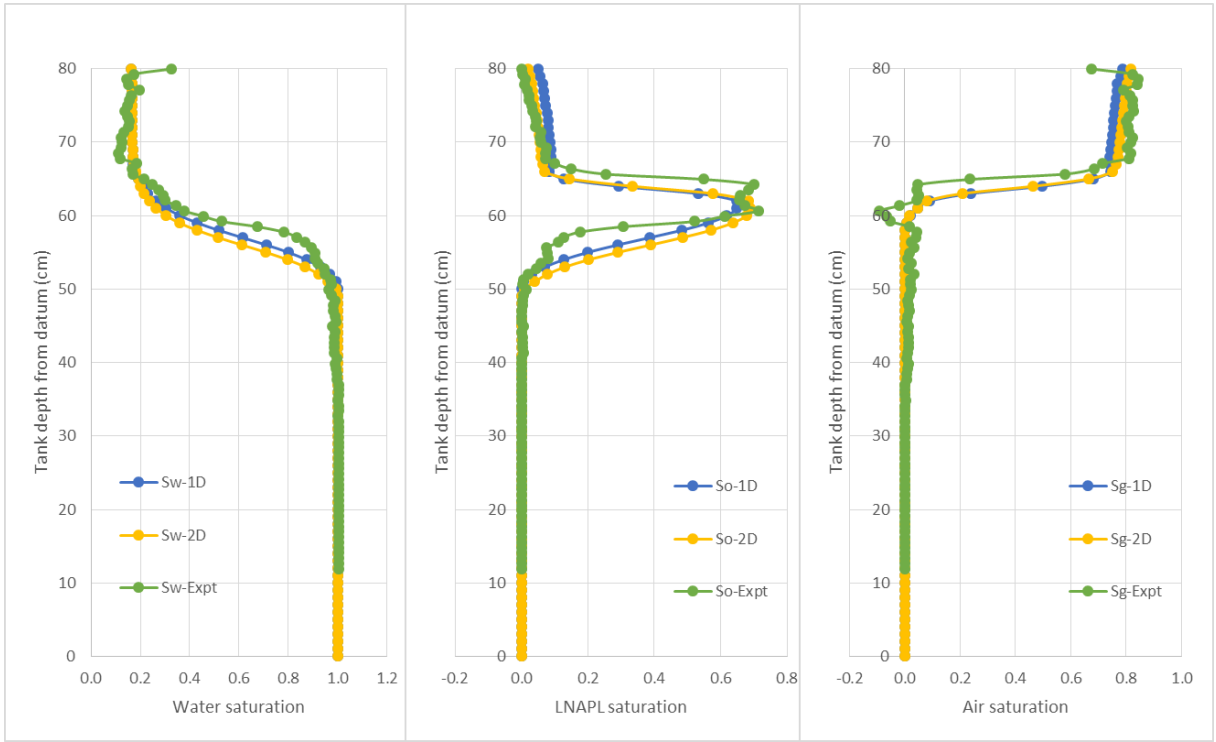

Figure 5-35 A comparison of the 1-D, 2-D modelling and experimental data for the beginning moment of the fluctuation simulation T=0h (Compared with Figure 5-21)

The simulation for the fluctuation period is illustrated in the following four figures. To highlight the hysteresis effect, the simulation was run twice, one with hysteresis and one without. The following

analysis will focus on the comparison between experimental and modelling results first. Following by the comparison between non-hysteretic and hysteretic modelling results.

A small disagreement was found for the LNAPL peaks in Figure 5-36 to Figure 5-38 where the modelling LNAPL saturation for both hysteretic and non-hysteretic was smaller than the experimental result. It was reckoned that the limitation of the image analysis at high saturated conditions was responsible for the difference, where the peak values predicted by the model was more accurate. It could be inferred from the gas distribution curves that the LNAPL peak values resulted in local negative gas saturation values, which confirmed that it was mostly likely to be an overestimation of LNAPL saturations by the image analysis. Furthermore, the image analysis was also considered to be responsible for the underestimation in low LNAPL values from 45~60cm elevation in Figure 5-38. This resulted in an increasing air saturation observed in the profiles where the trapped air volume should remain stable, where the modelling result was more accurate on this prediction.

Another disagreement was found in the gas profile in the saturated zone, where the experimental result showed a small amount of air entrapment (combining mobile and immobile air) within the residual LNAPL band at the lowest of the fluctuation position. As analysed previously, a small amount of air entrapment at this position was observed experimentally during LNAPL release and more air entrapment was induced by fast water drainage and corresponding LNAPL invasion. This phenomenon could only be obvious in a heterogeneous system which might increase air entrapment and prevent air from migrating upwards with water table ascending.

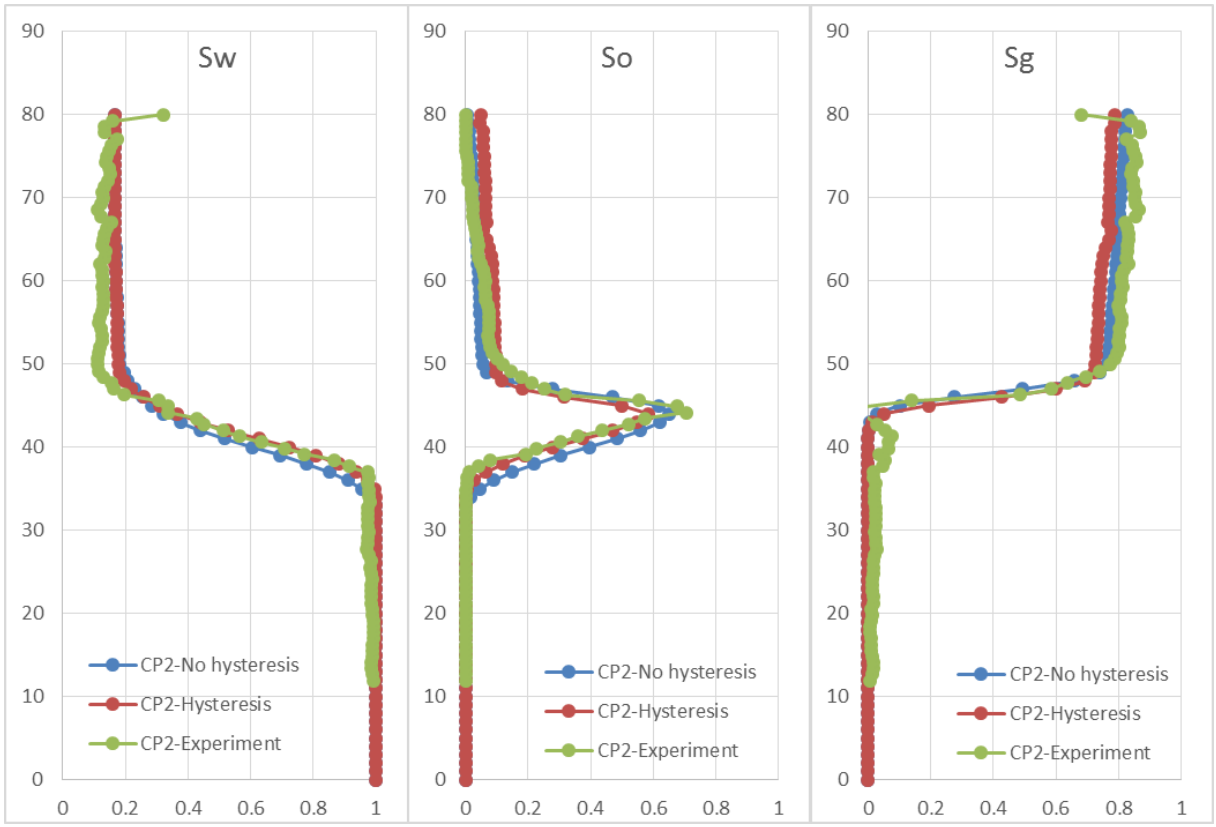

Figure 5-36 Modelling result in profiles of the first water table fluctuation at T=3h (In comparison with Figure 5-24)

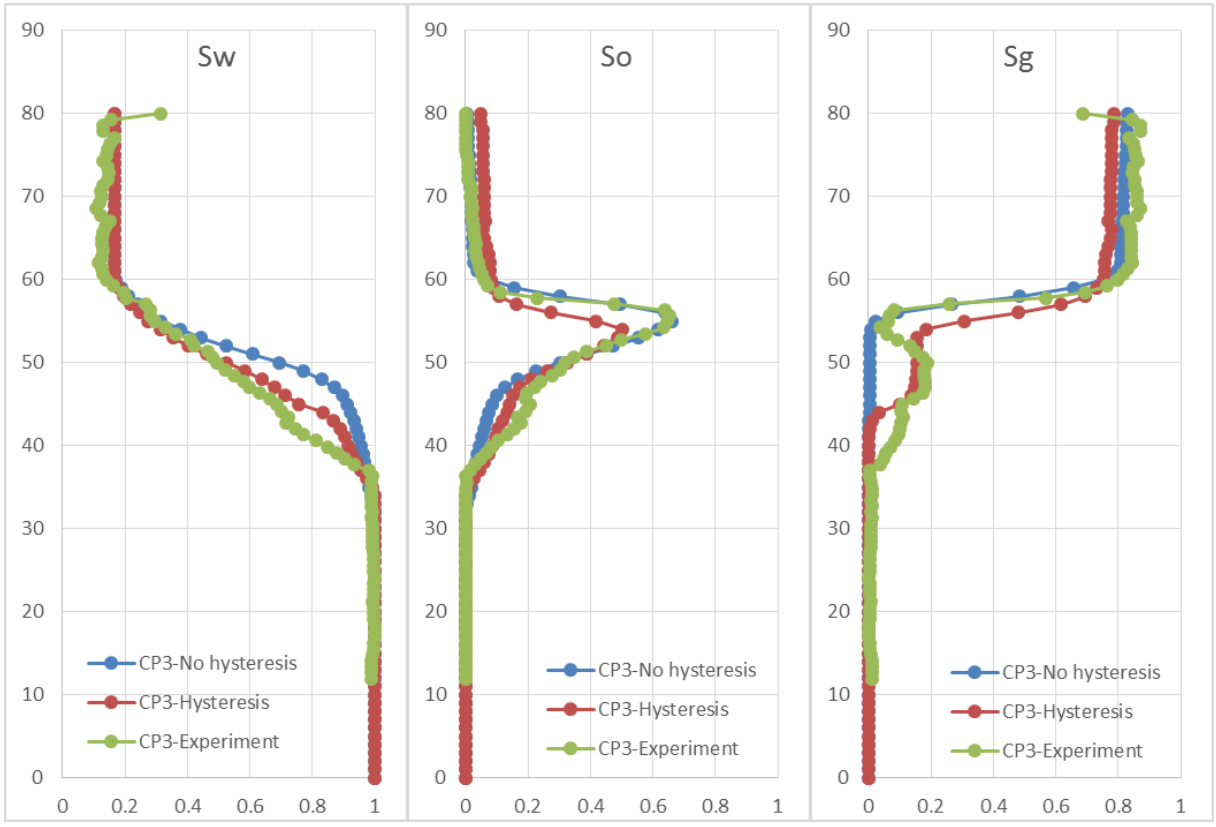

Figure 5-37 Modelling result in profiles of the first water table fluctuation at T=6h (In comparison with Figure 5-27)

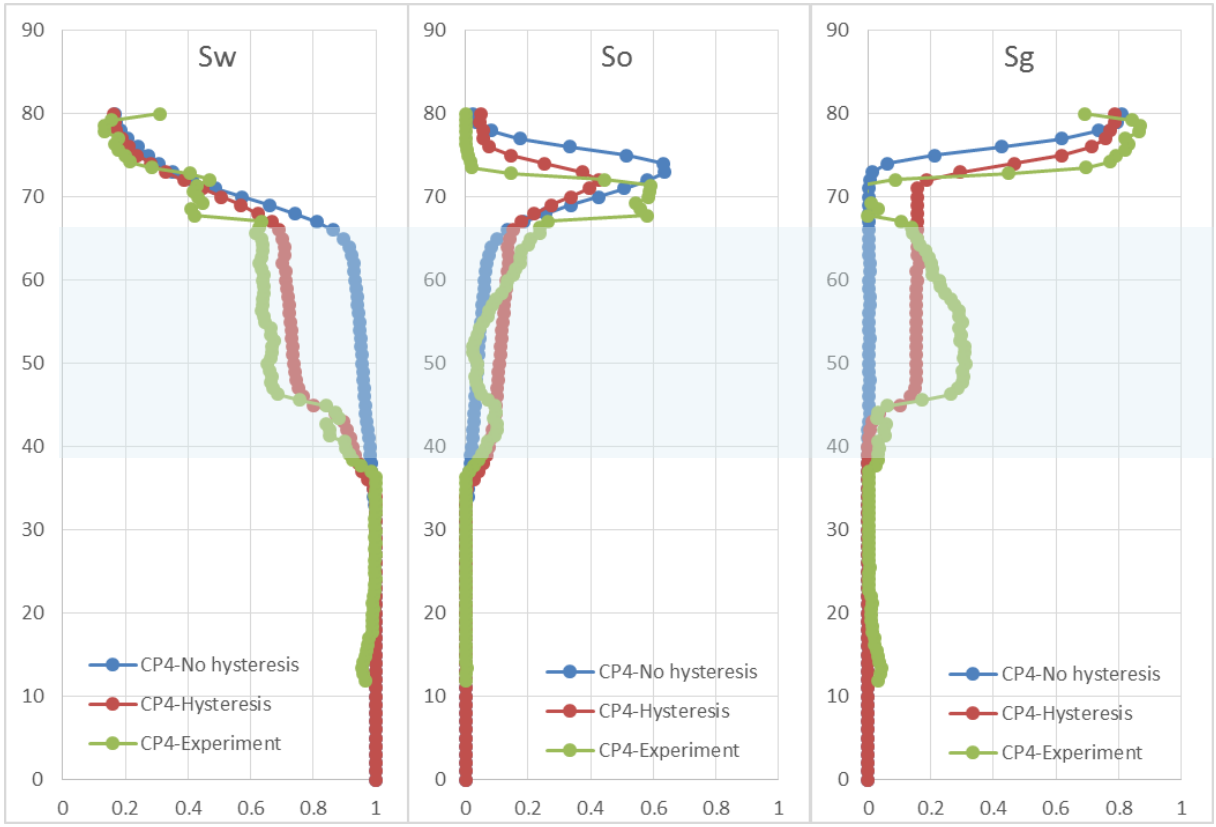

Figure 5-38 Modelling result in profiles of the first water table fluctuation at T=9h (Compared with Figure 5-30)

Figure 5-39 is a comparison between non-hysteretic, hysteretic and experimental results of a water drainage curve for and a water imbibition curve at WT=50cm. It is obvious that the hysteretic modelling captures more characteristics of the experimental results than the non-hysteretic modelling. Since the drainage curve is obtained from critical position 1 of the first cycle, the different effective saturations caused by hysteresis have not come into effect, the difference between non-hysteretic and hysteretic modelling remains small. However, at critical position 3 which is represented by the imbibition curve, the different effective saturation definitions had been taken effect since critical position 2. Therefore, the difference is significant. The red dashed square in Figure 5-39 highlights the significant difference in air saturation at elevation 35~55, which also reflects the difference in NAPL and water saturations at the same elevation. The variable effective saturations defined by the hysteretic modelling fit the experimental curves better; whereas the fixed saturation definition of all phases defined by non-hysteretic modelling cannot adequately represent the characteristics of a highly mixed three-phase system under transient water table fluctuation.

The shaded area in Figure 5-38 also highlights that the fixed definition of water, LNAPL and air saturations by the non-hysteretic modelling are significantly different from the experimental results. It is clear that these differences in Figure 5-38 (Critical position 4) have been aggravated from critical position 3. Thus it can be predicted that after several cycles of fluid mixing, the difference may be further exaggerated, which, however cannot be investigated here. Therefore it is recommended that the modelling of three-phase system under transient water table fluctuation conditions should include hysteresis.

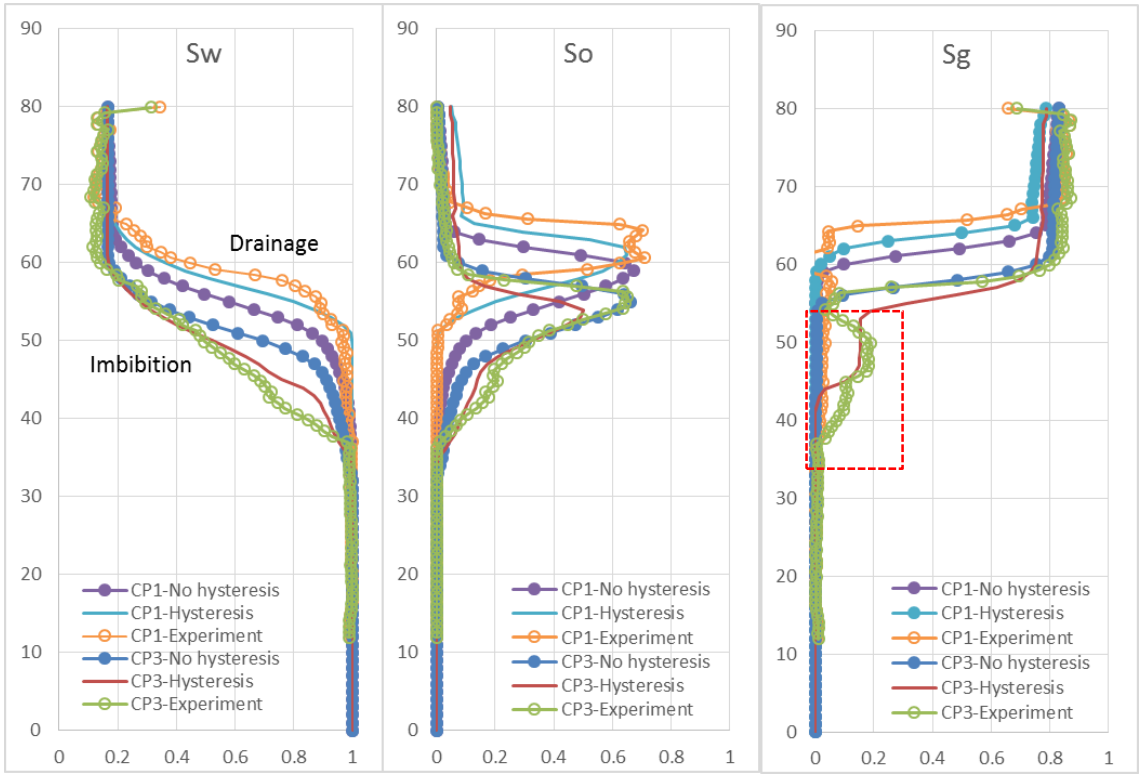

Figure 5-39 Scanning curve for non-hysteretic, hysteretic and experimental results (WT=50cm, critical position 1 and 3)

The simulation of the subsequent water table oscillations was attempted yet unsuccessful. The model stopped to converge at the beginning of the second oscillation, which may be caused by the complexity of effective fluid saturations redefined during every direction change of water table. Unfortunately, further investigation on the extremely complex hysteretic three-phase K-S-P modelling and corresponding sensitivity analysis could not be conducted due to time constraint.

5.5 Results and discussions of inter-cycle patterns during the water table fluctuation period

The main observations of the inter-cycle evolution are made by comparing the three-phase fluid distributions at four distinguished critical positions at different water table fluctuation cycles:

Critical position 1 (Figure 5-40): The starting point of every water table fluctuation cycle, which locates at the oscillation centre (at 50cm) with the water table descending;
Critical position 2 (Figure 5-41): The lowest water table position (at 35cm) of every fluctuation cycle;
Critical position 3 (Figure 5-42): The position at the water table oscillation centre (at 50cm) with the water table ascending;
Critical position 4 (Figure 5-43): The highest water table position (at 65cm) of every fluctuation cycle.

Key observations are summarised below and elaborated upon in the underlying discussion with reference to the figures.

- After the first water table fluctuation cycle, a band of immobile LNAPL formed upon and within the depressed capillary fringe at the lowermost water table position.
- Cyclic water table fluctuations enhanced the LNAPL smearing across the entire range. The aggravation on LNAPL entrapment by cyclic fluctuations was complicated. In general, the enhancement of residual LNAPL at the lowest water table position was evident. However, in the original unsaturated zone, cyclic fluctuations were shown to decrease the residual LNAPL saturation along the pathway.
- The biggest LNAPL peaks formed at the lowest water table position, where LNAPL lens thickness remained thin; and the largest LNAPL lens thickness occurred after reaching the highest water table position with water table descending, where the average LNAPL saturation of the lens was lower than the LNAPL lens at the lowermost positions.
- Due to the cyclic fluctuation, a small amount of air was permanently entrapped within the residual LNAPL band at the lowest water table position. Meanwhile, significant amount of air was mobilised with the water table and trapped below the changing water table.

For the visualisation of the complete process of water table fluctuation in the video format, refer to Appendices A.2.1.2 (2), and for the raw dataset of profiles refer to the Appendices A.2.1.1 (2).

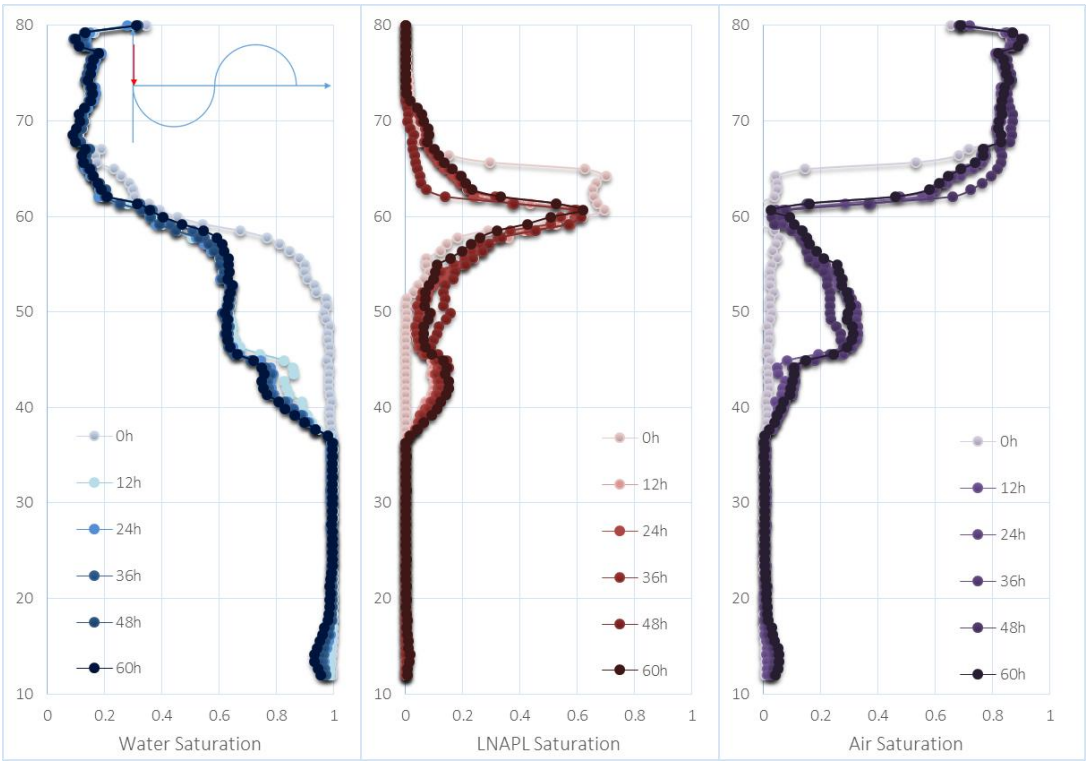

Figure 5-40 Inter-cycle fluid saturation profiles at critical position 1 during the cyclic water table fluctuation period

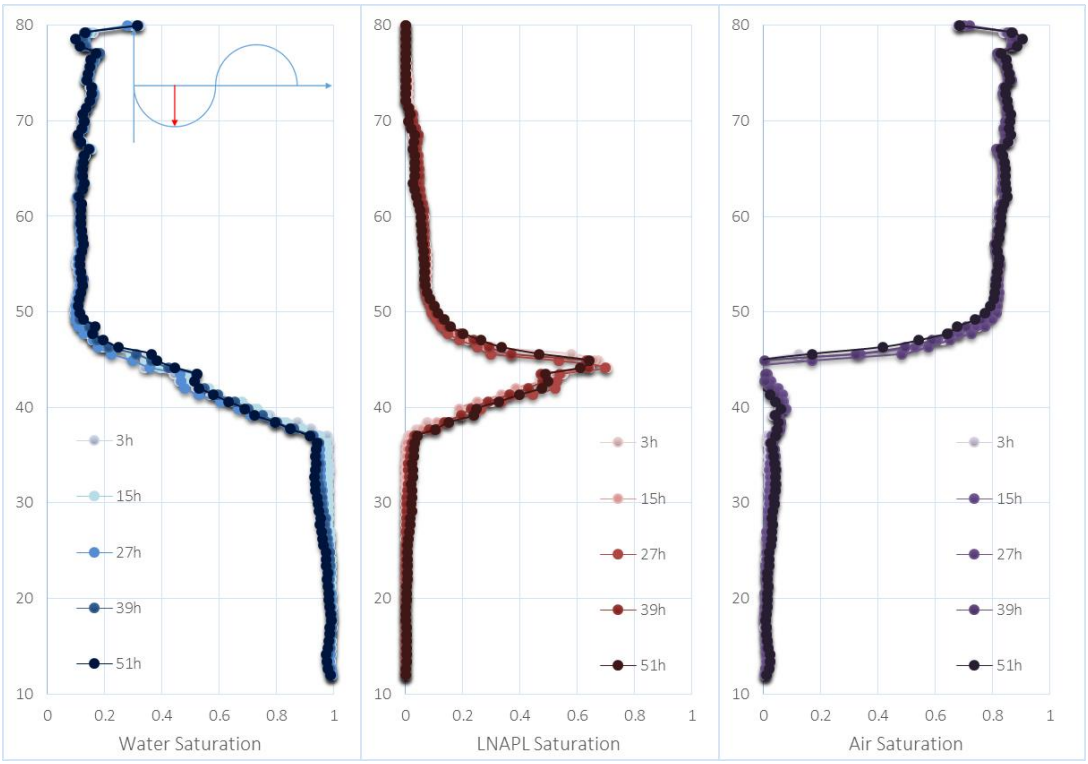

Figure 5-41 Inter-cycle fluid saturation profiles at critical position 2 during the cyclic water table fluctuation period

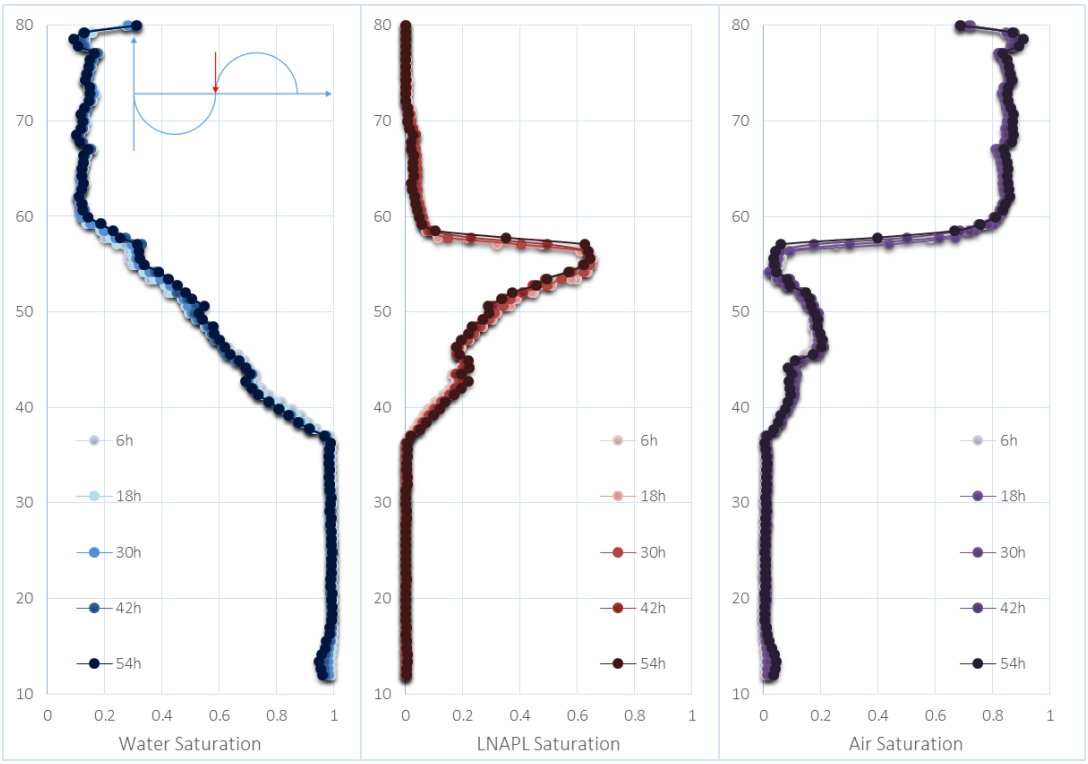

Figure 5-42 Inter-cycle fluid saturation profiles at critical position 3 during the cyclic water table fluctuation period

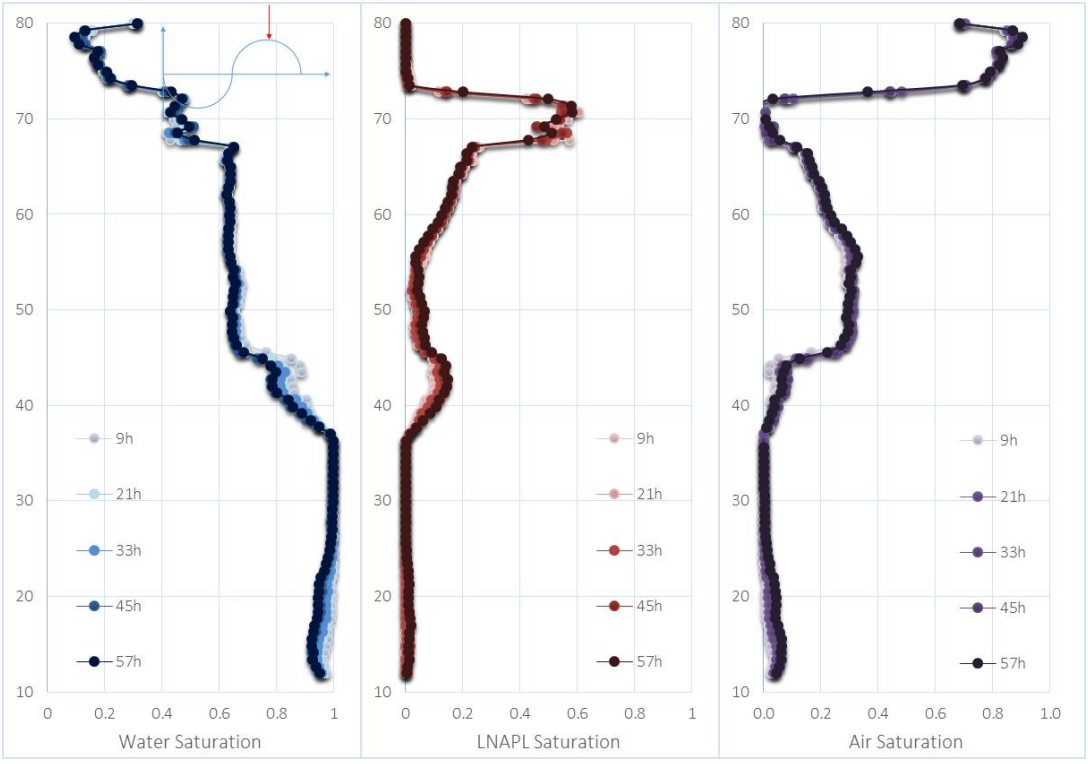

Figure 5-43 Inter-cycle fluid saturation profiles at critical position 4 during the cyclic water table fluctuation period

5.5.1 LNAPL migration and distribution variation during cyclic water table fluctuation

In general, visual observation of the experiment demonstrated fairly repeatable behaviour at subsequent four oscillations. However, the behaviour of LNAPL migration and redistribution was not identical by examining the detailed profiles and overall dynamics. A number of distinctive features and cyclic patterns could be discovered by comparing the following oscillations against the first oscillations.

Critical position 1 (Figure 5-40 (b)) displays the differences on fluid saturation distribution between the first oscillation and the four subsequent oscillations that a band of predominantly immobile LNAPL formed after the first oscillation near the depressed capillary fringe at the lowest water table position. Before the oscillation, only one LNAPL peak existed; whereas two peaks, one above the water table and the other below could be observed in the subsequent oscillations at critical position 1. The peak above the water table was the LNAPL lens, which sharply decreased from a maximal saturation of 0.72 at T=0h to 0.64 at T=12h, which is the start of cycle2, and gradually settled down to 0.63 at T=60 after five oscillations. A noticeable decrease in the thickness, as well as a slight uplifting of the LNAPL lens, were also found as the result of cyclic water table fluctuations. The LNAPL peak below the water table was the predominantly immobile LNAPL band comprising residual LNAPL and a small portion of mobile LNAPL. The maximum saturation was 0.0 before the first cycle; 0.10 at T=12h, the beginning of the second cycle; and 0.16 at T=60h, the end of the fifth cycle. Furthermore, from looking at the LNAPL volume ratio above and below the water table (Figure 5-45), the first oscillation brought 18.1% LNAPL below the water table, and after five oscillations, the volume trapped under the water table went up to 30.6%. This indicates that cyclic water table fluctuations enhance the LNAPL entrapment, but only below the initial water table position at this crucial moment, especially the residual LNAPL band above the lowest water table position; whereas in the original unsaturated zone, the residual LNAPL saturation is moderately diluted by the cyclic fluctuations.

At critical position 2 (Figure 5-41 (b)), the two peaks formed at critical position 2 converged near the capillary fringe at the lowest water table position, where the biggest LNAPL peaks formed during the fluctuation period. The maximal saturation of this band gradually subsided from 0.72 to 0.66 with the fluctuations. However, the thickness of this band steadily increased from 9cm to 11cm. On the contrary, the LNAPL saturation in the unsaturated zone slightly decreased as the fluctuation gradually relocated more mobile LNAPL downwards into the original saturated zone.

At critical position 3 (Figure 5-42 (b)), the single LNAPL peak, i.e. the LNAPL lens, was raised up by the ascending water table, leaving a significant amount of LNAPL below the water table. A divide was

formed at around 44cm, which was the former capillary fringe location when the water table was at the lowermost position. Below the divide, the residual LNAPL band reinforced with the fluctuations going on where the maximal saturation grew from 0.18 to 0.23; whereas above the divide, the LNAPL saturations was showing marginally decrease below and above the water table. Being retained by the pores in the residual LNAPL band, the peak saturation of LNAPL lens decreased to 0.62.

At critical position 4 (Figure 5-43 (b)), the longest LNAPL smearing length formed with three LNAPL bands. The lowermost was the residual LNAPL band, where, a noticeable increase in maximal LNAPL saturation could be observed, which was 0.10 at the end of Cycle 1 and rose to 0.17 at the end of Cycle 5. Between the residual LNAPL band and the current water table position (i.e., from 44cm to 65 cm), there was a highly mixed three-phase lowly saturated LNAPL band, which created the biggest image analysis error of the entire fluctuation period. This was because the calibration for low LNAPL saturated samples were challenging and low LNAPL saturated conditions were extremely sensitive towards light variation. LNAPL was underestimated at this position. Therefore air was overestimated. The band above the water table was the 6cm thick LNAPL lens with a maximal saturation of 0.59, which was slightly diluted by the fluctuation condition.

To summarise, the photographic records and the corresponding analysis of the 5th oscillation indicated a strong similarity of the LNAPL distributions of the 1st oscillation, except for the beginning of 1st oscillation. The positions of LNAPL banding were fairly repeatable, while the fluid saturation distributions for the banding were slightly different. This suggested that the first water table fluctuation was the key pattern for the following oscillations. Cyclic water table fluctuations were shown to aggravate both LNAPL smearing and entrapment. However, the enhancement on the entrapment mainly occurred near the lower range of the fluctuation, whereas in the original unsaturated zone, LNAPL body appeared to be slightly diluted with the increase of water table fluctuation.

5.5.2 Water and air migration and distribution variation during cyclic water table fluctuation

For all the water and air profiles during the cyclic fluctuation period, one irregularity was observed at the first node at the uppermost of the tank, where water saturation was found exceptionally large (e.g. Figure 5-40 (a)) and thus air saturation was usually small (e.g. Figure 5-40 (c)). It was because a thin line of reflection light was found on the upper right corner of the tank, which the image analysis regarded as the existence of water, and correspondingly showing less air. This error could also be found and confirmed in every photographic record of the fluctuation experiment (e.g. the upper right

corner in Figure 5-21 (a)). Another repetitive error was observed at the lowermost water profiles and air profiles. It was due to ununiformed illumination at the tank bottom above the grey scale bar.

In general, from the profiles in Figure 5-40 to Figure 5-43 and the dynamics of fluid saturation distribution in Figure 5-44 and Figure 5-45, the repeatability appears fairly good for all fluids. The major influence of cyclic water table fluctuations on water and air distribution was that cyclic fluctuations facilitated and enhanced permanent air entrapment within the residual LNAPL band at the lowermost water table position (e.g. Figure 5-42 (c)). With the water table being oscillated, a small amount of air was entrapped permanently from slightly below the lowest water table to the top margin of the capillary fringe when the water table was at the lowermost position (Z=37cm~44cm).

Another influence by the cyclic fluctuations was that a considerable amount of air was brought into the system below the water table and mobilised simultaneously with the transient water table. The largest air saturations occurred at critical position 1, where the LNAPL lens was brought down by the water table, depressing the residual air resided along the pathway in the previous cycle(s). However, the maximal air saturation (Z= 44cm to 55cm of tank elevation) appeared in the contours and profiles at this moment was considered larger than the real values. This cyclic error was mainly caused by the image analysis, which tended to generate inaccuracy in a highly mixed three-phase system with extremely low LNAPL saturation. At this moment between Z= 44cm to 55cm of the tank elevation, the LNAPL saturation was underestimated. Correspondingly, the air was overestimated because air saturation was derived from the volume balance by water and LNAPL. This assumption could be confirmed by: 1) the mass balance result, where for this crucial position, the total volume of LNAPL calculated was less than the released volume; 2) by the modelling result introduced later. This error could potentially be improved by conducting three-phase calibration test, where water, LNAPL and air would be associated directly with light properties directly without applying volume balance. Furthermore, another contribution towards this error was that the accuracy of calibration relied on the geological setting to be homogeneous. However, in the tank system, local heterogeneity was unavoidable.

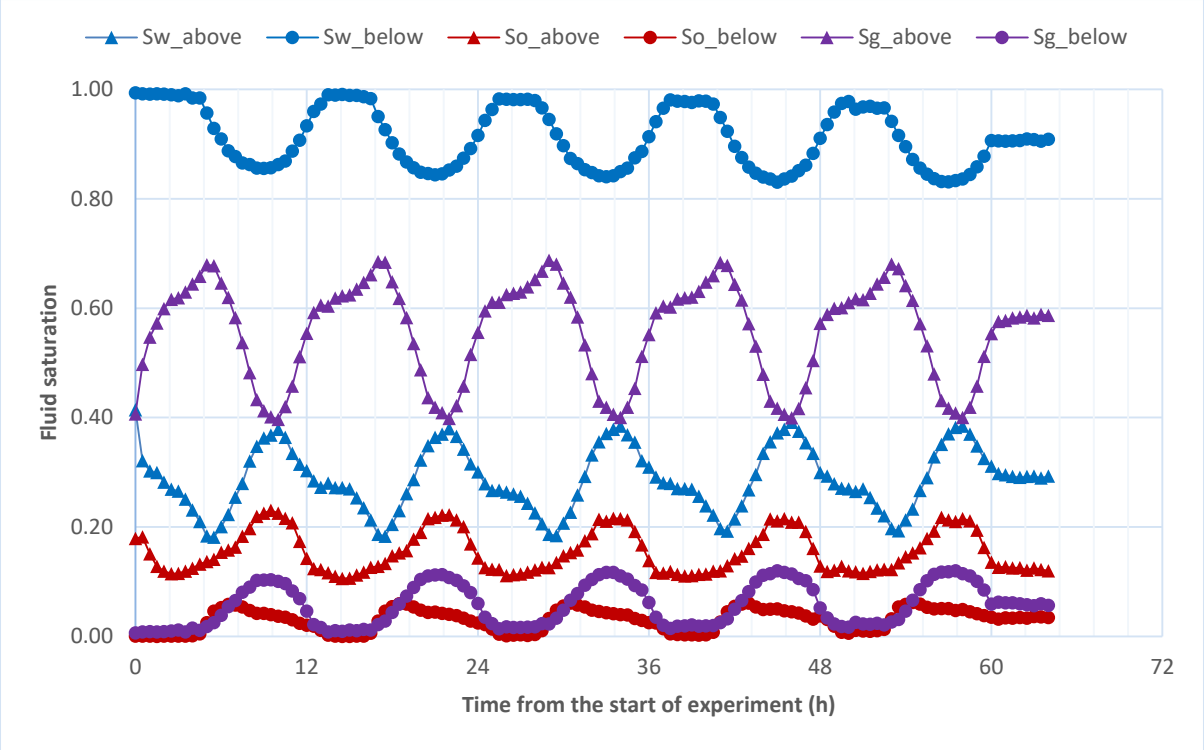

Figure 5-44 Time-dependent variation of the fluid saturation distributions (water, LNAPL and air) below and above water table during 5 cycles of water table fluctuation and the settling down period

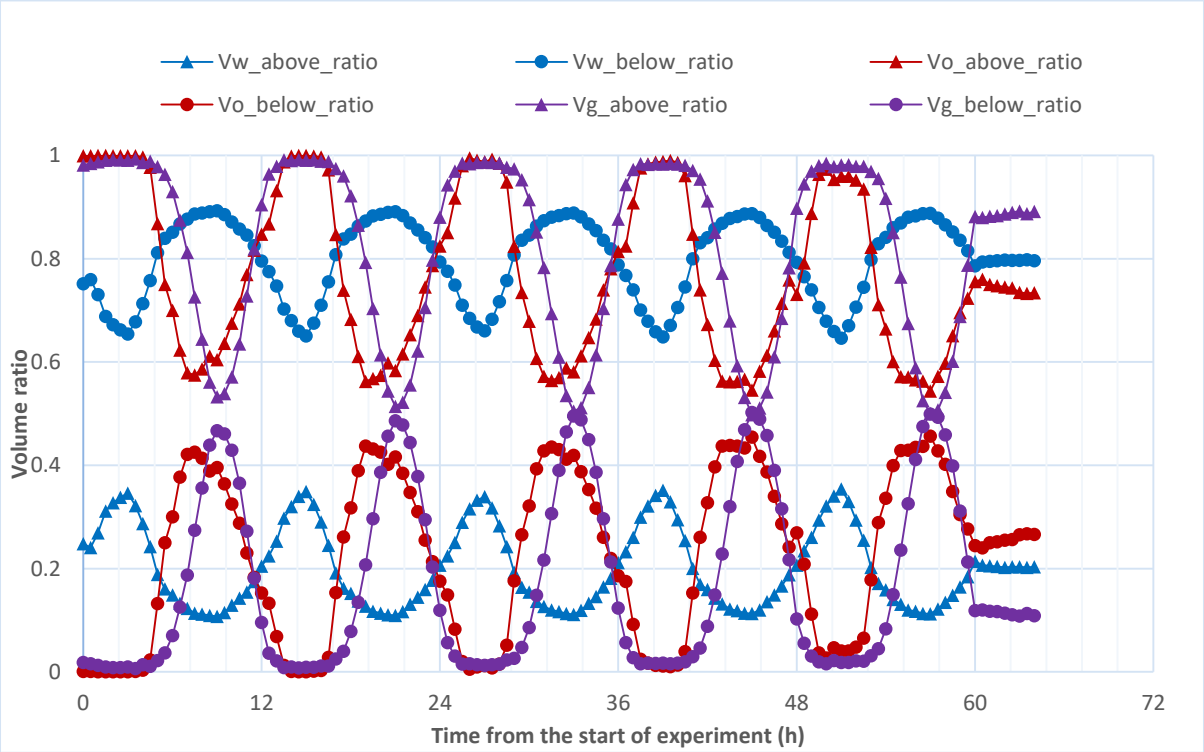

Figure 5-45 Time-dependent variation of the fluid volume distributions (water, LNAPL and air) below and above water table during 5 cycles of water table fluctuation and the settling down period

5.6 Summary

This chapter provided a detailed discussion on the photographic records, the interpreted multi-fluid saturation contours and profiles, and modelling perspectives of the base case scenario (Run4T3), which was utilised as a benchmark for the following variant scenarios. Key findings in this chapter included substantial quantitative dynamic features of all immiscible fluids during both LNAPL release process and the subsequent 5-cycled water table fluctuations.

A slow, continuous LNAPL release upon a static water table would result in a complete LNAPL body, in a shape of a Mexican sombrero, occupying the unsaturated zone, capillary zone and occasionally the upper saturated zone. The body initially developed from the original source zone with vertical expansion and then horizontal spreading predominately. Then, depending on the release history and ambient aquifer geology, LNAPL could sometimes even penetrate the water table and become entrapped in the saturated zone with a small amount of air entrapment.

The first cycle of water table fluctuation was the controlling factor of the follow-up LNAPL migration and redistribution, which repeated the LNAPL smearing pattern in later oscillations and affected the entrapment of LNAPL residuals across the entire fluctuation range.

The major influence of cyclic water fluctuations upon LNAPL migration and redistribution were: enhancing LNAPL smearing across the entire water table oscillation range, immobilising a considerable amount of LNAPL around the lowest water table position, and entrapping air along the fluctuation path. The LNAPL saturation in the original unsaturated zone was on the contrary slightly diluted by the cyclic fluctuations. The biggest LNAPL peaks formed at the lowermost water table position and the longest LNAPL smearing lengths occurred at the uppermost water table position.

The major implications inferred from the dynamics observed were as follows. Tt might be difficult to observe and quantify pollutant source terms at the low water table positions, such as late summer, low tide, or under a high groundwater abstraction rate. The LNAPL body might be completely dispersed along the water table pathway, leaving no LNAPL lens presented. It also indicated that by lowering the water table down, the original LNAPL source zone could further contaminate the deeper aquifer. LNAPL free phase might re-accumulate at the water table when the water table was around maximal elevation, which could potentially be used to locate, evaluate or evacuate the LNAPL lens (e.g. spring, high tide, artificial recharge).

From the experimental and modelling result, the repeatability and accuracy of the experimental setup and its corresponding analysis were reconfirmed. Despite many simplifications and approximations made to develop the constitutive relationships and initial and boundary conditions, the model built was considered having the capability of reasonably describing the dynamics and features of the LNAPL release and water table fluctuation process.

References

Aggregate-Industries. (2012). Sand type at Leighton Buzzard silica sand quarry. from http://www.aggregate.com/products-and-services/aggregates-and-specialist-sands/specialist-sand/specialist-sand-quarries/leighton-buzzard/

Aztec-Oils-Limited. (2014). Aztec oils MSDS.

CL:AIRE. (2014). An illustrated handbook of LNAPL transport and fate in the subsurface. In M. O. Rivett (Ed.). London: CL:AIRE.

Freeze, R. A., and Cherry, J. A. (1979). Groundwater.

Hudak, P. F. (2004). *Principles of hydrogeology*: CRC Press.

Morris-Lubricants. (2012). Largo GP2 MSDS: Morris Lubricants.

USGS. (2016). Unsaturated Zone. from http://water.usgs.gov/ogw/unsaturated.html

Wikipedia. (2016a). Density. from https://en.wikipedia.org/wiki/Density

Wikipedia. (2016b). Surface-tension values. from https://en.wikipedia.org/wiki/Surface-tension_values

Wikipedia. (2016c). Viscosity. from https://en.wikipedia.org/wiki/Viscosity

6 Results and discussions 2: variant scenarios

To outstretch current understandings on the key influential factors and their impacting mechanisms upon LNAPL migration and distribution, this chapter presents extensive interpretations on the various scenarios produced experimentally. The influential factors investigated include: the water table fluctuation speeds (Section 6.1), the release timing at the lowermost water table position (Section 6.2), the LNAPL release volumes (Section 6.3), the aquifer media (Section 6.4), and three different layered heterogeneous aquifer systems(Section 6.5, 6.6 and 6.7). Among which, the heterogeneous scenarios are particularly interesting. The results of each experimental scenario, focusing on LNAPL behaviour, have been investigated in detail, and relevant comparisons made among scenarios. Restrained by time, only key discoveries and implications will be demonstrated for each scenario, where the complete datasets can be found in Appendices A.2.

6.1 The low fluctuation speeds scenario

Two short videos of the LNAPL release and fluctuation periods for the current scenario can be found in Digital Appendices A.2.2.2.

This section discusses the influence of fluctuation speed on the migration and (re)distribution of LNAPL. Comparisons are made between the base case (Run4T3) and the low fluctuation speed case (Run5T1), which oscillated the water table twice as slow as the base case scenario. Incidentally, the low fluctuation speed scenario (Run5T1) released 110ml LNAPL into the system within 32 minutes, slightly larger than other scenarios. To highlight the influence of the fluctuation speeds, a group of compilations (Figure 6-1 to Figure 6-4) are assembled to illustrate the LNAPL saturation distribution profiles of both scenarios and corresponding photographic records at the four crucial moments defined previously.

In general, the LNAPL release process in the low fluctuation speed scenario was adequately similar to the base case release, only with the infiltration depth smaller. It is because LNAPL preferentially invades the pores with the lowest entry pressure which are big pores with small total fluid saturation. After quickly occupying the available pores beneath the source zone, LNAPL is forced to spread horizontally in search of the easiest occupant pores to reside, rather than invades the fluid saturated area which possesses much bigger resistance. On the contrary, a small continuous release with

sufficient release volume resulted in a deeper penetration into the capillary fringe or even the saturated zone.

The cyclic patterns of the low fluctuation speed scenario appears fairly analogous to the features depicted in the base case scenario. However, small discrepancies are found in the temporal pattern of LNAPL migration and distribution between the two scenarios, which mostly result from the difference in fluctuation speeds.

Figure 6-1(a) to Figure 6-4(a) present the inter-cycle LNAPL saturation profiles of both cases when the water table was at critical position 1 to 4 of every cycle, and Figure 6-1(b,c) to Figure 6-4 (b,c) illustrate the photographic records of the fluctuation speed case. Figure (b)s are the snapshots for the current critical position in Cycle 1, and Figure(c)s are the snapshots for the current critical position in Cycle 5. No LNAPL existence was found below the water table at T=0 in Figure 6-1(b). The single LNAPL peak, which consisted of a single LNAPL band at that moment, was 10cm thick and with a maximal saturation of 0.76 that situated within and above the capillary zone. Only after the first cycle of water table oscillation, LNAPL entrapment in the saturated zone occurred and three LNAPL bands formed as discussed in Section 5.4.1. Similar to the base case scenario, cyclic fluctuations kept dispersing the original LNAPL lens and the LNAPL residuals in the original unsaturated zone, while enhancing the entrapment within the lowermost entrapped LNAPL band. Therefore, by the end of the 5^{th} oscillation shown in Figure 6-1(c), besides the shrivel LNAPL lens, the lowermost entrapped LNAPL band became increasingly evident and persistent. The maximal peaks of LNAPL saturations were found at critical position 2, and the maximal LNAPL lens thickness occurred at critical position 4. The photographic records in Figure 6-2 and Figure 6-4 were fairly identical with small differences in the fingerings. The fingering pathways were also similar only with differences in saturations, which indicated that local heterogeneity was the primary cause of the fingering.

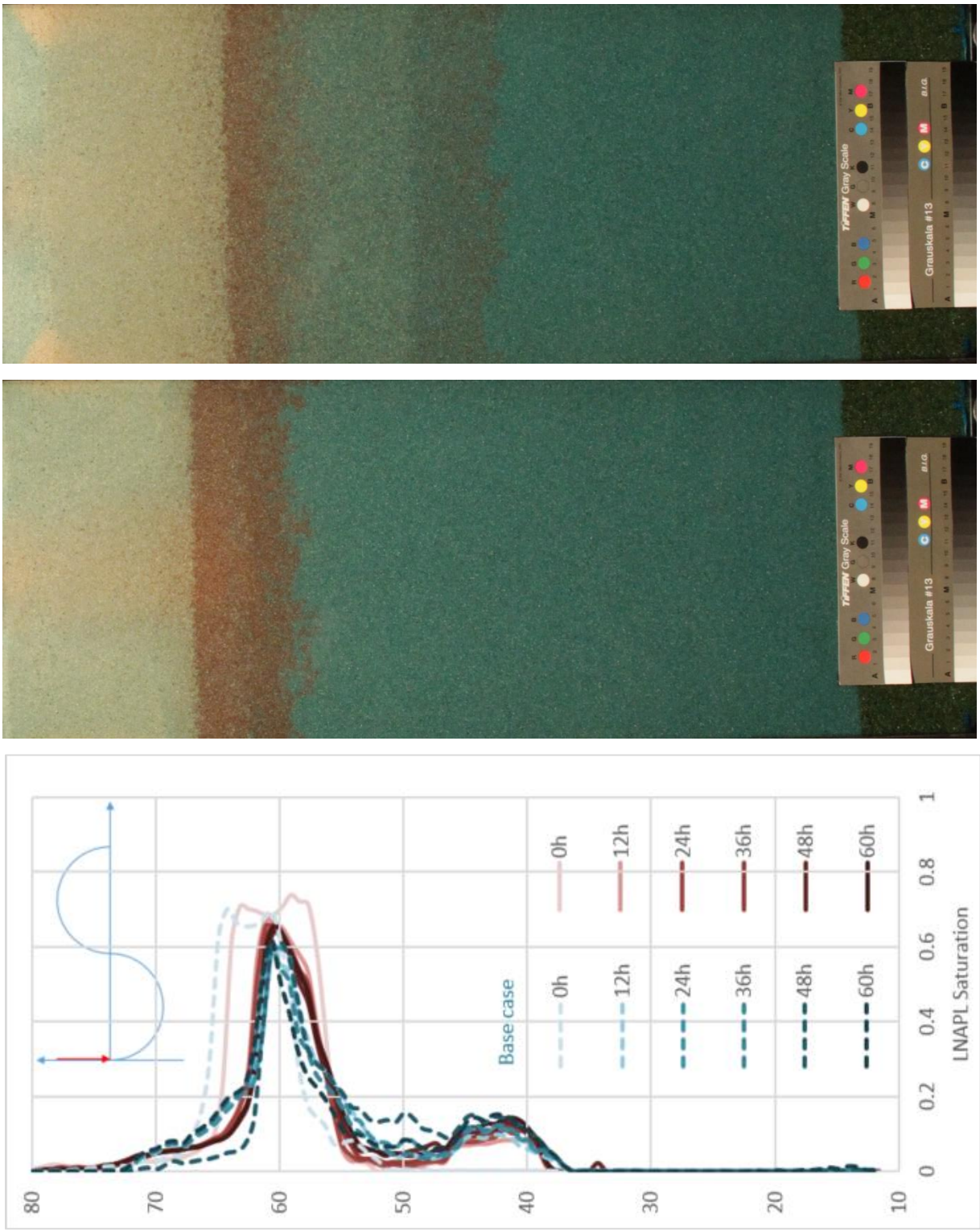

Figure 6-1 Inter-cycle saturation profiles at critical position 1 of the current scenario in red with the base case profiles superimposed in cyan, and photographic records of the 1st cycle and the 5th cycle of Run5T1 (WT=50cm)

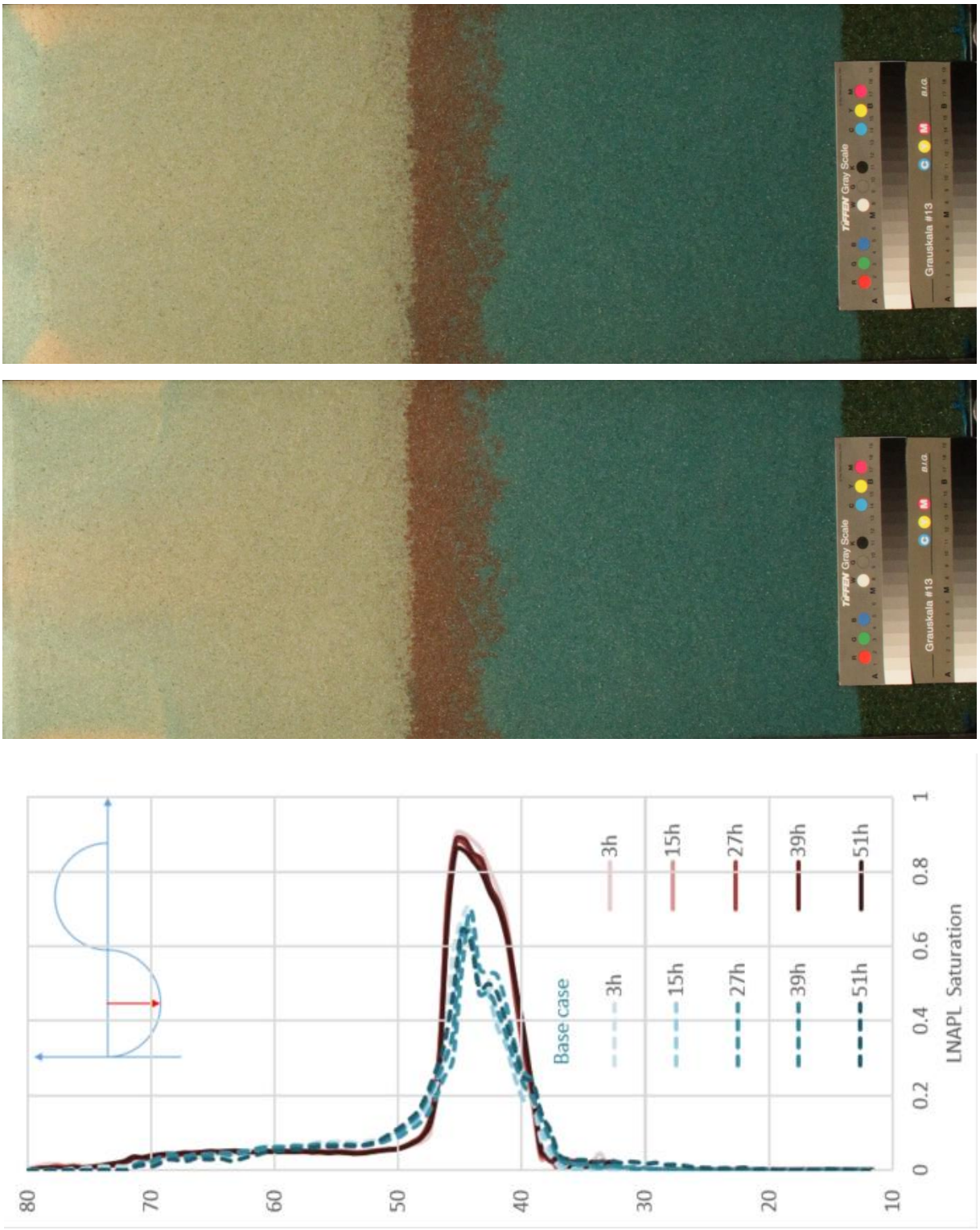

Figure 6-2 Inter-cycle saturation profiles at critical position 2 of the current scenario in red with the base case profiles superimposed in cyan, and photographic records of the 1st cycle and the 5th cycle of Run5T1 (WT=35cm)

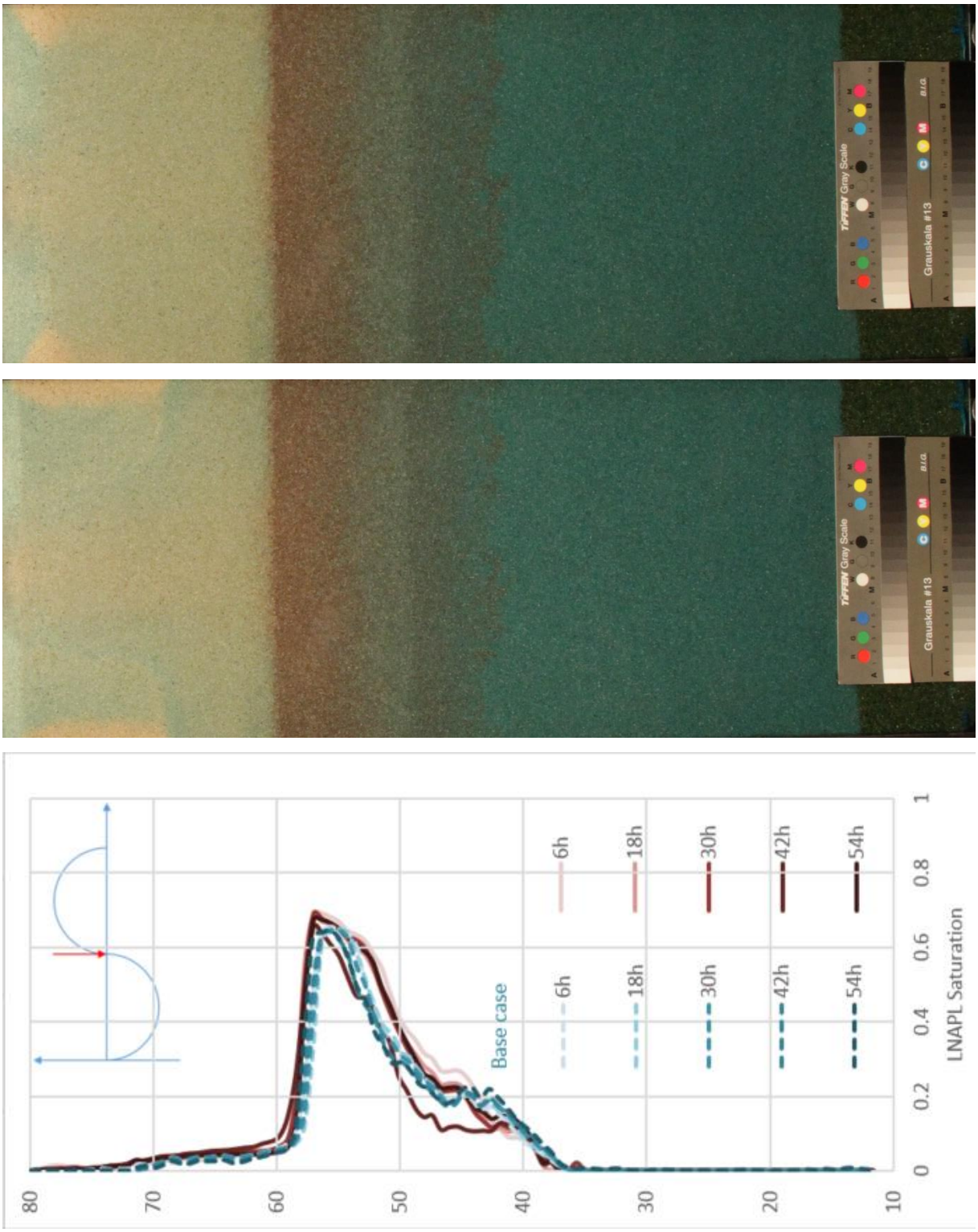

Figure 6-3 Inter-cycle saturation profiles at critical position 3 of the current run in red with the base case profiles superimposed in cyan, and photographic records of the 1st cycle and the 5th cycle of Run5T1 (WT=50cm)

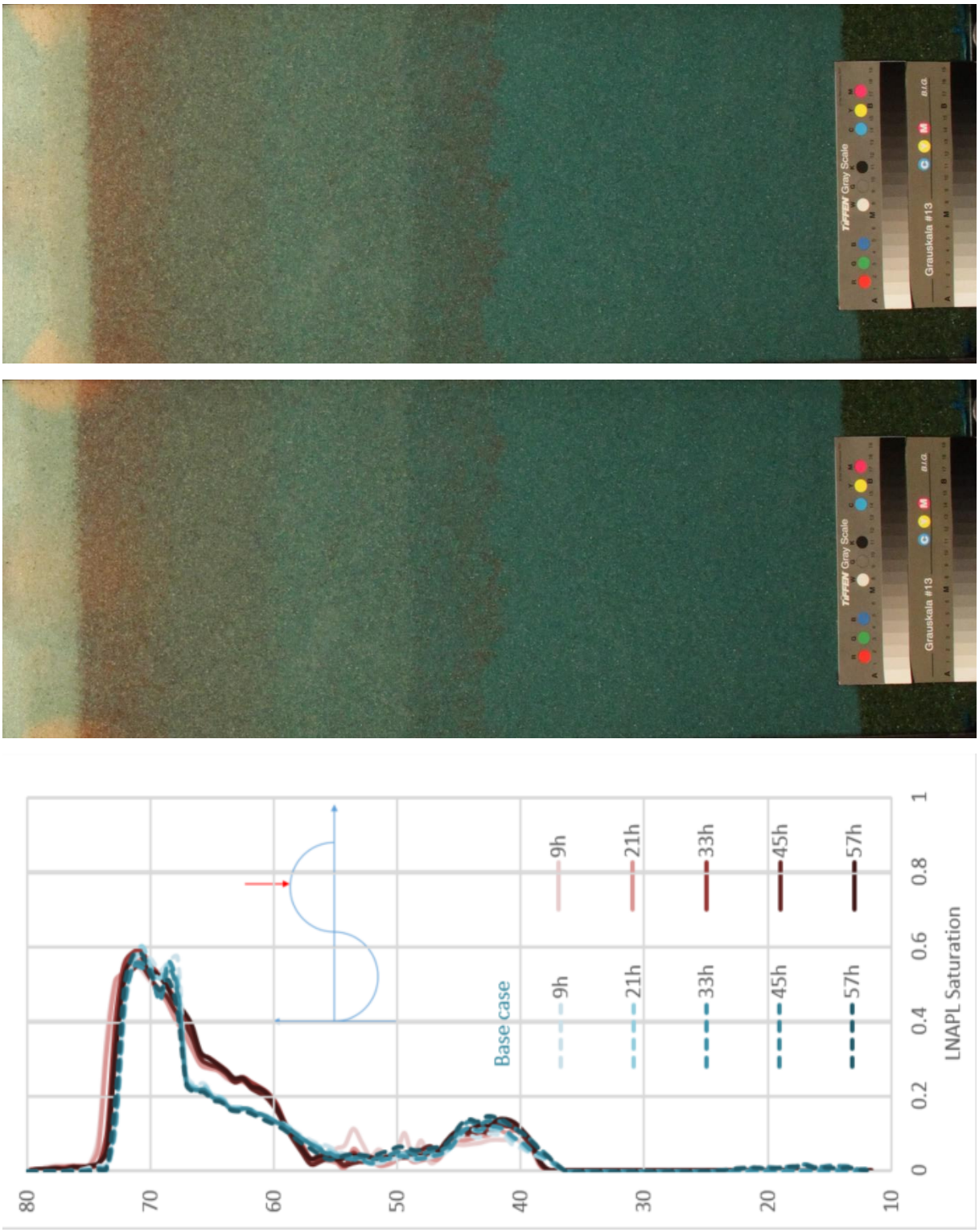

Figure 6-4 Inter-cycle saturation profiles at critical position 4 of the current run in red with the base case profiles superimposed in cyan, and photographic records of the 1st cycle and the 5th cycle of Run5T1 (WT=65cm)

By comparing the base case and the low fluctuation speed case, the key observations are:

- In the low fluctuation speed case, less entrapped LNAPL saturation was observed within the lowermost entrapped LNAPL band, and less LNAPL was trapped along the fluctuation range, which indicated that the residual saturations of LNAPL as both non-wetting fluid and wetting fluid were slightly smaller;
- Low fluctuation speed also resulted in more LNAPL content being mobilised by the water table;
- The average and maximal saturation of the LNAPL lens in the low fluctuation speed case was larger than those in the base case.

To briefly expand on the points above, a low fluctuation speed gives sufficient time for the phase displacement to carry out thoroughly, so that less LNAPL can be entrapped within the lowermost entrapped LNAPL band and along the pathway of water table fluctuation. Consequently, more LNAPL remains mobilised to follow the water table. Therefore, in Figure 6-1(a), above the water table, the average saturation and maximal saturation in the low fluctuation speed case appear larger than the base case, whereas the thickness of the combined LNAPL lens and the tail are smaller than the base case. In Figure 6-2(a), the maximal saturation of LNAPL peak of the low fluctuation speed case reached 0.9, yet leaving less LNAPL residual saturation beyond the LNAPL lens. It can also be observed that the thickness of the combined LNAPL lens and tail are smaller than the base case. It is because that in the low fluctuation speed case, LNAPL is more thoroughly mobilised so that it is allowed to follow the water table more tightly than the base case. In Figure 6-3(a) and Figure 6-4(a), only in the entrapped LNAPL band, the saturations appear smaller for the fluctuation speed case, whereas near the water table position, the quantities of mobile LNAPL emerge much higher than those in the base case.

6.2 The release timing at the lowermost water table positions scenario

Two short videos of the LNAPL release and fluctuation periods for the current scenario can be found in Digital Appendices A.2.3.2.

This section discusses the influence of the release timing relative to water table high or low positions. Comparisons are made between the base case (Run4T3) and the release timing scenario (Run9T1), which imposed the LNAPL release at the lowermost water table position at 35cm instead of the middle position at 50cm.

6.2.1 LNAPL release period

A total volume of 104ml of LNAPL was spilt into the system within 17 min, which was a relatively fast release that would result in a shallower puncture depth in the capillary zone. Most features of this process are reasonably similar to the base case scenario analysed in Section 5.3, except for the significantly thicker unsaturated zone. A selection of critical moments are presented in Figure 6-5 to Figure 6-8 to represent the characteristics of this release.

Figure 6-5 displays the vertical expansion within the unsaturated zone before LNAPL front started to invade the capillary zone. The shape of the LNAPL body at this moment appeared to be elliptical with the densest LNAPL saturation (0.6~0.7) distributed along the long axis. Water saturation in the unsaturated zone remained unchanged. It was because the fluid displacement occurred up till this moment was between LNAPL and air, where water saturation was residual, which would reveal a small decrease when the water-air two-phase system was gradually replaced by the water-LNAPL air three-phase system. Compared to the base case scenario, the long axis (length of the LNAPL body) and the short axis (the width) of the LNAPL body appeared larger, where the body width was 9.2cm in the base case and 11.8cm in the current scenario.

Figure 6-6 illustrates the end of LNAPL release. LNAPL intrusion was found within the capillary zone, where the LNAPL infiltration speed was dramatically slowed down, and the spreading speed accelerated. Two densest LNAPL saturated areas were located at the LNAPL front and beneath the LNAPL source zone. The LNAPL front thrust into the capillary fringe with the maximal saturation of 0.6, which was smaller than the base case release, albeit with a lower head. The reason was the sufficiently longer LNAPL pathway in the current scenario had led to a dramatic decrease in LNAPL pressure. Water displacement by LNAPL gradually took place. Air entrapment started to occur with a maximal saturation of 0.05 within the LNAPL front between Z=41cm to 45cm.

Figure 6-7 presents an example during the settling down period, where a considerable amount of LNAPL (with a maximal saturation of 0.7) had accumulated upon and within the capillary zone with significant water displacement and air entrapment (with an increased maximal saturation of 0.2). The LNAPL in the unsaturated zone had largely migrated downwards as the LNAPL source gradually exhausted. The shape of the LNAPL body was fully developed: the upper unsaturated zone body remained a thin ellipse; a tank-wide half ellipsoid spreading formed on top of the capillary fringe, and lower half ellipsoid spreading with fingering formed beneath the capillary fringe, which was only half the width of the body above the capillary fringe. As the capillary fringe acted as an LNAPL barrier and

highest LNAPL pressure was located at the central line of the LNAPL body, which could overcome the resistance of capillary zone and thrust the deepest. Whereas the LNAPL pressure around the edge of the body was exhausted by horizontal spreading, so that no LNAPL content could infiltrate beyond the capillary fringe.

Figure 6-8 demonstrated the end of the release monitoring where the LNAPL main lens was formed mostly upon and partially below the capillary fringe top boundary with a thickness of 4.5cm, which was significantly thinner than the thickness of 9cm in the base case scenario. A considerable amount of LNAPL was entrapped along the pathway, forming a larger contaminated body in the unsaturated zone. Therefore, the amount of LNAPL that reached the lower water table and constituted an LNAPL lens was considerably less. Meanwhile, air entrapment was reduced to a saturation of 0.1.

Figure 6-9 displays the 1-D dynamics of fluid profiles during the release, which quantitatively demonstrates the extension of LNAPL vertical infiltration and horizontal spreading before the end of release and the LNAPL shrinkage within the unsaturated zone during the settling down period. The decrease in the residual water saturation (from 0.14 to 0.11) due to fluid phase system change was also illustrated.

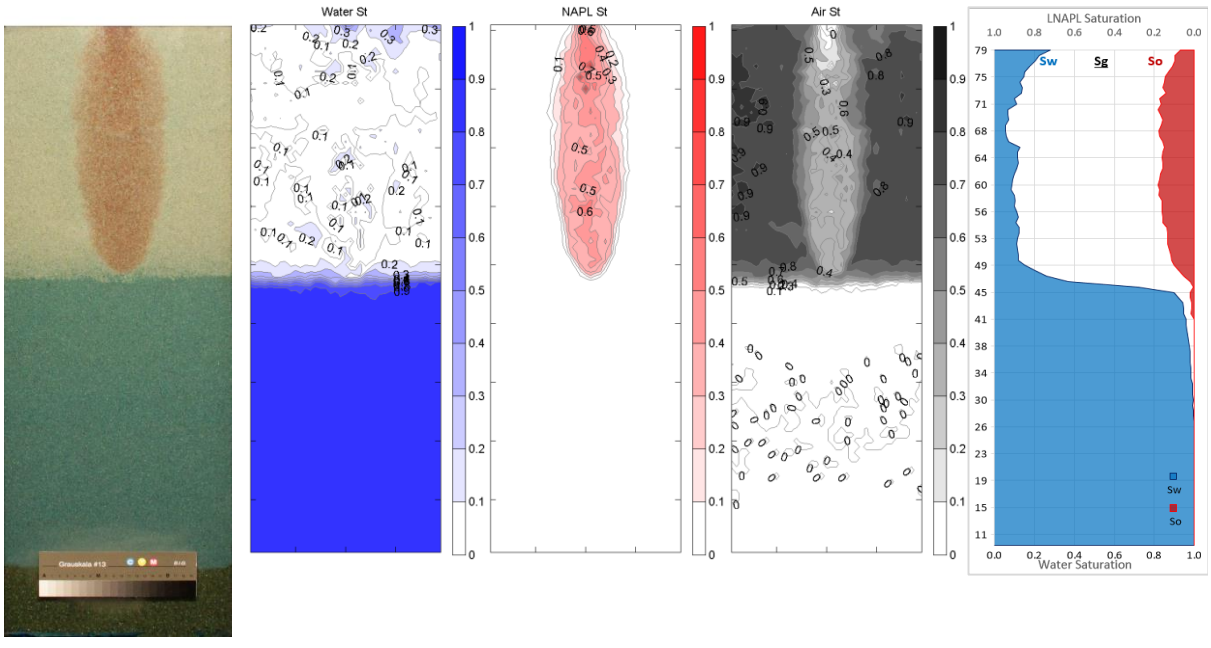

Figure 6-5 Compilation of saturation contours and profile for the LNAPL release of Run9T1 at T=12 min

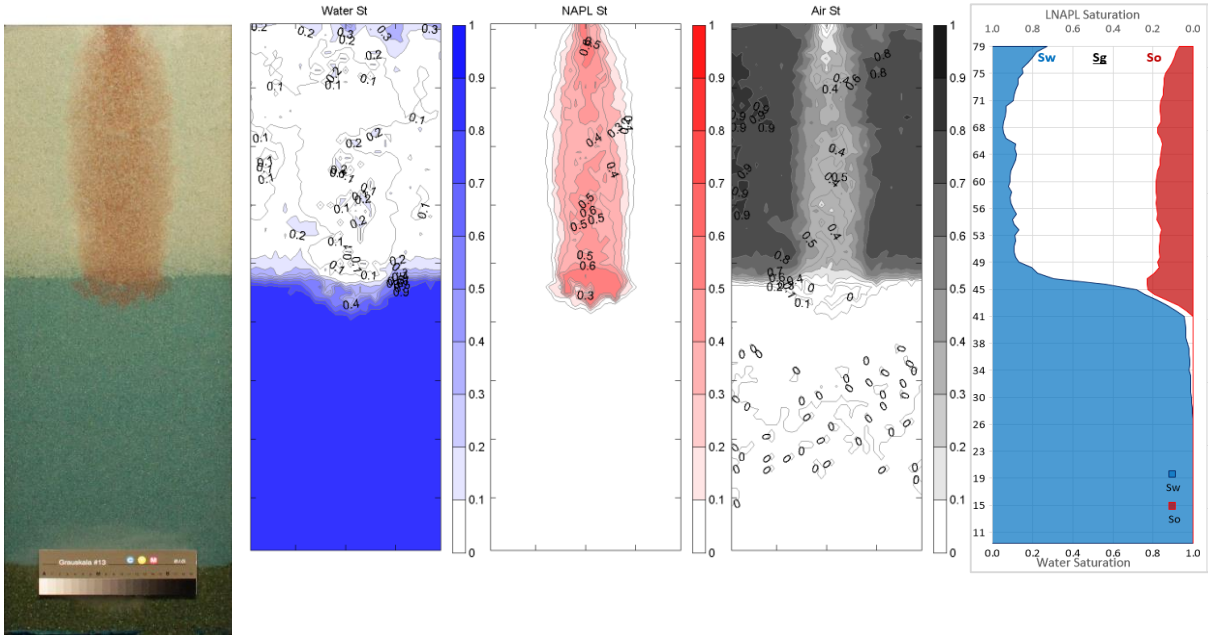

Figure 6-6 Compilation of saturation contours and profile for the LNAPL release of Run9T1 at T=18 min

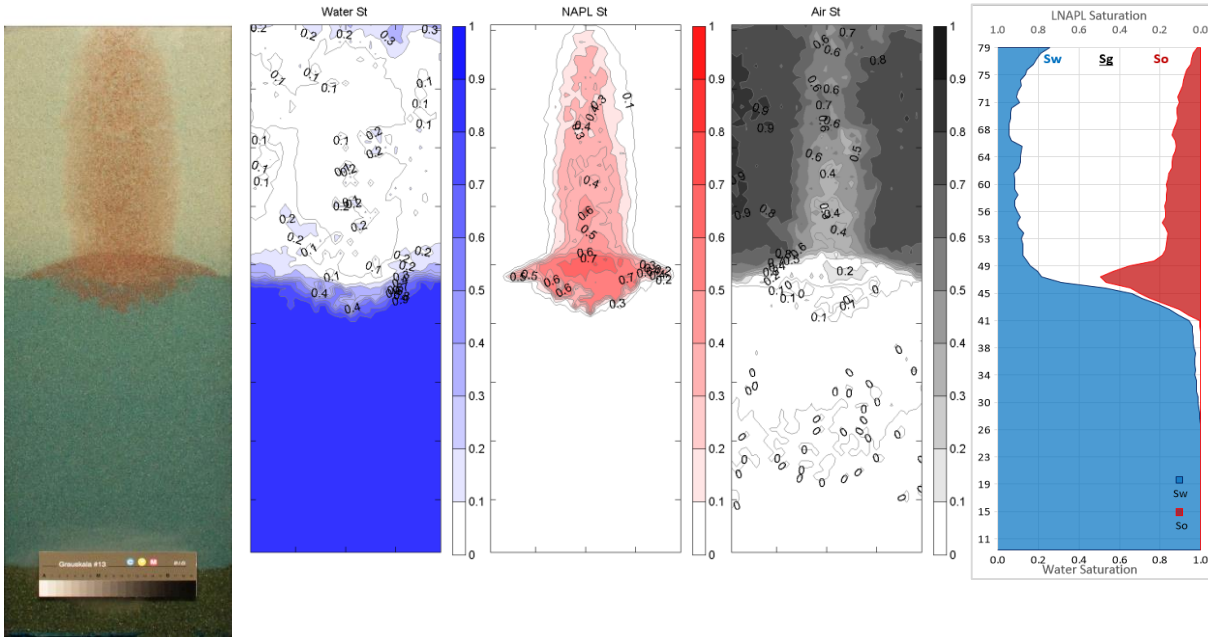

Figure 6-7 Compilation of saturation contours and profile for the LNAPL release of Run9T1 at T=24 min

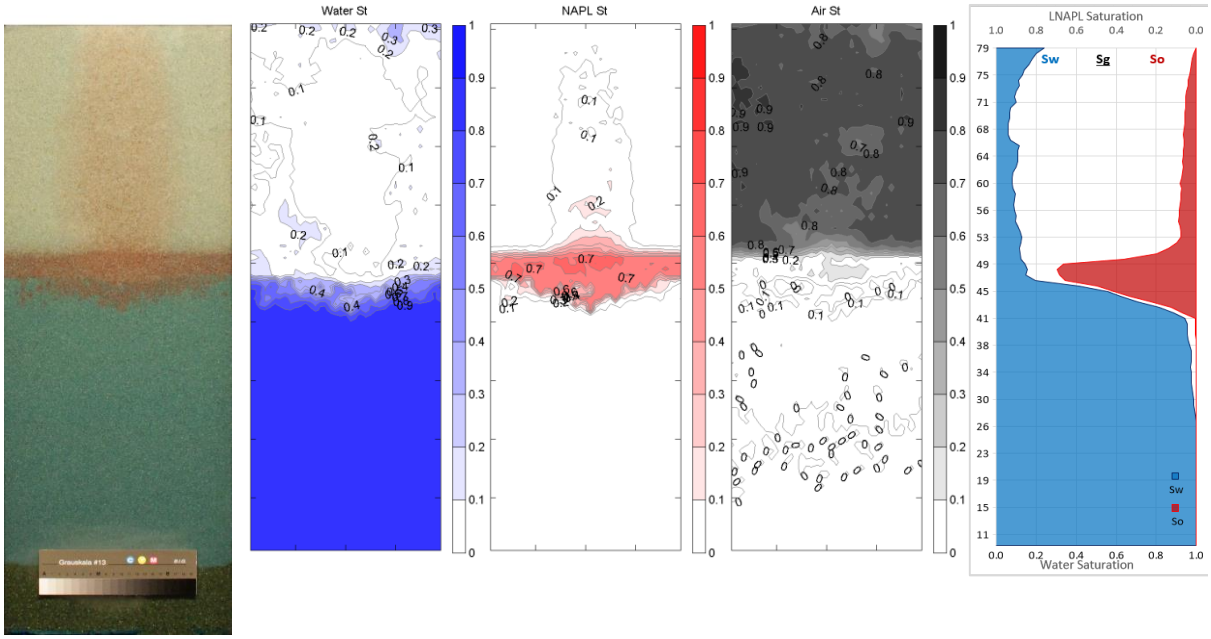

Figure 6-8 Compilation of saturation contours and profile for the LNAPL release of Run9T1 at T=90 min

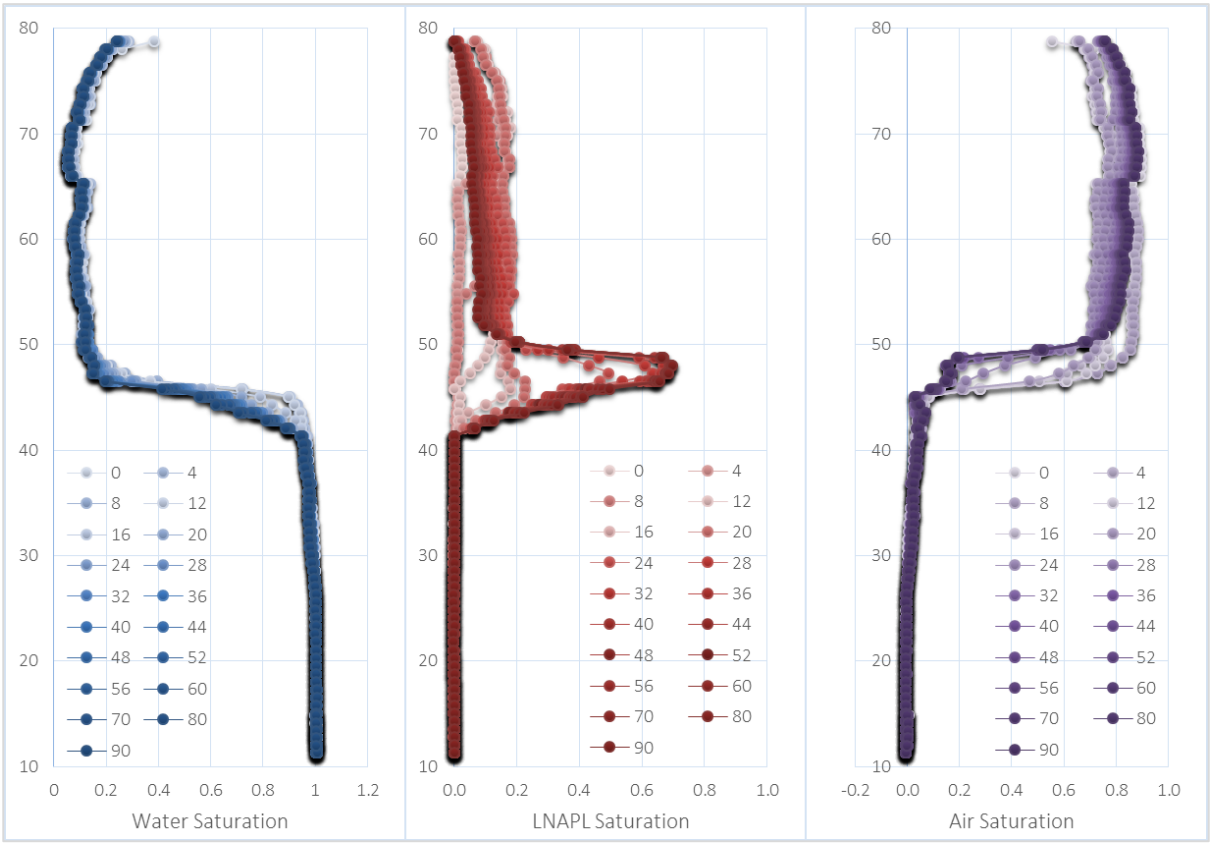

Figure 6-9 The water, LNAPL and air saturation distribution profiles advancing with time during the LNAPL release of Run9T1 (Unit: minutes)

6.2.2 Water table fluctuation period

From the inter-cycle dynamics in Figure 6-10, the release timing scenario demonstrated some similar inter-cycle features and dynamics during the fluctuation period as the base case, for instance, the entrapped LNAPL saturation at the lowermost position increased with the fluctuation number increased, and the greatest lens thickness occurred around the uppermost water table position and the smallest thickness at the lowermost position. The differences between these two scenarios are mainly due to the difference in the initial conditions, i.e. the LNAPL release. Since water table oscillation was started from the lowermost position at 35cm for the release timing case, the LNAPL body was more developed than the base case scenario, which formed a larger polluted area in the unsaturated zone and a thinner LNAPL lens in the capillary zone. Hence, the average saturation of LNAPL in the original unsaturated zone was greater than the base case (e.g. the unsaturated zone in Figure 6-10 (a)).

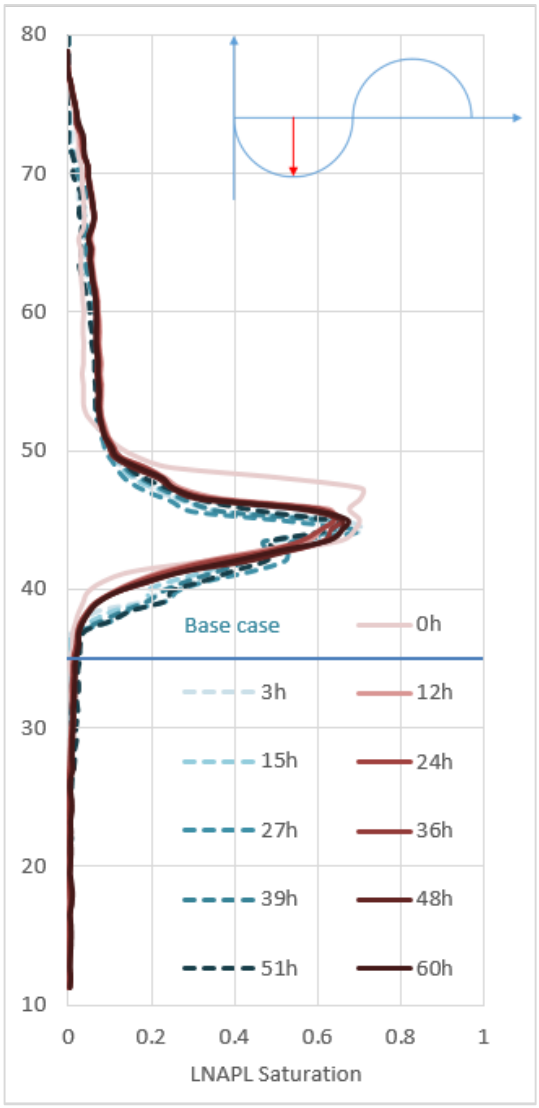

(a) Critical position 2, WT=35cm

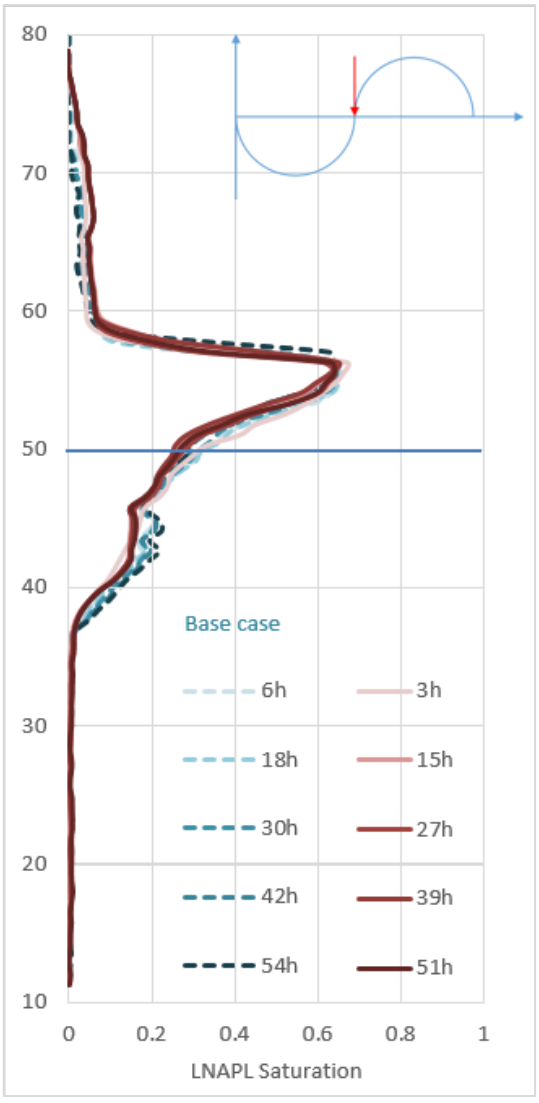

(b) Critical position 3, WT=50cm, ascending

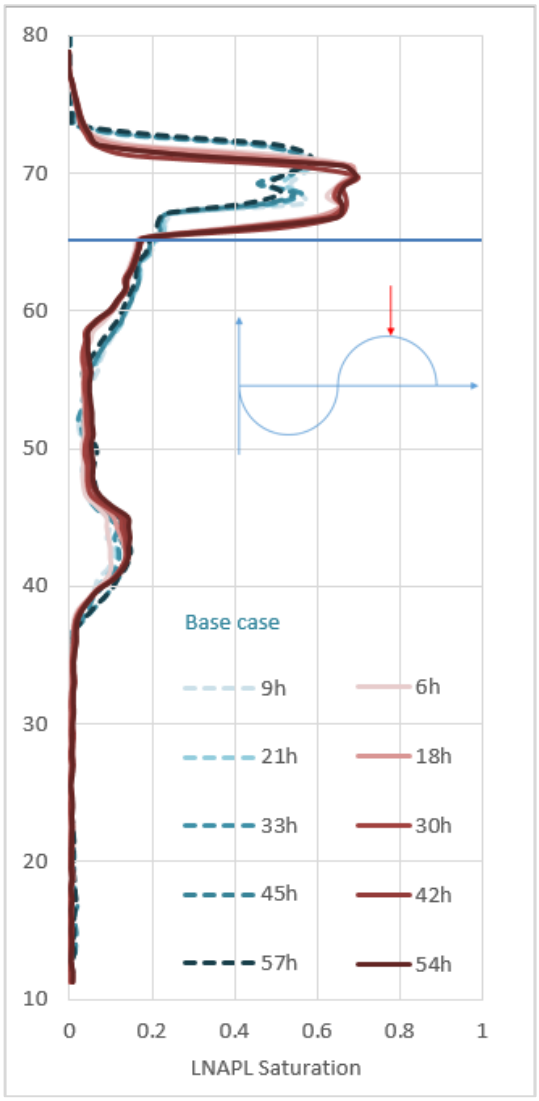

(c) Critical position 4, WT=65cm

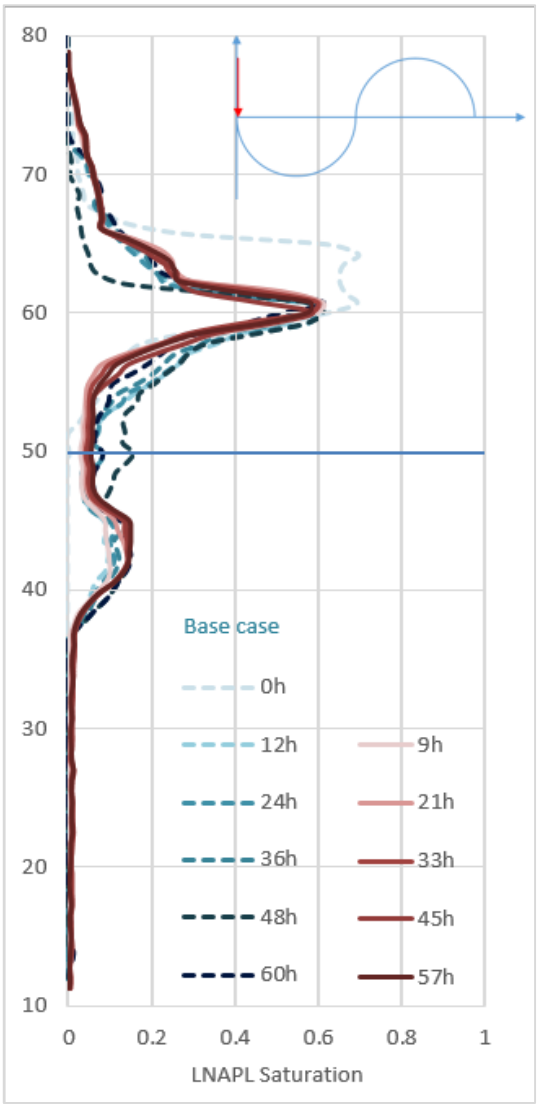

(d) Critical position 1, WT=50cm, descending

Figure 6-10 Inter-cycle LNAPL saturation profiles of the current scenario in red and the base case profiles superimposed in cyan from the 1st cycle to the 5th cycle. The 4 critical positions were defined in Section 5.5. There was a 3-hour lag between the current scenario and the base case. For instance, to compare the lowermost position (the critical position 2 defined in Section 5.5), the curve represents cycle 1 was the 3-hour curve in the base case, whereas it was the 0-hour curve for the current scenario

Another consequence of the release timing at the lowermost water table position is that the lowermost depth of the LNAPL body is shallower than the base case. Figure 6-11 provides an example of the comparison of the LNAPL distribution during the 5th cycle at critical position 1, where the lowermost boundary of the residual LNAPL band was at 37cm for the base case, whereas for the release timing scenario it was 38.5cm. LNAPL pressure decreases along the exceptionally long pathway

during the release and by reaching a deeper water table position, a bigger decrease in LNAPL pressure occurs. Thus, the infiltrating depth of LNAPL was shallower.

The significant role of the first cycle upon the LNAPL redistribution patterns is also confirmed. The lower boundary of the LNAPL lens in the base case (Figure 6-11(a)) was uneven with pronounced fingering. While in the release timing scenario, the lower boundary of the lens appeared to be slightly more even. These patterns in two different cases both resembled the LNAPL distribution in their first cycles. Due to a more homogenous sand packing, the release timing scenario displays a more homogeneous distribution in LNAPL lower boundary.

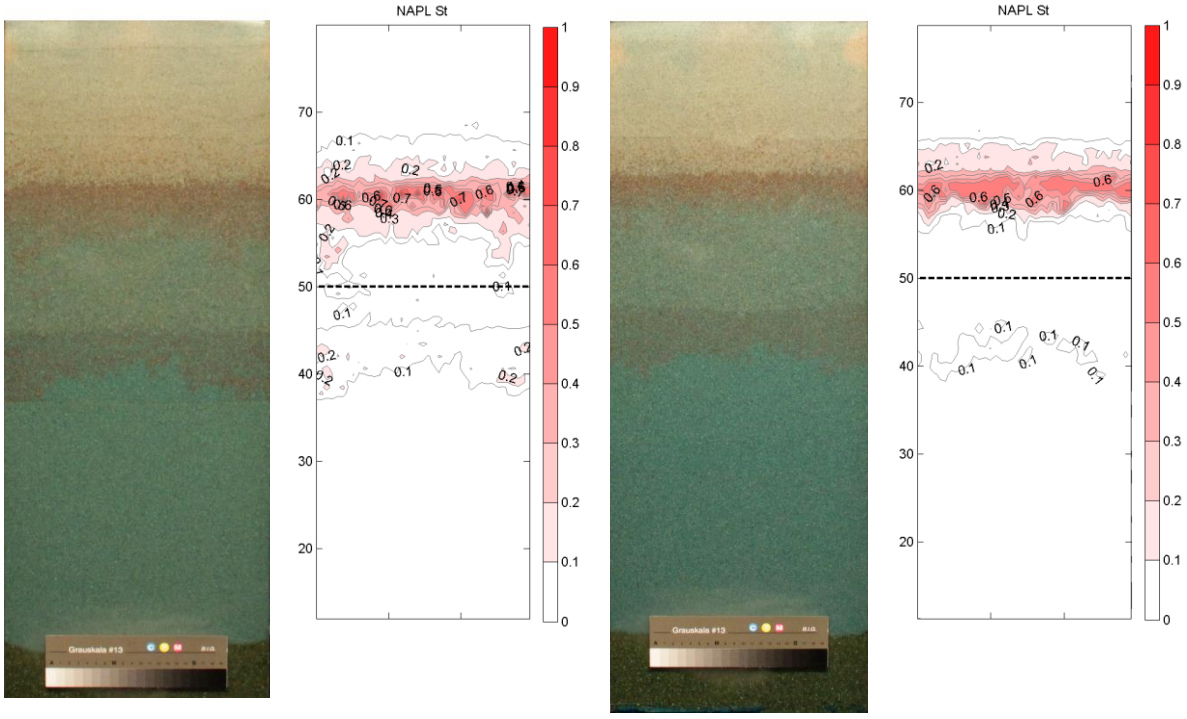

(a)Base case image (b)Base case contour (c)Release timing scenario image (d)Release timing scenario contour

Figure 6-11 Comparison of LNAPL saturation distribution of the base case (a,b) and the release timing scenario (c,d) of the 5th cycle at critical position 1 (WT=50cm, descending)

In summary, the influences of release timing at the lowermost water table position were mostly reflected in the initial condition setting, which meant that due to a sufficiently thicker unsaturated zone, LNAPL body was allowed to be fully developed with longer travelling depth, larger polluted area and spreading width. This phenomenon resulted in a thinner LNAPL lens and a shallower LNAPL infiltration depth at the end of release period as well as the repetitive distribution patterns during the subsequent oscillations. The implication of this scenario was that for an early discovered LNAPL

spillage, the polluted area and penetration depth could potentially be managed by seizing the downward movement of water table.

6.3 The small LNAPL release volume scenario

Two short videos of the LNAPL release and fluctuation periods for the current scenario can be found in Digital Appendices A.2.4.2.

This section discusses the influence of the release volume. Comparisons are made between the base case (Run4T3) and the small amount LNAPL (Run8T1), where 14 ml of LNAPL was spilt into the system within 6 mins. This scenario was designed to observe the LNAPL distribution without edge effects, which constantly occurred in other scenarios once LNAPL horizontal spreading reached the edges of the tank. The overall calculation errors for the image analysis in this scenario were big, yet the absolute differences in volume calculation were not large. This once again revealed the limitation of the image analysis method in three-phase lowly saturated LNAPL conditions. However, the interpreted saturation distribution pattern was accurate enough to discern the features of this scenario.

6.3.1 LNAPL release period

Figure 6-12 illustrates the end of the LNAPL release when only vertical infiltration occurred. The densest LNAPL saturation was the LNAPL front with a maximal saturation of 0.4 and an average saturation of 0.07. Fluid displacement was predominantly between LNAPL and air. Figure 6-13 illustrates the end of monitoring of the LNAPL release period, where horizontal spreading was observed with a maximal LNAPL saturation of 0.3. Although the release volume was adequately small, the primary horizontal water-air interface was depressed by the invading LNAPL and appeared as bowed. Other features of this period remained relatively similar as other scenarios.

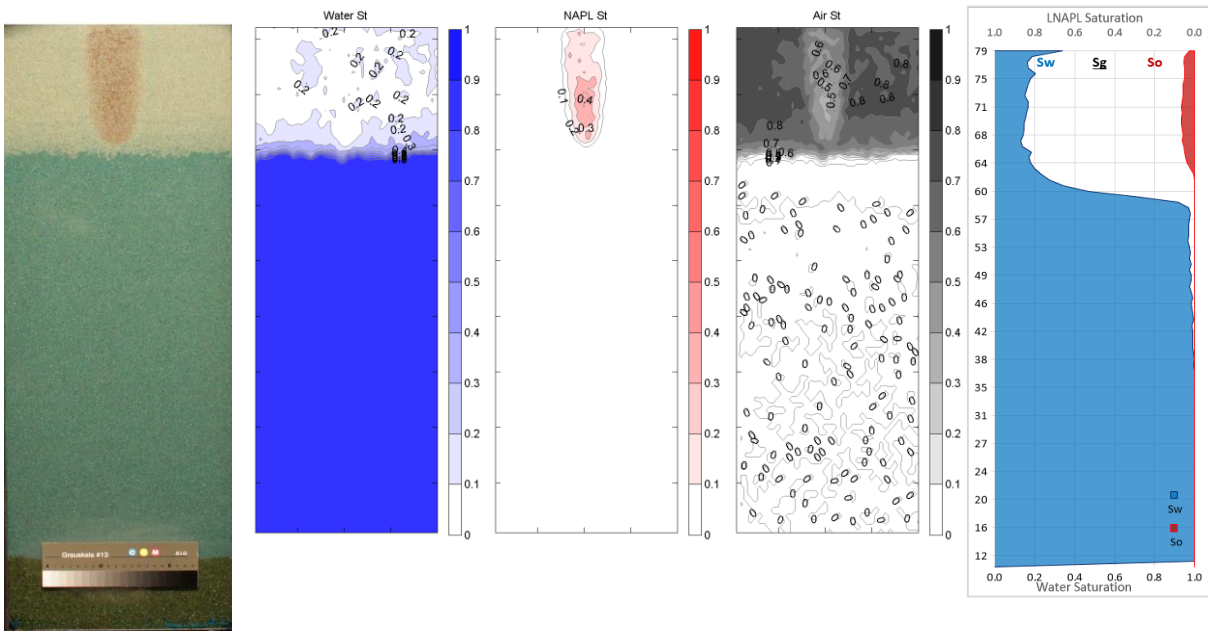

Figure 6-12 Compilation of saturation contours and profile for the LNAPL release of Run8T1 at T=6 min

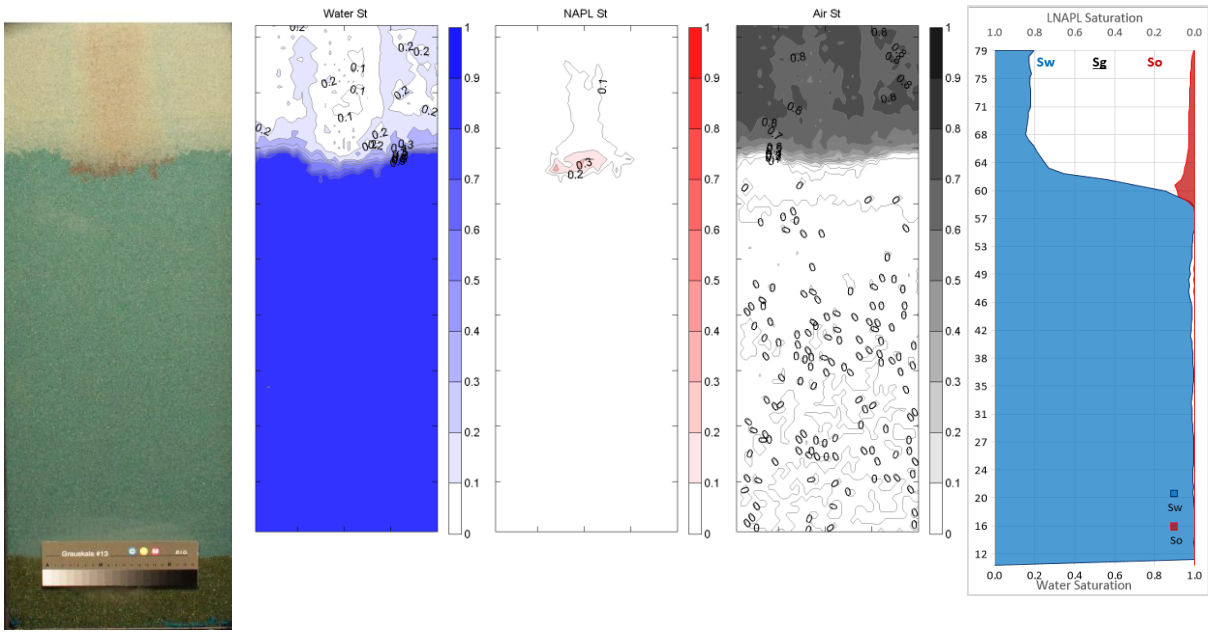

Figure 6-13 Compilation of saturation contours and profile for the LNAPL release of Run8T1 at T=110 min

6.3.2 Water table fluctuation period

Figure 6-14 to Figure 6-17 display the inter-cycle fluid saturation profiles of the four critical positions of the small LNAPL release scenario. The features and dynamics of this scenario appeared fairly different from the base case scenario with only few similarities. For instance, with the fluctuation number increased, the residual LNAPL saturation entrapped at the lowermost position increased

(Figure 6-14 (b)). However, throughout the fluctuation period, the residual LNAPL saturation shown in the profiles was much smaller (approximately 0.03) compared to the base case. The reason is that the width of the LNAPL body did not take up the full width and by averaging the saturation of a row, the residual saturations appear in the profiles are much smaller than the real values.

Most LNAPL content, in this scenario, became residual LNAPL within the water table fluctuation range without hitting the tank edge. No visible LNAPL lens above the water table was observed. The smearing range was between Z=43cm to 70cm, which was also significantly smaller than other scenarios (approximately from Z=37cm to 74cm). Since most LNAPL was held within pores, the mobile LNAPL left to fluctuate with the water table was not sufficient enough to form a visible LNAPL lens/body which resided above/around the water table. Whereas for other scenarios, the smearing length included the thickness of LNAPL lens. The main polluted body in this scenario with a maximal LNAPL saturation of 0.1 could only exist within the mobile capillary fringe. Moreover, a small amount release resulted in a shallower infiltration into the capillary fringe during release. Therefore, the total length of body could not exceed the mobile range of the capillary fringe (Figure 6-14 to Figure 6-17).

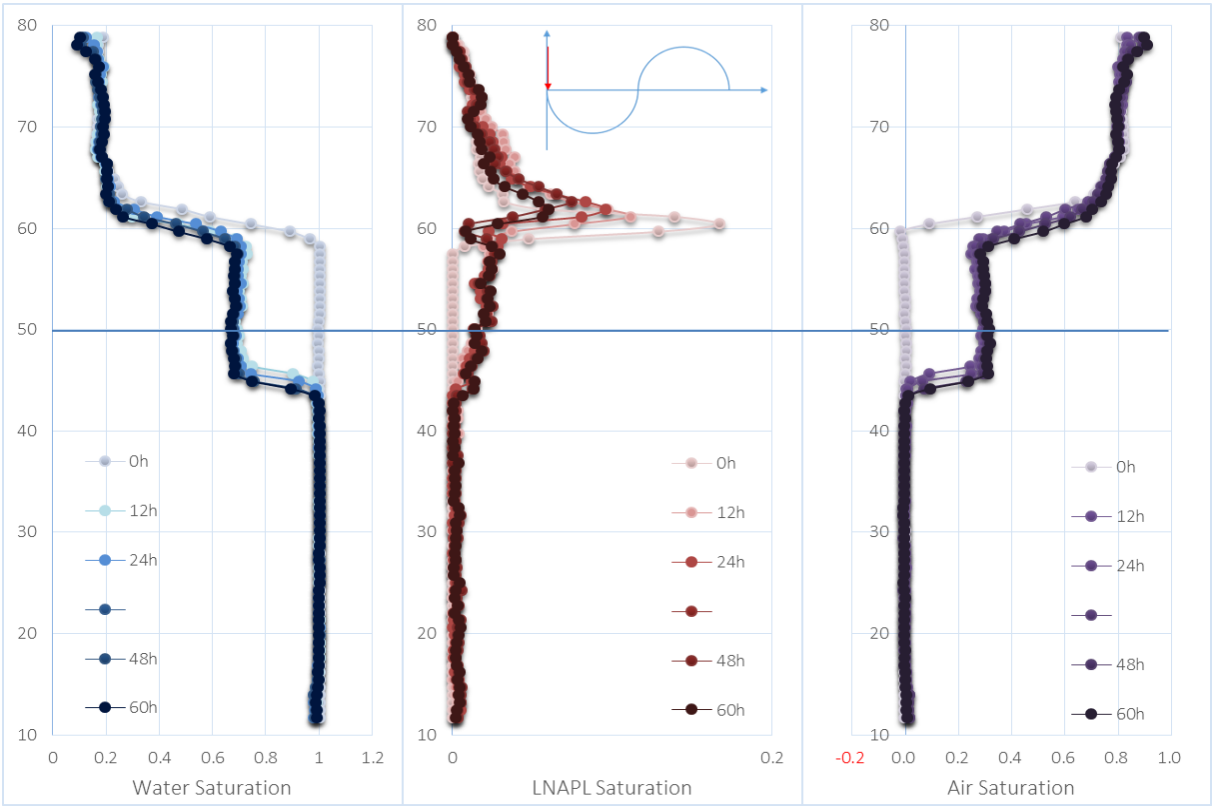

Figure 6-14 Inter-cycle fluid saturation profiles at critical position 1 during the cyclic water table fluctuation period of the small LNAPL release scenario

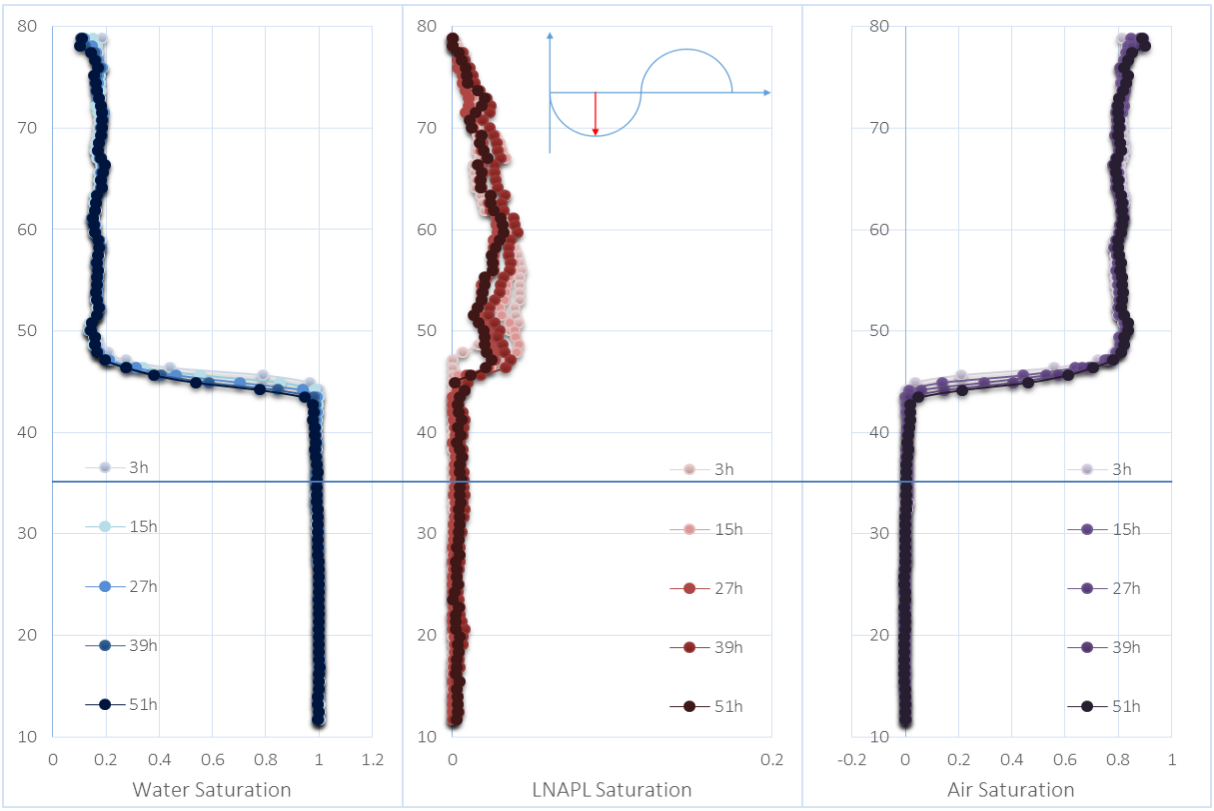

Figure 6-15 Inter-cycle fluid saturation profiles at critical position 2 during the cyclic water table fluctuation period of the small LNAPL release scenario

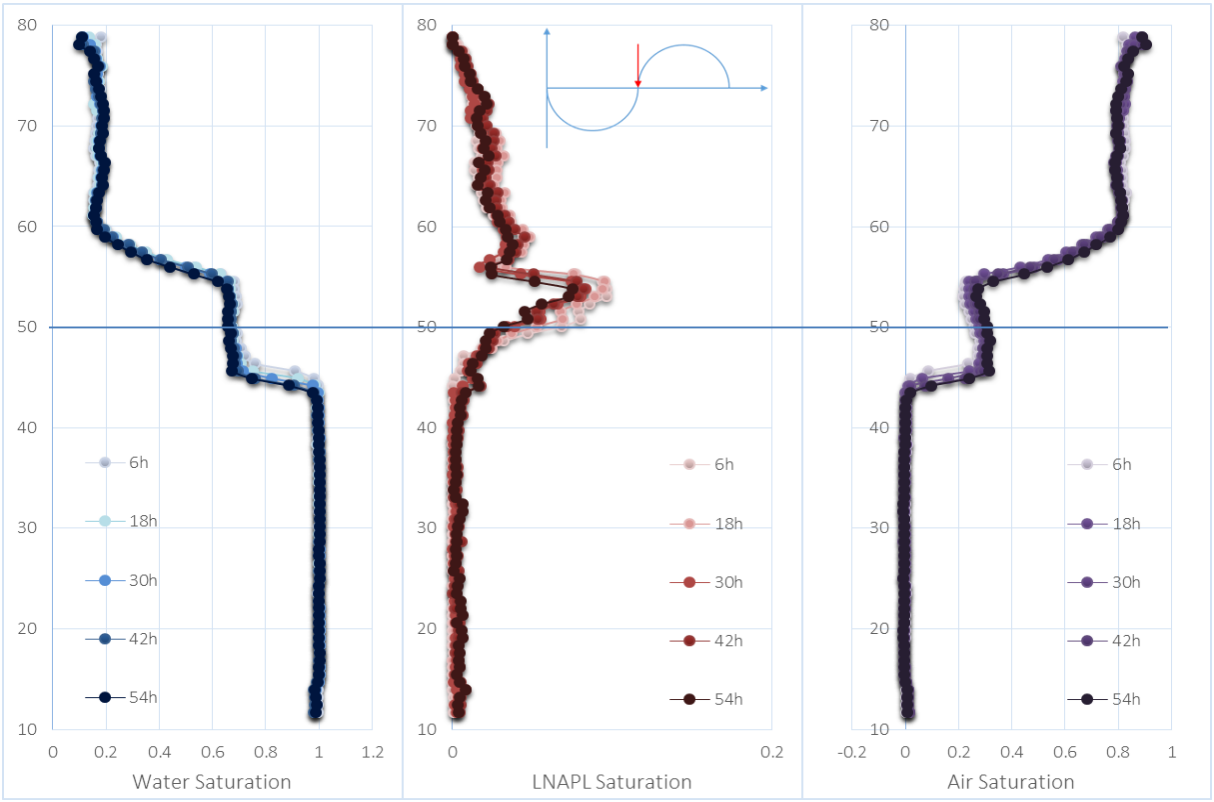

Figure 6-16 Inter-cycle fluid saturation profiles at critical position 3 during the cyclic water table fluctuation period of the small LNAPL release scenario

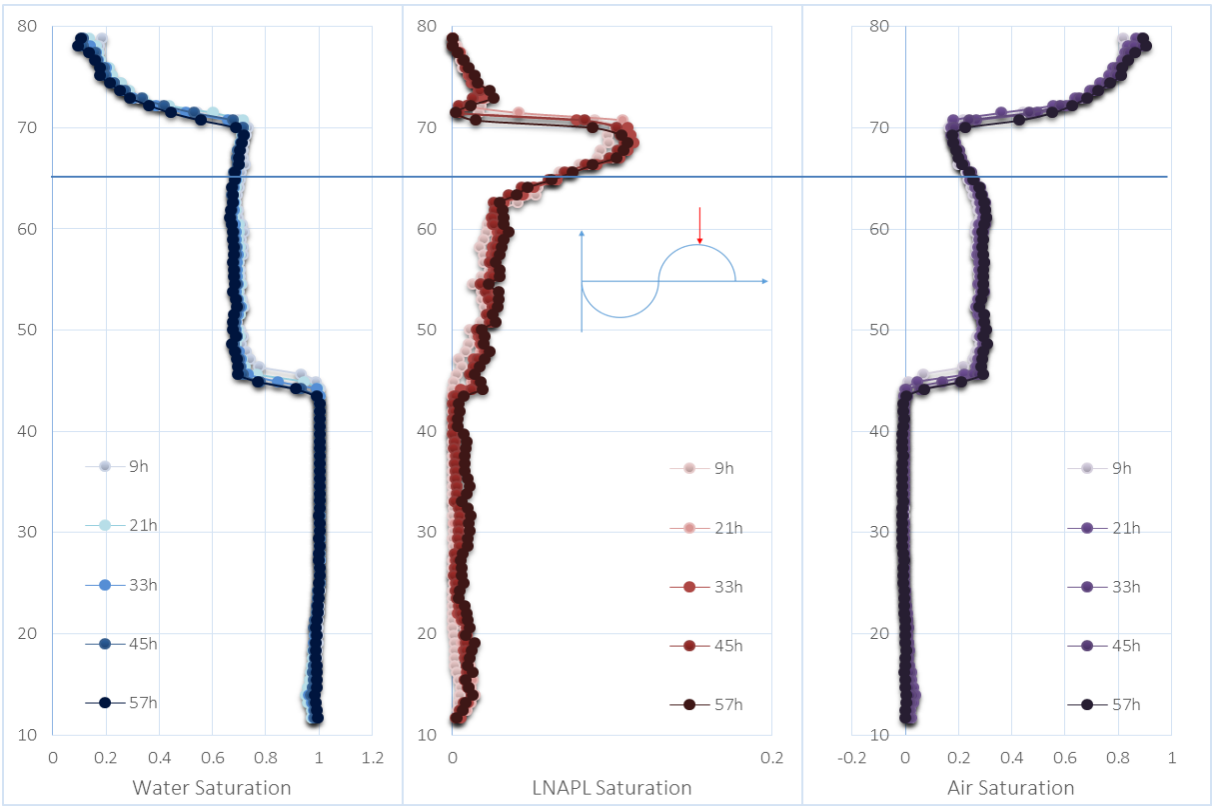

Figure 6-17 Inter-cycle fluid saturation profiles at critical position 4 during the cyclic water table fluctuation period of the small LNAPL release scenario

A turning point at around Z=45cm was found in the water and air saturation profiles, where a sudden increase of water content and a sudden decrease of air content was found below the point after the first water table descending occurred (Figure 6-14(b) to Figure 6-17(b)). This was because the original water-air system was replaced by the water-LNAPL-air three-phase system, where the effective saturation of water above this point decreased with the occupancy of both entrapped LNAPL and residual air.

In summary, in the small LNAPL release resulted in a much smaller smearing length, a shallower smearing depth, and no visible LNAPL lens. At high water tables, the LNAPL body was still visible, whereas, at lows, the LNAPL body could hardly be identified. Due to the averaging in the calculation, the residual LNAPL saturation values were shown lower in the profiles. The mobile LNAPL could only reside in the moving capillary fringe.

6.4 The fine sand aquifer scenario

Two short videos of the LNAPL release and fluctuation periods for the current scenario can be found in Digital Appendices A.2.5.2.

This section discusses the influence of different aquifer media. Comparisons are made between the base case scenario (Run4T3) and the find sand aquifer scenario (Run10T3), where 105ml of LNAPL was released into the system within 72min.

6.4.1 LNAPL release period

An error can be observed in the shaded profiles in Figure 6-19 and Figure 6-20, where LNAPL and water profiles are noticeably overlapped. After analysis, the water saturation error is considered the cause of this overlap. By comparing the mass balance result, at this moment T=72 min, the calculated LNAPL volume is 105.28ml, which matches the LNAPL release volume. This indicates that LNAPL volume is not overestimated. By further comparing the LNAPL distribution contour against the photographic record (Figure 6-23 (a, c)), the LNAPL saturation distribution interpreted seems fairly representable of the real distribution. Therefore, the cause of the error is reckoned the overestimated water saturation when LNAPL saturation is high. It is assumed that in the calibration test of fine sand, one or a few samples consisting of extremely high LNAPL saturation (>0.8) and low water saturation were inaccurately made or calibrated. By conducting a high-quality calibration test for the fine sand where samples are accurately made and calibrated may very likely resolve this error. Therefore it can be predicted that in the fluctuation period, similar errors may occur with highly LNAPL saturated yet lowly water saturated regions. The error does not negatively affect the LNAPL saturation distribution. Thus, analysis can be conducted for the LNAPL saturation distribution.

Figure 6-18 features one of the moments during the LNAPL release underway, where the LNAPL front had arrived and was penetrating into the capillary zone. Fluid saturation distributions became more sensitive to local heterogeneity in the fine sand aquifer scenario compared to medium sand scenarios. Therefore, the capillary fringe boundary, although was allowed sufficient time to settle down, appeared fairly dispersed. Moreover, due to the larger resistance caused by higher capillary force and slightly smaller pore space in the fine sand aquifer scenario, the LNAPL infiltration depth was much lower than those in the medium sand scenarios, and the horizontal spreading was more evident.

Figure 6-19 depicts the end of the LNAPL release, where the maximal LNAPL saturation reached 0.75 and the LNAPL front had inserted into the capillary zone, arrived at Z=59cm of the tank elevation. The LNAPL body shape appeared more curved due to the dramatic LNAPL decrease from the central line to both edges of the tank.

Figure 6-20 presents the end of the monitoring of the release period, where most LNAPL left in the upper unsaturated zone had migrated downwards and replenished the LNAPL lens. The maximal LNAPL saturation reached 0.79 at this moment. The thickness of the LNAPL lens was 11cm, which was larger than the base case scenario.

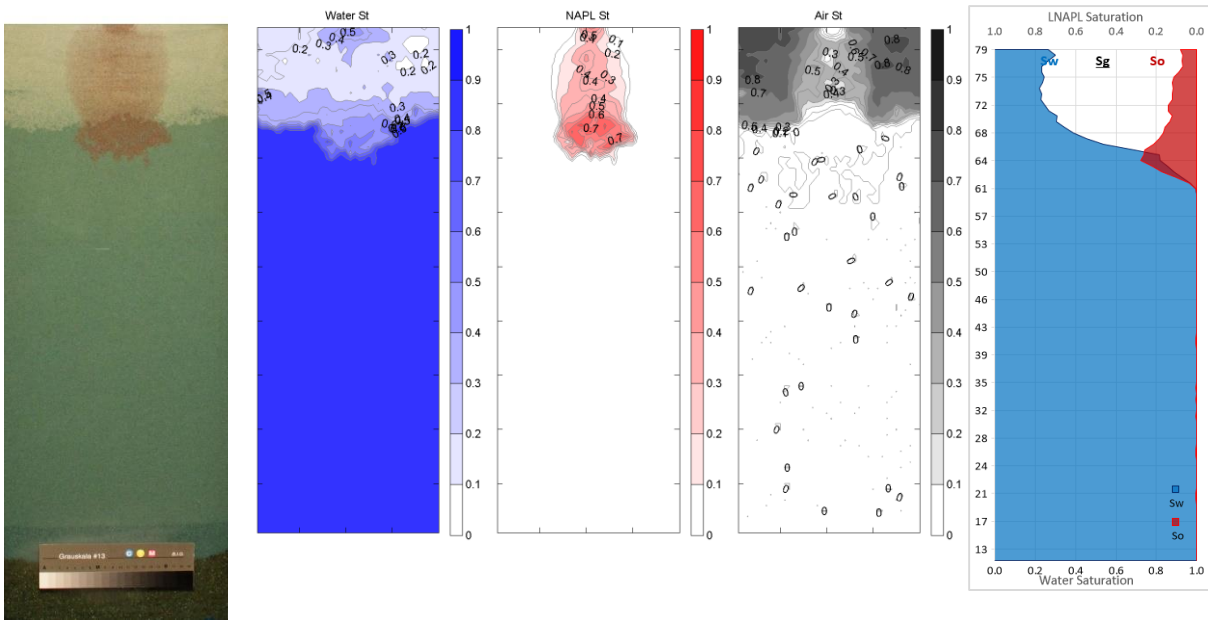

Figure 6-18 Compilation of the fluid saturation contours and profiles for the LNAPL release of Run10T3 at T=32 min

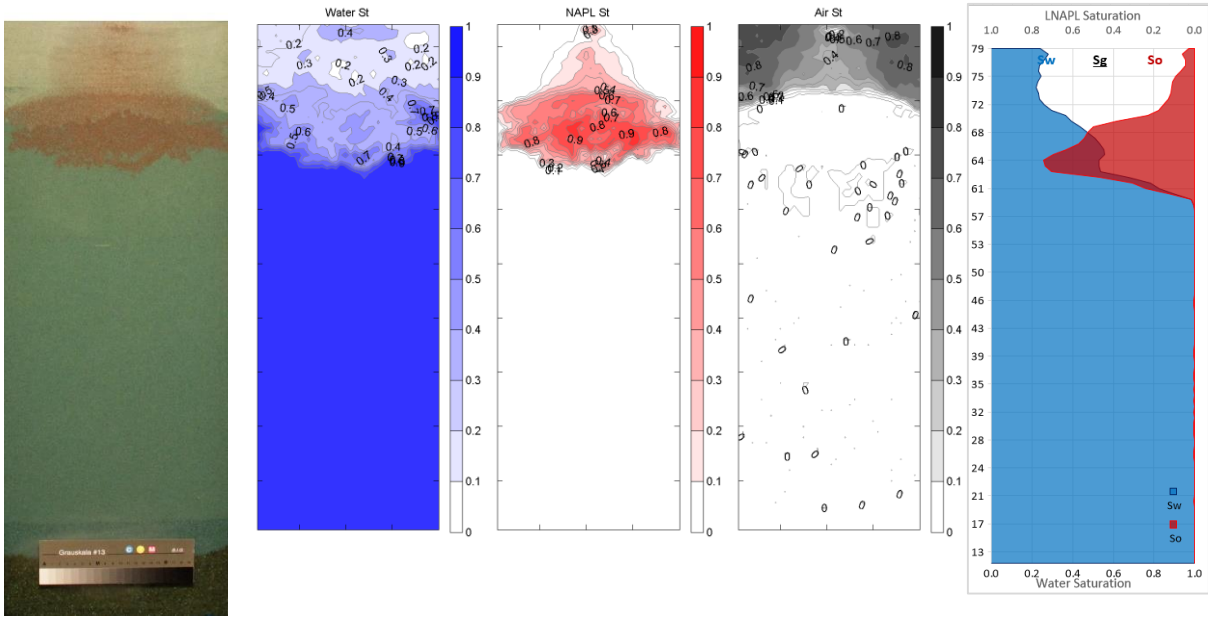

Figure 6-19 Compilation of the fluid saturation contours and profiles for the LNAPL release of Run10T3 at T=72 min

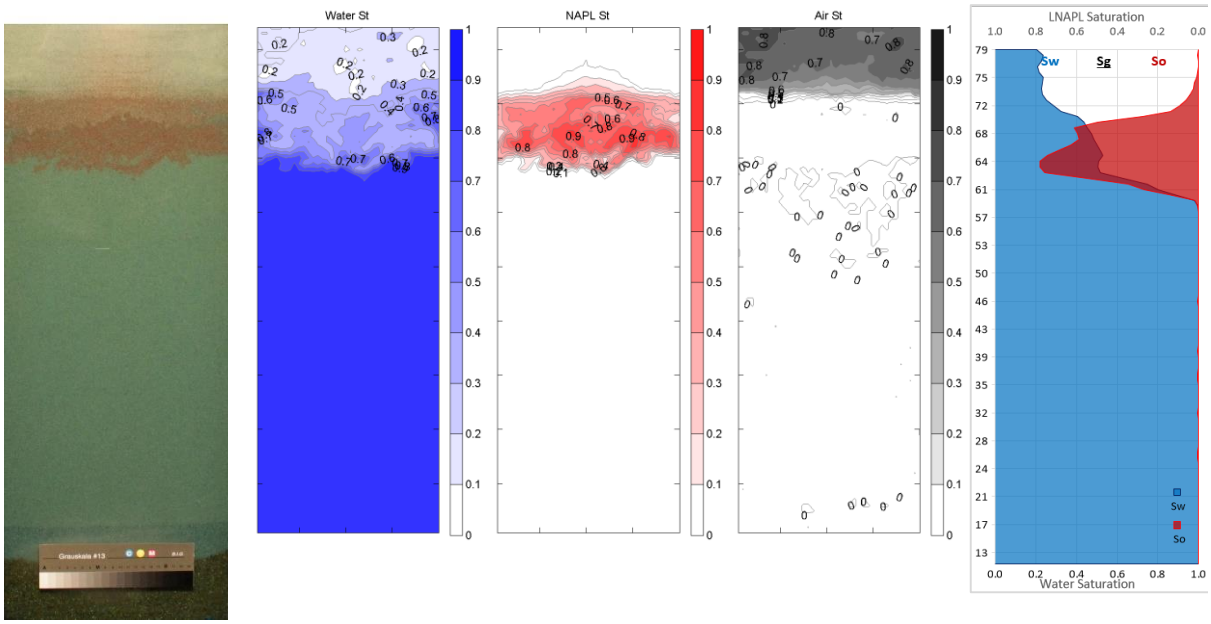

Figure 6-20 Compilation of the fluid saturation contours and profiles for the LNAPL release of Run10T3 at T=366 min

6.4.2 Water table fluctuation period

Figure 6-21 illustrates the difference in inter-cycle LNAPL profiles between the base case scenario and the fine sand aquifer scenario. The smearing length in the fine sand aquifer scenario was generally

found considerably shorter (approximately 30cm) than the base case scenario. Due to the higher capillary rise in the fine sand scenario, the LNAPL body was also shallower.

The thickness of LNAPL lens that oscillated with the water table is found larger in the fine sand scenario than all of the medium sand scenarios. It is because of the higher capillary rise caused by fine sand results in a thicker LNAPL-water mixing band floating upon the water table. Therefore, it could be observed from all critical positions in Figure 6-21 that the LNAPL lenses above the water table are thicker with smaller average and maximal saturations.

Compared to the base case scenario, the LNAPL residual saturation is found slight larger in the saturated zone, and the entrapped LNAPL band at the lowermost position (from Z=45~52cm) appears more evident (Figure 6-21(a,c,d)). The lower LNAPL effective permeability in the fine sand scenario also facilitates more mobile LNAPL being left behind by the moving water table. LNAPL saturation in the unsaturated zone is found significantly larger in the fine sand scenario than the medium sand scenarios. Therefore, the saturations of the LNAPL peaks in all critical positions are smaller than those in the medium sand scenarios.

Air entrapment is found much lower in the fine sand scenario with the maximal average air saturation of 0.1 below the water table. Due to smaller pore sizes, it was harder for the non-wetting fluid air to compete with the wetting and intermediate wetting fluids for pore space.

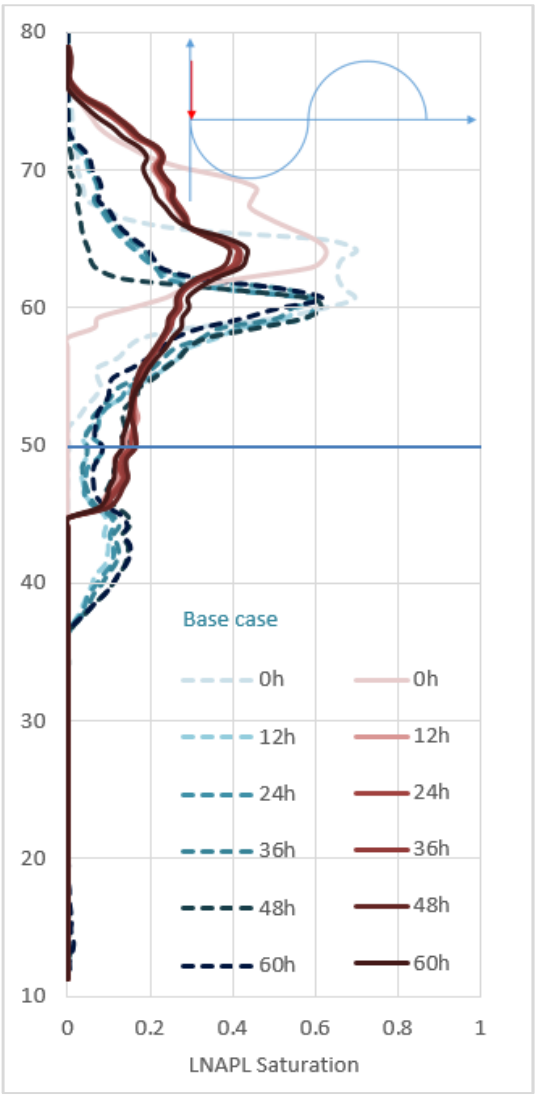

(a) Critical position 1, WT=50cm, descending

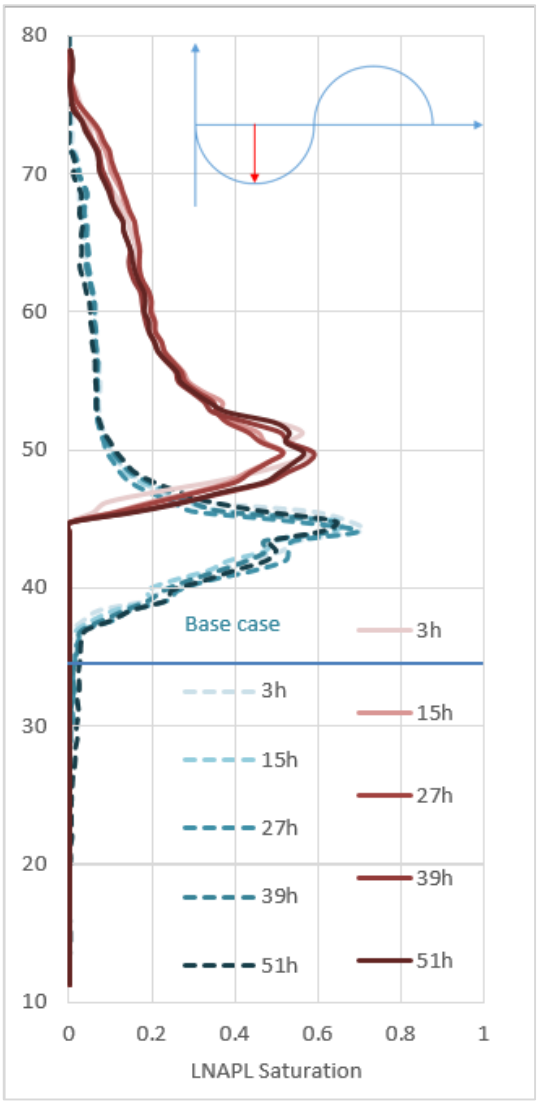

(b) Critical position 2, WT=35cm

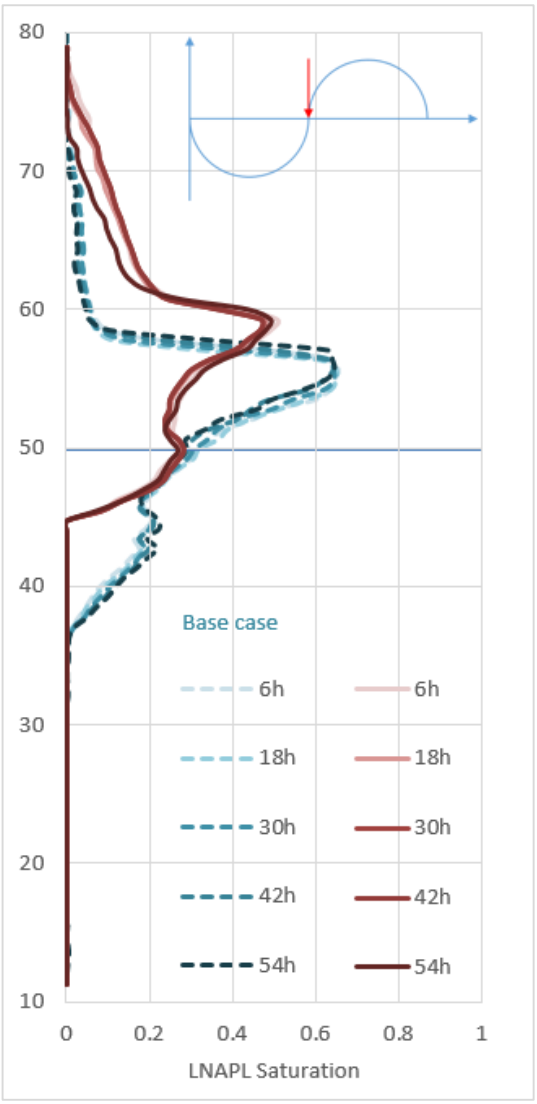

(c) Critical position 3, WT=50cm, ascending

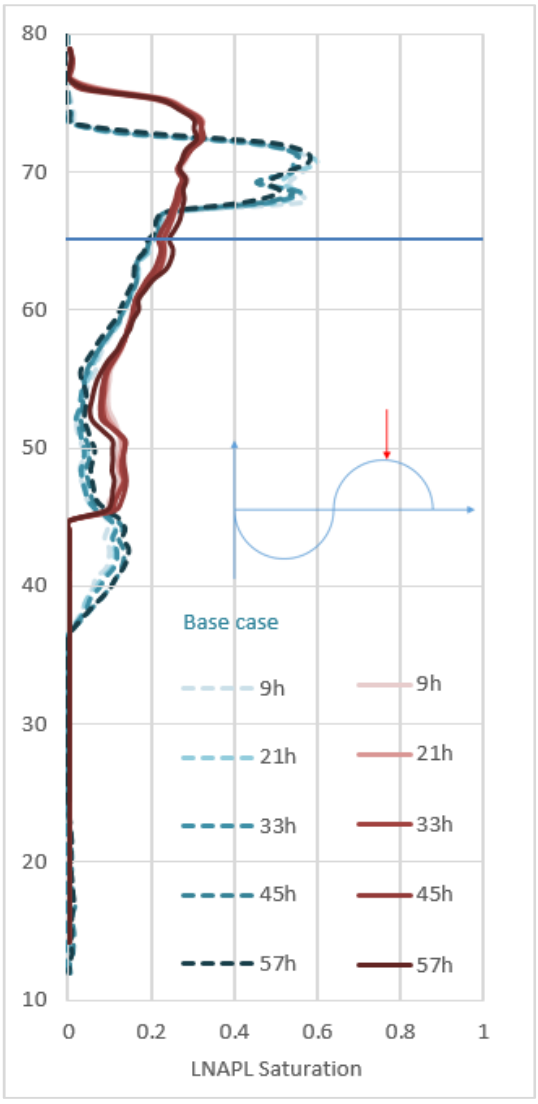

(d) Critical position 4, WT=65cm

Figure 6-21 Inter-cycle LNAPL saturation profiles of the current scenario in red and the base case profiles superimposed in cyan from the 1st cycle to the 5th cycle

In summary, the fine sand aquifer gives a higher capillary rise, which results in a thicker LNAPL lens with slightly smaller saturation and a more significant lateral spreading. Therefore, it also prevents LNAPL from infiltrating deeply into the capillary zone, hence, a shallower smearing depth. The smaller LNAPL effective permeability slows down the migration of mobile LNAPL, hence, leaving more LNAPL along the water table fluctuation pathway, particularly in the unsaturated zone.

6.5 The single partial fine grain layer scenario

Two short videos of the LNAPL release and fluctuation periods for the current scenario can be found in Digital Appendices A.2.6.2.

This section discusses the influence of aquifer heterogeneity. Specifically, the influence of an inserted fine grain layer made of fine sand that takes up half of the tank width and is positioned in the horizontal centre of the tank. Comparisons are drawn between the base case scenario (Run4T3) and the find sand aquifer scenario (Run7T1), where 100ml of LNAPL was released into the system within 34min. The approximately 2.5cm thick, 15cm wide fine sand layer was located between approximately Z=56cm to 58cm of the tank elevation, which was the upper boundary of the capillary zone. The fine sand layer was not entirely horizontal, where a downwards tilt towards the left was found. On the left hand side of the layer, a thin horizontal band of fine sand was accidentally formed during the sand packing, which was marked in Figure 6-22.

Figure 6-22 Illustration of the irregularity in the sand packing of the single partial fine grain layer scenario. The photo was cropped from the monitoring of the LNAPL release at T=150. The contrast and brightness of the photo were both increased by 20% for visual demonstration

6.5.1 LNAPL release period

A selection of critical moments was presents to emphasise the characteristics during this process.

Figure 6-23 exhibits the moment when the LNAPL front arrived at the fine grain layer and thus began to amass upon the layer. Before this moment, the migration and distribution of all fluids were moderately identical to the base case scenario. Except for the water-air interface, which appeared additionally dispersed due to the existence of the fine grain layer that possesses a different capillary rise than medium sand.

Figure 6-24 presents a moment during the on-going release as an example. Different from the base case scenario, where the LNAPL front penetrated into the capillary fringe with a moderating vertical

infiltration rate, the LNAPL front in this scenario bypassed the partial fine sand layer without infiltration. Consequently, the saturation of the LNAPL front was significantly higher (with the saturation ranging between 0.6~0.8) due to the obstruction of the fine grain layer. As illustrates in Figure 6-22, the thin band of fine sand accidentally slide to the left corner of the fine sand layer played a major role in preventing LNAPL from accumulating upon and passing through.

Figure 6-25 illustrates the end of the LNAPL release, where the LNAPL body was developed. Unlike the base case where the upper half of the body was a symmetrical cone shape, the shape of the top half of the body in this scenario was asymmetrical, and the width of the smearing was larger. This was due to the obstruction brought by the heterogeneity of the fine sand layer, which provided an uneven capillary pressure across the tank width. The LNAPL lens was developed unevenly without any infiltration into the fine sand layer. Until the end of the monitoring shown in Figure 6-26, most LNAPL in the unsaturated zone moved downwards and merged with the highly compact LNAPL lens upon the fine sand layer. Similarly to the base case, small air entrapment was found during the release period.

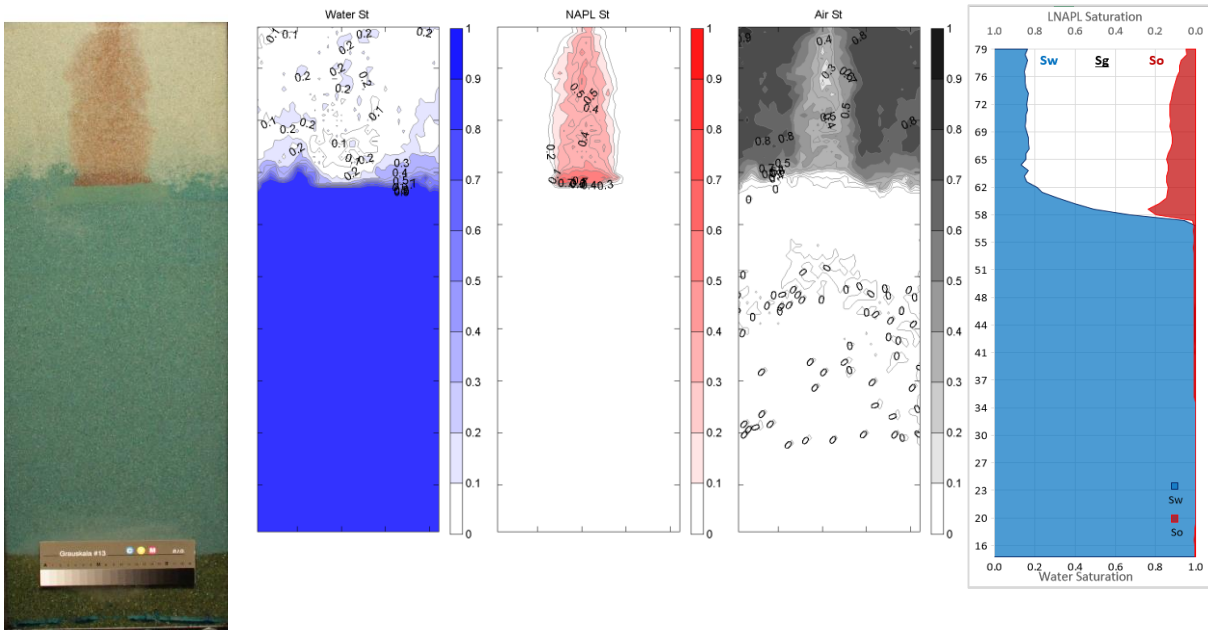

Figure 6-23 Compilation of fluid saturation contours and profiles for the LNAPL release of Run7T1 at T=16 min

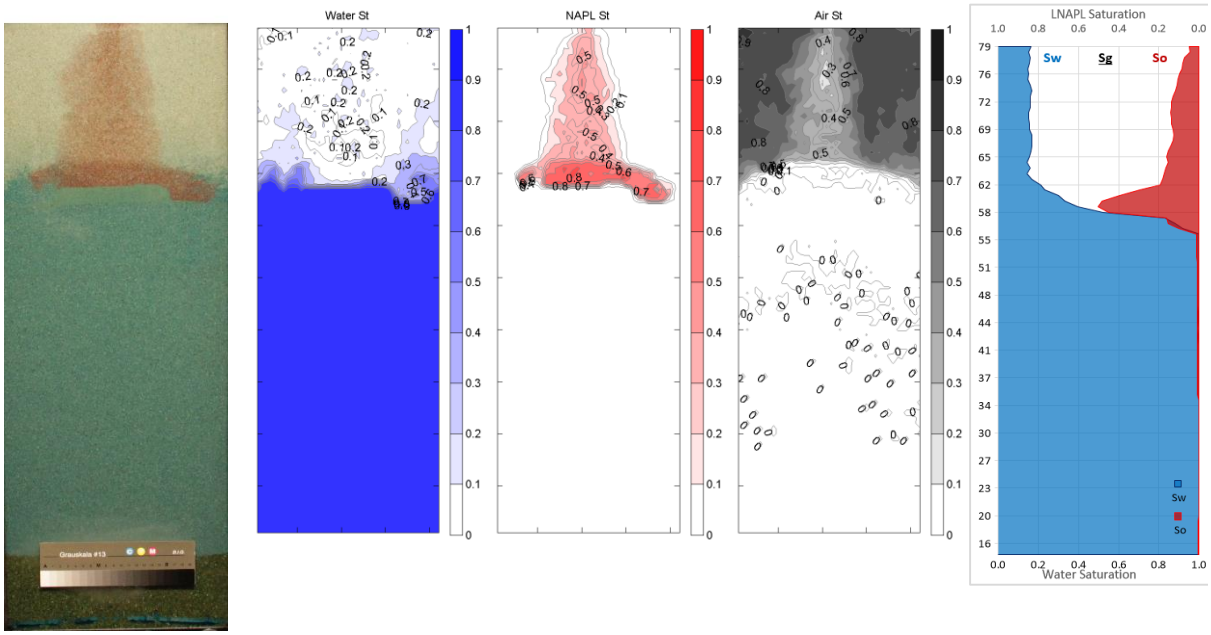

Figure 6-24 Compilation of fluid saturation contours and profiles for the LNAPL release of Run7T1 at T=24 min

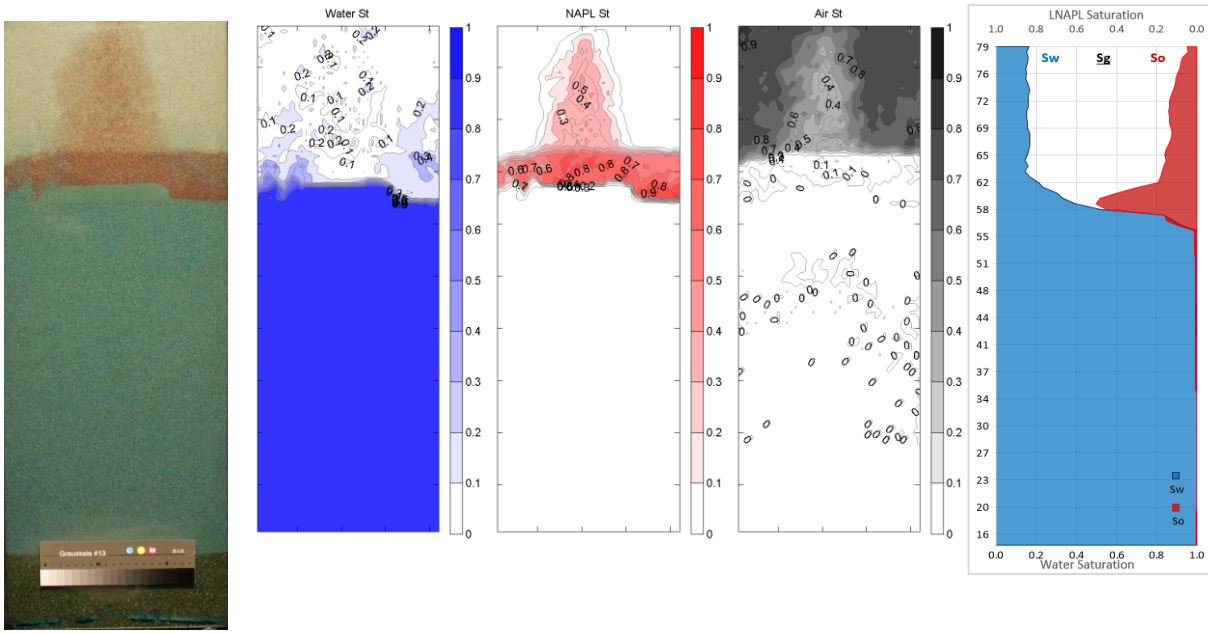

Figure 6-25 Compilation of fluid saturation contours and profiles for the LNAPL release of Run7T1 at T=34 min

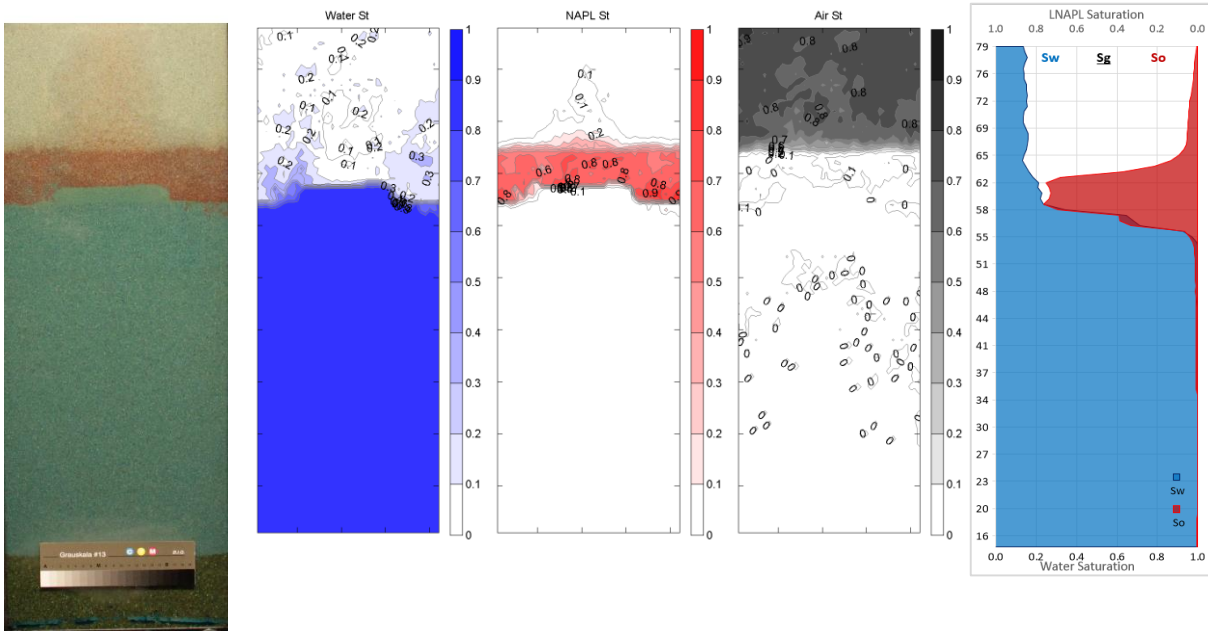

Figure 6-26 Compilation of fluid saturation contours and profiles for the LNAPL release of Run7T1 at T=150 min

6.5.2 Water table fluctuation period

Under the influence of the fine grain layer, detailed fluid distributions and dynamics of a water drainage process and a water imbibition process are illustrates in Figure 6-27 and Figure 6-28 respectively, taking the cycle 1 as an example. During the water drainage, the LNAPL lens was brought downwards, where no visible LNAPL infiltration into the fine sand layer was found initially (Figure 6-27(a)). As the water table continued to descend, the fine sand layer, originally fully water saturated, began to drain. And the remaining LNAPL left behind by the water table started to coat over the top of the fine sand layer (Figure 6-27(b)). As water table continued to plummet, the “coating” LNAPL began to infiltrate into the fine sand layer as more water drained from the layer (Figure 6-27(c)). These LNAPL contents became immobile despite the subsequent water content change (Figure 6-27(d)).

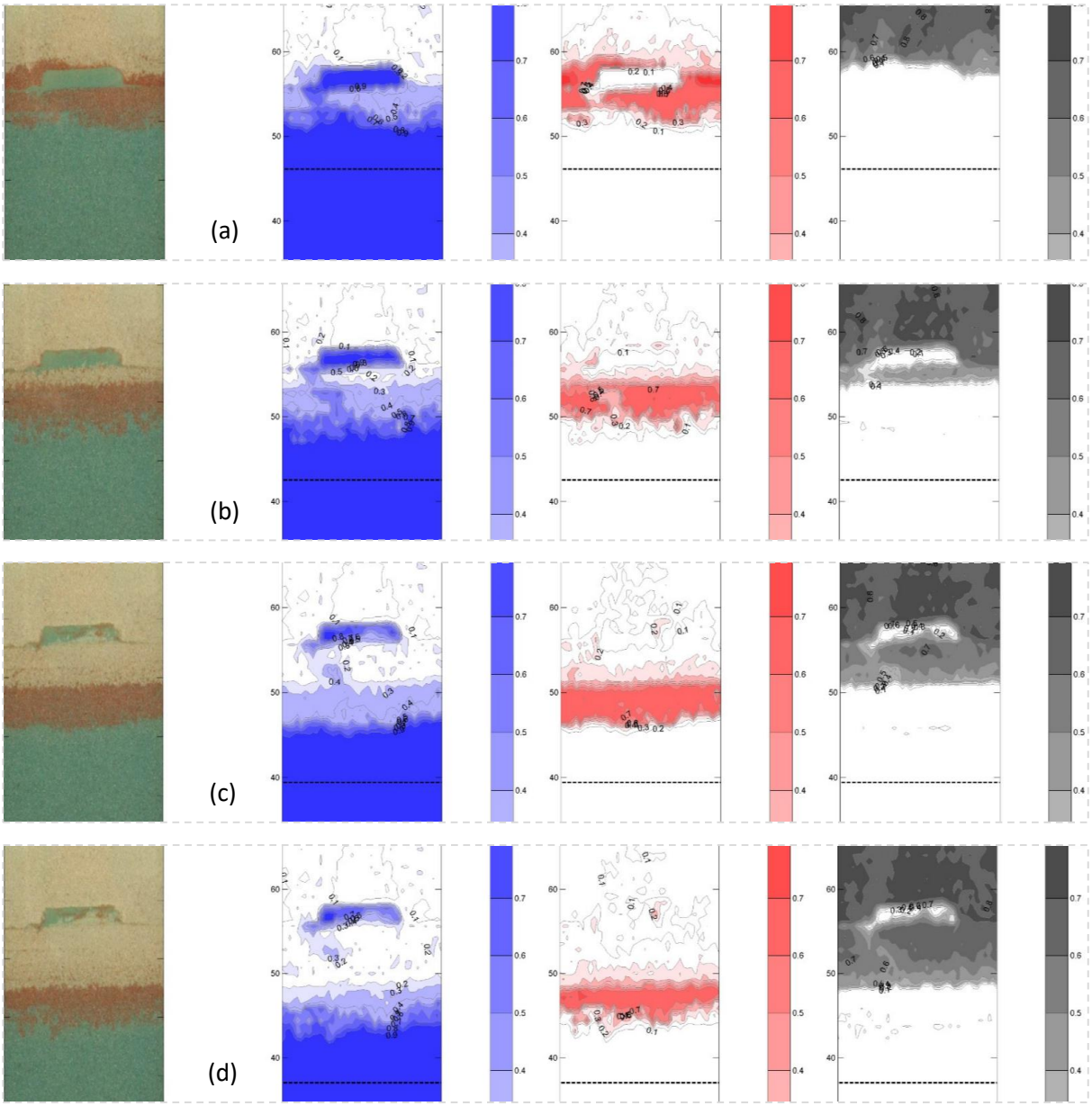

Figure 6-27 An example of fluid distributions and dynamics under the influence of partial fine grain layer during water table descending (4 continuous moments during Cycle 1: 0.5h, 1.0h, 1.5h and 2.0h)

A small amount of air was found entrapped within the fine sand layer after the first water drainage (Figure 6-28(a)), in addition to the residual water and LNAPL contents. As the water table moved upwards, the LNAPL lens was elevated and approached the fine sand layer again (Figure 6-28(b)). However, the fine sand layer was saturated with residual LNAPL and air and water saturation. The LNAPL front had to surround the fine sand layer and went up with a small amount of water-air displacement. A densely LNAPL saturated layer with LNAPL saturation of 0.6 was temporarily seized

beneath the fine sand layer (Figure 6-28(c)) and finally went past the fine sand layer via bypassing (Figure 6-28(d)).

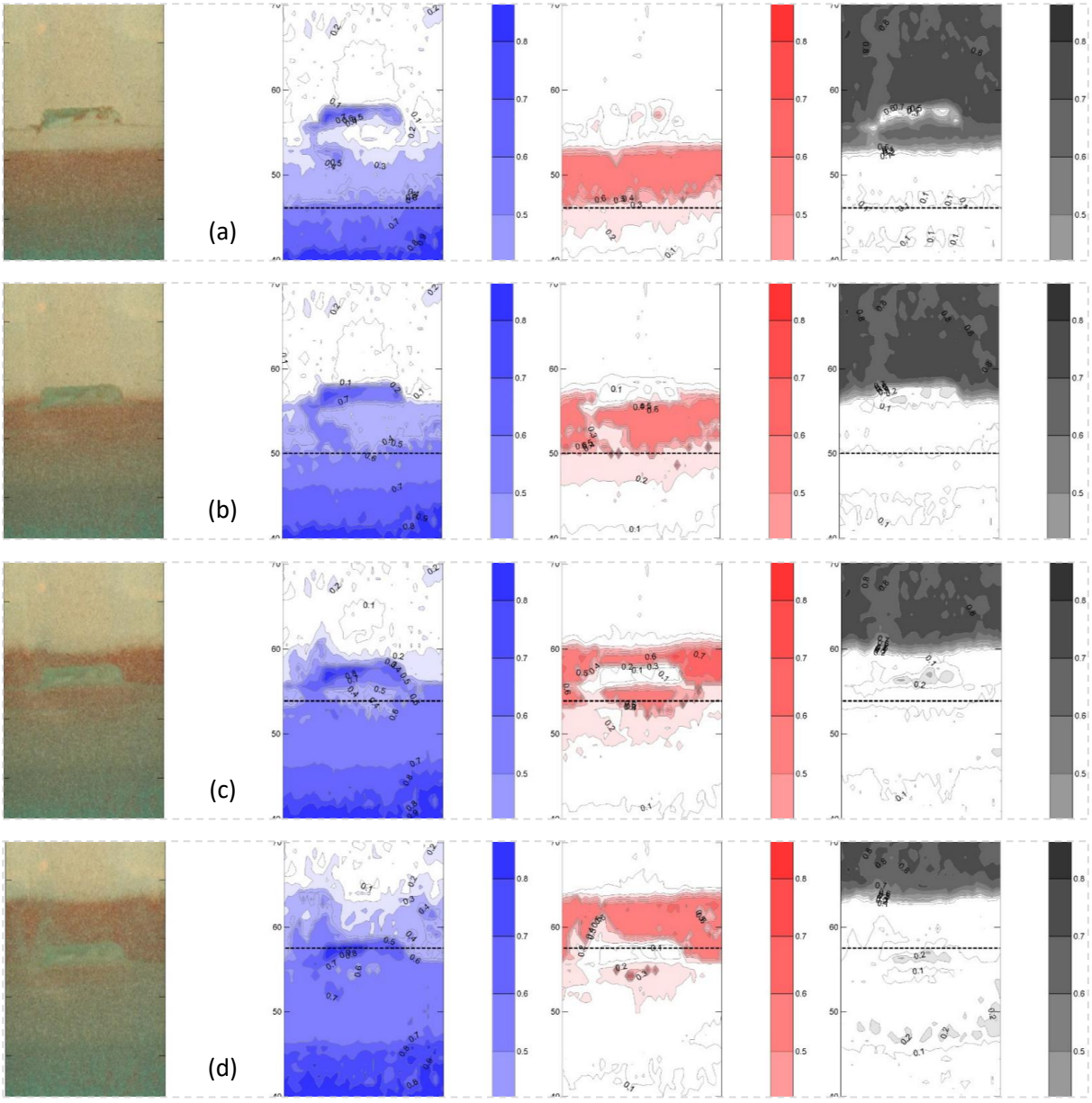

Figure 6-28 An example of fluid distributions and dynamics under the influence of partial fine grain layer during water table ascending (4 continuous moments during Cycle 1: 5.5h, 6.0h, 6.5h and 7.0h)

Figure 6-29 demonstrates the comparison of the inter-cycle LNAPL saturation profiles between the base case scenario and the fine grain layer scenario. Before the water table fluctuation started at crucial moment 1, the average saturation of the LNAPL lens (0.75) was notably higher in the current scenario than the base case (Figure 6-29(a)). The LNAPL lens was thinner than the base case scenario

at critical position 1. At critical position 2, an increasing amount of LNAPL was shown to be trapped in the fine sand layer (Figure 6-29(b)). Consequently, the LNAPL lens in the fine grain layercase was shown to be thinner and with smaller saturation than the base case scenario after the first water table oscillation. At critical position 3, the location of the LNAPL lens was lower in the current case compared to the base case scenario owing to the obstruction by the fine sand layer (Figure 6-29(c)). At critical position 4, the thickness of the LNAPL lens was substantially smaller than the base case. Hence, the smearing length was shorter. A layer of mobile LNAPL was seized behind the fine sand layer with a maximal saturation of 0.19 (Figure 6-29(d)).

The LNAPL saturation shown between Z=13~20cm of the tank elevation was an error, resulting from the light source irregularity at the bottom of the tank.

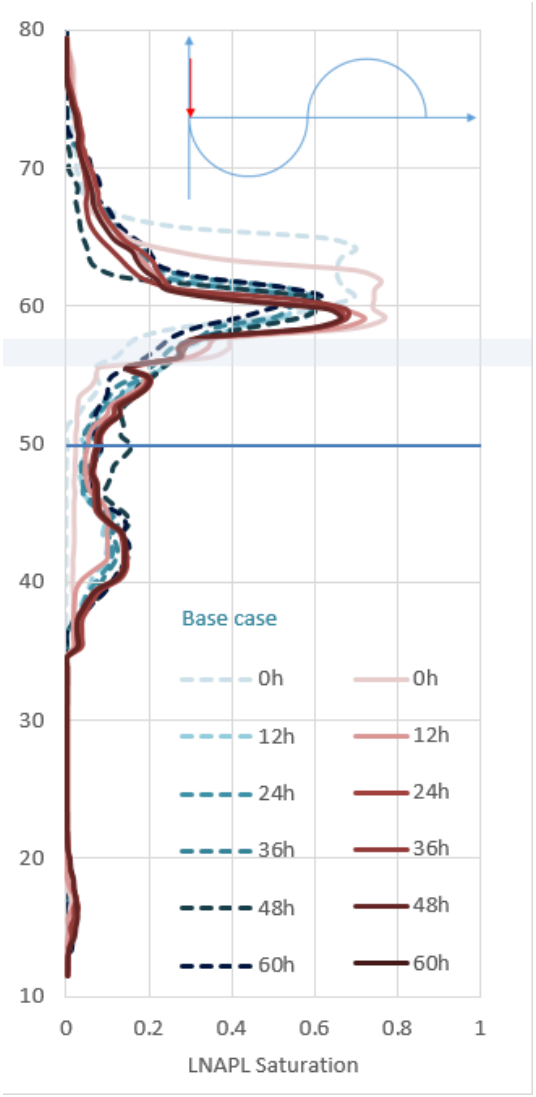

(a) Critical position 1, WT=50cm, descending

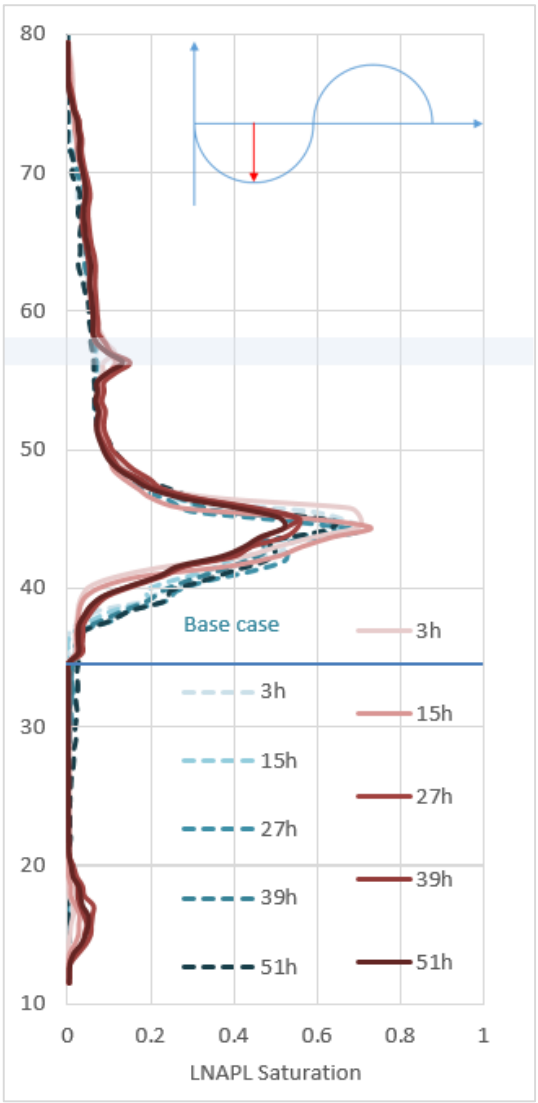

(b) Critical position 2, WT=35cm

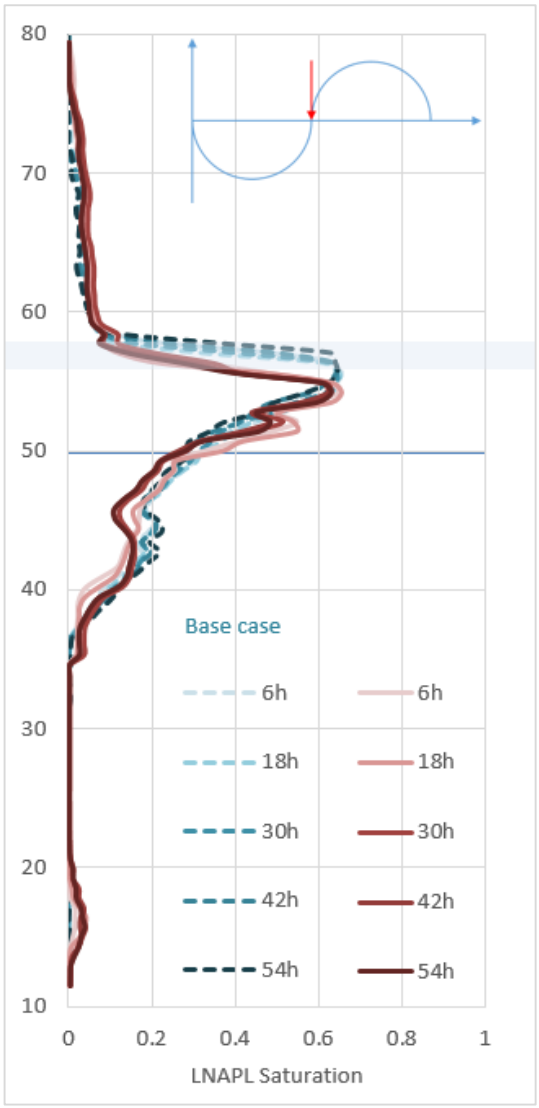

(c) Critical position 3, WT=50cm, ascending

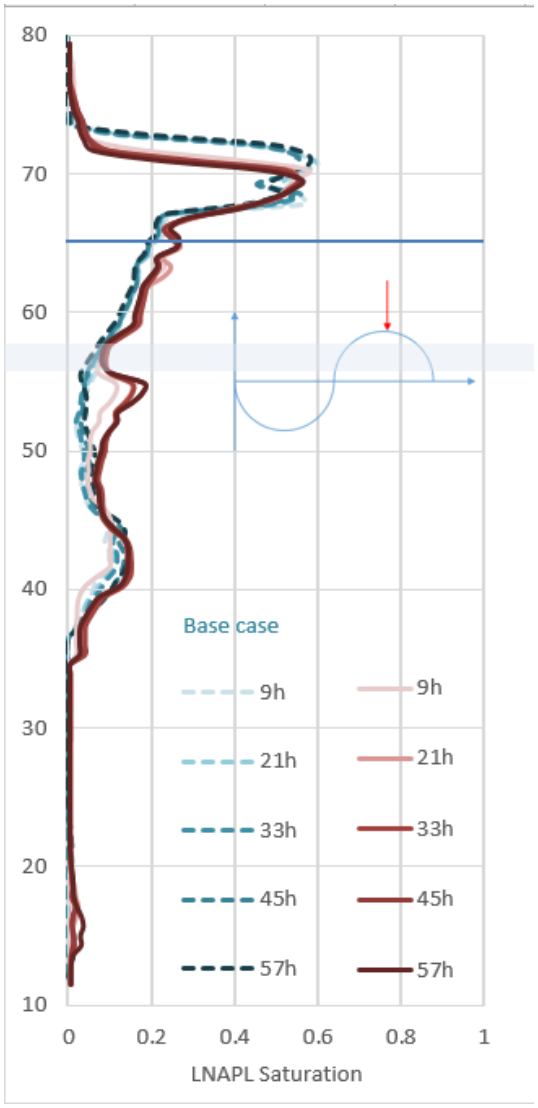

(d) Critical position 4, WT=65cm

Figure 6-29 Inter-cycle LNAPL saturation profiles of the current scenario in red and the base case profiles superimposed in cyan from the 1st cycle to the 5th cycle, where the approximate location of the fine sand layer was shaded in the plots

In summary, a partial fine grain layer within a homogenous high permeability layer generates difference in capillary resistance to multiphase flow. Therefore, water saturation distribution, particularly the upper boundary of the capillary fringe appears uneven. Meanwhile, LNAPL favoures high permeability areas where capillary pressures are relatively low. Thus, the LNAPL merely bypasses the fine grain layer without infiltration and entrapment. Under a high water or LNAPL gradient, LNAPL may coat onto and infiltrate into the fine sand layer during water drainage and becomes entrapped afterwards. With multiple water table fluctuations, an increasing amount of LNAPL becomes entrapped in the fine grain layer, yet the total amount of LNAPL entrapped within remains small.

The implications can be drawn from this scenario are that an incomplete low permeable layer embedded within a relatively high permeable aquifer cannot be retain or intercept large amount of LNAPL, thus, is not sufficient enough to be used as an LNAPL container or barrier.

6.6 The single complete fine grain layer scenario

Two short videos of the LNAPL release and fluctuation periods for the current scenario can be found in Digital Appendices A.2.7.2.

This section discusses the influence of an embedded fine grain layer made of fine sand that took up the full tank width. Comparisons are made among the base case scenario (Run4T3), the partial fine grain layer scenario (Run7T1) and the single complete fine grain layer scenario (Run6T2), where 98ml of LNAPL was released into the system within 58min. The approximately 2 cm thick, 29.5cm wide fine sand layer was located between approximately Z=58cm to 60cm of the tank elevation, which was the upper boundary of the capillary zone. The top boundary of the fine sand layer was slightly uneven.

6.6.1 LNAPL release period

A selection of critical moments are presented to emphasise the characteristics during this process.

Figure 6-30 features the photographic event when the LNAPL front reached the complete fine grain layer and began to accumulate upon. Different from the partial fine grain layer scenario, the water-air interface appeared adequately even, since the complete fine grain layer provides a relatively even capillary pressure distribution over the tank width. Before this moment, the feature and dynamic of all fluids were relatively identical to the base case scenario and the partial fine grain layer scenario. A black shadow appeared on the top right corner of the tank caused by the shadow of the Mariotte's bottle tubing, which was considered as fluid saturation by the image analysis.

Figure 6-31 demonstrates a moment during the on-going release as an example, where the LNAPL body was developed into two parts, the upper cone-shaped body, and the main lens. Due to the obstruction of the complete fine sand layer, the saturation of the LNAPL lens was exceptionally higher than all other cases due to the obstruction of the complete fine layer, where the saturation was averagely 0.8~0.9.

Figure 6-32 displays the end of the LNAPL release, where the thickness of LNAPL lens grew to 5cm. Two visible LNAPL leaks emerged below the fine sand layer, which indicated that the LNAPL pressure accumulated upon the fine sand layer was sufficient enough to locate preferential paths within the layer and infiltrated through. The a considerable amount of LNAPL intercepted below the fine grain layer may be mistakenly anticipated as DNAPL occurrence by practitioners, if chemical analysis is not viable or not undertaken structure channels with lower entry pressures to conquer, which were formed as the consequences of the heterogeneity occurred during sand packing. The LNAPL infiltration into and through the fine sand layer decreased the total LNAPL head. However, it was replenished by the downward LNAPL mass from the upper unsaturated zone. Therefore, the LNAPL infiltration continued after the LNAPL release ceased.

Figure 6-33 illustrates the end of the monitoring during the LNAPL release period, where two LNAPL lenses coexisted. The main lens, with a slightly decreased saturation, remained above the fine sand layer; whereas below the layer, there formed a thin LNAPL lens with a maximal saturation of 0.38, which possessed significant development of fingering due to low LNAPL pressure. Only less than 1% of LNAPL volume was found residing within the fine sand layer. And air entrapment was only found within the LNAPL main lens.

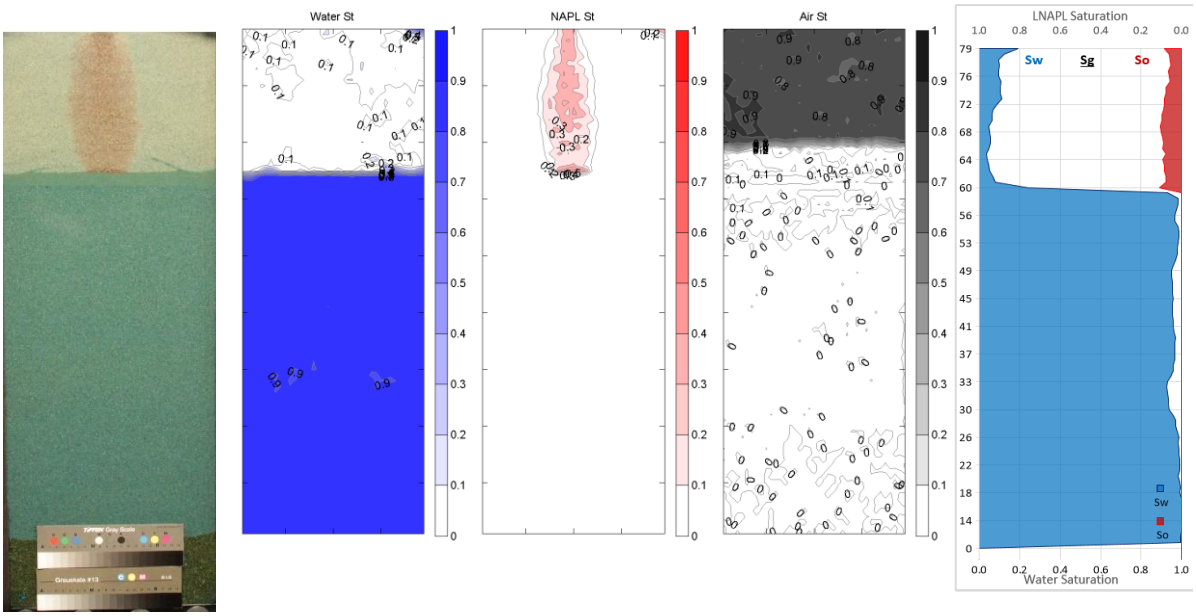

Figure 6-30 Compilation of fluid saturation contours and profiles for the LNAPL release of the single complete fine grain layer scenario at T=20 min

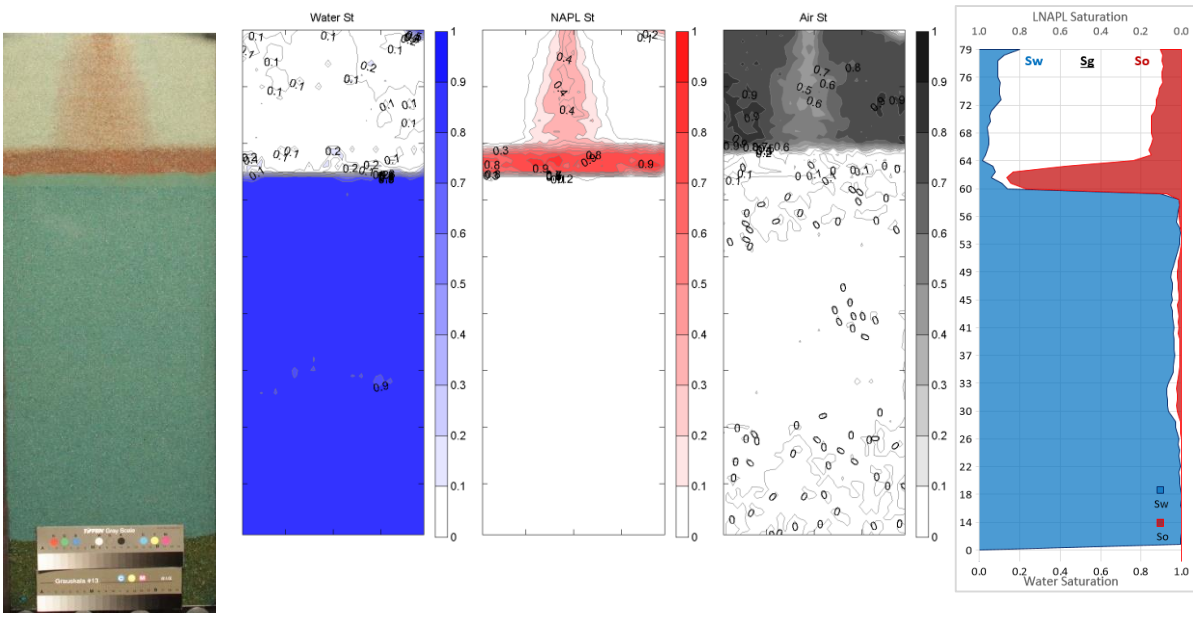

Figure 6-31 Compilation of fluid saturation contours and profiles for the LNAPL release of the single complete fine grain layer scenario at T=52 min

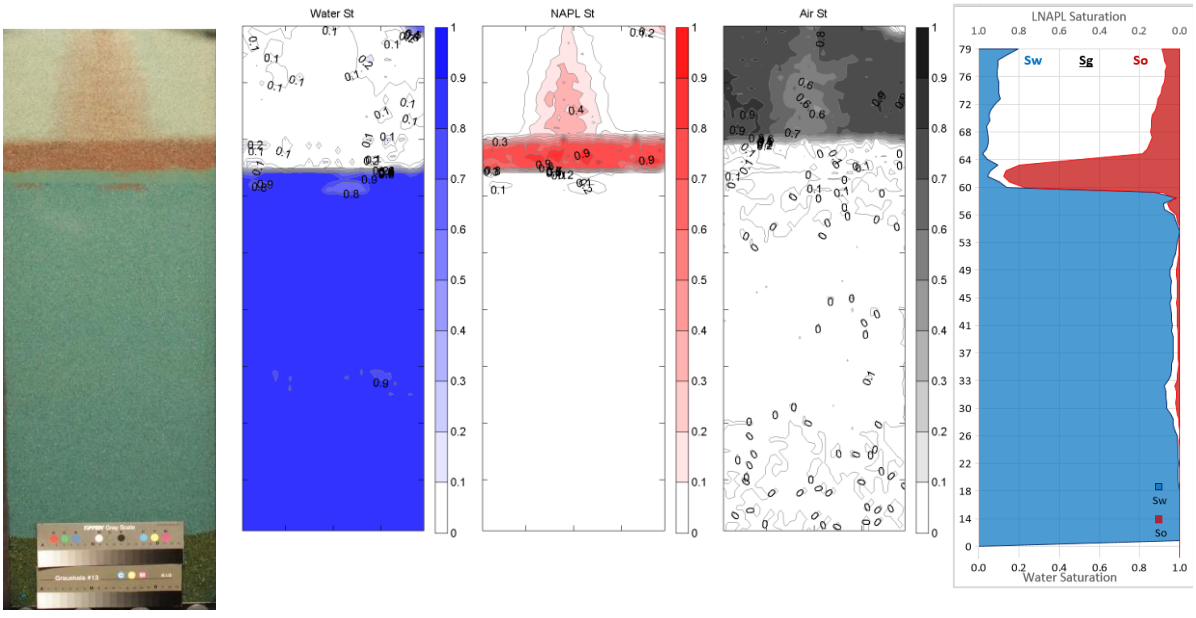

Figure 6-32 Compilation of fluid saturation contours and profiles for the LNAPL release of the single complete fine grain layer scenario at T=58min

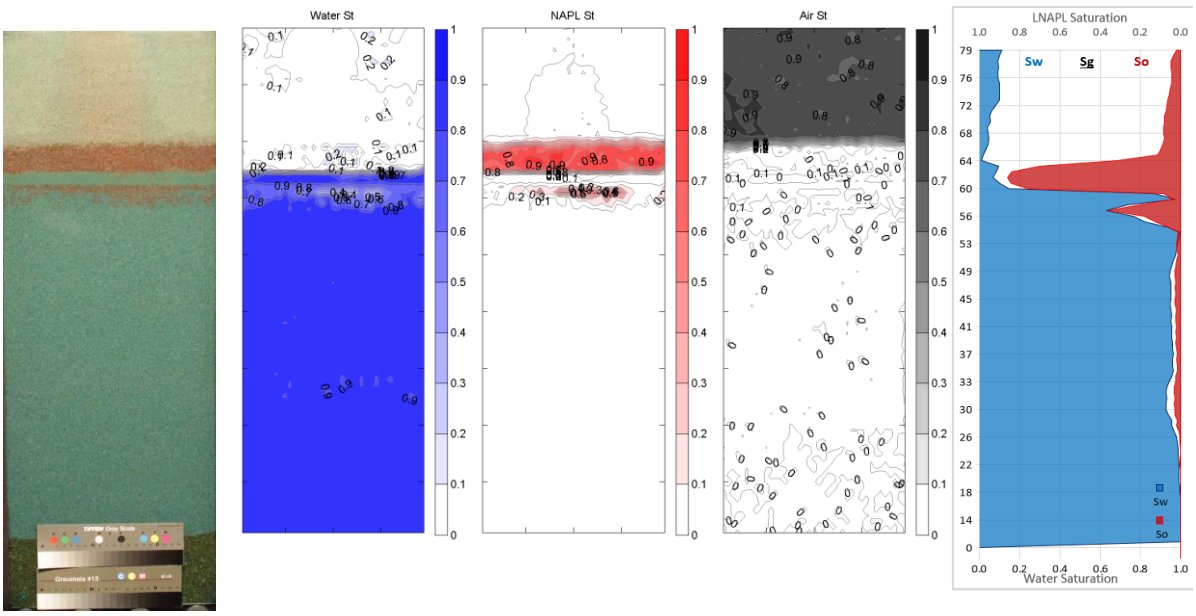

Figure 6-33 Compilation of fluid saturation contours and profiles for the LNAPL release of the single complete fine grain layer scenario at T=120 min

6.6.2 Water table fluctuation period

Under the influence of a complete fine grain layer, detailed fluid distributions and dynamics of a water drainage process and a water imbibition process are demonstrated in Figure 6-34 and Figure 6-35 respectively, taking the cycle 1 as an example. To highlight the LNAPL dynamics within the complete fine grain layer, Figure 6-36 was plotted to illustrate the variations of the LNAPL saturation and LNAPL volume ratio within the layer during the fluctuation period.

During the water drainage, the duel LNAPL lenses were brought downwards, where the LNAPL above the fine grain layer kept infiltrating through the preferential paths it located during the release (Figure 6-34(a)). As the water table being lowered down, LNAPL below the fine sand layer kept expanding downwards through significant fingering (Figure 6-34(b)). Both LNAPL lenses were highly saturated with LNAPL with the approximate saturation of 0.8. The LNAPL saturation and volume ratio of the fine sand layer increased with an average saturation of 0.09. By T=1h shown in Figure 6-34(c), both LNAPL lenses went through the fine sand layer and continued to migrate downwards. Consequently, the residual LNAPL within the fine sand layer decreased to a saturation of 0.05 (Figure 6-36). It is reckoned that between the

However, a small increase in the volume and saturation of LNAPL within the layer was observed after this moment, which was due to the replenishment by the remaining downward LNAPL in the original unsaturated zone (Figure 6-34(d) and Figure 6-36).

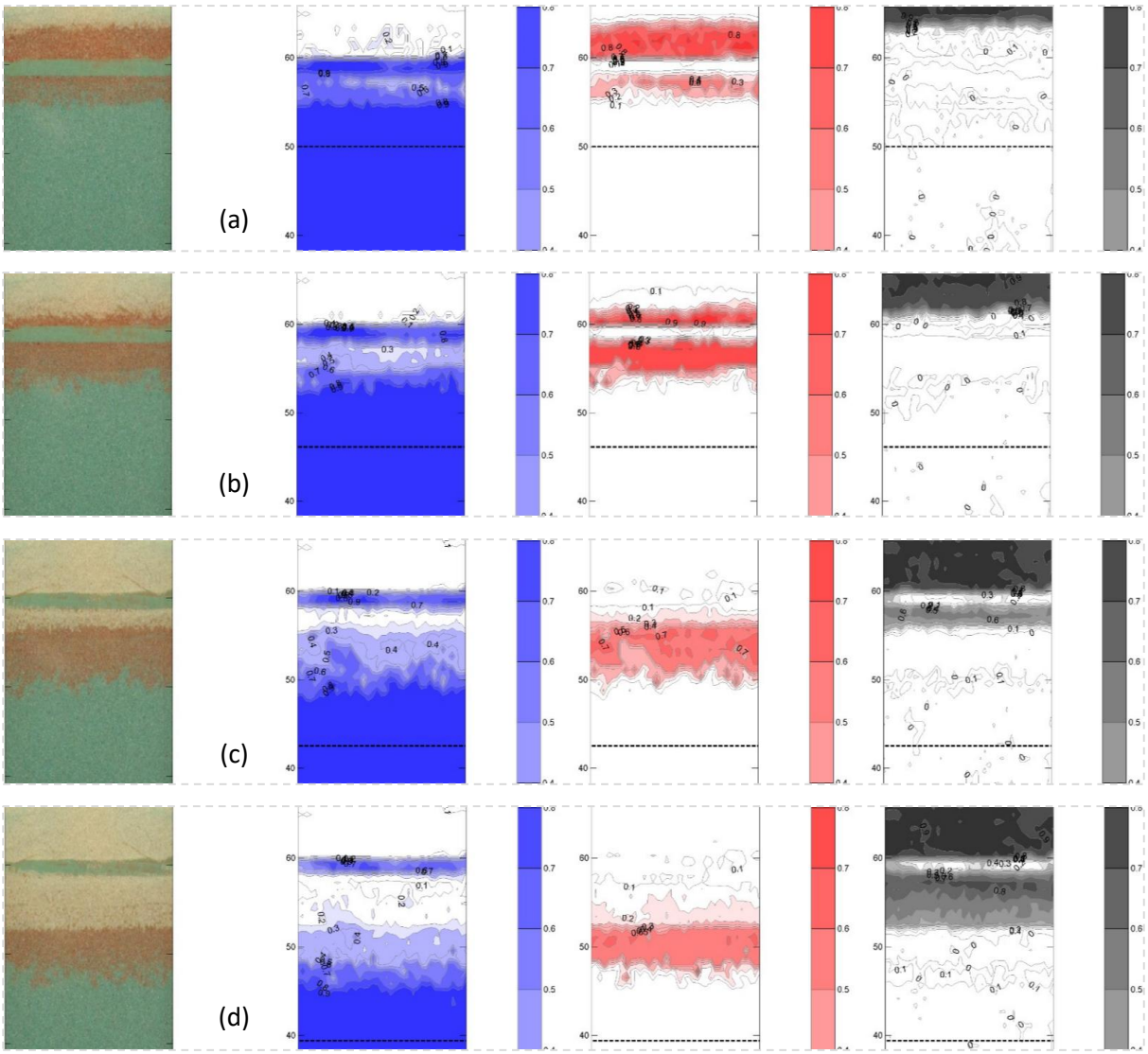

Figure 6-34 An example of fluid distributions and dynamics under the influence of complete fine grain layer during water table descending (4 continuous moments during Cycle 1: 0.0h, 0.5h, 1.0h, and 1.5h)

During the water imbibition process, strong LNAPL and air displacement by water occurred and a continuous decrease in LNAPL saturation was observed within the fine sand layer (Figure 6-36). Via the preferential paths, the LNAPL, mixed with air, was gradually pushed upwards through the fine sand layer. A duel lenses system formed again at T=7h with saturation in both lenses decreased due to the residual LNAPL saturation entrapped in the entrapped LNAPL band at the lowermost water table

position (Figure 6-35(c)). A significant amount of LNAPL was intercepted below the fine sand layer with an average saturation of 0.4 when water table surpassed the fine sand layer (Figure 6-35(d)). At this moment, the fine sand layer was predominantly saturated with water and both residual air and LNAPL within.

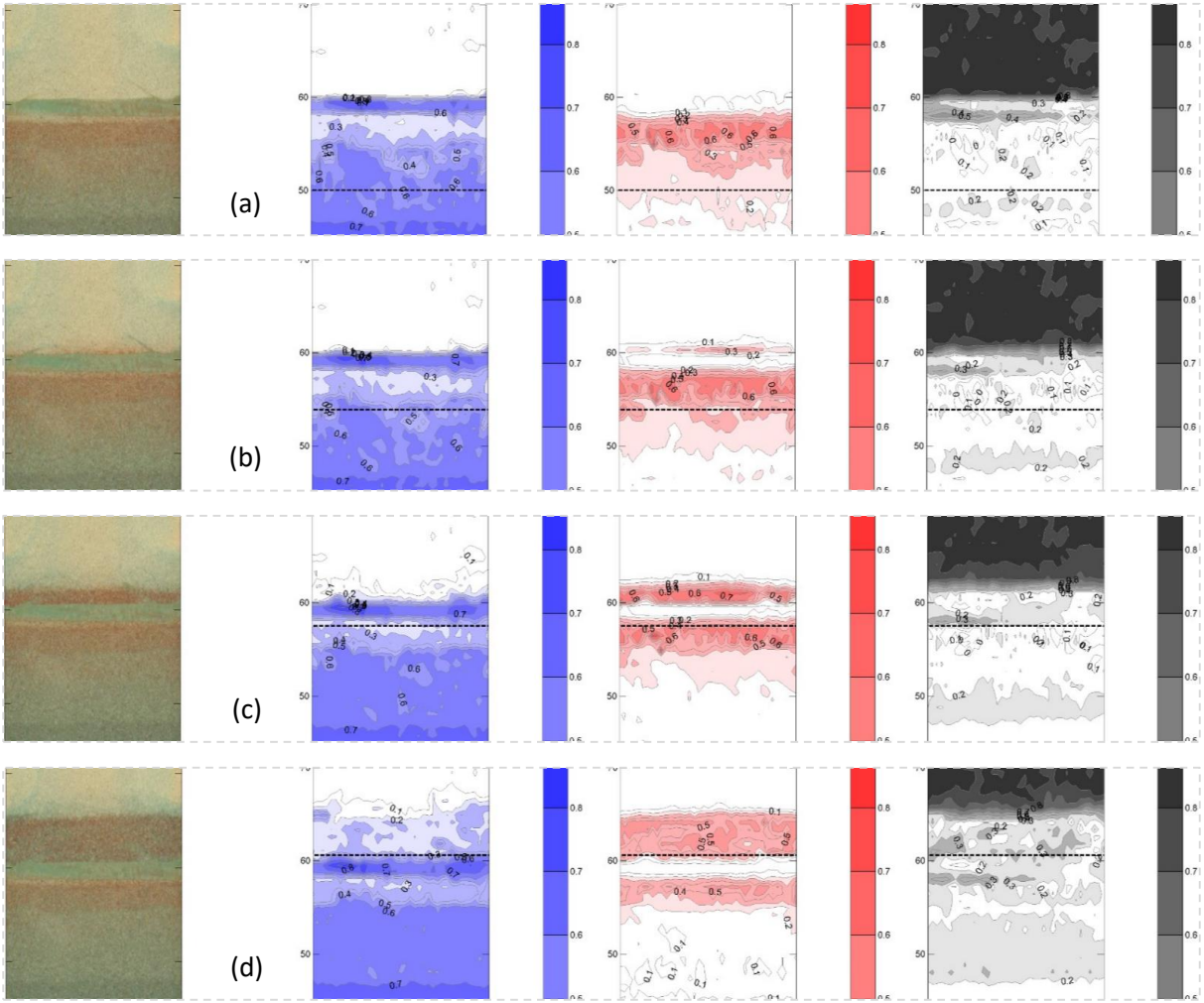

Figure 6-35 An example of fluid distributions and dynamics under the influence of complete fine grain layer during water table ascending (4 continuous moments during Cycle 1: 6.0h, 6.5h, 7.0h, and 7.5h)

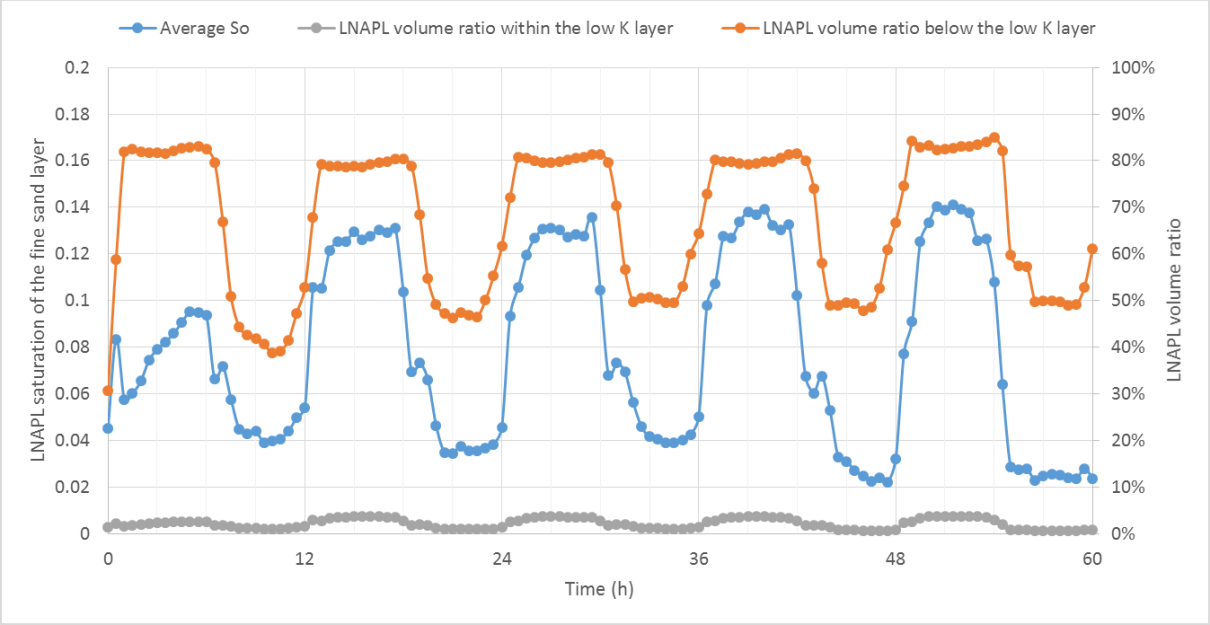

Figure 6-36 Average LNAPL saturation (So) and LNAPL volume ratio within the complete fine sand layer, LNAPL volume ratio below the layer during the water table fluctuation period

From the inter-cycle plots (Figure 6-37) with comparison against the base case, main observations are concluded as follows.

At critical position 1 and 4 (Figure 6-37(a,d)), the saturation of the LNAPL lens below the fine sand layer increased over oscillations. At critical position 1 and 3 (Figure 6-37(a,c)), an increasing amount of residual LNAPL saturation was observed as the oscillation went on, which, compared to the base case, was smaller. Due to the influence of a complete low-K layer, the LNAPL smearing length was significantly shorter than the base case. From Figure 6-37(b), the deepest smearing depth in the current case was Z=41cm compared to Z=37cm of the base case and Z=38.5cm of the partial fine grain layer case, due to the exhaustion of the LNAPL pressure by passing through the fine sand layer. The residual LNAPL within the fine sand layer increased over the oscillations from 2.5% of the total LNAPL volume during the 1st cycle to 4% during the last cycle Figure 6-37(b).

A significant amount of LNAPL volume was permanently held below the fine sand layer after the first water table descending. Most LNAPL content was still mobile. However, the mobility range of the LNAPL was between the bottom of the LNAPL body (Z=41cm) to the lower boundary of the fine sand layer (Z=58cm). It was because after the first water descending, the total amount of mobile LNAPL largely decreased due to entrapment. The residual pressure of LNAPL within the LNAPL lens, despite pushed up by the ascending water table, still could not exceed the entry pressure of the fine sand

layer and thus became intercepted below the fine sand layer. Therefore, it could be observed from Figure 6-36 that during the 1st cycle, roughly 41% of LNAPL was held below the fine sand layer; whereas 50% of LNAPL was found during the last cycle. Besides the permanent intercepted LNAPL mass, a complete fine sand layer was shown in Figure 6-36 to temporarily hold as much as 85% of the total LNAPL mass around the lowermost water table positions, during the cycle 5.

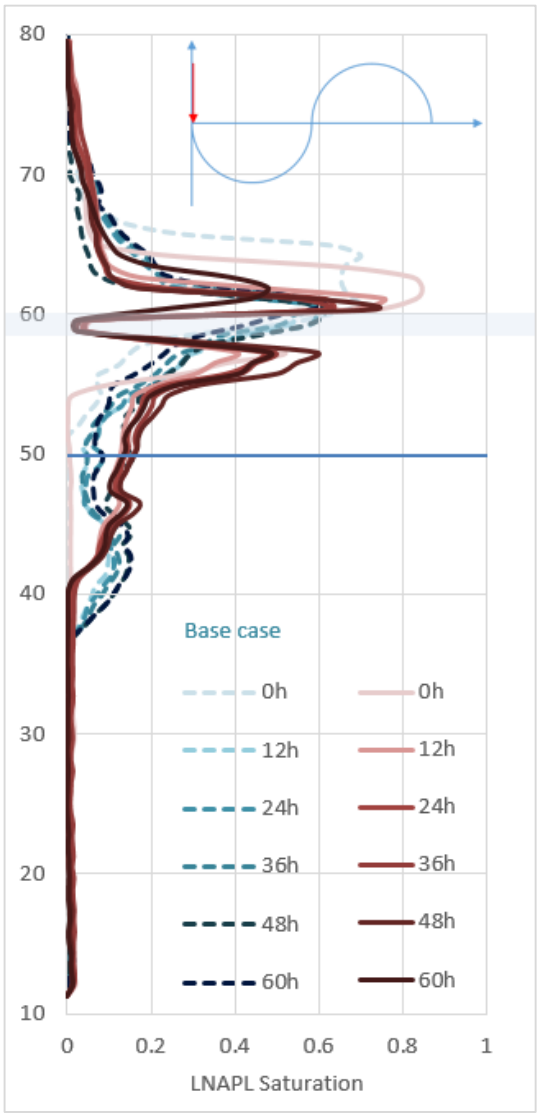

(a) Critical position 1, WT=50cm, descending

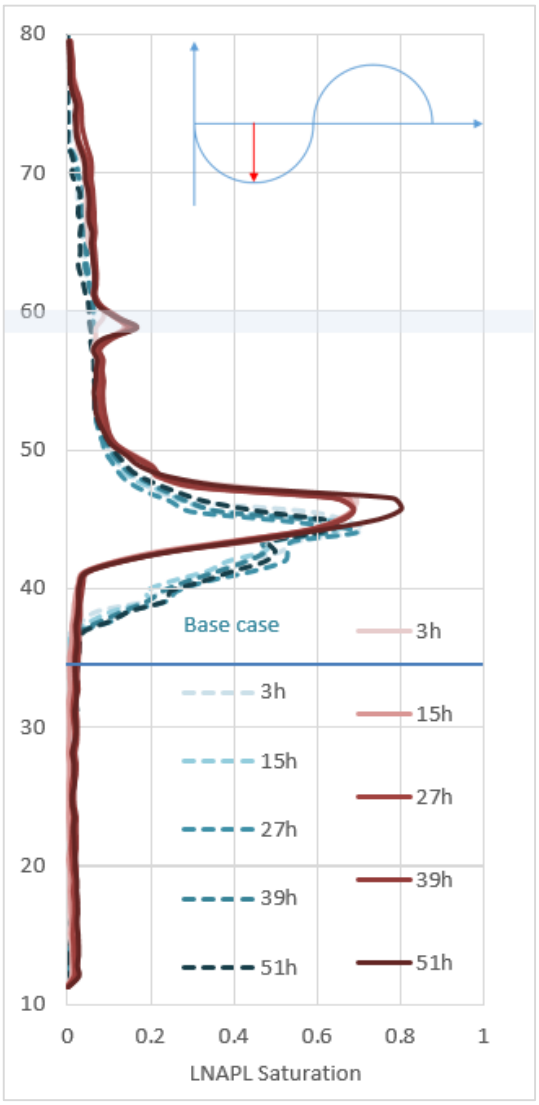

(b) Critical position 2, WT=35cm

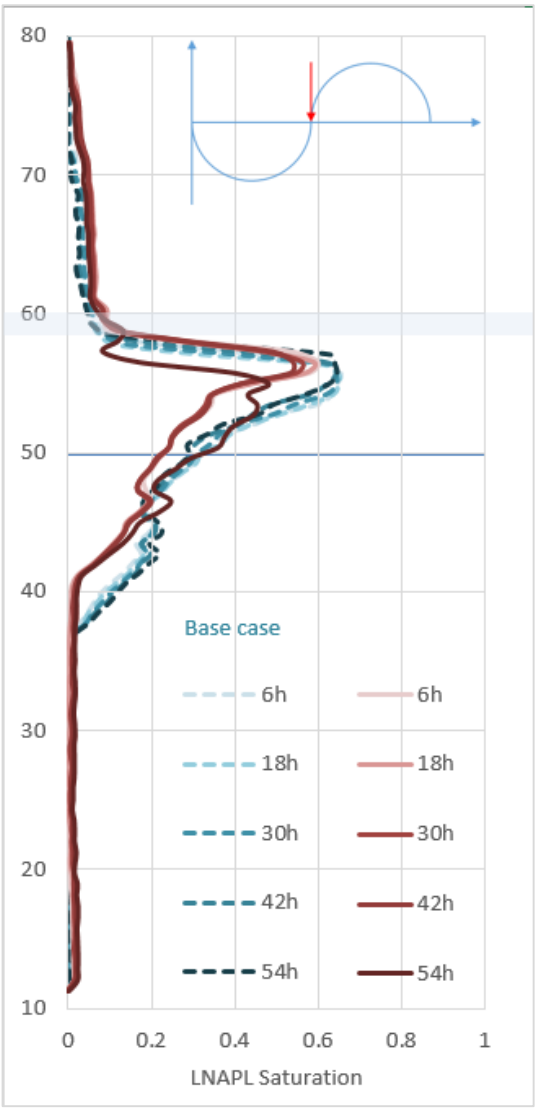

(c) Critical position 3, WT=50cm, ascending

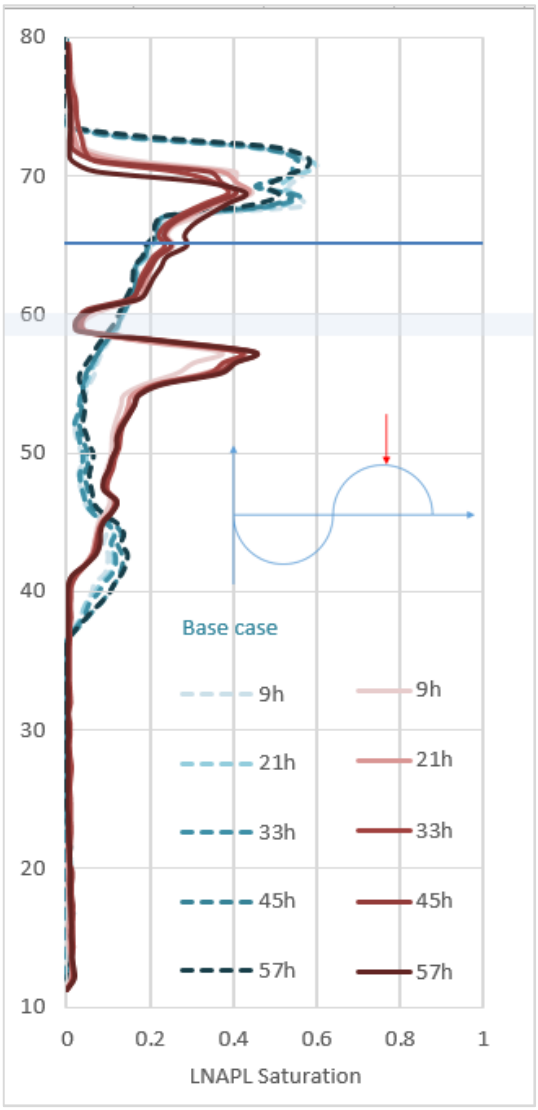

(d) Critical position 4, WT=65cm

Figure 6-37 LNAPL saturation profiles of the current scenario in red and the base case profiles superimposed in cyan from the 1st cycle to the 5th cycle, where the approximate location of the complete fine sand layer was shaded in the plots.

In summary, not only the permeability of the aquifer plays an important role in LNAPL behaviour, but also the entry pressure, which is vividly demonstrated in the heterogeneous scenarios due to the contrast. Considering that the permeability difference between the fine and medium sand used in this study is fairly small, the entry pressure is more likely to be controlling factor here. A complete fine grain layer within a relatively highly permeable aquifer system results in a shorter smearing length and depth. The fine grain layer only preserves a small portion of released LNAPL. However, incorporating with the transient cyclic water table, a considerable amount of LNAPL (in this scenario, half of the total LNAPL mass), although mostly mobile, has been permanently seized below the fine grain layer and formed a second LNAPL lens.

One implication from the site characterisation perspective can be inferred that a considerable amount of LNAPL intercepted below the fine grain layer may be mistakenly anticipated as DNAPL occurrence by practitioners, if chemical analysis is not viable or not undertaken. Depending on the seasonal fluctuation range and daily fluctuation range, the LNAPL seized below the fine grain layer can be at depth during high water table periods. The misleading characterisation may give rise to ineffective remediation strategies. Therefore, further investigation should be conducted at layered heterogeneous sites to verify the NAPL composition, and attention should be given to the area below the fine grain layer.

An implication from the remediation perspective can also be inferred that a complete fine grain layer may potentially be utilised, not to retain LNAPL content, but to intercept LNAPL content incorporating with a controllable water table fluctuation scheme.

6.7 The multiple complete fine grain layers scenario

Two short videos of the LNAPL release and fluctuation periods for the current scenario can be found in Digital Appendices A.2.8.2.

This section discusses the influence of multiple complete fine grain layers embedded within medium permeability aquifer. Comparisons are made between the base case scenario (Run4T3), and the multiple complete fine grain layers scenario (Run12T1), where 103ml of LNAPL was released into the system within 32min. Three approximately 2.5 cm thick, 29.5cm wide fine sand layers which took up the full width of the tank, were packed into the medium sand aquifer. The locations of the layers were at Z=59.5~62.0cm, Z=48.5~51.0cm, and Z=38~40.5cm of the tank elevation. The top layer was slightly higher than the upper boundary of the capillary zone; the middle layer was at the centre of the water table oscillation, and the bottom layer was slightly higher than the lowermost water table position.

6.7.1 LNAPL release period

A selection of critical moments are presented to emphasise the characteristics during this process.

Figure 6-38 features one of the photographic events when the LNAPL front was infiltrating through the first fine grain layer. Different from the single complete fine grain layer case, where a 4cm LNAPL lens was developed upon the fine grain layer prior to the infiltration, the LNAPL infiltration into the first low permeability was achieved without a significant accumulation of LNAPL thickness. It was

because the first fine grain layer was not entirely within the capillary zone, which implied that it was not originally water saturated. In fact, the boundary of the capillary fringe was found within this layer, where the upper half of the fine grain layer was unsaturated, and the bottom half was water saturated. Therefore, LNAPL could easily infiltrate into the vacant pore space within the unsaturated part under a small pressure head over the entire width of the tank. Once LNAPL front hit the capillary zone boundary as shown in Figure 6-38, leakage was achieved only through preferential paths instead of an even linear infiltration.

Figure 6-39 illustrates the end of LNAPL release when the LNAPL body was fully developed, which was divided by the boundary of capillary fringe into two lenses. The upper body was a sombrero shape with a highly LNAPL saturated lens above the boundary, where the maximal LNAPL saturation reached 0.9. The lower was developing bowl shape body with a maximal LNAPL saturation of 0.53. A 1cm low LNAPL saturated band was found between the lenses with a saturation of 0.18.

Figure 6-40 demonstrates the end of the monitoring of the release period, where the saturations of the duel LNAPL peaks switched. The saturation of the upper LNAPL lens decreased to 0.53 with no evident LNAPL thickness upon the fine grain layer. On the contrary, the saturation of the lower lens spikes at a maximal of 0.8 with a thickness of 6cm. Under gravity, most LNAPL mass had moved downwards to replenish the lower LNAPL lens. An error could be observed in the shaded profile in Figure 6-40(e), where LNAPL and water profile overlapped. The overlap was considered as an error in water saturation. By comparing the mass balance result, at the moment T=60, the calculated LNAPL volume was 100.07, which was slightly less than the LNAPL release volume. This confirmed that LNAPL volume was not overestimated. By further comparing the LNAPL distribution contour against the photographic record (Figure 6-40(a, c), the LNAPL saturation distribution predicted seemed fairly representable of the real distribution. Therefore, the error should result from the overestimation of water saturation.

A repeated error was found at the bottom of the water saturation profile in every moment, where the bottom of the tank was shown not fully water saturated. It was induced by the tank surface smearing above the grey scale bar.

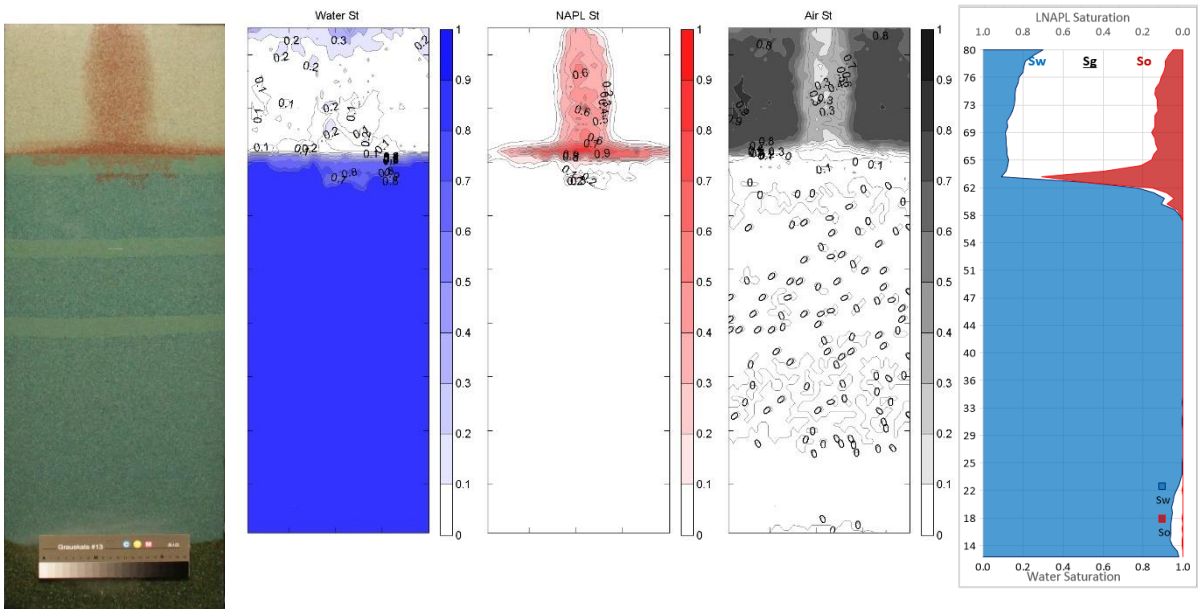

Figure 6-38 Compilation of saturation contours and profile for the LNAPL release of Run12T1 at T=24 min

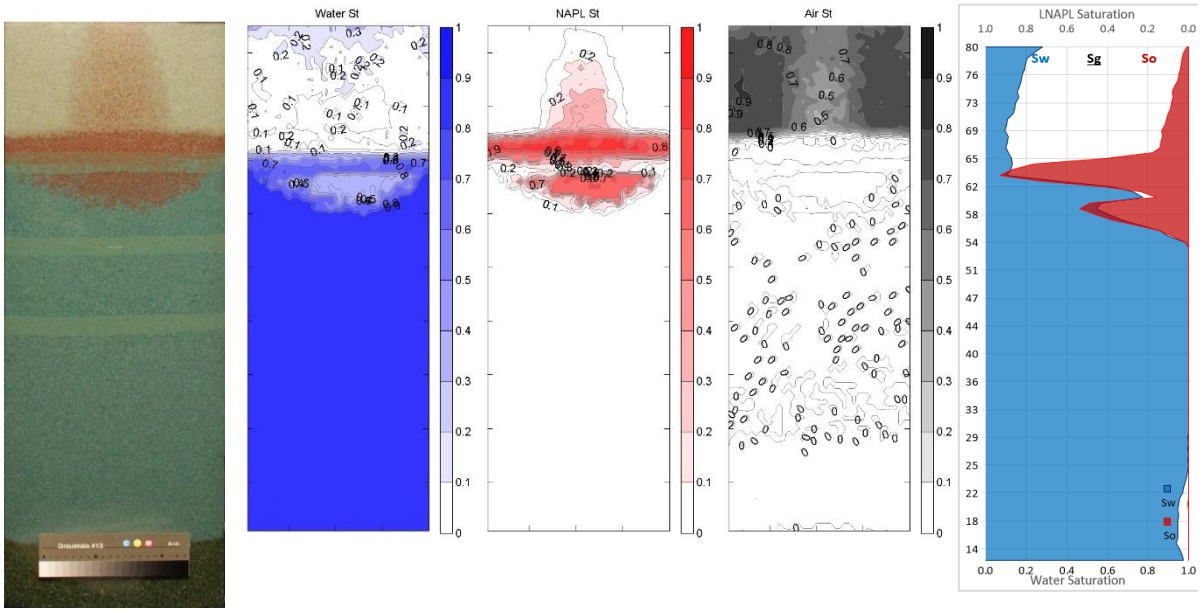

Figure 6-39 Compilation of saturation contours and profile for the LNAPL release of Run12T1 at T=34 min

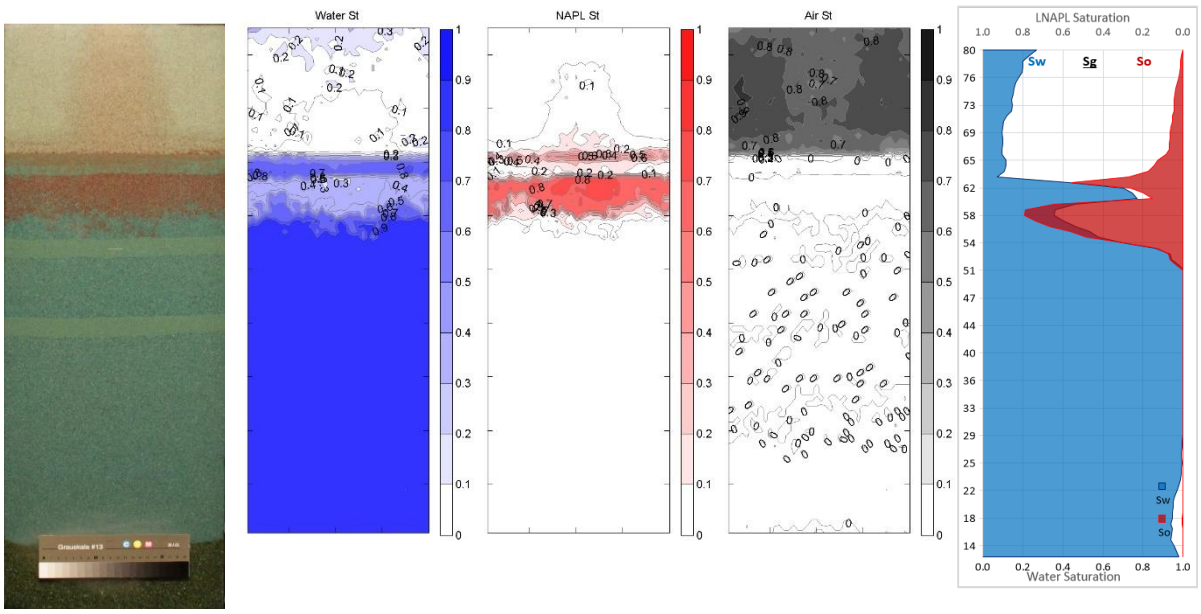

Figure 6-40 Compilation of saturation contours and profile for the LNAPL release of Run12T1 at T=60min

6.7.2 Water table fluctuation period

Under the influence of three complete fine grain layers, detailed fluid distributions and dynamics of a water drainage process and a water imbibition process are demonstrated in Figure 6-41 and Figure 6-42 respectively, taking Cycle 1 as an example. To illuminate the LNAPL dynamics within these complete fine grain layers and between the layers, Figure 6-43 was plotted to illustrate the variations of the LNAPL volume ratio within the three fine grain layers and between the layers during the fluctuation period.

After the settling down of the release, the LNAPL main lens situated below the 1st fine grain layer further extended, which took up almost the entire length between the 1st and the 2nd layer, where 68% of LNAPL total volume was found (Figure 6-41 (a)). A small amount (16%) of LNAPL was left within the 1st fine grain layer, which was gradually drained as the water table moving downwards.

LNAPL was then accumulated upon the 2nd fine grain layer, forming a 7cm thick LNAPL lens which was accountable for 87.6% of the LNAPL total volume. The process at the moment resembled the LNAPL release in the single complete fine grain layer scenario since the fine grain layer was originally water saturated and the 2nd layer was still within the capillary zone (Figure 6-41 (b)). Sufficient LNAPL head was needed to locate the preferential paths for LNAPL to penetrate the 2nd layer. The volume of LNAPL retained within the 1st layer decreased to 7.0%.

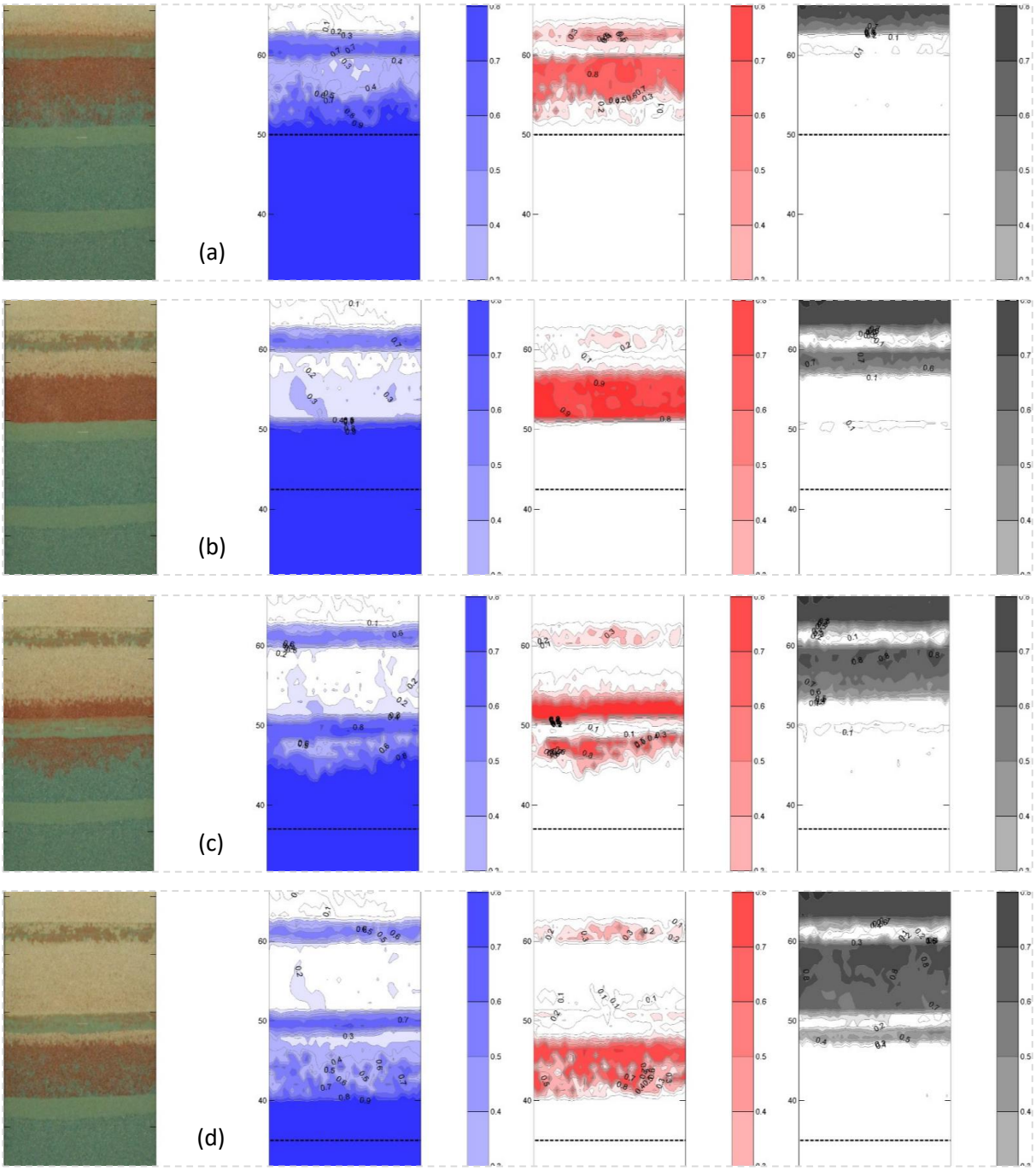

Figure 6-41 An example of fluid distributions and dynamics under the influence of multiple low-K layers during water table descending (4 moments during Cycle 1: 0.0h, 1.0h, 2.0h and 3.0h)

During the LNAPL penetrating through the 2nd layer in Figure 6-41 (c), as the water table continued to descend, the 2nd layer was transformed into the unsaturated zone with no further support from the capillary zone. Consequently, LNAPL was allowed to infiltrate into the pore space left by water drainage and quickly penetrate through the 2nd layer. Once the LNAPL lens went through the 2nd layer in Figure 6-41 (d), LNAPL quickly smeared the space between the 2nd and 3rd layer, where 69.7% of LNAPL total volume was found. At this moment, only 8.7% of LNAPL total volume was found between

the 1st and 2nd layer, while 9.6% of LNAPL total volume was left in the 1st layer and 5.3% was left in the 2nd layer (Figure 6-43). More LNAPL was entrapped within the 1st layer was due to that, compare to the 2nd layer, the 1st layer was initially less water saturated, which provided more pore space for LNAPL to occupy and became entrapped.

During the first water imbibition process, the total volume seized between the 2nd and 3rd layer decreased from 75.0% (Figure 6-42(a)) to 47.7% (Figure 6-42(c)). These LNAPL contents were seized permanently below the 2nd layer, although most remain mobile. After the water table was raised above the 2nd layer, the LNAPL front could not provide an LNAPL lens with evident thickness. The saturation of the front was only around 0.2(Figure 6-42(b)). Most of the LNAPL front was further seized below the 1st layer, where 31.7% of LNAPL total volume resided. As the water table arrived at the highest position, three LNAPL bands formed, where the band on top of the 1st layer only possessed an average saturation of 0.1 and a total volume of 4.4%.

From Figure 6-41 and Figure 6-42, an error was found that the water saturation was overestimated when the band highly saturated with LNAPL. Once again, both calculated LNAPL mass and distribution were examined and concluded accurately. Therefore, it was found that for layered heterogeneity which created exceptionally high LNAPL saturation, the current calibration test result could not provide an accurate prediction on the extremely low water saturated points.

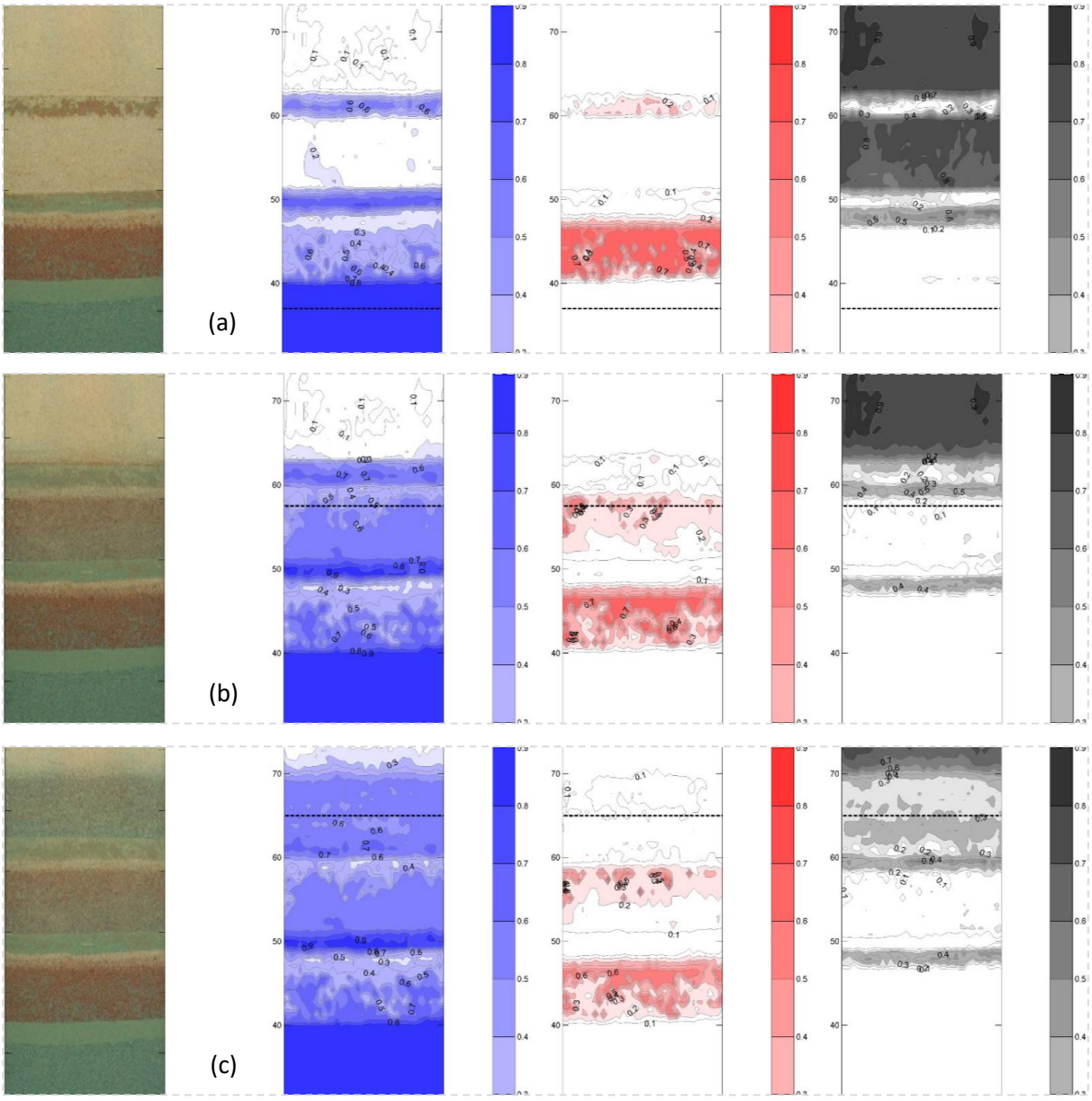

Figure 6-42 An example of fluid distributions and dynamics under the influence of multiple low-K layers during water table ascending (3 moments during Cycle 1: 4.0h, 7.0h, and 9.0h)

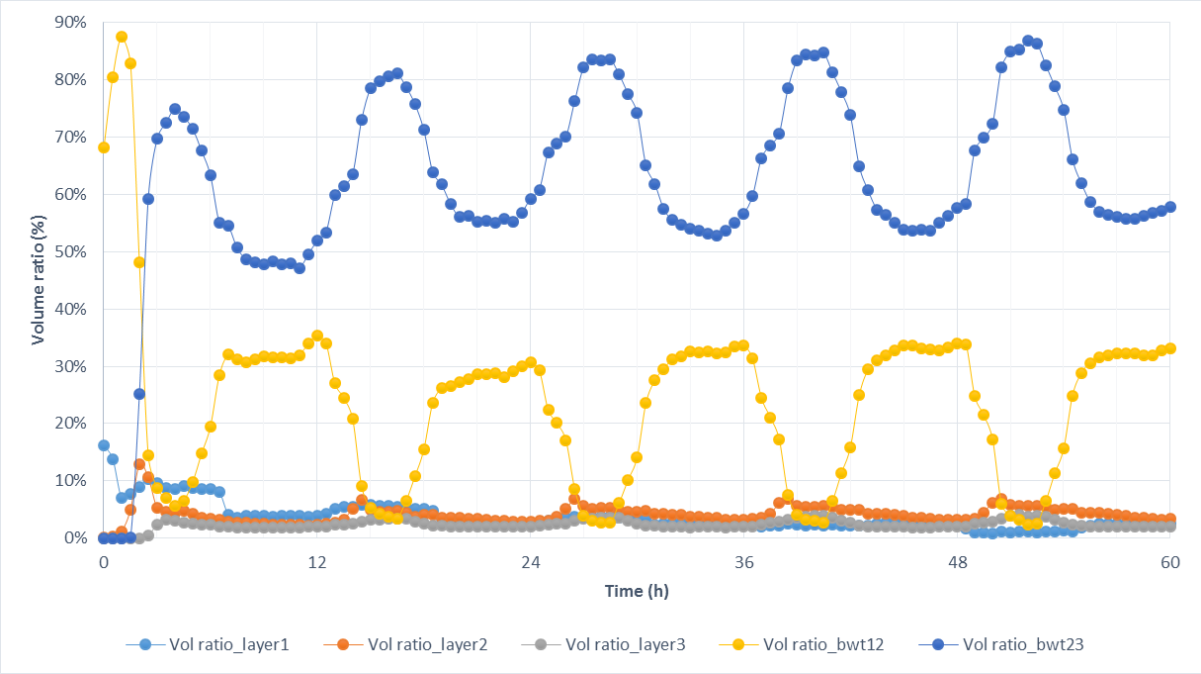

Figure 6-43 LNAPL volume ratio within the 3 complete fine sand layers, LNAPL volume ratio between the 1st and 2nd layers, and LNAPL volume ratio between the 2nd and 3rd layers during the water table fluctuation period

Interestingly, looking at the inter-cycle dynamics in this scenario, the LNAPL permanently retained between the 2nd and 3rd layer increased from 47.2% during Cycle 1 to 55.7% during the last cycle (Figure 6-43). While the maximal temporary retained LNAPL volume reached 87.5% of the total volume when the water table was situated around critical position 2 (Figure 6-44 (b)). The water table fluctuation "collected" an increasing amount of LNAPL and facilitated LNAPL to be "sandwiched" between the two fine grain layers located at the fluctuation bottom. Such incorporation between cyclic water table fluctuations and fine grain layers may potentially provide the possibility of an LNAPL recovery scheme, that LNAPL can be controllably relocated at a target depth of an aquifer to be safely collected.

Moreover, it is discovered from Figure 6-44 at critical position 2, 3 and 4 that the LNAPL saturation above the 1st fine grain layer decreased as the fluctuation proceeded. The total smearing length of the current case (30cm) was notably shorter compared to the base case and all the other scenarios.

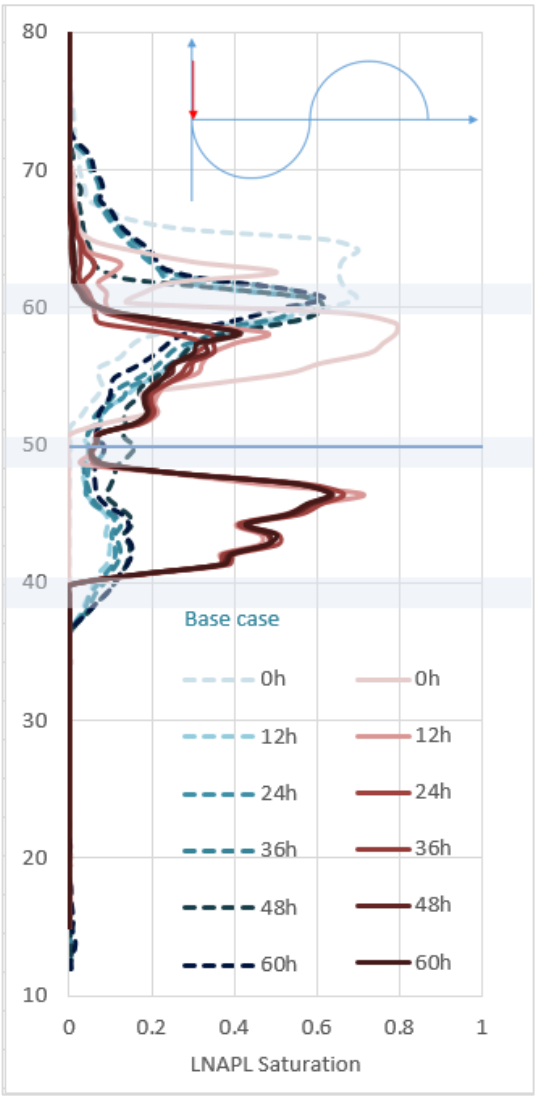

(a) Critical position 1, WT=50cm, descending

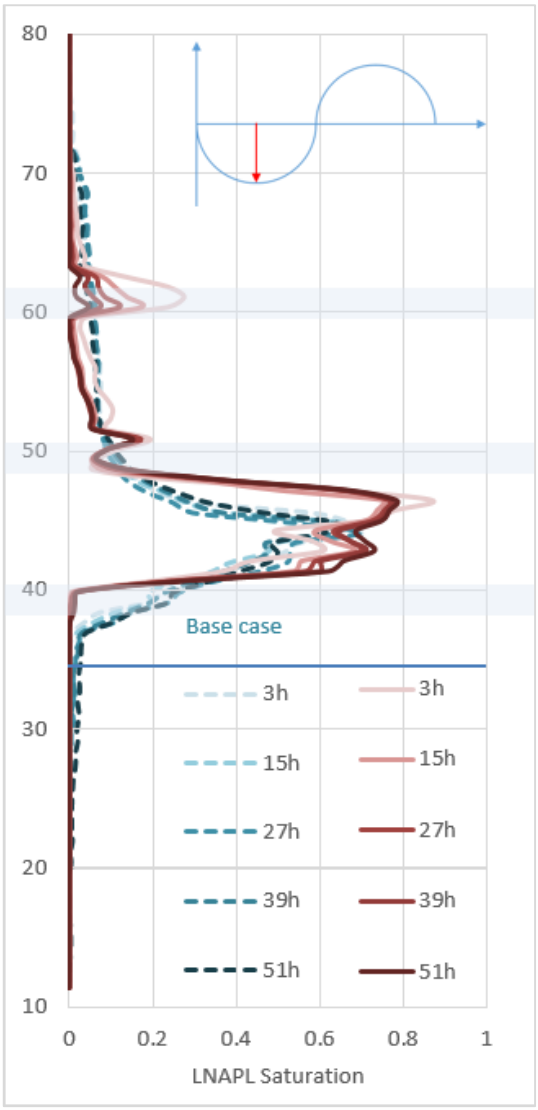

(b) Critical position 2, WT=35cm

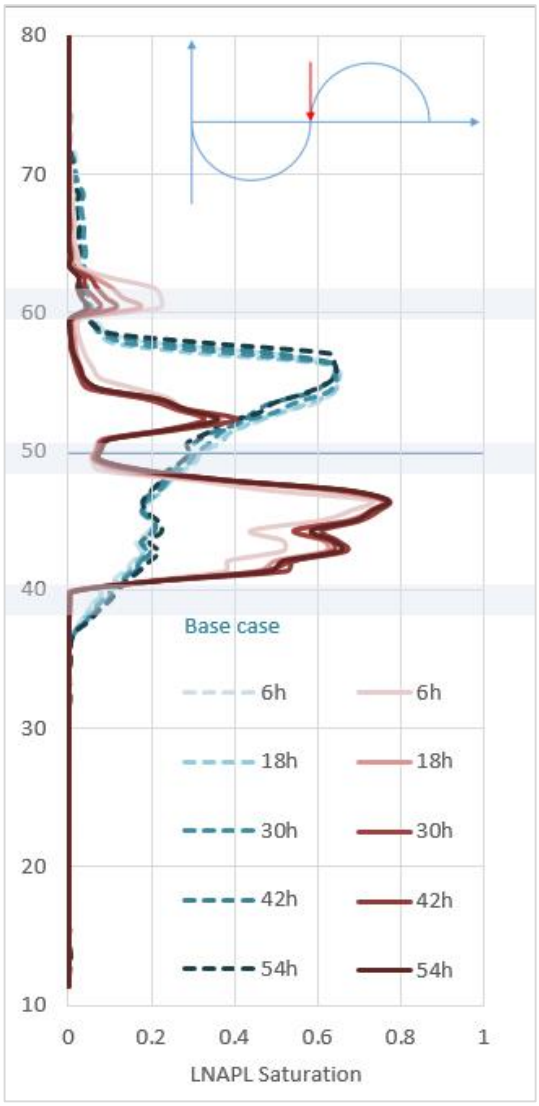

(c) Critical position 3, WT=50cm, ascending

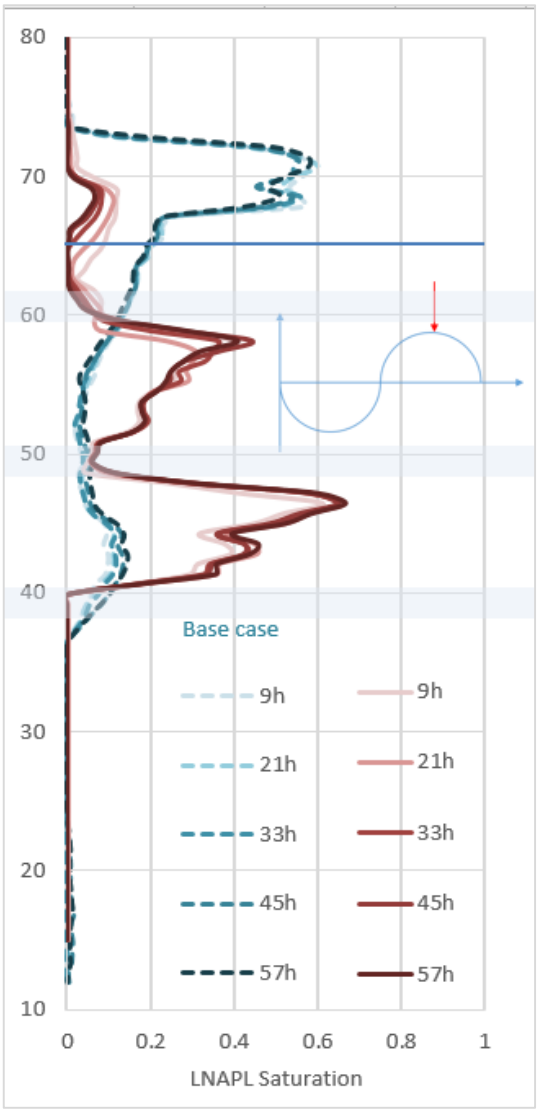

(d) Critical position 4, WT=65cm

Figure 6-44 Inter-cycle LNAPL saturation profiles of the current scenario in red and the base case profiles superimposed in cyan from the 1st cycle to the 5th cycle, where the approximate location of the three complete fine sand layers was shaded in the plots.

In summary, the three heterogeneous scenarios performed experimentally demonstrated the significant impacts of geological heterogeneities on the migration and entrapment behaviour of LNAPL. Specifically, instead of serving as an LNAPL storage, a fine grain layer acts as an LNAPL barrier when the layer was originally or predominantly water saturated. The multiple fine grain layers incorporating with cyclic water table fluctuations may "sandwich" the most of the released LNAPL mass in-between the layers, in particular between the layers that are situated close to the lowermost water table positions. Residual LNAPL within the fine grain layers and above the highest fine grain layer are insignificant.

One implication inferred from this scenario is that the complete low permeable layers incorporating with cyclic water table fluctuations may intercept a significant volume of LNAPL at depth in the zone of water table fluctuation, which may potentially be designed as a clean-up scheme: A sandwich-like multiple fine grain layered system incorporating with controllable water table fluctuations, where the majority of LNAPL mass can be relocated at a target area (i.e., LNAPL being sandwiched between two fine grain layers at lowermost water table positions) for evacuation or borehole extraction.

Another key observation from the heterogeneous scenarios reveals that the downward migration of LNAPL through a low permeability zone leading to a layer of "confined LNAPL" below the water table by some distance. A significant amount of LNAPL, brought down by descending water table through a fine grain layer, will not be able to re-surface through by the follow-up sequences of ascending water table due to not being able to overcome the entry pressure without the assistance of gravity. This "one-way ticket" of LNAPL downward migration, resulting a considerable amount of LNAPL intercepted by the fine grain layer, may reside at depth below the water table, which most likely will be anticipated as the residence of DNAPL by practitioners. Accordingly, this inaccurate site characterisation may mislead the decision on remediation schemes.

6.8 Summary

The experimental system developed and the image analysis method redeveloped provided a valuable means to not only implement different influential factors combined with transient water table fluctuation conditions, but also to achieve high-resolution, high-frequency, full-domain and real-time monitoring of multiphase fluid behaviours. It allowed a substantial number of variant scenarios conducted experimentally and investigated extensively to discern the incorporated influences of cyclic water table fluctuation conditions and crucial influential factors upon LNAPL migration and distribution in porous media. For the homogenous scenarios, the influencing mechanisms of water table fluctuation speed, release timing relative to water table high or low positions, LNAPL release volume and aquifer media were investigated. For heterogeneous scenarios, the influencing mechanisms of a single partial fine grain layer, a single complete fine grain layer and multiple complete fine grain layers were investigated. A substantial amount of data was harvested and vividly demonstrated in the format of video, comprising photographic record, interpreted fluid distribution in 2-D contours and 1-D profiles of water, LNAPL and air, which truly advanced the quantification of continuous and transient LNAPL dynamics. Mechanisms of different influential factors upon LNAPL migration and distribution were analysed in detail with summaries and implications in each section.

The experimental results revealed various detailed phenomena and processes which were either not quantified before, or had not been investigated due to lack of detailed, visulised, quantified data. For instance, the experiment results demonstrated significant impacts of geological heterogeneities on the migration and entrapment behaviour of LNAPL, which, if wisely applied, may provide possible LNAPL recovery schemes to controllably redistribute and then collect LNAPL mass. This also indicated that the confined LNAPL, which may be mistakenly characterised as DNAPL without chemical analysis aside due to its permanent, deep residence below the water table, should be given extra care during site characterization.

7 Conclusions

7.1 Development of a new methodology to measure accurate and precise LNAPL distribution in simple homogeneous porous media and porous media with discrete heterogeneous features for transient water table systems

There has long a need to provide real-time, detailed laboratory datasets that allow validation of theories and associated (numerical) model representations of LNAPL transport in dynamic water table environments. The study has strived to provide a detailed quantitative perspective of LNAPL behaviours in subsurface porous media aquifers under the combined influences of transient water table fluctuations, and possible influential factors via a set of newly developed laboratory scale techniques. Three major tasks were achieved in this experiment and modelling study.

The first 2-D fully automated multiphase flow experimental system, including both hardware and software, was developed during the course of this study, to allow customised implementation and visualisation of LNAPL migration and redistribution within controllable aquifer systems and transient water table conditions, particularly cyclic oscillations. The setup possessed significant automated functionality, including the capacities to: 1) automatically mimic and flexibly program cyclic water table fluctuations; 2) automatically image the real-time saturation distributions of all fluids (red-dyed-LNAPL, blue-dyed-water and air phase by mass difference) using high temporal frequency and spatial resolution multi-spectral photography; 3) efficiently interpret the extensive detailed datasets by the advanced multi-spectral image analysis to an arbitrary resolution, which was redeveloped by exercising a combination of physical, mathematical and numerical methods that provided a tight-fit of the experimentally calibrated samples. The realisation of batch-processing allowed sizeable datasets to be interpreted reliably, precisely and efficiently. The accuracy of the advanced multi-spectral image analysis was quantitatively scrutinised against the present LNAPL total volume within the system and was qualitatively examined against all fluid distributions recorded for every photographic event. The overall errors that represents pixel-wise interpretations of sets of high-frequency, long-term datasets, were found small, whereas errors in the existing literature were often evaluated with a very limited selection of datasets collected at a much lower special and temporal resolution. Such automated data acquisition and processing techniques permitted the LNAPL release

and its redistribution under oscillating water table conditions to be demonstrated in vivid short video formats of original time-lapse photographic records, contoured fluid saturations and vertical profiles for every fluid phase. The effortlessly replicating system, which comprised inexpensive electronic components, was capable of producing more experimental variations beyond the designated scenarios conducted in this study. The significant advancement and novelty of this comprehensive methodology were that it could potentially transcend the conventional manual monitoring in NAPL mechanism laboratory studies to the long-term high-frequency automatic data acquisition era, which might very likely lead to an unprecedented level of new and meticulous discoveries.

Eight main experimental scenarios were successfully produced and investigated in detail to discern the incorporated mechanisms of cyclic water table fluctuation conditions and potential influential factors upon LNAPL migration and distribution in porous media. Each scenario comprised an LNAPL release process and a five-cycle sinusoidal water table fluctuation period. A detailed documentation of more than 200 photographic events was interpreted for each scenario, which featured the intricate mechanisms and continuous dynamics of water, LNAPL and air. The variations in the scenarios could be sub-categorised into homogeneous cases, including aquifer media, fluctuation speed, LNAPL release timing relative to water table positions, release volume; and heterogeneous cases, including a single partial fine grain layer, a single complete fine grain layer and multiple discrete, complete fine grain layers. A significant amount of high-resolution and high-frequency data was harvested, which advanced the quantification of transient water-LNAPL-air three-phase flow dynamics. The dataset could be applied to validate numerical models for further studies on LNAPL migration and distribution in homogeneous and layered heterogeneous aquifer systems. The dataset could be used to provide more detailed, accurate characterization for conceptual models, which may potentially provide guidance to practitioners. This set of data had bettered current insights and supplemented theories on LNAPL transport and distribution in porous media systems, which served as fundamental knowledge to achieve effective and accurate site characterization, contamination evaluation, remediation strategy and subsequent prediction. The highly illustrative dataset also yielded useful educational resources to contaminant based practitioners, regulators and research communities.

Applicability of the standard model from NAPL simulator was exercised and tested with a selection of experimental data, which provided:

- Good general match of the overall features of the dynamics with inferred and calibrated parameters which are physically reasonable. LNAPL simulator appropriate to match higher permeability phreatic aquifer contamination and where specific pseudo steady conditions

apply (i.e. neglect compressibility and storage effects);

- Ability to match the LNAPL release and redistribution under cyclic water table conditions;
- Examination of the reliability of experimental data interpretation and highlighted the crucial features of the dynamics.

The migration and fate of NAPL are governed by complex geological formation, transient groundwater dynamics and convoluted physical, chemical and biological properties of the contaminants and interactions amongst. To infer and potentially give a solution to the utter complexity and uncertainty of the multiphase flow system, a revisit to theoretical fundaments via well controlled and characterised laboratory datasets is evident. Laboratory quantitative visualization studies on the mechanism of multiphase flow serve as the cornerstone of both the theories in quantitative contaminant hydrogeology and the development of numerical tools in practice, which are used as the primary and cost-effective techniques that decide the success or failure or the feasibility in site characterization, site evaluation and body prediction as well as efficient remediation. Furthermore, as the technical and financial costs of the applications of automated systems continue to decrease, and the demands of high-precision low human cost monitoring and control techniques in multiphase flow studies continue to escalate, it is imperative and rewarding to upgrade current laboratory capabilities by implementing automation in the development of experimental apparatus, monitoring and interpretation methodologies.

7.2 Insight into LNAPL redistribution under transient water table conditions

The LNAPL behaviour including migration and distribution is strongly dependent on transient water table conditions in unconfined aquifers which is often not emphasised in the existing literature. Implications were drawn from the experimental results as follows.

- LNAPL is dispersed through the range of water table fluctuation (the capillary zone inclusive). Depending on the water table high or low positions, sometimes it may be difficult to observe and quantify pollutant source terms. The maximal saturation of LNAPL accumulated within a thin LNAPL lens can be observed at low water table levels (e.g. late summer, low tide, or under a high groundwater abstraction rate). The maximal lens thickness with slightly lower maximal saturation of LNAPL can be discovered at or shortly after high water table levels (e.g. spring, high tide, artificial recharge). This indicates that LNAPL accumulates at the minimal elevation when the water table is at minimal elevation and re-accumulates when the water table is

around maximal elevation, which can potentially be used to locate, evaluate or evacuate LNAPL source zones.

- The contamination affected depth and area can be extended under a dramatic decrease in groundwater table (e.g. artificial abstraction). For early discovered contaminated sites when LNAPL has not been brought to the deep unsaturated aquifer by seasonal water table variation, seizing the water table may prevent downwards migration of contamination.
- When characterising LNAPL spills (typically petrol station, pipeline, fuel store, lubricant manufacture, etc.) this work shows it is vital to have an understanding of the range of water table fluctuations and when collecting time series data, for instance, remediation or monitored natural attenuation, it is essential to make observations at consistent water table conditions or to have interpretive models to correct for water table redistribution effects. A recommendation may be to attach more significance to monitoring during high water tables.
- The capillary zone and the underlying water table are efficient barriers to preclude or decelerate LNAPL penetrating in depth, which namely indicates that without such barrier, sufficient and continuous LNAPL spill may further migrate downwards until such barrier is finally reached and/or LNAPL pressure is exhausted (e.g. thick unsaturated aquifer).
- In homogeneous systems, there is a small but significant accumulation of higher residual phase LNAPL at the base of the water table fluctuation associated with aquifer conditions where there has not been a residual air/gas phase higher in the column, the residual LNAPL is reduced by the simultaneous residual gas phase. This has implications for the magnitude and duration of risk to aquifer water quality. This is not generally appreciated in existing literature.
- In heterogeneous systems, an incomplete low permeable layer embedded within a relatively high permeable aquifer cannot retain or intercept a significant amount of LNAPL mass, thus, is not sufficient enough to be used as an LNAPL container or barrier.
- Heterogeneous systems with complete low permeable layers can intercept substantial quantities of LNAPL spillage at depth in the zone of water table fluctuation, again with implications for pollutant source characterisation and remediation or monitored natural attenuation (i.e. confined LNAPL being mistakenly anticipated as DNAPL providing chemical analysis not viable or not undertaken, or not sufficient to investigate at/above the water table for fuel spills). A sandwich-like multiple fine grain layer system incorporating with controllable water table fluctuations can potentially be applied as a remediation strategy, where the majority of LNAPL mass can be relocated to a target area of an aquifer for evacuation or borehole collection. Again this is not generally accentuated in existing literature.

- The findings are also particularly important for erosion of the NAPL by dissolution and volatilization, where mechanism of NAPL transport serves as the foundation of the NAPL fate. Reliable assessment, risk-management and remediation strategies rely on informative conceptual and quantified understanding of LNAPL transport and fate

This is particularly a concern for coastal aquifers which are important as many industrial centres susceptible to pollution are located in coastal systems, including for example industrialised areas often found in and around estuary port areas and associated upstream, but still tidal, river reaches.

Findings are more widely applicable to any site where there are water table changes. These include, for example, monitoring landfill leachate in landfills where liquid wastes have been disposed and also contaminated land remediation schemes that may involve groundwater extraction or perhaps physical barrier installations that alter water table elevations.

7.3 Future work

Throughout the development, experimental and modelling stage of this study, tremendous efforts have been made to better the experimental system, the adequacy and execution of experimental scenarios, the accuracy, resolution and processing capability of the interpretation methodology, and the visualisation of results. However, some improvements and future opportunities were recognised without further implementation due constraints of time and resources. The improvements and opportunities can be classified into four categories: experimental system, data interpretation method, experimental scenarios and models.

1) Experimental system

The Illumination method adopted, which include the tungsten light source, the light diffuser, framework and the temporary darkroom setup, is reckoned to be the vulnerability of the 2-D automated multiphase flow experimental system developed. The tungsten floodlight was introduced to provide a broad spectral band of light (including visible light and near infra-red) required by the Kechavarzi multi-spectral image analysis during the intended replication of the method, which should be incorporating with a spacious darkroom. Due to an unexpected laboratory relocation during the study, no dark room could be made available. Thus, a temporary darkroom without ventilation became the only option, which could not relieve the heat emission from the floodlight, so that light source became more fragile and interruptive to data collection. Furthermore, the luminance emitted

by the floodlight was shown to vary spatially and temporally. It was captured in two scenarios that the non-uniform dispersion of light over the tank elevation resulted in an abnormal water saturation distribution detected at the bottom of the tank, which although did not injure the experimental data, should be eliminated to protect the data integrity. Moreover, the near infra-red spectrum, which was assessed as the least attractive spectral band in the experimented multiphase flow system, was deprecated eventually so that the experiments were recorded and interpreted with only within the visible light spectrum. As a consequence, more light sources became available. An ideal illumination method to apply the methodology designed should comprise a light source that provides constant visible light, a spacious solid darkroom with ventilation options depending on the light source emission, and possibly an automatic control embedded in the main control script.

2) Data interpretation method

In the redeveloped multi-spectral imaging method, both water and NAPL saturations were acquired via a calibrated relationship between reflective light intensities and fluid saturations, whereas the air saturation was obtained by the mass balance. Consequently, the mass balance of LNAPL, literally applied as a volume balance, was the only quantitative means to examine the accuracy of the image analysis, where the calculated LNAPL volume was compared against the total LNAPL volume released at the time. Therefore, the water and air saturations were not participants in the quantitative examination, which were qualitatively inspected by the distribution contours and profiles. Accordingly, it occurred in one scenario that the water saturation was overestimated while the LNAPL saturation was accurate. Hence the sole quantitative indicator of experimental error appeared fine. This error could not have been detected before detailed contour analysis. It will be beneficial to escalate the two-phase calibration to a three-phase calibration where the calibrated relationship takes into account water, NAPL and air simultaneously. Consequently, two quantitative approaches could be established, the total fluid volume balance (the sum of fluid saturation should be equal to 1) to review all fluid phases, and LNAPL volume balance as explained before. The three-phase calibration is also believed to improve the data interpretation with well-controlled samples.

For the interpretation of the heterogeneous scenarios that comprised two aquifer media, only one calibration standard was applied during the image analysis which was the calibration result for the medium sand. It is technically feasible to implant two calibration standards in the one flow domain based on the special distribution of the aquifer media, which is believed to improve the interpretation accuracy.

To improve the reflective light intensities and fluid saturations calibration, despite that several upgrades have been made including the algorithm and experimental setup, the method is deemed improvable. The distribution density of samples can be increased due to the high occurrence rate in the experiments, which are: samples with low water and LNAPL saturation, samples with low water saturation and extremely high LNAPL saturation, and samples with low LNAPL saturation and extremely high water saturation. This would allow a more detailed accurate interpolation among frequent saturation values. The coverage of the front of sample boxes should be slightly enlarged which could give a larger photographic vision to extract average reflective light intensities with less shadow interference. A better seal should be applied to the box covers to avoid any accidental leakage. Specifically, the calibration result of fine sand should be improved and tested against experimental data to provide a better interpretation of water saturation.

Besides adopting the reflective light intensity approach, the colour intensity approach may yield a more competent result. The withdrawal of the colour intensity approach that was attempted in this study was essentially due to the lack of colour intensity calibration bar, which resulted in the sample colour not being adequately calibrated. Accordingly, by producing/ purchasing segmented colour intensity bars, the colour intensity approach may become applicable, which provides more information than greyscale images.

3) Experimental scenarios

The experimental system is competent in producing more variant scenarios than the cases carried out in this study with no or minimal modification to the system, for instance, variations in water fluctuation amplitudes, patterns and durations, complicated heterogeneous geological settings, LNAPL release upon transient water tables, etc. By duplicating partial of the control system, water table gradients can be implemented over the tank width by two sets of pumps and pressure sensors. The water gradient scenarios may give rise to the monitoring of LNAPL dissolution, vaporisation and biodegradation under transient water table fluctuation conditions. The system may also be adapted to allow the installation of a borehole, which will enable the monitoring of formation thicknesses of LNAPL under transient water table conditions. Scenarios that discern the seasonal water table fluctuation conditions, or the remediation efficiency can be implemented and assessed. Moreover, the monitoring frequency can be intensified to capture more continuous dynamics.

4) Numerical models and conceptual models

The datasets harvested from the seven variant scenario experiments may be used to build descriptive and predictive numerical models that target the influences of specific influential factor upon LNAPL redistribution. The substantial amount of highly quantitative experimental data can serve as a validation of numerical models that target the three-phase hysteretic K-S-P relationship under multiple drainage and imbibition processes or predictive models that inform the transport and fate of three-phase flow system, which provide guidance in site characterisation, pollution evaluation and prediction, as well as remediation formulation. It can be beneficial to conceptualise the quantitative data into a series of illustrative pellucid LNAPL contamination scenarios which, associating with the dynamic videos, can be used as educational resources to non-specialists.

A. Digital Appendices

The digital appendices comprise two types of components: original scripts written during the course of the study, and the datasets harvested during the experimental stage. A folder system is organized with folder paths for each object specified in the following sections.

A.1 Crucial scripts

A.1.1 Script example of control of water table fluctuation and multi-spectral photography

[Location, name, format] Appendices\A1_scripts\1_Main_control.py

[Computer language] Python 3

[Script attached as follows]

```
#This script is the main control script to generate flexible water table fluctuations and to conduct multi-spectral photography
#Developed by Simiao Sun (Simiaosun@hotmail.com) 2014

import datetime
import time
import math #Cosine wave
import pifacedigitalio as pfio
import quick2wire.i2c as i2c
import re
import sys
import smtplib #SMPT Email
from subprocess import call #Photography
import subprocess #Photography
import usb.core #Filter wheel
import usb.util #Filter wheel
import os #Filter wheel
pfio.init()

adc_address1 = 0x68
adc_address2 = 0x69

adc_channel1 = 0x98 #Why do we need both address and channel?
adc_channel2 = 0xB8
adc_channel3 = 0xD8
adc_channel4 = 0xF8


formatter_sensor="%s\t%f\t%s\n" #Printing format function for Pressure Sensor
```

```
formatter_sinewave="%f\t%f\t%f\t%f\t%s\n" #Printing format function for Sine Wave
formatter_parameter="%s\n%s\t%s %s\n%s\t%s %s\n%s\t%s %s\n%s\t%s %s\n %s\t%s %s\n"
#Printing format function for parameter config
formatter_dir_name="%s%s" #For image file dirctory and file name
filename_sensor=input("File name for Pressure Seneor is? \n") #Filename for Pressure Sensor
filename_sinewave=input("File name for Sine Wave is?: \n") #Filename for Sine Wave

#pump_threshold_max=float(input ("Input the max value for pump threshold\n"))
#pump_threshold_min=float(input ("Input the min value for pump threshold\n"))


#***Filter wheel configuration starts:

connected = False      # Flag to indicate connection to USB
endPointIn = None      # IN endpoint (EP1)
sxFw = None              # Usb Device Handle
newFilter = 1


#Allocate device name to USB Filter Wheel
sxFw = usb.core.find(idVendor=0x1278, idProduct=0x0920)
print("sxFw=",sxFw)

#Check for Filter Wheel
if sxFw is None:
    raise ValueError("Sx Filter Wheel not Found")

# Detach from Kernel driver if needed
if sxFw.is_kernel_driver_active(0):
    try:
        sxFw.detach_kernel_driver(0)
    except usb.core.USBError as e:
        sys.exit("Could not detach kernel driver: %s" % str(e))
# Set Configuration
try:
    sxFw.set_configuration()
    sxFw.reset()
    sxFw.timeout = 5000
except usb.core.USBError as e:
    sys.exit("Could not set Configuration: %s" % str(e))

cfg = sxFw.get_active_configuration()
print("cfg=",cfg)
intf = usb.util.find_descriptor(cfg, bInterfaceNumber=0)
print("intf=",intf)
```

```
        # Find the IN endpoint (EP1)
        # Use Control transfers for IN reports (EP0)
try:
        endPointIn = usb.util.find_descriptor(intf, custom_match = lambda e: \
                usb.util.endpoint_direction(e.bEndpointAddress) == usb.util.ENDPOINT_IN)
except usb.core.USBError as e:
        sys.exit("Could not access IN endpoint: %s" % str(e))

print("endpointin", endPointIn)
bytesOut = sxFw.ctrl_transfer(0x21, 0x09, 0x200, 0, [00, 00], 5000)
print("bytesOut=", bytesOut)

try:
        result = endPointIn.read(2, 5000)
except usb.core.USBError as e:
        sys.exit("USB Read Error: %s" % str(e))

#Set connected flag
connected    = True
print ("Connected Successfully")


#Filter wheel configuration ends.***

def pump_standby():
        pfio.digital_write(1,0)
        pfio.digital_write(0,0)

def pump_pumping():
        pfio.digital_write(1,0)
        pfio.digital_write(0,1)

def pump_draining():
        pfio.digital_write(1,1)
        pfio.digital_write(0,0)

def writefile_sensor():
        #This is how data is written into a file. "a" means appending rather than "w" writing
        datafile=open(filename_sensor, "a")
        datafile.write(formatter_sensor % ("Channel 8", getadcreading(adc_address2, adc_channel4),
time.ctime()))
        datafile.close()

def writefile_sinewave():
```

```
    datafile=open(filename_sinewave, "a") #The following 3 lines are data writing command
    datafile.write(formatter_sinewave % (x,
sensor_value,set_watertable,read_watertable,executetime))
    datafile.close()

def capture_image():
    pfio.digital_write(1,0)
    pfio.digital_write(0,0)

    image_name="%s-"%filter_colour + "%s-"%x + "%Y%m%d%H%M%S.jpg" #Image name formatter
    gphoto_output1=subprocess.Popen("gphoto2 --set-config shutterspeed="+shutterspeed,
stdout=subprocess.PIPE, shell=True)
    (output, err)=gphoto_output1.communicate()
    print(gphoto_output1, "/n")

    gphoto_output2=subprocess.check_output(["gphoto2","--capture-image-and-download","--
filename",formatter_dir_name%(file_directory,image_name)])
    print(gphoto_output2, "/n")


def program_initiate():
    global email_subject, email_content
    email_subject="EXPT ALART: Program Just started"
    email_content="""Program has just been started at """ +"    " + "%s" % executetime
    #send_email()
    sensor_value=getadcreading(adc_address2, adc_channel4)
    read_watertable=sensor_value*49.022-25.366#Calibration date:2015/03/10  7kpa
    print(read_watertable)
    sensor_value=getadcreading(adc_address2, adc_channel4)
    read_watertable=sensor_value*49.022-25.366#Calibration date:2015/03/10  7kpa
    print(read_watertable)



def program_terminate():

    global email_subject, email_content
    print("Run time in total:",datetime.datetime.now()-starttime,"\n")
    pfio.digital_write(1,0)
    pfio.digital_write(0,0)
    print("Pump0 and Pump1 have been shut down. Program terminated.")
    print(datetime.datetime.now())

    datafile=open(filename_sinewave, "a") #The following 3 lines are data writing command
```

```
        datafile.write(formatter_parameter % ("Parameter Config:","Target water table:", centre, "cm","Amplitude", amplitude, "cm", "Frequency:", frequency, "oscillation(s) / d" , "Duration:", duration_day, "d" , "Starting degree:", start_degree, "degree"))
        datafile.close()
        capture_image()
        email_subject="EXPT ALART: Program terminates successfully."
        email_content="""Pump0 and Pump1 have been shut down. Program terminated.
Congratulations! """+ "\n" + "%s" % datetime.datetime.now()
        #send_email()
        print (datetime.datetime.now())

def program_emergency_terminate():
        global email_subject, email_content
        print("Run time in total:",datetime.datetime.now()-starttime,"\n")
        pfio.digital_write(1,0)
        pfio.digital_write(0,0)
        print("Warning: Program terminates emergently.")
        print("Pump0 and Pump1 have been shut down. Program terminated irragulately.")
        print("Time to go:",terminaltime-executetime)
        email_subject="EXPT ALART: Program terminates emergently."
        email_content="""Warning: Program terminates emergently.
Pump0 and Pump1 have been shut down. Program terminated irragulately.""" + "\n" + "%s" % datetime.datetime.now()
        send_email()
        sys.exit()

def send_email():
        To = 'simiaosun@hotmail.com' #Multiple receivers use ";"

        gmail_account = 'sunsimiao.work@gmail.com' # Gmail login account
        gmail_passwd = 'genius14' # Gmail login password

        server = smtplib.SMTP('smtp.gmail.com', 587)
        server.ehlo()
        server.starttls()
        server.login(gmail_account, gmail_passwd)

        BODY = '\r\n'.join(['To: %s' % To,
                                'From: %s' % gmail_account,
                                'Subject: %s' % email_subject,
                                '''', email_content])

        try:
                server.sendmail(gmail_account, [To], BODY)
                print ('Email successfully sent to %s' % To)
```

```
        except:
                print ('Error: fail in sending email')

        server.quit()

def filter_wheel_reconfig():
        print("\n")
        print("***Filter wheel reconfiguration starts***")
        #Allocate device name to USB Filter Wheel
        sxFw = usb.core.find(idVendor=0x1278, idProduct=0x0920)
        print("sxFw read: DONE",sxFw)

        #Check for Filter Wheel
        while sxFw is None:
                sxFw = usb.core.find(idVendor=0x1278, idProduct=0x0920)
                print(sxFw)
                time.sleep(1)
                if sxFw is not None:
                #Used to be:          raise ValueError("Sx Filter Wheel not Found")
                        print("sleep 15s") #Everytime when filter wheel is repowered, it takes roughly 15s for
sort of default reboot
                        time.sleep(15)

                        print("sxFw=",sxFw)
                        break


                # Detach from Kernel driver if needed
        if sxFw.is_kernel_driver_active(0):
                try:
                        sxFw.detach_kernel_driver(0)
                        print("Kernel driver detection: DONE")
                except usb.core.USBError as e:
                        #Used to be:                 sys.exit("Could not detach kernel driver: %s" % str(e))
                                print("Could not detach kernel driver: %s" % str(e))
                                while usb.core.USBError:
                                        sxFw.detach_kernel_driver(0)
                                        if not usb.core.USBError:
                                                break


                # Set Configuration
        try:
                sxFw.set_configuration()
                sxFw.reset()
```

```
            sxFw.timeout = 5000
        except usb.core.USBError as e:
            #Used to be:    sys.exit("Could not set Configuration: %s" % str(e))
            print("Could not set Configuration: %s" % str(e))
            sxFw.set_configuration()
            sxFw.reset()
            sxFw.timeout = 5000



        cfg = sxFw.get_active_configuration()
        print("cfg=",cfg)
        intf = usb.util.find_descriptor(cfg, bInterfaceNumber=0)
        print("intf=",intf)



            # Find the IN endpoint (EP1)
            # Use Control transfers for IN reports (EP0)
        try:
            endPointIn = usb.util.find_descriptor(intf, custom_match = lambda e: \
                usb.util.endpoint_direction(e.bEndpointAddress) == usb.util.ENDPOINT_IN)
        except usb.core.USBError as e:
            #Used to be:          sys.exit("USB Read Error: %s" % str(e))
            print("Could not access IN endpoint: %s" % str(e))

            cfg = sxFw.get_active_configuration()
            intf = usb.util.find_descriptor(cfg, bInterfaceNumber=0)
            endPointIn = usb.util.find_descriptor(intf, custom_match = lambda e: \
                usb.util.endpoint_direction(e.bEndpointAddress) == usb.util.ENDPOINT_IN)

        bytesOut = sxFw.ctrl_transfer(0x21, 0x09, 0x200, 0, [00, 00], 5000)
        try:
            result = endPointIn.read(2, 5000)
        except usb.core.USBError as e:
            print("USB Read Error: %s" % str(e))
            bytesOut = sxFw.ctrl_transfer(0x21, 0x09, 0x200, 0, [00, 00], 5000)
            result = endPointIn.read(2, 5000)



        #Set connected flag
        connected    = True
        print ("Re-Connected Successfully")

def moveToFilter(newFilter):
        if connected:
```

```
        print("new Filter position",newFilter)
        newFilter = newFilter
        time_before_filter_swap=datetime.datetime.now()
    try:
        bytesOut = sxFw.ctrl_transfer(0x21, 0x09, 0x200, 0, [newFilter, 0], 5000)
    except usb.core.USBError as e:
        filter_wheel_reconfig()

    atFilter = False
    while not atFilter:
        # Check every 20ms for arrival at target filter
        time.sleep(0.02)

        # Request current filter will be zero if moving
        try:
            bytesOut = sxFw.ctrl_transfer(0x21, 0x09, 0x200, 0, [0, 0], 5000)
            result = endPointIn.read(2, 5000)
        except usb.core.USBError as e:
            filter_wheel_reconfig()
            break

        # Have we arrived at Target?
        if (result[0] & 0xF) == newFilter:
            atFilter = True
            print(result[0])
            print(0xF)
            print(result[0] & 0xF)
            print("Filter position at", result[0])
            time_after_filter_swap=datetime.datetime.now()
            print("Time for current filter swap:", time_after_filter_swap-time_before_filter_swap)


# Target water table and Amplitude inputs which should satisfy the range required, as well as frequency and duration.
print("0<=centre+-amplitude/2<=96")

centre=float(input("Centre (cm): \n")) # Defination: Where will be the water table fluctuation centred in cm
while centre<0.0 or centre>96.0:
    centre=float(input("Must be within the range 0<=centre<=96. \n Centre (cm): \n"))

amplitude=float(input("Amplitude (cm): \n")) # Defination: How many cm will the water wave be at the most.
while amplitude>52.0:
    amplitude=float(input("Must be within the range 0<=amplitude<=52. \n Amplitude(cm): \n"))
```

```
half_amplitude=amplitude/2.0
sum=centre+half_amplitude
sub=centre-half_amplitude
while ((sum>94 or sub>94)or(sum<0 or sub<0)):
    centre=float(input("Target water table (cm): \n"))
    while centre<0.0 or centre>96.0:
        centre=float(input("Must within the range 0<=centre<=96. \n Target water table (cm): \n"))

    amplitude=float(input("Amplitude (cm): \n"))
    while amplitude>52.0:
        amplitude=float(input("Must within the range 0<=amplitude<=52. \n Amplitude(cm): \n"))
    print("Must be within the range: 0<= Target water table +- Amplitude/2 <=96")
    if not ((sum>96 or sub>96)or(sum<0 or sub<0)): break
    print("Target water table=",centre,"Amplitude=", amplitude,"Highest=", sum, "Lowest=",sub)

file_directory="/home/pi/Run3T1/5Run/" #The folder to store images, case sensitive
#image_name="%n-%Y%m%d%H%M.jpg" #Image name formatter

# Defination of parameters associated with frequency and time
frequency=float(input("Frequency (oscillation/day): \n")) # Defination: How many oscillations per day
cycle_length=86400/frequency # Defination: How long does it take to run a cycle (2*pi)
duration_day=float(input("Duration (day): \n")) # Defination: How many days will the experiment keep running?
duration_second=float(duration_day*86400)
start_degree=float(input("Start-degree: \n"))
capture_frequency=input("About auto-photography, how many degree(s) per photo to set(degree/photo): \n")
settle_down=float(input("How long to settle down (d):"))
settle_down_second=float(settle_down*86400)
settle_down_photography_frequency=float(input("During settling down, how many degree(s) per photo to set(degree/photo): \n"))

max_threshold=94 # If adjustment is needed, do it manually in program
min_threshold=10 # If adjustment is needed, do it manually in program

step=cycle_length/360.0 #How many seconds to print 1 degree value
starttime = datetime.datetime.now() #Defination: The start time of experiment running
executetime = datetime.datetime.now() #Defination: The execution time of each degree
steptime = starttime + datetime.timedelta(seconds=step) #Defination: The execution time schedule
terminaltime = starttime + datetime.timedelta(seconds=duration_second) #Defination: The termination time of experiment running
terminaltime_settle_down = terminaltime +datetime.timedelta(seconds=settle_down_second)

for line in open('/proc/cpuinfo').readlines():
```

```
        m = re.match('(.*?)\s*:\s*(.*)', line)
        if m:
                (name, value) = (m.group(1), m.group(2))
                if name == "Revision":
                        if value [-4:] in ('0002', '0003'):
                                i2c_bus = 0
                        else:
                                i2c_bus = 1
                        break

with i2c.I2CMaster(i2c_bus) as bus:

        def getadcreading(address, channel):
                bus.transaction(i2c.writing_bytes(address, channel))
                time.sleep(0.05)
                h, l, r = bus.transaction(i2c.reading(address,3))[0]
                time.sleep(0.05)
                h, l, r = bus.transaction(i2c.reading(address,3))[0]

                t = (h << 8) | l
                v = t * 0.000154 #What is that?
                if v < 5.5:
                        return v
                else: # must be a floating input
                        return 0.000


        email_subject=""
        email_content=""
        program_initiate()
        sensor_value=getadcreading(adc_address2, adc_channel4)
        start_watertable=sensor_value*49.022-25.366#Calibration date:2015/03/10    7kpa
        print("start water table=",start_watertable)
        time.sleep(2)
        x=start_degree

        while executetime<terminaltime:
                i=1 # To control just print one time in each degree

                while                                   datetime.timedelta(seconds=0.0)<=(steptime-
executetime)<=datetime.timedelta(seconds=step):
                        set_watertable= centre+math.cos(x/180.0*math.pi)*half_amplitude
                        sensor_value=getadcreading(adc_address2, adc_channel4)
                        time.sleep(0.2)
                        read_watertable=sensor_value*49.022-25.366#Calibration date:2015/03/10    7kpa
```

```
            executetime=datetime.datetime.now()


            if ((read_watertable>=max_threshold or read_watertable<min_threshold)) or
(abs(read_watertable-set_watertable)>50.0): #Pump idling prevention, change threshold if necessary
                program_emergency_terminate()

            if read_watertable>set_watertable:
                pump_draining()
                while read_watertable<set_watertable:
                    pump_standby()

            elif read_watertable<set_watertable:
                pump_pumping()
                while read_watertable>set_watertable:
                    pump_standby()

            else:
                pump_standby()


            if i==1:

print(x,"\t","set_watertable=",set_watertable,"\t","read_watertable=",read_watertable,"\t",execute
time)
                print("Time to go:",terminaltime-executetime)
                writefile_sinewave()
                writefile_sensor()
                i=i+1
                if (x-start_degree)%float(capture_frequency)==0:
                    pump_standby() #To stop pumps
                    filter_number=1 #To control filter wheel
                    while filter_number<=4:
                        moveToFilter(filter_number)
                        if filter_number==1:
                            filter_colour="c" #Filter wheel, filter No.1, ISO=1600, without any
filter

                            shutterspeed="1/200"
                            print("shutterspeed=1/200")
                        if filter_number==2:
                            filter_colour="g" #Filter wheel, filter No.2, ISO=1600, green filter
                            shutterspeed="1/13"
                            print("shutterspeed=1/13")
                        if filter_number==3:
                            filter_colour="r" #Filter wheel, filter No.3, ISO=1600, red filter
```

```
                                shutterspeed="0.5"
                                print("shutterspeed=0.5")
                            if filter_number==4:
                                filter_colour="i" #Filter wheel, filter No.4, ISO=1600, IR filter
                                shutterspeed="1.3"
                                print("shutterspeed=1.3")
                            time.sleep(0.1)
                            capture_image()
                            filter_number=filter_number+1
                            if filter_number==5:
                                filter_number=1
                                moveToFilter(filter_number)
                                break


        else:
            x=x+1
            steptime=steptime+datetime.timedelta(seconds=step)
            executetime=datetime.datetime.now()
            print("***")

    print("***************")
    print("Start settling down")
    print("***************")


    while executetime<terminaltime_settle_down:
        i=1
        while                                   datetime.timedelta(seconds=0.0)<=(steptime-
executetime)<=datetime.timedelta(seconds=step):
            set_watertable= centre

            sensor_value=getadcreading(adc_address2, adc_channel4)
            read_watertable=sensor_value*49.022-25.366#Calibration date:2015/03/10    7kpa
            executetime=datetime.datetime.now()


            if read_watertable>set_watertable:
                pump_draining()
            else:
                read_watertable<set_watertable
                pump_pumping()

            if i==1:
```

```
print(x,"\t","set_watertable=",set_watertable,"\t","read_watertable=",read_watertable,"\t",execute
time)
                    print("Time to go:",terminaltime_settle_down-executetime)
                    writefile_sinewave()
                    writefile_sensor()
                    i=i+1
                    if (x-start_degree)%float(settle_down_photography_frequency)==0:
                        filter_number=1 #To control filter wheel
                        while filter_number<=4:
                            moveToFilter(filter_number)
                            if filter_number==1:
                                filter_colour="c" #Filter wheel, filter No.1, ISO=1600, without any
filter
                                shutterspeed="1/200"
                                print("shutterspeed=1/200")
                            if filter_number==2:
                                filter_colour="g" #Filter wheel, filter No.2, ISO=1600, green filter
                                shutterspeed="1/13"
                                print("shutterspeed=1/13")
                            if filter_number==3:
                                filter_colour="r" #Filter wheel, filter No.3, ISO=1600, red filter
                                shutterspeed="0.5"
                                print("shutterspeed=0.5")
                            if filter_number==4:
                                filter_colour="i" #Filter wheel, filter No.4, ISO=1600, IR filter
                                shutterspeed="1.3"
                                print("shutterspeed=1.3")
                            time.sleep(0.3)
                            capture_image()
                            filter_number=filter_number+1
                            if filter_number==5:
                                filter_number=1
                                moveToFilter(filter_number)
                                break
            else:
                x=x+1
                steptime=steptime+datetime.timedelta(seconds=step)
                executetime=datetime.datetime.now()
                print("***")

    else:program_terminate()
```

[The end of script]

A.1.2 Script example of calibration for the redeveloped multi-spectral image analysis

[Location, name, format] Appendices\A1_scripts\ 2_Calibration_20150904.m

[Computer language]: MATLAB

[Script attached as follows]

```
%Requiring additional functions:
%sortStruct.m                  For sorting the image names
%suplabel.m                    For generating a superlable across subplot images
%rsquare.m                     For calculation R2 values for fittings
%customcmap.m                  For customizing the range, colour and shape of colorbars
%freezeColors                  For freezing the colormap colors in subplots
%cbfreeze                      For freezing the colorbar colors in subplots
%cbhandle                      Dependency of cbfreeze
%tight_subplot                 For tightening subplots and setting marginsclear
%intersections                 For finding the intersect of two curves


%% Initialization
clear
clc
close all %close all opened graphs
%Import image Convert image to gray scale and image unit matrix to normal double accuracy matrix
and %cut the image
imageg=double(rgb2gray(imread('E:\01Work\06Study\201508-New calibration\Test1-
medium\Photo1\g-20150809173255.jpg')));
imager=double(rgb2gray(imread('E:\01Work\06Study\201508-New calibration\Test1-
medium\Photo1\r-20150809173353.jpg')));
imageall=cat(3, imageg, imager); %Concatenate arrays along specified dimension
%p_save=[]; %To save the results of polinomial fitting

%Input a number that represents the interpolation precision
precision_value=150;
[m,n,k]=size(imageall);

%%
figure('Name', 'Convert pixel value to OD via poly3 curve fitting','units','normalized','outerposition',[0
0 1 1])
for i=1:2

    X=[];
    % Change x y coordinates when analyzing Sample_OD for different runs.
    % Cali20150809-Photo1
```

```
X(1) = mean( mean (imageall(1943:1983,123:145,i) ) );
X(2) = mean( mean (imageall(1943:1983,150:172,i) ) );
X(3) = mean( mean (imageall(1943:1983,177:199,i) ) );
X(4) = mean( mean (imageall(1943:1983,204:226,i) ) );
X(5) = mean( mean (imageall(1943:1983,231:253,i) ) );
X(6) = mean( mean (imageall(1943:1983,257:279,i) ) );
X(7) = mean( mean (imageall(1943:1983,284:306,i) ) );
X(8) = mean( mean (imageall(1943:1983,311:333,i) ) );
X(9) = mean( mean (imageall(1943:1983,338:360,i) ) );
X(10) = mean( mean (imageall(1943:1983,365:387,i) ) );
X(11) = mean( mean (imageall(1943:1983,391:413,i) ) );
X(12) = mean( mean (imageall(1943:1983,418:440,i) ) );
X(13) = mean( mean (imageall(1943:1983,445:467,i) ) );
X(14) = mean( mean (imageall(1945:1981,474:494,i) ) );
X(15) = mean( mean (imageall(1943:1983,499:521,i) ) );
X(16) = mean( mean (imageall(1943:1983,525:547,i) ) );
X(17) = mean( mean (imageall(1943:1983,552:574,i) ) );
X(18) = mean( mean (imageall(1943:1983,579:601,i) ) );
X(19) = mean( mean (imageall(1943:1983,606:628,i) ) );
X(20) = mean( mean (imageall(1943:1983,633:655,i) ) );

X=transpose(X); % transpose X from row to column
Y=[];
for j = 0: 0.1 :1.9    %each segment represents 0.1 OD from 0 to 1.9
Y = [Y;j]; % A column of numbers
end
%%%%% plot figure1 curve fit result

% http://uk.mathworks.com/help/curvefit/list-of-library-models-for-curve-and-surface-
fitting.html#btbcvnl
[fitresult, gof] = fit( X, Y, 'poly3' ); % Curve fitting, method changable

r2=gof.rsquare;
rmse=gof.rmse;

subplot(2,1,i)

plot(X,Y,'o'); %Plot the origional data in small circles
hold on;

plot(fitresult); %Plot the ditting curve in small circles
% axis([0,200,0,3]); %customize axis limits, firstly x then y
```

```
legend('Read ODs from GrayScale', 'Curve fitting');
xlabel('Pixel value'); %x-axis label
ylabel('Absorbance'); %y-axis label
if i==1
    title(strcat(['Conversion from Pixel Value to Absorbance for Green via poly3 fitting    ' 'R2 = '
num2str(r2) '; RMSE = ' num2str(rmse)]));
    xlabel('Pixel value'); %x-axis label
    ylabel('Absorbance'); %y-axis label
else
    title(strcat(['Conversion from Pixel Value to Absorbance for Red via poly3 fitting    ' 'R2 = '
num2str(r2) '; RMSE = ' num2str(rmse)]));
    xlabel('Pixel value'); %x-axis label
    ylabel('Absorbance'); %y-axis label
    %%%%% end of plot
end
hold off;
OD_image_temp = feval(fitresult,imageall(:,:,i)); %   convert pixal values of entire image into OD
value with fitting result above
OD_image(:,:,i) = reshape(OD_image_temp,[m,n]); % Result of feval() is vector. Reshape vector into
matrix
end
clear OD_image_temp m n k r2 rmse %Clear some variables

data=xlsread('E:\01Work\06Study\201504-Scripts\Sample saturations_delete_2p_2') %Read the
water and NAPL saturations for calibration samples. 32 samples in total
Sample_Sw=data(:,1);
Sample_So=data(:,2);
coeffvals_save=[];
r2=[];
rmse=[];
Sample_OD=[];


for i=1:2
    % change coordinates when analying different runs. Cali20150809
    % customized
    % delete 10%-20% and 70%-30%
    Sample_OD(1,i)   = mean( mean (OD_image(562:611,28:93,i) ) );
    Sample_OD(2,i)   = mean( mean (OD_image(561:610,131:196,i) ) );
    Sample_OD(3,i)   = mean( mean (OD_image(563:611,231:296,i) ) );
    Sample_OD(4,i)   = mean( mean (OD_image(565:614,331:398,i) ) );
```

```
    Sample_OD(5,i)    = mean( mean (OD_image(568:617,430:497,i) ) );
    Sample_OD(6,i)    = mean( mean (OD_image(563:614,532:598,i) ) );
    Sample_OD(7,i)    = mean( mean (OD_image(565:616,633:699,i) ) );
    Sample_OD(8,i)    = mean( mean (OD_image(571:619,733:799,i) ) );

    Sample_OD(9,i)    = mean( mean (OD_image(667:715,28:94,i) ) );
    Sample_OD(10,i)    = mean( mean (OD_image(663:712,126:194,i) ) );
    Sample_OD(11,i)    = mean( mean (OD_image(664:713,226:294,i) ) );
    Sample_OD(12,i)    = mean( mean (OD_image(669:718,327:395,i) ) );
    Sample_OD(13,i)    = mean( mean (OD_image(669:717,529:597,i) ) );
    Sample_OD(14,i)    = mean( mean (OD_image(666:717,628:696,i) ) );
    Sample_OD(15,i)    = mean( mean (OD_image(671:719,727:792,i) ) );
    Sample_OD(16,i)    = mean( mean (OD_image(769:817,28:94,i) ) );

    Sample_OD(17,i)    = mean( mean (OD_image(767:815,129:195,i) ) );
    Sample_OD(18,i)    = mean( mean (OD_image(767:817,231:297,i) ) );
    Sample_OD(19,i)    = mean( mean (OD_image(768:818,329:395,i) ) );
    Sample_OD(20,i)    = mean( mean (OD_image(772:821,430:497,i) ) );
    Sample_OD(21,i)    = mean( mean (OD_image(768:816,530:598,i) ) );
    Sample_OD(22,i)    = mean( mean (OD_image(770:818,628:694,i) ) );
    Sample_OD(23,i)    = mean( mean (OD_image(771:818,727:792,i) ) );
    Sample_OD(24,i)    = mean( mean (OD_image(870:916,31:97,i) ) );

    Sample_OD(25,i)    = mean( mean (OD_image(869:917,131:197,i) ) );
    Sample_OD(26,i)    = mean( mean (OD_image(870:918,231:298,i) ) );
    Sample_OD(27,i)    = mean( mean (OD_image(870:918,330:397,i) ) );
    Sample_OD(28,i)    = mean( mean (OD_image(871:919,431:498,i) ) );
    Sample_OD(29,i)    = mean( mean (OD_image(871:919,629:695,i) ) );
    Sample_OD(30,i)    = mean( mean (OD_image(869:917,730:793,i) ) );

end

% Surface fit green. Linear Interception method. Methods changable
[surffit_g, gof_g] = fit( [Sample_Sw,Sample_So],Sample_OD(:,1), 'thinplateinterp');
% Surface fit red. Linear Interception method. Methods changable
[surffit_r, gof_r] = fit( [Sample_Sw,Sample_So],Sample_OD(:,2), 'thinplateinterp');

r2(1)=gof_g.rsquare
rmse(1)=gof_g.rmse %R2 value for green
r2(2)=gof_r.rsquare
rmse(2)=gof_r.rmse %R2 value for red
predicted_OD(:,1)=feval(surffit_g,[Sample_Sw,Sample_So]);
```

```
predicted_OD(:,2)=feval(surffit_r,[Sample_Sw,Sample_So]);

%%%%Start to plot figure2
figure ('Name', 'Surface fit (thinplateinterp) for OD_green and OD-Red',
'units','normalized','outerposition',[0 0 1 1])
plot(surffit_g,[Sample_Sw,Sample_So],Sample_OD(:,1));
hold on
plot(surffit_r,[Sample_Sw,Sample_So],Sample_OD(:,2));
xlabel('Water Saturation'); %x-axis label
ylabel('NAPL Saturation');    %y-axis label
zlabel('Optical density');    %z-axis label

title(strcat([ 'Green: R2 = ' num2str(r2(1)) '; RMSE = ' num2str(rmse(1)) , '     ', 'Red: R2 = '
num2str(r2(2))...
      '; RMSE = ' num2str(rmse(2))]))
hold off

%%%%Start to plot figure3
figure('Name','Figure3: meshgrid and surface plot');
% Define the input grid
% When the x,y values are between 0 and 1, sometimes the surface go over
% than the boundary. Therefore set them to more than 1
[x_grid,y_grid]=meshgrid(linspace(0,1.01,precision_value)) %x,y are 101 values between 0 and 1.01

surffit_evaluation_g=surffit_g(x_grid,y_grid); % the array of surface fit evaluation result for the
green
surffit_evaluation_r=surffit_r(x_grid,y_grid); % the array of surface fit evaluation result for the red
% Surface plot for green
surface(x_grid,y_grid,surffit_evaluation_g,'EdgeColor', 'none'); %'FaceColor', 'green','EdgeColor',
'none'

hold on
% Surface plot for red
surface(x_grid,y_grid,surffit_evaluation_r,'EdgeColor', 'none'); %'FaceColor', 'red','EdgeColor', 'none'
xlabel('Water Saturation'); %x-axis label
ylabel('NAPL Saturation');    %y-axis label
zlabel('Optical density');    %z-axis label
view(3);
axis vis3d;
grid on;
hold off
```

```
%%%%Start to plot figure4
[m,n]=size(x_grid);
z_plane_g=[];%OD planes for green
z_plane_r=[];%OD planes for red
Saturation_water=[];
Saturation_oil=[];


max_g=max(max(surffit_evaluation_g));
max_r=max(max(surffit_evaluation_r));
min_g=min(min(surffit_evaluation_g));
min_r=min(min(surffit_evaluation_r));

z_value_g=transpose(linspace(min_g,max_g,precision_value)); %OD planes for green
z_value_r=transpose(linspace(min_r,max_r,precision_value)); %OD planes for red

for k=1:precision_value
    z_plane_g(:,:,k)=ones(m,n).*z_value_g(k,1);
    z_plane_r(:,:,k)=ones(m,n).*z_value_r(k,1);
end

Calibration_result=[];
for k1=1:precision_value
    for k2=1:precision_value
    % Take the difference between the two surface heights and find the contour
    % where that difference is zero.
    zdiff_g = surffit_evaluation_g - z_plane_g(:,:,k1);
    zdiff_r = surffit_evaluation_r - z_plane_r(:,:,k2);
    C_g = contours(x_grid, y_grid, zdiff_g, [0 0]);
    C_r = contours(x_grid, y_grid, zdiff_r, [0 0]);
    % Extract the x- and y-locations from the contour matrix C. Fitst column
    % are numbers, so extract 2:end. Normally numbers of G and R are different
    xL_g = C_g(1, 2:end);
    yL_g = C_g(2, 2:end);
    xL_r = C_r(1, 2:end);
    yL_r = C_r(2, 2:end);

    % Interpolate on the surfaces to find z-locations for the intersection line
    zL_g = interp2(x_grid,y_grid, surffit_evaluation_g, xL_g, yL_g);
    zL_r = interp2(x_grid,y_grid, surffit_evaluation_r, xL_r, yL_r);
    %Vq = interp2(___,method) specifies an optional, trailing input argument
```

```
        %that you can pass with any of the previous syntaxes.
        %The method argument can be any of the following strings that specify
        %alternative interpolation methods: 'linear', 'nearest', 'cubic', or
        %'spline'. The default method is 'linear'.

        xL_g=transpose(xL_g);
        yL_g=transpose(yL_g);
        zL_g=transpose(zL_g);
        xL_r=transpose(xL_r);
        yL_r=transpose(yL_r);
        zL_r=transpose(zL_r);

        Calibration_result(k1,k2,1)=z_value_g(k1,1) %OD green
        Calibration_result(k1,k2,2)=z_value_g(k2,1) %OD red

        %OD_G=[OD_G;z_value_g(k1,1)];
        %OD_R=[OD_R;z_value_r(k2,1)];
        if or(or(numel(xL_g)<3, numel(yL_g)<3), or(numel(xL_r)<3, numel(yL_r)<3))
            Calibration_result(k1,k2,3)=-1;
            Calibration_result(k1,k2,4)=-1;
        else
            [X0,Y0] = intersections(xL_g,yL_g,xL_r,yL_r,false);
            if or(isempty(X0),isempty(Y0))
                X0 =-2;
                Y0 =-2;
            end
            [mx,nx]=size(X0);
            if mx>1
                X0=X0(1,1); Y0=Y0(1,1);
            end
            Calibration_result(k1,k2,3)=X0;
            Calibration_result(k1,k2,4)=Y0;

        end
        % Looking for the formula of the line via surface fit

     %}
        end
    end

    %%Result printing
    % Save in excel format
```

```
filename='Calibration_20150904_150.xlsx';
sheet_OD_green='OD_green';
sheet_OD_red='OD_red';
sheet_Cal_Sw='Cal_Sw';
sheet_Cal_So='Cal_So';
sheet_Cal_result='Cal_result';
Cal_result_print=[];

for i=1: precision_value
    for j=1: precision_value
        if Calibration_result(i,j,3)>=0
            Cal_result_print=[Cal_result_print; Calibration_result(i,j,1) Calibration_result(i,j,2)
Calibration_result(i,j,3) Calibration_result(i,j,4)]
        end
    end
end


xlswrite(filename, Calibration_result(:,:,1), sheet_OD_green, 'A2');
xlswrite(filename, Calibration_result(:,:,2), sheet_OD_red, 'A2');
xlswrite(filename, Calibration_result(:,:,3), sheet_Cal_Sw, 'A2');
xlswrite(filename, Calibration_result(:,:,4), sheet_Cal_So, 'A2');
xlswrite(filename, Cal_result_print, sheet_Cal_result, 'A2');
disp('It is done.. Tada!!!')


% Save variable for image analysis to load
filename_var= 'Calibration_20150904_150.mat'
save(filename_var, 'Cal_result_print', 'Calibration_result',
'Sample_OD','predicted_OD'); %Sample_OD(11,:),predicted_OD(11,:) are the water saturated values
```

[The end of script]

A.1.3 Script example of the image analysis of experimental results

[Location, name, format] Appendices\A1_scripts\3_Run_20150825_Run4T3_contour_profile.m

[Computer language] MATLAB

[Script attached as follows]

```
%Requiring additional functions:
%sortStruct.m                  For sorting the image names
%suplabel.m                    For generating a superlable across subplot images
```

```
%rsquare.m                          For calculation R2 values for fittings
%customcmap.m                       For customizing the range, colour and shape of colorbars
%freezeColors                       For freezing the colormap colors in subplots
%cbfreeze                           For freezing the colorbar colors in subplots
%cbhandle                           Dependency of cbfreeze
%tight_subplot                      For tightening subplots and setting margins
%intersections                      For finding the intersect of two curves
%searchclosest.m                    For finding the clostest point and its location in a vector

%Calibration_20150904_dif_fitting_delete_2p_2_150.mat          Call calibration result

clear
clc
close all %Close all opened graphs
%% Parameter and coefficients inputs
load E:\01Work\06Study\201504-Scripts\Calibration_20150904_150.mat;

%Sorting rows value to be ascending.
%Rows that have equal elements in the specified column, Specify two columns to sort by: columns 1
and 2.
Cal_result_print=sortrows(Cal_result_print,[1 2]);

grid_size = 20;    %Define the size of AOI to be analysed
released_NAPL = 99; % Released volume of LNAPL in ml

tank_thickness = 1.6;      %Tank thickness in cm
porosity = 0.376;       %Porosity of the sand aquifer
tank_bottom_cut_thickness = 11.947      %cm,from the cutting point to the tank base, not from top
ot the grey scale. measure every time
gray_scale_length =20.3
gray_scale_length_in_pixel = 576    %Measure for every experiment

% Parameter input
wt_centre= 50;      % The centre of water table oscillation in cm
half_wt_amplitude= 15;      % The amplitude is 30 and half is 15 in cm
start_degree_of_settling_down = 1890;      % The degree number on when the settling down period
starts. After this moment, water table stops oscillating

Save_subplot_directory ='E:\01Work\06Study\201508-Run4T3\12Run result\Subplot\' %Save batch
subplots from folder
Save_image_directory ='E:\01Work\06Study\201508-Run4T3\12Run result\Single\' %Save batch
images from folder
Save_profile_directory ='E:\01Work\06Study\201508-Run4T3\12Run result\Profiles\' %Save batch
images from folder
```

```
Save_profile_wt_directory ='E:\01Work\06Study\201508-Run4T3\12Run result\Profiles_wt\' %Save batch images from folder
Read_image_directory = 'E:\01Work\06Study\201508-Run4T3\8Cut run\';%Read batch images from folder
output_excel_filename='E:\01Work\06Study\201508-Run4T3\14Data\Run_20150825_Run4T3.xlsx';
FileNames_g = dir(fullfile(Read_image_directory, 'g-*.jpg'));
FileNames_r = dir(fullfile(Read_image_directory, 'r-*.jpg'));
FileNames_c = dir(fullfile(Read_image_directory, 'c-*.jpg'));


%% Manipulation of file names for the loop

fields = {'date','bytes','isdir','datenum'}; %remove all fields except filenames in the structure
FileNames_g = rmfield(FileNames_g,fields);    %rmfield()- removing fields    struct2cell()- convert structure to cell array
FileNames_r = rmfield(FileNames_r,fields);    %rmfield()- removing fields    struct2cell()- convert structure to cell array
FileNames_c = rmfield(FileNames_c,fields);    %rmfield()- removing fields    struct2cell()- convert structure to cell array

for i= 1 : length(FileNames_g) %file numbers of variable

      number=sscanf(FileNames_g(i).name,'%*c-%f%-%f',[1 Inf]); %extract number from file names
      [FileNames_g(i).number]=deal(number); %assign number
      [FileNames_r(i).number]=deal(number); %assign number
      [FileNames_c(i).number]=deal(number); %assign number
      [FileNames_g(i).newname]=['g-',int2str(number)]; %give new names of all images into 'g-***'
      [FileNames_r(i).newname]=['r-',int2str(number)]; %give new    names of all images into 'r-***'
      [FileNames_c(i).newname]=['c-',int2str(number)]; %give new    names of all images into 'c-***'

end

FileNames_g = sortStruct(FileNames_g, 'number', 1);%sort structure array according to FileNames_g.number's ascending order
FileNames_r = sortStruct(FileNames_r, 'number', 1);%sort structure array according to FileNames_r.number's ascending order
FileNames_c = sortStruct(FileNames_c, 'number', 1);%sort structure array according to FileNames_c.number's ascending order

%Calculate current water table for each image

for i= 1 : length(FileNames_g) %file numbers of variable
      current_degree = FileNames_g(i).number;
       if current_degree <=start_degree_of_settling_down
            current_wt = wt_centre + cos(current_degree / 180 * pi) * half_wt_amplitude
```

```
        else
            current_wt = FileNames_g(i-1).current_wt
        end
        [FileNames_g(i).current_wt]= current_wt
        [FileNames_r(i).current_wt]= current_wt
        [FileNames_c(i).current_wt]= current_wt
    end
image1g=double(rgb2gray(imread('E:\01Work\06Study\201508-Run4T3\10Cut saturation\g-20150825132704.jpg'))); % Fully water saturated image for deduction method--green filter
image1r=double(rgb2gray(imread('E:\01Work\06Study\201508-Run4T3\10Cut saturation\r-20150825132714.jpg'))); % Fully water saturated image for deduction method--red filter

clear i number current_degree current_wt wt_centre half_wt_amplitude ;

Sw2_save=[];
So2_save=[];
Sg2_save=[];


%% Image impotation and conversion
%Convert images to gray scale images and change the image matrix to normal double accuracy matrix for calculation purpose

for File_number=1:length(FileNames_g)
    FullFile_g = fullfile(Read_image_directory, FileNames_g(File_number).name);
    FullFile_r = fullfile(Read_image_directory, FileNames_r(File_number).name);
    FullFile_c = fullfile(Read_image_directory, FileNames_c(File_number).name);
    image2g = double(rgb2gray(imread(FullFile_g)));
    image2r = double(rgb2gray(imread(FullFile_r)));
    image2c_org = (imread(FullFile_c));

    imageall=cat(3, image1g, image2g, image1r, image2r); %Concatenate arrays along specified dimension

    %Start to calibrate gray scale bar for each image
        for i=1:4
        % change coordinates when analyzing different runs. This is 20150825-Run4T3
        X=[];
        X(1) = mean( mean (imageall(2064:2100,140:156,i) ) );
        X(2) = mean( mean (imageall(2064:2100,168:184,i) ) );
        X(3) = mean( mean (imageall(2064:2100,197:213,i) ) );
        X(4) = mean( mean (imageall(2064:2100,225:241,i) ) );
        X(5) = mean( mean (imageall(2064:2100,253:269,i) ) );
        X(6) = mean( mean (imageall(2064:2100,281:297,i) ) );
        X(7) = mean( mean (imageall(2064:2100,310:326,i) ) );
```

```
            X(8) = mean( mean (imageall(2064:2100,338:354,i) ) );
            X(9) = mean( mean (imageall(2064:2100,366:382,i) ) );
            X(10) = mean( mean (imageall(2064:2100,394:410,i) ) );
            X(11) = mean( mean (imageall(2064:2100,423:439,i) ) );
            X(12) = mean( mean (imageall(2064:2100,451:467,i) ) );
            X(13) = mean( mean (imageall(2064:2100,479:495,i) ) );
            X(14) = mean( mean (imageall(2064:2100,507:523,i) ) );
            X(15) = mean( mean (imageall(2064:2100,536:552,i) ) );
            X(16) = mean( mean (imageall(2064:2100,564:580,i) ) );
            X(17) = mean( mean (imageall(2064:2100,592:608,i) ) );
            X(18) = mean( mean (imageall(2064:2100,620:636,i) ) );
            X(19) = mean( mean (imageall(2064:2100,649:665,i) ) );
            X(20) = mean( mean (imageall(2064:2100,677:693,i) ) );

            X = transpose(X); % transpose X from row to column
            Y = [];
                for j = 0: 0.1 :1.9    %Each segment represents 0.1 OD, from 0 to 1.9
                    Y = [Y;j];
                end
            %%%%% plot figure1 fit result
            %p = fit(X,Y,'pchipinterp'); %Fittype changable
            [fitresult, gof] = fit( X, Y, 'poly3' ); % Linear Interception method. Methods changable

            r2=gof.rsquare;
            rmse=gof.rmse;
            [m,n]=size(imageall(:,:,i));
            image(:,:,i)=imageall(2:0.90*m,1:n,i); % Cut the grayscale bars at the top and bottom of the
image
            [m,n,k]=size(image(:,:,i));
            OD_image_temp = feval(fitresult,image(:,:,i)); %    convert pixal values of entire image into
OD value with fitting result above
            OD_image(:,:,i) = reshape(OD_image_temp,[m,n]); % Result of feval() is vector. Reshape
vector into matrix

        end
        %The end of grayscale bar calibration for each image
        [m,n]=size(imageall(:,:,i));
        image2c=image2c_org(2:0.90*m,1:n,:); % Cut the grayscale bar at the bottom of the clear
image

        % For mass balance calculation
        pixel_density = gray_scale_length/gray_scale_length_in_pixel;
        grid_size_cm = grid_size * pixel_density;
        % For profile y value calculation
        tank_width = pixel_density * n;      %Tank width in cm
```

```
[m,n,k]=size( image2c);
tank_depth_cut_colorbar=pixel_density *m+tank_bottom_cut_thickness; % The top of the flow boundary


%% Averaging OD for proposed grid size (averaging first then calculation, since the calculation takes much longer)

[m,n,k]=size(OD_image);
m=m-mod(m,grid_size);
n=n-mod(n,grid_size);
image2c=image2c(1:m,1:n,:); % Cut the second time for the clear image to remain the same size as image2g and image2c

for kk=1:k

    c1=0;
    c2=1;

    for i=1:grid_size:m
        c1=c1+1;
        c2=0;

        for j=1:grid_size:n
            c2=c2+1;
            OD_image_grid_size(c1,c2,kk)=mean(mean(OD_image(i:i+grid_size-1,j:j+grid_size-1,kk)));
        end
    end
end

%% Sw and So calculation (by indexing the calibration result sheet)

[k1,k2,k3]=size(OD_image_grid_size);
OD_sg_corrected=ones(k1,k2).*Sample_OD(11,1); %Predicted_OD(11,1) is G for fully water saturated sample with no glare
OD_sr_corrected=ones(k1,k2).*Sample_OD(11,2); %Predicted_OD(11,2) is R for fully water saturated sample with no glare

OD_green=OD_image_grid_size(:,:,2)-OD_image_grid_size(:,:,1)+OD_sg_corrected; %Original_pic-Saturated_pic+water saturated sample with no glare
OD_red=OD_image_grid_size(:,:,4)-OD_image_grid_size(:,:,3)+OD_sr_corrected; %Original_pic-Saturated_pic+water saturated sample with no glare
```

```
    Sw2=[];
    So2=[];
    for j=1:k2
        % Find k-nearest neighbors using data
        IDX = knnsearch(Cal_result_print(:,1:2),[OD_green(:,j) OD_red(:,j)]);
        Sw2=[Sw2 Cal_result_print(IDX,3)];
        So2=[So2 Cal_result_print(IDX,4)];
    end

    Sg2=ones(k1,k2); % A matrix filled with 1
    Sg2=1-Sw2-So2;

    % Save saturation results into matrices
    Sw2_save(:,:,File_number)=Sw2;
    So2_save(:,:,File_number)=So2;
    Sg2_save(:,:,File_number)=Sg2;


%% Mass balance
    mass_balance=So2 * grid_size_cm^2 * tank_thickness *porosity; % in ml
    Total_NAPL_volume(:,File_number)=sum(sum(mass_balance)); % in ml

    disp_mass=['mass_balance=',num2str( Total_NAPL_volume(:,File_number))];
    disp(disp_mass);

%% Profile plotting

    % Calculating the x values of the profile plots
    Profile_Sw2 = transpose(mean(Sw2.')); % Calculate mean value of each row of the array and
transpose
    Profile_So2 = transpose(mean(So2.')); % Calculate mean value of each row of the array and
transpose
    Profile_Sg2 = transpose(mean(Sg2.')); % Calculate mean value of each row of the array and
transpose

    % Save profile data into matrices for output
    Profile_Sw2_save(:,File_number)=Profile_Sw2;
    Profile_So2_save(:,File_number)=Profile_So2;
    Profile_Sg2_save(:,File_number)=Profile_Sg2;

    % Calculating the y values of the profile plots
    [m,n]=size(So2);
    Depth_col = linspace(tank_bottom_cut_thickness,tank_depth_cut_colorbar,m);
    % Calculating the depth of each row of grids
```

```
Depth_col = transpose (Depth_col); % Transpose row to column
% Calculating the axes of the profile plots
axis_x1 = 0; %figure generation axis x low bound, should range from 0--1
axis_x2 = 1; %figure generation axis y high bound, should range from 0--1
axis_y1 = 0; %figure generation axis x low bound, should be the size of the tank
axis_y2 = tank_depth_cut_colorbar; %figure generation axis y high bound, should be the size (depth) of the tank

current_wt=FileNames_g(File_number).current_wt
%% Calculate average value below the water table and above
[i,current_wt_in_vector] = searchclosest(Depth_col,current_wt) % Find the location of the current water table in the vector of Depth_col

wt_position_in_depth_col=m+1-i; % The Depth_col was up side down, so find the counting down loction
V_above_WT=(tank_depth_cut_colorbar-current_wt_in_vector)*tank_width * tank_thickness *porosity % Pore space volume above the water table
V_below_WT=(current_wt_in_vector-tank_bottom_cut_thickness)*tank_width * tank_thickness *porosity % Pore space volume below the water table

Average_Sw_above_WT=mean(Profile_Sw2(1:wt_position_in_depth_col));
Average_Sw_below_WT=mean(Profile_Sw2(wt_position_in_depth_col+1:m));
Average_So_above_WT=mean(Profile_So2(1:wt_position_in_depth_col));
Average_So_below_WT=mean(Profile_So2(wt_position_in_depth_col+1:m));
Average_Sg_above_WT=mean(Profile_Sg2(1:wt_position_in_depth_col));
Average_Sg_below_WT=mean(Profile_Sg2(wt_position_in_depth_col+1:m));

Average_Sw_above_WT_save(:,File_number)=Average_Sw_above_WT;
Average_Sw_below_WT_save(:,File_number)=Average_Sw_below_WT;
Average_So_above_WT_save(:,File_number)=Average_So_above_WT;
Average_So_below_WT_save(:,File_number)=Average_So_below_WT;
Average_Sg_above_WT_save(:,File_number)=Average_Sg_above_WT;
Average_Sg_below_WT_save(:,File_number)=Average_Sg_below_WT;

Vw_above_save(:,File_number)= Average_Sw_above_WT*V_above_WT; %Volume of water above the water table
Vw_below_save(:,File_number)= Average_Sw_below_WT*V_below_WT; %Volume of water below the water table
Vw_sum_save(:,File_number)=Vw_above_save(:,File_number)+Vw_below_save(:,File_number);
Vw_above_ratio_Save(:,File_number)=
Vw_above_save(:,File_number)/Vw_sum_save(:,File_number);
Vw_below_ratio_Save(:,File_number)=
Vw_below_save(:,File_number)/Vw_sum_save(:,File_number);
```

```
    Vo_above_save(:,File_number)= Average_So_above_WT*V_above_WT; %Volume of water
above the water table
    Vo_below_save(:,File_number)= Average_So_below_WT*V_below_WT; %Volume of water
below the water table

Vo_sum_save(:,File_number)=Vo_above_save(:,File_number)+Vo_below_save(:,File_number); %
Suppose to be close to mass balance
    Vo_above_ratio_Save(:,File_number)=
Vo_above_save(:,File_number)/Vo_sum_save(:,File_number);
    Vo_below_ratio_Save(:,File_number)=
Vo_below_save(:,File_number)/Vo_sum_save(:,File_number);

    Vg_above_save(:,File_number)= Average_Sg_above_WT*V_above_WT; %Volume of water
above the water table
    Vg_below_save(:,File_number)= Average_Sg_below_WT*V_below_WT; %Volume of water
below the water table
    Vg_sum_save(:,File_number)=Vg_above_save(:,File_number)+Vg_below_save(:,File_number);
    Vg_above_ratio_Save(:,File_number)=
Vg_above_save(:,File_number)/Vg_sum_save(:,File_number);
    Vg_below_ratio_Save(:,File_number)=
Vg_below_save(:,File_number)/Vg_sum_save(:,File_number);


%% Plot the normal profiles***
    figure
    subplot(1,3,1);
    plot(flipud(Profile_Sw2), Depth_col, 'b-o');
    axis([axis_x1 axis_x2 axis_y1 axis_y2]);
    %set(gca,'Ydir','reverse');
    xlabel('Depth (cm)');
    ylabel('Sw');
    title('Sw');

    subplot(1,3,2);
    plot(flipud(Profile_So2), Depth_col, 'b-o');
    axis([axis_x1 axis_x2 axis_y1 axis_y2]);
    %set(gca,'Ydir','reverse');
    xlabel('Depth (cm)');
    ylabel('So');
    title('So')

    subplot(1,3,3);
    plot(flipud(Profile_Sg2), Depth_col, 'b-o');
    axis([axis_x1 axis_x2 axis_y1 axis_y2]);
    %set(gca,'Ydir','reverse');
```

```
        xlabel('Depth (cm)');
        ylabel('Sg');
        title('Sg');

        [ax,h]=suplabel( ['Three-phase saturation distribution profiles. Time:    '
num2str(FileNames_g(File_number,1).number)],'t');
        set(h,'FontSize',24);
        set(gcf,'PaperUnits','inches','PaperPosition',[0 0 22 12]);    %Set the location and size of the
entire subplot figure
        print(gcf,'-dpng',[Save_profile_directory,'Profile-
',num2str(FileNames_g(File_number,1).number)]);


        close(gcf);

%% Plot profiles with water table***

        figure
        subplot(1,3,1);
        plot(flipud(Profile_Sw2), Depth_col, 'b-o');
        hold on
        plot([axis_x1,axis_x2],[current_wt,current_wt],'--','Color','k', 'LineWidth',3);
        axis([axis_x1 axis_x2 axis_y1 axis_y2]);
        %set(gca,'Ydir','reverse');
        xlabel('Depth (cm)');
        ylabel('Sw');
        title('Sw');

        subplot(1,3,2);
        plot(flipud(Profile_So2), Depth_col, 'b-o');
        hold on
        plot([axis_x1,axis_x2],[current_wt,current_wt],'--','Color','k', 'LineWidth',3);
        axis([axis_x1 axis_x2 axis_y1 axis_y2]);
        %set(gca,'Ydir','reverse');
        xlabel('Depth (cm)');
        ylabel('So');
        title('So')

        subplot(1,3,3);
        plot(flipud(Profile_Sg2), Depth_col, 'b-o');
        hold on
        plot([axis_x1,axis_x2],[current_wt,current_wt],'--','Color','k', 'LineWidth',3);
        axis([axis_x1 axis_x2 axis_y1 axis_y2]);
        %set(gca,'Ydir','reverse');
        xlabel('Depth (cm)');
```

```
        ylabel('Sg');
        title('Sg');

        [ax,h]=suplabel( ['Three-phase saturation distribution profiles. Time:    '
num2str(FileNames_g(File_number,1).number)],'t');
        set(h,'FontSize',24);
        set(gcf,'PaperUnits','inches','PaperPosition',[0 0 22 12]);    %Set the location and size of the
entire subplot figure
        print(gcf,'-dpng',[Save_profile_wt_directory,'Profile-wt-
',num2str(FileNames_g(File_number,1).number)]);
        close(gcf);

%
%% Contour plotting

        %Plot final results. Three image above are unprocessed contours.

        figure %('units','normalized','outerposition',[0 0 1 1])
        minVal = 0;    %Range of colormap for customcmap
        maxVal = 1;    %Range of colormap for customcmap
        cbar_labels = [0:0.1:1]; % user defined ranges

        [ms,ns]=size(Sw2);
        contour_x=linspace(0,tank_width,ns); % The axis X of the contour plot
        contour_y=Depth_col % The axis Y of the contour plot

        ha = tight_subplot(1,4,0,[.05 .1],[.05 .05])    %ha = tight_subplot(row, column, gaps between
the axes, margin[lower, upper], margin[left, right])

        axes(ha(1)); imagesc(image2c);    %axes=subplot tightened subplots
        h=colorbar;      %generate a colorbar but keep it invisible so that the size of 4 pics match
        set(h,'Visible','off');
        set(gca,'YTickLabel','','XTickLabel','')      %delete tick lables since it's showing pixel values
        title('Original Image');

        axes(ha(2));[C2,h2]= contourf(contour_x,contour_y,flipud(Sw2));
        user_cmap_blue = transpose([1:-0.1:0.1;1:-0.1:0.1;ones(1,10)]); % user defined color of
colorbar :blue
        customcmap(cbar_labels,user_cmap_blue,[minVal maxVal]); %customed color bar plot
        title('Water St');
        set(h2, 'ShowText', 'on','LineColor', [.5 .5 .5], 'LevelList',[0:.1:.9], 'LabelSpacing', 1000 )
        %set(gca,'box','off')      %delete axes ticks on the right and top
        set(gca,'XTickLabel','')        %delete tick lables
        freezeColors; % freeze colors of colormap
        cbfreeze; % freeze colors of colorbar
```

```
        hold on
        plot([0,ns],[current_wt,current_wt],'--','Color','k', 'LineWidth',2);
        hold off

        axes(ha(3)); [C3,h3]=contourf(contour_x,contour_y,flipud(So2));
        user_cmap_red = transpose([ones(1,10);1:-0.1:0.1;1:-0.1:0.1]); % user defined color of
colorbar :red
        customcmap(cbar_labels,user_cmap_red,[minVal maxVal]);%customed color bar plot
        title('NAPL St');
        set(h3, 'ShowText', 'on','LineColor', [.5 .5 .5], 'LevelList',[0:.1:.9], 'LabelSpacing', 1000 )
        %set(gca,'box','off')      %delete axes ticks on the right and top
        set(gca,'XTickLabel','')        %delete tick lables
        freezeColors; % freeze colors of colormap
        cbfreeze; % freeze colors of colorbar
        hold on
        plot([0,ns],[current_wt,current_wt],'--','Color','k', 'LineWidth',2);
        hold off

        axes(ha(4)); [C4,h4]=contourf(contour_x,contour_y,flipud(Sg2));
        user_cmap_green = transpose([1:-0.1:0.1;1:-0.1:0.1;1:-0.1:0.1]); % user defined color of
colorbar :gray
        customcmap(cbar_labels,user_cmap_green,[minVal maxVal]);%customed color bar plot
        title('Air St');
        set(h4, 'ShowText', 'on','LineColor', [.5 .5 .5], 'LevelList',[0:.1:.9], 'LabelSpacing', 1000 )
        %set(gca,'box','off')      %delete axes ticks on the right and top
        set(gca,'XTickLabel','')        %delete tick lables
        freezeColors; % freeze colors of colormap
        cbfreeze; % freeze colors of colorbar
        hold on
        plot([0,ns],[current_wt,current_wt],'--','Color','k', 'LineWidth',2);
        hold off

        [ax4,h3]=suplabel( ['Three-phase saturation distribution contours '
num2str(FileNames_g(File_number,1).number)],'t');
        set(h3,'FontSize',12)
        set(gcf,'PaperUnits','inches','PaperPosition',[0 0 22 12])        %Set the location and size of the
entire subplot figure

        print(gcf,'-dpng',[Save_subplot_directory,'Contour-
',num2str(FileNames_g(File_number,1).number)]);
        close(gcf);
%
  %% Save subplot individually
%
        figure('visible', 'off');
```

```
[C2,h2]= contourf(contour_x,contour_y,flipud(Sw2));
user_cmap_blue = transpose([1:-0.1:0.1;1:-0.1:0.1;ones(1,10)]); % user defined color of
colorbar :blue
customcmap(cbar_labels,user_cmap_blue,[minVal maxVal]); %customed color bar plot
title('Water St');
set(h2, 'ShowText', 'on','LineColor', [.5 .5 .5], 'LevelList',[0:.1:.9], 'LabelSpacing', 1000 )
%set(gca,'box','off')      %delete axes ticks on the right and top
set(gca,'XTickLabel','')       %delete tick lables
freezeColors; % freeze colors of colormap
cbfreeze; % freeze colors of colorbar
hold on
plot([0,ns],[current_wt,current_wt],'--','Color','k', 'LineWidth',2);
hold off
set(gcf,'PaperUnits','inches','PaperPosition',[0 0 3.6 8])       %Set the location and size of the
entire subplot figure
print(gcf,'-dpng',[Save_image_directory,'Contour-Sw-
',num2str(FileNames_g(File_number,1).number)]);

figure ('visible', 'off');
[C3,h3]= contourf(contour_x,contour_y,flipud(So2));
user_cmap_red = transpose([ones(1,10);1:-0.1:0.1;1:-0.1:0.1]); % user defined color of
colorbar :red
customcmap(cbar_labels,user_cmap_red,[minVal maxVal]);%customed color bar plot
title('NAPL St');
set(h3, 'ShowText', 'on','LineColor', [.5 .5 .5], 'LevelList',[0:.1:.9], 'LabelSpacing', 1000 )
%set(gca,'box','off')      %delete axes ticks on the right and top
set(gca,'XTickLabel','')       %delete tick lables
freezeColors; % freeze colors of colormap
cbfreeze; % freeze colors of colorbar
hold on
plot([0,ns],[current_wt,current_wt],'--','Color','k', 'LineWidth',2);
hold off
set(gcf,'PaperUnits','inches','PaperPosition',[0 0 3.6 8])       %Set the location and size of the
entire subplot figure
print(gcf,'-dpng',[Save_image_directory,'Contour-So-
',num2str(FileNames_g(File_number,1).number)]);

figure ('visible', 'off');
[C4,h4]= contourf(contour_x,contour_y,flipud(Sg2));
user_cmap_green = transpose([1:-0.1:0.1;1:-0.1:0.1;1:-0.1:0.1]); % user defined color of
colorbar :gray
customcmap(cbar_labels,user_cmap_green,[minVal maxVal]);%customed color bar plot
title('Air St');
set(h4, 'ShowText', 'on','LineColor', [.5 .5 .5], 'LevelList',[0:.1:.9], 'LabelSpacing', 1000 )
%set(gca,'box','off')      %delete axes ticks on the right and top
```

```
        set(gca,'XTickLabel','')        %delete tick lables
        freezeColors; % freeze colors of colormap
        cbfreeze; % freeze colors of colorbar
        hold on
        plot([0,ns],[current_wt,current_wt],'--','Color','k', 'LineWidth',2);
        hold off
        set(gcf,'PaperUnits','inches','PaperPosition',[0 0 3.6 8])        %Set the location and size of the
entire subplot figure
        print(gcf,'-dpng',[Save_image_directory,'Contour-Sg-
',num2str(FileNames_g(File_number,1).number)]);

        clear current_wt

%}
end


%%    Calculation result output for Mass Balance
Total_NAPL_volume=transpose(Total_NAPL_volume);

sheet_Sw2='Sw2';
sheet_So2='So2';
sheet_Sg2='Sg2';
[m,n,k]=size(So2_save);
Sw2_output=[];
So2_output=[];
Sg2_output=[];
Filename_row = cell2mat({FileNames_c.number});
for i=1:k
        Sw2_output=cat(2,Sw2_output,mean(Sw2_save(:,:,i),2));    %row mean values=mean(matrix, 2)
        So2_output=cat(2,So2_output,mean(So2_save(:,:,i),2));    %row mean values=mean(matrix, 2)
        Sg2_output=cat(2,Sg2_output,mean(Sg2_save(:,:,i),2));    %row mean values=mean(matrix, 2)
end
xlswrite(output_excel_filename, flipud(Depth_col), sheet_Sw2, 'A2');
xlswrite(output_excel_filename, flipud(Depth_col), sheet_So2, 'A2');
xlswrite(output_excel_filename, flipud(Depth_col), sheet_Sg2, 'A2');
xlswrite(output_excel_filename, Filename_row, sheet_Sw2, 'B1');
xlswrite(output_excel_filename, Filename_row, sheet_So2, 'B1');
xlswrite(output_excel_filename, Filename_row, sheet_Sg2, 'B1');
xlswrite(output_excel_filename, Sw2_output, sheet_Sw2, 'B2');
xlswrite(output_excel_filename, So2_output, sheet_So2, 'B2');
xlswrite(output_excel_filename, Sg2_output, sheet_Sg2, 'B2');

%% Output for Mass Balance
sheet_mass_balance='Mass balance';
```

```
release_NAPL_vector=transpose(linspace(released_NAPL,released_NAPL,File_number)); % Generate a vector of released NAPL volume
NAPL_volume_error= abs(Total_NAPL_volume-release_NAPL_vector)./release_NAPL_vector

%xlswrite(output_excel_filename, FileNames_g(File_number,1).number, sheet_mass_balance, 'A1');
xlswrite(output_excel_filename, transpose(Filename_row), sheet_mass_balance, 'A3');
xlswrite(output_excel_filename, release_NAPL_vector, sheet_mass_balance, 'B3');
xlswrite(output_excel_filename, Total_NAPL_volume, sheet_mass_balance, 'C3');
%xlswrite(output_excel_filename, NAPL_volume_error, sheet_mass_balance, 'D3');


%% Output for profile data

sheet_profile_Sw2='Profile_Sw';
sheet_profile_So2='Profile_So';
sheet_profile_Sg2='Profile_Sg';
xlswrite(output_excel_filename, flipud(Depth_col), sheet_profile_Sw2, 'A2');
xlswrite(output_excel_filename, flipud(Depth_col), sheet_profile_So2, 'A2');
xlswrite(output_excel_filename, flipud(Depth_col), sheet_profile_Sg2, 'A2');
xlswrite(output_excel_filename, Filename_row, sheet_profile_Sw2, 'B1');
xlswrite(output_excel_filename, Filename_row, sheet_profile_So2, 'B1');
xlswrite(output_excel_filename, Filename_row, sheet_profile_Sg2, 'B1');
xlswrite(output_excel_filename, Profile_Sw2_save, sheet_profile_Sw2, 'B2');
xlswrite(output_excel_filename, Profile_So2_save, sheet_profile_So2, 'B2');
xlswrite(output_excel_filename, Profile_Sg2_save, sheet_profile_Sg2, 'B2');

%% Output profile below/above wt calculation data


sheet_Saturation_WT='Saturation_WT';
xlswrite(output_excel_filename, Average_Sw_above_WT_save, sheet_Saturation_WT, 'B2');
xlswrite(output_excel_filename, Average_Sw_below_WT_save, sheet_Saturation_WT, 'B3');
xlswrite(output_excel_filename, Average_So_above_WT_save, sheet_Saturation_WT, 'B4');
xlswrite(output_excel_filename, Average_So_below_WT_save, sheet_Saturation_WT, 'B5');
xlswrite(output_excel_filename, Average_Sg_above_WT_save, sheet_Saturation_WT, 'B6');
xlswrite(output_excel_filename, Average_Sg_below_WT_save, sheet_Saturation_WT, 'B7');

xlswrite(output_excel_filename, Vw_above_save, sheet_Saturation_WT, 'B9');
xlswrite(output_excel_filename, Vw_below_save, sheet_Saturation_WT, 'B10');
xlswrite(output_excel_filename, Vw_sum_save, sheet_Saturation_WT, 'B11');
xlswrite(output_excel_filename, Vw_above_ratio_Save, sheet_Saturation_WT, 'B12');
xlswrite(output_excel_filename, Vw_below_ratio_Save, sheet_Saturation_WT, 'B13');

xlswrite(output_excel_filename, Vo_above_save, sheet_Saturation_WT, 'B14');
```

```
xlswrite(output_excel_filename, Vo_below_save, sheet_Saturation_WT, 'B15');
xlswrite(output_excel_filename, Vo_sum_save, sheet_Saturation_WT, 'B16');
xlswrite(output_excel_filename, Vo_above_ratio_Save, sheet_Saturation_WT, 'B17');
xlswrite(output_excel_filename, Vo_below_ratio_Save, sheet_Saturation_WT, 'B18');

xlswrite(output_excel_filename, Vg_above_save, sheet_Saturation_WT, 'B19');
xlswrite(output_excel_filename, Vg_below_save, sheet_Saturation_WT, 'B20');
xlswrite(output_excel_filename, Vg_sum_save, sheet_Saturation_WT, 'B21');
xlswrite(output_excel_filename, Vg_above_ratio_Save, sheet_Saturation_WT, 'B22');
xlswrite(output_excel_filename, Vg_below_ratio_Save, sheet_Saturation_WT, 'B23');


%% In this case, the display window is Mass balance.
sheet_mass_balance='Mass balance';
xlswrite(output_excel_filename, mean(NAPL_volume_error), sheet_mass_balance, 'C2');
xlswrite(output_excel_filename, tank_depth_cut_colorbar, sheet_mass_balance, 'A1');
clear sheet_profile_Sw2 sheet_profile_So2 sheet_profile_Sg2 sheet_Sw2 sheet_So2 sheet_Sg2
sheet_mass_balance
clear Filename_row axis_x1 axis_x2 axis_y1 axis_y2 k1 k2 k3

disp('It is done.. Tada!!!')
beep
```

[The end of script]

A.1.4 Script example of the improvements made for NAPL simulator

[Location, name, format] Appendices\A1_scripts\4_2D.xls (To access the scripts, activate VBA and check modules)

[Computer language] VBA

[Script attached as follows]

```
Option Explicit
Sub Fluctuation_loop_up()

' Macro written 20/06/2016 by Simiao Sun
' Incorporating with NAPL simulator file: 2D.xls

' **************INPUT*PARAMETERS*DECLARE*******************

' Water table related

Dim wt_centre As Double: wt_centre = 50        ' Defination: Where will be the water table fluctuation
centred in cm
```

```
Dim wt_amplitude As Double: wt_amplitude = 30 ' Defination: How many cm will the water table fluctuation be at the most
Dim half_wt_amplitude As Double: half_wt_amplitude = wt_amplitude / 2
Dim wt_frequency As Double: wt_frequency = 2 ' Defination: How many oscillations per day
Dim wt_duration_day As Double: wt_duration_day = 2.5 ' Defination: How many days will the experiment keep running?
Dim wt_degree_interval As Integer: wt_degree_interval = 15 'Defination: how many degrees for one calculation, normally 15 degree representing 30/60mins for expts
Dim wt_start_degree As Integer: wt_start_degree = 90 ' Defination: from which degree the water table starts to fluctuate, normally 90 or 180
Dim wt_end_degree As Integer: wt_end_degree = wt_duration_day * wt_frequency * 360 + wt_start_degree ' Defination: till which degree the water table stops fluctuating
Dim wt_total_iteration_number As Integer: wt_total_iteration_number = (wt_end_degree - wt_start_degree) / wt_degree_interval + 1

' Previous stage related

Dim m_length_of_release As Long: m_length_of_release = 19800 '(s), duration of release period in seconds

' Changing excel modelling sheet related

Dim m_node_number As Integer: m_node_number = 31 ' Defination: Node number for boundary condition
Dim m_time_of_initial_data As Long
Dim m_print_interval As Long: m_print_interval = 1800 ' For release:120s, for fluctuation 1800s (3600s only for Run5T1)
Dim m_initial_time_to_print As Long
Dim m_final_time_to_print As Long ' For release:change every run; For fluctuation =wt_duration_day* 86400 (s)
Dim m_previous_run As Integer


'
**********OTHER*PARAMETERS*DECLARE**********
**********
' Iteration related
Dim current_degree As Long
Dim current_wt As Double
Dim i As Long

Const PI = 3.14159265358979
```

```
'**************************************************MAIN*LOOP*****************
************************************

For i = 9 To wt_total_iteration_number

    current_degree = wt_start_degree + (i - 1) * wt_degree_interval

    current_wt = wt_centre + Cos(current_degree / 180 * PI) * half_wt_amplitude


' **Step 1: change parameters in excel*****
    If current_degree = wt_start_degree Then

        m_time_of_initial_data = m_length_of_release
        m_initial_time_to_print = 0 'Time difference from m_time_of_initial_data
        m_final_time_to_print = m_time_of_initial_data + m_print_interval
        m_previous_run = 1

    Else
        m_time_of_initial_data = m_final_time_to_print
        m_initial_time_to_print = m_print_interval 'Time difference from m_time_of_initial_data
        m_final_time_to_print = m_time_of_initial_data + m_print_interval
        m_previous_run = 1

    End If

    Worksheets("WT").Range("A1").Offset(Miller and Durnford).Value = current_degree
    Worksheets("WT").Range("B1").Offset(Miller and Durnford).Value = current_wt
    Worksheets("WT").Range("C1").Offset(Miller and Durnford).Value = m_time_of_initial_data
    Worksheets("WT").Range("D1").Offset(Miller and Durnford).Value = m_initial_time_to_print
    Worksheets("WT").Range("E1").Offset(Miller and Durnford).Value = m_final_time_to_print

    Worksheets("sm").Range("A7") = m_time_of_initial_data
    Worksheets("sm").Range("A8") = m_initial_time_to_print
    Worksheets("sm").Range("B8") = m_print_interval
    Worksheets("sm").Range("C8") = m_final_time_to_print
    Worksheets("sm").Range("A70") = m_previous_run

    Change_boundary_condition m_node_number, current_wt          ' change boundary condition
    Application.Wait (Now + TimeValue("0:00:03"))

' **Step 2: Export parameters into .in files*****
    Call twoD_export
    Application.Wait (Now + TimeValue("0:00:05"))
```

```
' **Step 3: Run modelling*****
        Call DemoShellAndWait_Run_NAPL2D_BAT
        Application.Wait (Now + TimeValue("0:00:02"))

' **Step 4: Reformat sat.out and save*****
        Call Open_satout_and_save
        Application.Wait (Now + TimeValue("0:00:01"))

' **Step 5: Reformat sat.out and save*****
        Call Split_file
        If current_degree = wt_start_degree Then
        Application.Wait (Now + TimeValue("0:00:05"))
        Else
        Application.Wait (Now + TimeValue("0:00:05"))
        End If
Next i


End Sub

Sub Change_boundary_condition(node_number As Integer, wt_value As Double)

Dim i As Integer

For i = 1 To node_number

        Worksheets("bc_flow").Cells(2 * node_number + 2 * i, 1) = wt_value 'Stage 1
        'Worksheets("bc_flow").Cells(6 * node_number + 2 * i, 1) = wt_value 'Stage 2
        'Worksheets("bc_flow").Cells(10 * node_number + 2 * i, 1) = wt_value 'Stage 3

Next i

End Sub


Sub Change_water_table_in_bc_flow()
' Change water table in bc_flow for the bottom boundaries for different stages
Dim node_number As Integer
Dim wt_value As Double
Dim stage As String
Dim i As Integer

node_number = Worksheets("sm").Range("B6").Value + 1
wt_value = Worksheets("sm").Range("O5").Value
stage = Worksheets("sm").Range("P5").Value
```

```
For i = 1 To node_number
    If InStr(1, stage, "1") Then
        Worksheets("bc_flow").Cells(2 * node_number + 2 * i, 1) = wt_value 'Stage 1
    End If
    If InStr(1, stage, "2") Then
        Worksheets("bc_flow").Cells(6 * node_number + 2 * i, 1) = wt_value 'Stage 2
    End If
    If InStr(1, stage, "3") Then
        Worksheets("bc_flow").Cells(10 * node_number + 2 * i, 1) = wt_value 'Stage 3
    End If
Next i

End Sub

Option Explicit

Sub Split_file()
    'Declar variables. csv_name also are numbers, it's easier to make them string as file names
    Dim csv_number As Double
    Dim x_node_number As Double
    Dim y_node_number As Double
    Dim csv_row_number As Double
    Dim csv_col_number As Double
    Dim title_row_number As Double
    Dim csv_name As String
    Dim file_direction As String
    Dim file_save_direction As String
    Dim i As Double

    ' Activate worksheet
    Dim wkb As Workbook
    Dim sht As Worksheet

    '**************************************************Change
Here**********************************************
    file_direction = "E:\2D\"
    file_save_direction = "E:\2D\1Datafiles\"
      '**************************************************Change
Here**********************************************
    Set wkb = Workbooks.Open(file_direction & "Sat_backup.csv")
    Set sht = wkb.Sheets("Sat_backup")
    sht.Activate
    Range(ActiveSheet.Cells(1, 1), ActiveSheet.Cells(LastRow, LastCol)).Select
```

```
    title_row_number = 2
    csv_number = count_word_frequency
    ' node number= number of elements in the x or y +1
    x_node_number = Application.Workbooks("2D.xls").Worksheets("sm").Range("A6").Value + 1
    y_node_number = Application.Workbooks("2D.xls").Worksheets("sm").Range("B6").Value + 1
    csv_row_number = x_node_number * y_node_number
    csv_col_number = LastCol


    Set wkb = Workbooks.Open(file_direction & "Sat_backup.csv")
    Set sht = wkb.Sheets("Sat_backup")
    sht.Activate
    For i = 1 To csv_number


        'Extract csv_name from each moment (first row and col in each moment)
        csv_name = Cells((i - 1) * (csv_row_number + title_row_number) + 1, 1).Value
        'Sometimes it can be a float number, better round up

            If csv_name - Int(csv_name) <> 0 Then
                csv_name = Round(csv_name)
            End If
        ' Extract data, range from row 3 col 1 of the data to the last row and col
        Range(Cells((i - 1) * (csv_row_number + title_row_number) + 3, 1), Cells((csv_row_number
+ title_row_number) * i, LastCol)).Select

        Selection.Copy
        Workbooks.Add
        ActiveSheet.Paste
        Application.CutCopyMode = False
        ActiveWorkbook.SaveAs Filename:=file_save_direction & csv_name, _
        FileFormat:=xlCSVWindows, CreateBackup:=False
        ActiveWorkbook.Close SaveChanges:=True
    Next i

    Beep
    ActiveWindow.Close
End Sub

Function count_word_frequency() As Long


    ' Open the sat.out file and activate it, change directory
```

```
    Dim wkb As Workbook
    Dim sht As Worksheet

    Set wkb = Workbooks.Open("E:\2D\Sat_backup.csv")
    Set sht = wkb.Sheets("Sat_backup")
    sht.Activate

    Range(ActiveSheet.Cells(1, 1), ActiveSheet.Cells(LastRow, LastCol)).Select

    Dim FoundCell As Range
    Dim LastCell As Range
    Dim FirstAddr As String
    Dim TotalCount As Integer
    TotalCount = 0

    With Range(ActiveSheet.Cells(1, 1), ActiveSheet.Cells(LastRow, LastCol))
        Set LastCell = .Cells(.Cells.Count)
    End With
    Set FoundCell = Range(ActiveSheet.Cells(1, 1), ActiveSheet.Cells(LastRow,
LastCol)).Find(what:="time,dtmax", after:=LastCell)

    If Not FoundCell Is Nothing Then
        FirstAddr = FoundCell.Address
    End If
    Do Until FoundCell Is Nothing
        TotalCount = TotalCount + 1
        Debug.Print FoundCell.Address
        Set FoundCell = Range(ActiveSheet.Cells(1, 1), ActiveSheet.Cells(LastRow,
LastCol)).FindNext(after:=FoundCell)
        If FoundCell.Address = FirstAddr Then
            Exit Do
        End If
    Loop

    'Application.Workbooks("2D").Worksheets("sm").Range("O21").Value = TotalCount
    count_word_frequency = TotalCount

End Function



Function LastRow() As Long

'Find the last used row in a Column: column A in this example
```

```
    With ActiveSheet
        LastRow = .Cells(.Rows.Count, "A").End(xlUp).Row
    End With

End Function

Function LastCol() As Long
'Find the last used column in a Row: row 2 in this example (Row 1 in this case has only 3 cells but Row 2 is normal)

    With ActiveSheet
        LastCol = .Cells(2, .Columns.Count).End(xlToLeft).Column
    End With

End Function
```

[The end of script]

A.2 Database of the LNAPL migration and redistribution experiments

The database of the LNAPL migration and redistribution experiments comprises the data of the eight scenarios produced in this study, including the mass balance result, the vertical profile data of the saturation distributions of LNAPL, water and air for all photographic events and the videos demonstrating the photographic record and fluid saturation distributions in contours. It is unrealistic to include all raw data for every pixel in every image, which contains millions of values. Every experimental run contains hundreds of images. The pixel-wise data, however, is accessible through the matrices calculated by running the image analysis MATLAB script, and has been visualized by the videos.

A.2.1 The base case scenario (Run4T3)

A.2.1.1 Mass balance and fluid saturation distribution profiles

[Location, name, format]=Appendices\A2_expt_data\1_Run4T3\Release_20150825_Run4T3.xlsx

[Location, name, format]=Appendices\A2_expt_data\1_Run4T3\Run_20150825_Run4T3.xlsx

A.2.1.2 Fluid saturation distribution videos

[Location, name, format]=Appendices\A2_expt_data\1_Run4T3\Run4T3-Release.mp4

[Location, name, format]=Appendices\A2_expt_data\1_Run4T3\Run4T3-Entire.mp4

A.2.2 The low fluctuation speed scenario (Run5T1)

A.2.2.1 Mass balance and fluid saturation distribution profiles

[Location, name, format]=Appendices\A2_expt_data\2_Run5T1\Release_20150507_Run5T1.xlsx

[Location, name, format]=Appendices\A2_expt_data\2_Run5T1\Run_20150507_Run5T1.xlsx

A.2.2.2 Fluid saturation distribution videos

[Location, name, format]=Appendices\A2_expt_data\2_Run5T1\Run5T1-Release.mp4

[Location, name, format]=Appendices\A2_expt_data\2_Run5T1\Run5T1-Entire.mp4

A.2.3 The release timing at the lower most water table position scenario (Run9T1)

A.2.3.1 Mass balance and fluid saturation distribution profiles

[Location, name, format]=Appendices\A2_expt_data\3_Run9T1\Release_20150723_Run9T1.xlsx

[Location, name, format]=Appendices\A2_expt_data\3_Run9T1\Run_20150723_Run9T1.xlsx

A.2.3.2 Fluid saturation distribution videos

[Location, name, format]=Appendices\A2_expt_data\3_Run9T1\Run9T1-Release.mp4

[Location, name, format]=Appendices\A2_expt_data\3_Run9T1\Run9T1-Entire.mp4

A.2.4 The small LNAPL release volume scenario (Run8T1)

A.2.4.1 Mass balance and fluid saturation distribution profiles

[Location, name, format]=Appendices\A2_expt_data\4_Run8T1\Release_20150714_Run8T1.xlsx

[Location, name, format]=Appendices\A2_expt_data\4_Run8T1\Run_20150714_Run8T1.xlsx

A.2.4.2 Fluid saturation distribution videos

[Location, name, format]=Appendices\A2_expt_data\4_Run8T1\Run8T1-Release.mp4

[Location, name, format]=Appendices\A2_expt_data\4_Run8T1\Run8T1-Entire.mp4

A.2.5 The fins sand aquifer scenario (Run10T3)

A.2.5.1 Mass balance and fluid saturation distribution profiles

[Location, name, format]=Appendices\A2_expt_data\5_Run10T3\Release20150906_Run10T3.xlsx

[Location, name, format]=Appendices\A2_expt_data\5_Run10T3\Run_20150906_Run10T3.xlsx

A.2.5.2 Fluid saturation distribution videos

[Location, name, format]=Appendices\A2_expt_data\5_Run10T3\Run10T3-Release.mp4

[Location, name, format]=Appendices\A2_expt_data\5_Run10T3\Run10T3-Entire.mp4

A.2.6 The single partial fine grain layer scenario (Run7T1)

A.2.6.1 Mass balance and fluid saturation distribution profiles

[Location, name, format]=Appendices\A2_expt_data\6_Run7T1\Release_20150630_Run7T1.xlsx

[Location, name, format]=Appendices\A2_expt_data\6_Run7T1\Run_20150630_Run7T1.xlsx

A.2.6.2 Fluid saturation distribution videos

[Location, name, format]=Appendices\A2_expt_data\6_Run7T1\Run7T1-Release.mp4

[Location, name, format]=Appendices\A2_expt_data\6_Run7T1\Run7T1-Entire.mp4

A.2.7 The single complete fine grain layer scenario (Run6T2)

A.2.7.1 Mass balance and fluid saturation distribution profiles

[Location, name, format]=Appendices\A2_expt_data\7_Run6T2\Release_20150530_Run6T2.xlsx

[Location, name, format]=Appendices\A2_expt_data\7_Run6T2\Run_20150530_Run6T2.xlsx

A.2.7.2 Fluid saturation distribution videos

[Location, name, format]=Appendices\A2_expt_data\7_Run6T2\Run6T2-Release.mp4

[Location, name, format]=Appendices\A2_expt_data\7_Run6T2\Run6T2-Entire.mp4

A.2.8 The multiple complete fine grain layers scenario (Run12T1)

A.2.8.1 Mass balance and fluid saturation distribution profiles

[Location, name, format]=Appendices\A2_expt_data\8_Run12T1\Release_20150825_Run12T1.xlsx

[Location, name, format]=Appendices\A2_expt_data\8_Run12T1\Run_20150825_Run12T1.xlsx

A.2.8.2 Fluid saturation distribution videos

[Location, name, format]=Appendices\A2_expt_data\8_Run12T1\Run12T1-Release.mp4

[Location, name, format]=Appendices\A2_expt_data\8_Run12T1\Run12T1-Entire.mp4